ISSN 0972 –1320

JOURNAL

of the

TRIPURA MATHEMATICAL SOCIETY

VOLUME — 23 2021

Proceedings of the International Conference on Emergent Reesearch in Mathematics and Engineering during May 17-18, 2019, NIT, Agartala

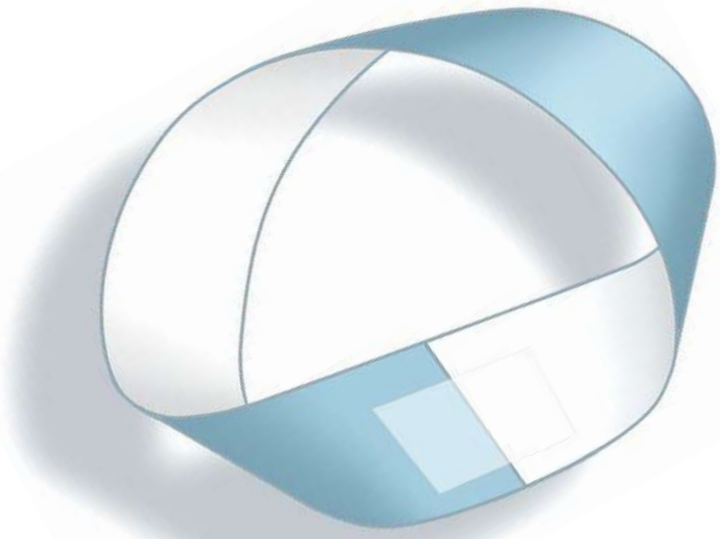

Published by

TRIPURA MATHEMATICAL SOCIETY
Agartala, Tripura, Society

JOURNAL OF THE TRIPURA MATHEMATICAL SOCIETY

website: https://sites.google.com/view/tms-in/home
Email: information.tms@gmail.com

Editor - in - charge
Prof. Binod Chandra Tripathy
Dept. of Mathematics, Tripura University
Suryamaninagar-799022, Agartala, India, Email tripathybc@gmail.com

Softcopy (doc & pdf) of the manuscript may be sent to the Editor-in-Chief or any of the area editors

Editorial

In order to give an exposure to the mathematics community of Tripura, to the International Community in general and National Community in particular, the "Journal of the Tripura Mathematical Society" was brought out. The idea was storming in the brain of Professor Rabi Nanda Bhaumik, the founder Editor-in-Chief, which took the shape in the year 1999 by bringing out its first volume. The journal is publishes one volume annually. It is devoted for publishing research articles following the peer-review process. Occasionally few quality invited review articles from the reputed mathematicians are also published.

The Tripura Mathematical Society organises National/Internal conferences at different Higher Education Institutes in Agartala in order to motivate the young talents to choose mathematics as their career. This gives an opportunity to the young talents to get an exposure to some of the renowned mathematicians. The papers presented in the conferences are brought out as a special volume, in the name of Proceedings of the said conference, following thorough review process.

An International Conference on "Emergent Research in Mathematics and Engineering" (ICERME-2019), was organised by the Department of Mathematics, National Institute of Technology, Agartala during May 17-18, 2019. The volume 23 (2021) is dedicate for the proceedings of this conference. The participants of the conference, includes Professor Valentina Emilia Balas, the renowned fuzzy set theorist of the University of Arad, Romania. A total of 23 number of articles were cleared by the review process for inclusion in the Proceedings for publication. These include the articles not only in the domain area of mathematics, but its application in other areas of science and technology, such as Image processing, Energy development in adsorption refrigeration system, Artificial neural network, Decision making, Approximate entropy, Analysis of Cancer data, Analysis of cardiac Arrhythmia, Hankel transform etc.

Editorial Office

Agartala Journal of the Tripura Mathematical Society

A Notefrom the Organizers of the Conference

The first **International Conference on "Emergent Research in Mathematics and Engineering-2019** (**ICERME-2019**)" is the debut edition of an envisaged series of biennial academic extravaganza, organised by the Department of Mathematics, National Institute of Technology, Agartala (NIT Agartala). This book is the proceedings of**ICERME-2019**.

The conference was organized under the aegis of Technical Education Quality Improvement Programme (**TEQIP**) phase–III of the Ministry of Higher Education, Government of India.

The first issue includes selected peer reviewed research reports and invited addresses as well as contributed papers. Efforts taken by the peer reviewers contributed to improve the quality of papers, provided constructive critical comments, improvements and corrections to the articles are gratefully appreciated.

The primary goal of the conference was to provide a platform to present, discuss, and interact with the researchers in diverse fields of Pure Mathematics, Applied Mathematics and Application of Mathematics in Engineering and giving the unique opportunity to acquaint themselves with the current trend of research. The conference brought Researchers, Educators, Professional Engineers and Technologists under a single forum to discuss/ debate on research in the above said emerging areas. A total of 103 research articles were submitted in the conference, out of which 80 papers were accepted and presented orally during the three days of conference.Finally, among these articles 27 are accepted for publication in the Journal of Tripura Mathematical Society.The Proceeding of ICERME-2019 provides an up-to-date reference book for researcher working in the areas of Mathematical Science and Engineering.

We are very grateful to the International/National Advisory Committee Members, Session Chairs, and Administrative Assistancefrom Institute management, who selflessly contributed to the success of this Conference. Also, we are thankful to all the authors from USA, Nigeria, Bangladesh, and India, who submitted their research contributions in ICERME-2019, because of which the conference became a story of success. It was the quality of their presentation and their passion to communicate with the other participants that really made this conference a grand success.

We wish to express our sincere thanks toProf. H. K. Sharma, Director NIT Agartala for his constant encouragement and all round support to make this event a grand success. We are extremely thankful to Prof.Dr. Alexander Pott (Germany), Prof. Dr. Alexander Blokh (USA), Prof. R.N. Bhaumik (Emeritus Fellow,UGC)Rtd. Prof. of Math,Tripura University, Prof. B.C. Tripathy (Tripura Central University)Prof. AncaRalescu (USA), Prof. Adriana Coroiu (Romania), Prof.Guojun Wang (China), Prof.Lakhmi C. Jain (Australia), all the faculties of the Department of NIT Agartala for their dedicated help to organise this prestigious academic event. We sincerely appreciate the tireless effort extended by the scholars of the Department of Mathematics, NIT Agaratala who made it possible to organize the event a successful one.

Last, but most importantly, we are thankful for the enormous support of Tripura Mathematical Society for supporting us in publishing the selected papers in the form of a Special Volume from presented research articles in ICERME-2019.

Edited by:

Prof. Debasish Bhattacharya (ICERME, Co-Chairperson)

Dr. Baby Bhattacharya (ICERME, Organizing Secretary)

Message from the Patron & Chairperson

Professor Harish Kumar Sharma
Director, NIT Agartala

Its gives me immense pleasure to note that the Department of Mathematics, NIT Agartala is organizing an "International Conference on Emergent Research in Mathematics and Engineering-(ICERME-2019)" during May 17-18, 2019. Under the competitive environment, productive research findings have become increasingly important to the researchers and society. In this respect, this type of conferences has immense importance, therefore the Institute actively encourages conferences, training programs and workshops in the relevant areas. I hope that this multifaceted endeavor will enrich the minds of all the participants especially, our young Mathematicians and Engineers.

It gives me sense of satisfaction in mentioning that a great amount of collective efforts have been put in to organizing the conference. I feel free to state that the conversation and interlocution by distinguished academicians and resource persons during the conference will impel and enlighten the young participants with latest trend of research in the target fields.

I on behalf of NIT Agartala fraternity, heartily welcome all my dear academicians, corporate delegates and all the presenters, attending this conference and wish a grand success to ICERME-2019.

Prof. H. K. Sharma

Message from Keynote Speaker

Professor Valentina E. Balas
"Aurel Vlaicu" University from Arad, Romania

I am pleased to welcome you all to participate in the International Conference on "Emergent Research in Mathematics and Engineering - (ICERME-2019), organized by NIT Agartala, India, during May 17th & 18th, 2019.

We live in an age where research and technology have become King. Technology is changing the way we live, learn and work. In recent years a lot of research took place in the field of Mathematics and Engineering, area that is concerned with the development of next generation of intelligent systems.

I congratulate National Institute of Technology Agartala for such an initiative and hope that the conference will be used to enrich the knowledge through valuable researches. I am sure the conference will evolve to become one of the most important international conferences.

I would like to express my warm thanks to the organizing committee, speakers, reviewers, authors and to all people that supported the conference.

The International Conference on "Emergent Research in Mathematics and Engineering - (ICERME-2019) is serving to establish an international community of scientists and engineers for exchange of ideas and information. I know that all participants will return home with a great deal of information which you will acquire at the conference and with fond memories after staying in Agartala, a beautiful city.

Thank you all for your active participation and wish you to enjoy the conference with fruitful results.

Valentina Emilia Balas, Arad, Romania

Message from Chief Guest

Professor Parthasarathi Chakraborty
Director, IIEST Shibpur

It is heartening to note that the Department of Mathematics, National Institute of Technology, Agartala is going to organize 'International Conference on Emerging Research in Mathematics and Engineering (ICERME-2019)' during May17-18, 2019.

The Conference will provide a platform where the researchers from various disciplines, professionals, academicians and representatives from various industries can discuss, deliberate and share knowledge on various issues and challenges before the researchers in view of unprecedented advancement of technology in recent years. It would also provide a unique opportunity to young researchers to learn for the experiences of their papers.

I, on behalf of the IIEST, Shibpur congratulate the organizers for their untiring efforts in organizing the conference.

Wish the Conference a great success!

09.05.2019

Prof. Parthasarathi Chakraborty

Message from a Distinguished Mathematician of Tripura

Professor Rabi Nanda Bhaumik
Distinguished Mathematician of Tripura

The first International Conference on "Emergent Research in Mathematics and Engineering-2019 (ICERME-2019)", was organized by the Department of Mathematics, National Institute of Technology, Agartala, (NITA) Tripura, India on May 17th & 18th, 2019.

Mathematical Research in the state of Tripura during 1970's was an initiative undertaken by me. I take immense pride that one of my students who was also, the first Ph.D. in Mathematics from Tripura University, Dr. Debasish Bhattacharya along with NITA and I collaborated in this venture. I would like to express my warm thanks to the Department of Mathematics, NIT Agartala, Tripura for this International Conference in Mathematics.

I am also delighted to share that it will be published in the Journal of Tripura Mathematical Society, which I established in 1999. I hope that the deliberations of this conference would be good guidance, source of inspiration and bring new ideas to the scholars and research students on the recent trends.

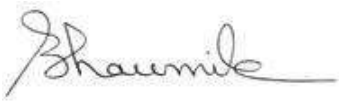

Prof. R. N. Bhaumik

Message from Dean R&C and TEQIP Coordinator

Professor Ardhendu Saha
Dean R&C and TEQIP Coordinator, NIT Agartala

Greeting to the conveners and organizers of the conference - International Conference on "Emergent Research in Mathematics and Engineering 2019 (ICERME 2019)" hosted at NIT Agartala during 17- 18th May, 2019.

This conference promises to provide a platform for researchers, engineers and academicians with diverse research interest to present their research results and development activates in Mathematics, Applied Mathematics and Engineering Application of Mathematics. I hope this will foster interactions between researchers and practitioners focused on disciplinary, inter-disciplinary and trans-disciplinary issues, ideas, concepts, theories, methodologies and applications. The exchange of concepts, research ideas, and other results could contribute not only to the academic arena but also benefit business, and the industrial community.

The Technical Education Quality Improvement Program (TEQIP) is a World Bank assisted program initiated by the Government of India. It aims at quality improvement in technical education system of India by sponsoring support to the students, faculties, and PhD scholars for attending Conference, Workshop, and Seminars etc. Under the program the Departments conduct Seminars, Conference, Workshops, and Short-Term Training Programs etc.

I wish all the very success of the conference. I am delighted and look forward to be a part of this conference.

With Regards

Prof. Ardhendu Saha

NIT Agartala

2D Pose Information Extraction in a Manhattan World from a Single Image Based on Cross Ratio

Ajay Kumar Chaurasiya[1], Navin Karanth P[2]
, and K V Gangadharan[3]

[1,2,3]Department of Mechanical Engineering, NITK Surathkal, Mangalore, Karnataka, India
[1]aj.ac2095@gmail.com, [2]navinkaranth@gmail.com, [3]kvganga@nitk.edu.in

Abstract. Pose estimation in robotics and computer vision is a typical problem of determining an object's position and orientation relative to some coordinate system. This paper assesses the indoor 2D pose estimation problem using a monocular camera in a Manhattan world. Proposed method utilizes transformations in homogeneous coordinate system, cross ratio - a projective geometry technique along with vanishing points found in indoor environment. This approach is facilitated by the fact that most of the indoor environments are rich in horizontal and vertical lines that are used to detect vanishing points. Cross ratio enables the estimation of unknown 2D pose on a coplanar surface. Experimental results of the proposed method show that using a single image of indoor environment, 2D positioning can be achieved effectively. A maximum of 1.12% and 1.08% error was found during pose estimation in the selected X and Y axis respectively.

Keywords: pose estimation, cross ratio, homogeneous coordinate, projective geometry, vanishing point, single image, perspective

1 Introduction

Measurement and positioning of static and moving objects is a fundamental challenge and also one of the important tasks in computer vision, robotics and photogrammetry. Various sensors and techniques for positioning and distance measurement have been developed such as ultrasonic sensors, laser sensors, bluetooth, radar systems, etc., [1], [2] and [3]. Each has its own advantages and disadvantages over the others.

A positioning system making use of camera as sensory input followed by different image processing techniques to define the image characteristics and estimate target position is called visual positioning system. Unlike other sensory inputs, a camera image is a rich source of visual information. It provides data about the envirionment in a way humans perceive them. Interests towards image based techniques have grown recently due to many reasons such as ease of availability of cameras, powerful computing devices, right balance of reliability, cost and usability. The existing image based techniques can be classified into two categories: monocular vision and stereo vision. Stereo vision requires two cameras and hence more expensive in terms of cost and computation, but is highly accurate [4], [5] and [6]. In comparison, monocular vision having only one camera is less accurate but cheaper and easier to handle [7], [8], [9], [10], [11], [12] and [13].

This work aims at using a single image from a monocular camera to estimate 2D pose on a coplanar surface. The proposed method makes use of cross ratio and vanishing points to estimate 2D pose. Amount of computation involved is very less i.e., equivalent to a couple of simple arithmetic operations.

2 Related Work

Numerous researchers over the years have worked on positioning and measurement using camera. Most of the work is using stereo vision which requires two cameras and are quite accurate in estimation. Such works find applications in wide range of areas like robotics, location and position

estimation, object tracking, intelligent transport systems. In recent years interest towards indoor positioning using monocular camera has grown. Many researchers have already contrubuted and are still working in this research area. Positioning is fundamentally a distance measurement task. A camera to surface distance measurement method using monocular camera is illustrated in [14]. It requires two images of the object such that both the images are captured while moving the camera along its optical axis. Depth estimation with monocular camera using camera parameters and image geometry is discussed in [7]. Basic camera parameters such as focal length, field of view, camera resolution and height of camera mounting must be known. Image based distance measurement proposed in [9] is quite accurate with a maximum of 1.15% error. It makes use of a laser beam projected on the image such that laser beam is almost parallel to the optical axis of camera.

A low cost fuzzy logic based 2D positioning system is developed in [15]. A dual axis accelerometr along with signal processing algorithms was used. Based on wireless sensor network technology an indoor 2D positioning system was developed by Mikhail in [16]. The author had implemented different algorithms and positioning methods: fingerprinting, triangulation and fingerprinting with K weighted nearest neighbour algorithm. A similar 2D positioing system for indoor environments can be found in [17]. It is based on usage of GPS signals with repeaters.

The method proposed in this paper utilizes only a monocular camera as sensory input. It does not require a prior knowledge of camera parameters such as focal length, field of view, camera orientation, etc. or a laser beam to be projected on the image for depth estimation. Only one image is required to do the computation and estimate unknown 2D pose. Proposed method aims to help in developing less sophisticated applications which can be used in everyday activities.

Rest of the paper is organized as follows, section 3 provides a brief background on principles of the proposed method. Section 4 gives details on the proposed methodlogy along with a pseudocode. Section 5 discusses results of the experiments carried out followed by conclusions in section 6.

3 Background

3.1 Cross Ratio

Cross ratio in geometry is a number associated with a list of four collinear points, particularly points on a projective line. On any line l, for a set of given four points A, B, C and D, the cross ratio is defined as,

$$CR(A, B; C, D) = \frac{AC.BD}{BC.AD} \tag{1}$$

For a set of any given four points the cross ratio will always remain constant. Cross ratio is invariant to perspective transforms. In fig. 1, the two cross ratio expressions of a given line l and its transformed version l' will always be equivalent. This can be written as,

$$CR(A, B; C, D) = CR(A', B'; C', D') \tag{2}$$

3.2 Vanishing Points

One of the distinguishing features of perspective projection is that image of an object that stretches off to infinity can have finite extent. For example, an infinite seen line is imaged as a line terminating at a point. This point is called as vanishing point. The parallel world lines such as railway lines, are imaged as converging lines in perspective projection i.e., an image. The image intersection of parallel lines is called vanishing point. A comprehensive text on vanishing points in the field of computer vision can be found in [18] and [19]. It has applications in various fields such as camera calibration, robotic navigation, scene understanding, 3d reconstruction, etc. Fig. 2 shows the imaged vanishing point of a railway track and a hallway.

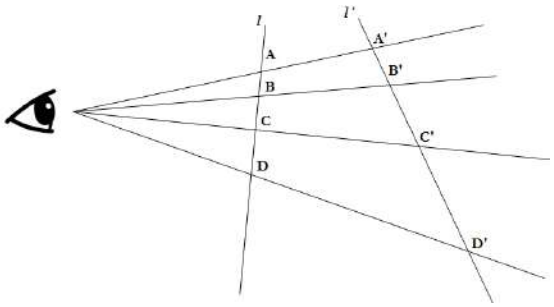

Fig. 1. Invariant cross ratio

(a) Railway track (b) Hallway

Fig. 2. Imaged vanishing points of (a) Railway track and (b) Hallway

3.3 2D Lines as Geometric Primitives

Under the category of geometric primitives, there are many topics to be studied. Since this work is more concerned with 2D lines in projective space, only those have been covered here. For a more detailed theory and understanding of the geometric primitives, readers may refer to [18] and [19]. 2D lines in homogeneous coordinates can be represented as $\tilde{\boldsymbol{l}} = (a, b, c)$. The corresponding line equation is

$$\bar{\boldsymbol{x}}.\tilde{\boldsymbol{l}} = ax + by + c = 0 \tag{3}$$

where $\bar{\boldsymbol{x}} = (x, y, 1)$. In homogeneous coordiates, intersection of two lines can be computed as

$$\tilde{\boldsymbol{x}} = \tilde{\boldsymbol{l_1}} \times \tilde{\boldsymbol{l_2}} \tag{4}$$

where, $\times$ is the cross product operator. Similarly, the line joining two points can be written as,

$$\tilde{\boldsymbol{l}} = \tilde{\boldsymbol{x_1}} \times \tilde{\boldsymbol{x_2}} \tag{5}$$

From eqn. 4 and eqn. 5 it is clear that points and lines are dual in projective space. Cross product of two points gives a line passing through them. And the cross product of two lines gives the point of intersection. This duality holds true only in projective space.

4 Methodology

4.1 Assumptions

Like most other methods, the proposed method here makes a few assumptions with respect to environment and the camera used. They are listed in detail as follows,

- Imaged environment follows the Manhattan world assumption i.e., the scene observed is made up of natural cartesian x, y, z coordinate system.
- Plane used for 2D pose estimation is coplanar.
- On this plane 2 collinear distances for X-axis and 2 for Y-axis are known.
- Images used, have no lens distortions i.e., straight lines in real world remain straight in the image as well.
- If the camera images are distorted, camera calibration is already done to undistort the images.

The camera used in this work had slight lens distortions and hence camera calibration had to be done. Camera calibration helps to estimate true parameters of a camera using images of a special calibration pattern. It is an important preprocessing step in computer vision. Camera calibration is not included in the scope of this paper, as calibration process itself is a considerable amount of task to be studied and implemented. Though it is not been discussed in detail in this paper, readers are encouraged to have a look at [20]. The calibration process developed by Zhang et al. in [20] was used in this work.

4.2 Proposed Method

The cross ratio of a line on a plane will always be constant irrespective of its perspective transform. Consider a line $\boldsymbol{l_x}$ on the ground plane with four points $\boldsymbol{A, B, C, D}$ marked on it. Distances between those points are known in metres. When this line $\boldsymbol{l_x}$ is imaged, its perspective transform $\boldsymbol{l'_x}$ will have corresponding four points $\boldsymbol{A', B', C', D'}$ in image. The distances between these four points in image can be found in terms of pixels. Since the corresponding four points considered in image and on the ground plane are same, their cross ratios in terms of pixels and metric will be equivalent. This is given by eqn 2. Using this fact, one unknown distance between the given four points $\boldsymbol{A, B, C, D}$ can be computed if pixel cross ratio is known. Since a plane is made up of lines, the concept of cross ratio can hence be extended froma a line to a plane. This can be explained using fig 3.

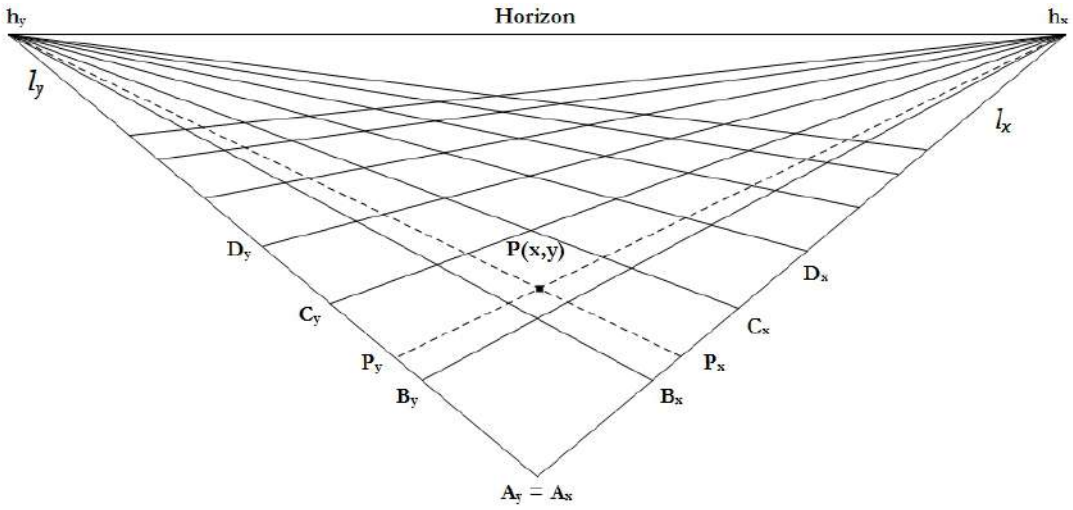

Fig. 3. Vanishing points on a plane meeting at the horizon

All the parallel lines meet at a common vanishing point as shown in fig. 3. Using eqn. 2 distance between any two points on lines $\boldsymbol{l_x}$ and $\boldsymbol{l_y}$ individaully can be computed. For any arbitrary point $\boldsymbol{P(x, y)}$ on the plane, its projection on lines $\boldsymbol{l_x}$ and $\boldsymbol{l_y}$ gives two new points. These new points can be denoted by $\boldsymbol{P_x}$ and $\boldsymbol{P_y}$ on the lines $\boldsymbol{l_x}$ and $\boldsymbol{l_y}$ respectively. The two new cross ratio eqns for the points $\boldsymbol{Ax, P_x, C_x, D_x}$ and $\boldsymbol{Ay, P_y, C_y, D_y}$ can be written as,

$$CR(A_x, P_x; C_x, D_x) = \frac{A_xC_x.P_xD_x}{P_xC_x.A_xD_x} \qquad along\ \ l_x \tag{6}$$

$$CR(A_y, P_y, C_y; D_y) = \frac{A_yC_y.P_yD_y}{P_yC_y.A_yD_y} \qquad along\ \ l_y \tag{7}$$

Equations. 6 and 7, each has only one unknown to be solved. Equating the two cross ratios individually to its equivalent pixel cross ratio gives the solution for unknown distance. A pseudocode explaining the entire pose estimation process is provided in subsection 4.3.

4.3 Pseudocode for the Proposed Method

Algorithm 1 2D Pose Estimation

Input: Perspective Image of a ground plane similar to fig. 3 or fig. 5
Output: 2D coordinates of a randomly selected point on the ground plane
Process:
1: Select a point $\bar{A}_x = \bar{A}_y = (x_0, y_0)$ chosen to be origin on the ground plane
2: Select any 2 points $\bar{A}'_x$ and $\bar{B}'_x$ in the image such that corresponding line (A_xB_x) is parallel to X in real world
3: Select any 2 points $\bar{A}'_y$ and $\bar{B}'_y$ in the image such that corresponding line (A_yB_y) is parallel to Y in real world
4: Convert all the inhomogeneous coordiantes to homogeneous form (Eg. $\bar{A}_x = \bar{A}_y = (x_0, y_0) \Rightarrow \tilde{A}_x = \tilde{A}_y = (x_0, y_0, 1)$ and so on.)
5: Compute $\tilde{\boldsymbol{l_x}} = \tilde{\boldsymbol{A_x}}\tilde{\boldsymbol{B_x}}$
6: Compute $\tilde{\boldsymbol{l_y}} = \tilde{\boldsymbol{A_y}}\tilde{\boldsymbol{B_y}}$
7: Compute $\tilde{\boldsymbol{l'_x}} = \tilde{\boldsymbol{A'_x}}\tilde{\boldsymbol{B'_x}}$
8: Compute $\tilde{\boldsymbol{l'_y}} = \tilde{\boldsymbol{A'_y}}\tilde{\boldsymbol{B'_y}}$
9: Compute vanishing point along X axis $\tilde{\boldsymbol{h_x}} = \tilde{\boldsymbol{l_x}}\tilde{\boldsymbol{l'_x}}$
10: Compute vanishing point along Y axis $\tilde{\boldsymbol{h_y}} = \tilde{\boldsymbol{l_y}}\tilde{\boldsymbol{l'_y}}$
11: Select two points $\bar{B}_x$ and $\bar{C}_x$ on the imaged line chosen to be X axis on the ground such that $d(A_xB_x)$ and $d(A_xC_x)$ is known
12: Select two points $\bar{B}_y$ and $\bar{C}_y$ on the imaged line chosen to be Y axis on the ground such that $d(A_yB_y)$ and $d(A_yC_y)$ is known
13: **loop**
14: **if** New point P selected **then**
15: Convert the inhomogeneous P to homogeneous form: $\bar{\boldsymbol{P}} = (P_x, P_y) \Rightarrow \tilde{\boldsymbol{P}} = (P_x, P_y, 1)$
16: Compute line formed by P parallel to X: $\tilde{\boldsymbol{lp_x}} = \tilde{\boldsymbol{P}}\tilde{\boldsymbol{h_x}}$
17: Compute line formed by P parallel to Y: $\tilde{\boldsymbol{lp_y}} = \tilde{\boldsymbol{P}}\tilde{\boldsymbol{h_y}}$
18: Compute projection P_x of point P on l_x: $\tilde{\boldsymbol{P_x}} = \tilde{\boldsymbol{l_x}}\tilde{\boldsymbol{lp_y}}$
19: Compute projection P_y of point P on l_y: $\tilde{\boldsymbol{P_y}} = \tilde{\boldsymbol{l_y}}\tilde{\boldsymbol{lp_x}}$
20: Compute $d(A_xP_x)$ using cross ratio: $\boldsymbol{CR(A_x, B_x; C_x, P_x)} = \frac{(\boldsymbol{A_xC_x}).(\boldsymbol{B_xP_x})}{(\boldsymbol{B_xC_x}).(\boldsymbol{A_xP_x})}$
21: Compute $d(A_yP_y)$ using cross ratio: $\boldsymbol{CR(A_y, B_y; C_y, P_y)} = \frac{(\boldsymbol{A_yC_y}).(\boldsymbol{B_yP_y})}{(\boldsymbol{B_yC_y}).(\boldsymbol{A_yP_y})}$
22: Display: $\boldsymbol{P = (P_x, P_y)}$
23: **else**
24: Wait for the new point P to be selected
25: **end if**
26: **end loop**

4.4 Tools and Equipments Used

The camera used in this work is a commercially available IP camera with focal length of 3.6 mm, from Dahua Technology. Images with a resolution of 704x576 pixels were used. Computations were done on a laptop having intel Core i5 7^{th} Gen processor. OpenCV library was put to use for basic operations on images. Results obtained are discussed in the following sections.

5 Results and Discussions

All the measurements discussed here are in SI units. In order to evaluate the proposed method, experiments were carried out to estimate 2D pose of any arbitrarily selected point on the ground plane. To do so, images of the ground plane were taken from a surveillance camera mounted near ceiling. A snip of the calibrated image from the surveillance camera is shown in fig. 4.

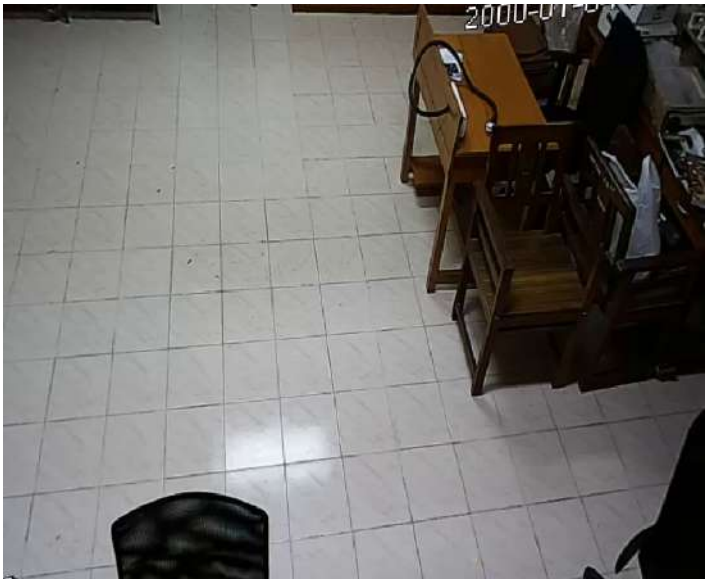

Fig. 4. Calibrated image of the ground plane used for evaluation of the proposed method

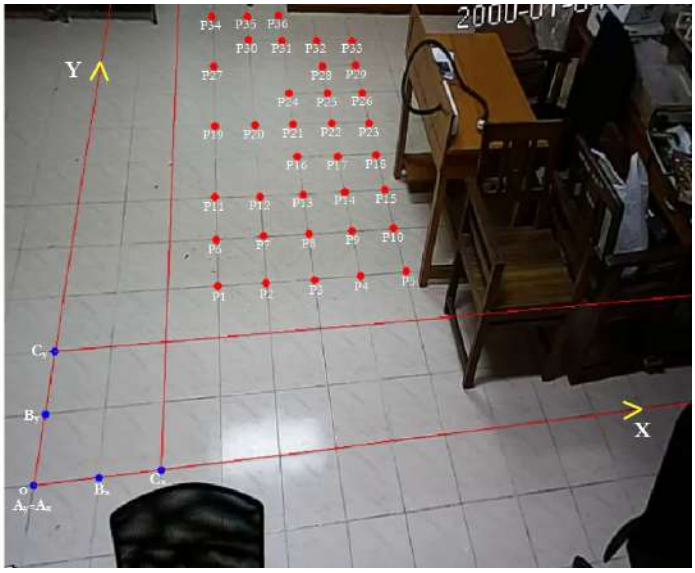

Fig. 5. Points selected on the ground plane for 2D pose estimation

5.1 2D Pose Estimation on a Ground Plane

As observed in fig. 5, an origin point O ($A_x = A_y$) was chosen in the image followed by defining of X and Y axis lines shown in red colour. Next, two more lines were defined in the image, each parallel to X and Y axis in real world. These pairs of real world parallel lines were then used to establish vanishing points in X and Y directions. As seen in fig. 5 both the vanishing points $\tilde{\boldsymbol{h_x}}$ and $\tilde{\boldsymbol{h_y}}$ do not lie in the image space. Instead they exist somewhere outside the image space. Still the mathematical realtion of intersection of points and lines makes it possible to define their existence using homogeneous coordiante system. Next, two points on each axis ($\boldsymbol{B_x}, \boldsymbol{C_x}$ and $\boldsymbol{B_y}, \boldsymbol{C_y}$) with known distance from origin were defined. The lines $\tilde{\boldsymbol{C_x}}\tilde{\boldsymbol{h_y}}$ and $\tilde{\boldsymbol{C_y}}\tilde{\boldsymbol{h_x}}$ define the lower limit of usable workspace in the image space. Later, various points were selected in the imaged ground plane to get 2D pose estimated by the algorithm. As illustrated in fig. 5, the various points selected, are marked sequentially and the estimated and actual pose was recorded.

5.2 Results and Error

The results obtained are plotted in fig. 6 showing the acutal as well as estimated 2D pose for each point selected in the imaged ground plane. As observed in fig. 6, the proposed method could effectively give the 2D pose estimate. Of course, there were slight deviations in the estimation. The maximum error was found to be 1.12% in X direction and 1.08% in Y direction on the ground plane. A plot of percentage error for each selected point in X and Y directions is illustrated in fig. 7. It is interesting to note that the error did not increase gradually with increase in distance.

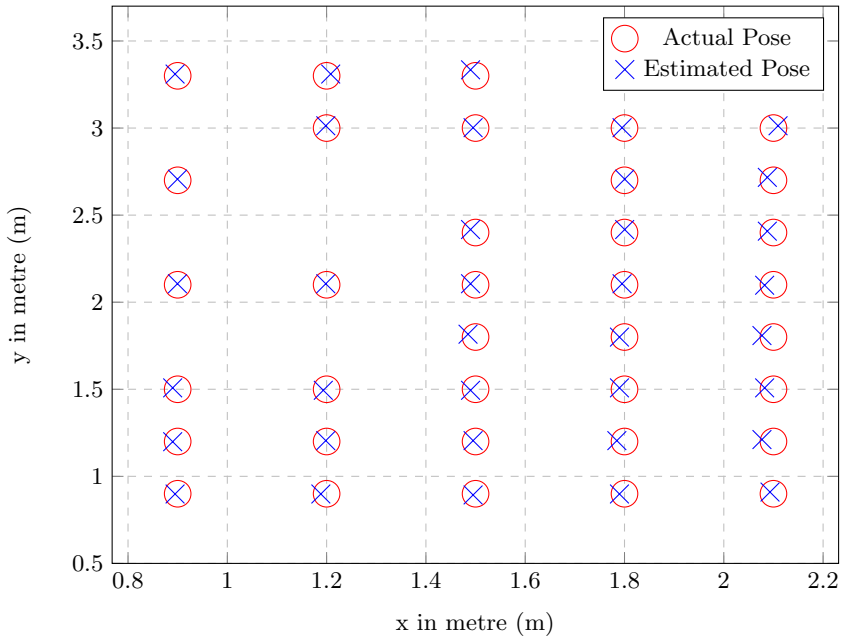

Fig. 6. Comparison between actual and estimated pose of selected points on the ground plane

5.3 Important Discussions

Throughout the process of 2D pose esetimation, no information on camera parameters were provided to the algorithm. Still the proposed algorithm could effectively estimate the 2D pose on the ground plane. Also, the images used were not captured from a predefined standard camera

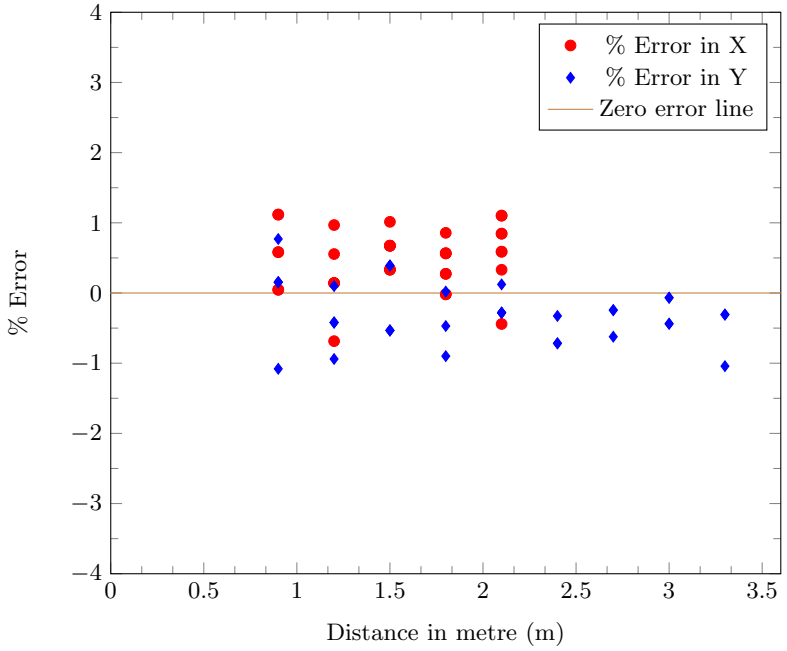

Fig. 7. % Error in X and Y directions in pose estimaion

orientation like parallel to ground plane. This provides a proof of concept that cross ratio is not affected by perspective transformation. Though the image used did not follow euclidean coordinate system due to perspective projection, the pose estimation algorithm could still do the job. This is due to existence of vanishing points in a perspective space and the invariance of cross ratio.

6 Conclusion

In this paper we have proposed a method of estimating 2D pose on a coplanar surface using a single image from a monocular camera. This is achieved using cross ratio technique. Two cross ratio expressions, one in terms of pixel and the other in terms of metric, are equated to obtain the estiamted 2D pose. Proposed method is validated with the experimental results shown. Using a single image captured from an unknown camera orientation, the proposed algorithm could estimate the 2D pose on a coplanar surface with a good accuaracy. The amount of computation required in this method includes only a few simple arithmetic operations. Hence, the processing time is very low. This can be used in development of less sophisticated applications not demanding very high accuracy.

As a part of future work, techniques to detect parallel lines in image and thereby estimate vanishing points can be incorporated. This will reduce the uncertainity involved due to human interference. Later, this technique may be extended from a plane to 3D space.

Acknowledgment

The authors acknowledge the support and experimental facility provided by Centre for System Design (CSD): A Centre of Excellence at NITK-Surathkal.

References

1. F. Rivard et al., “Ultrasonic relative positioning for multi-robot systems”, Robotics and Automation 2008. ICRA 2008. IEEE International Conference on, pp. 323-328, 2008.

2. M. S. Bargh, R. D. Groote, "Indoor localization based on response rate of bluetooth inquiries", Proceedings of the first ACM international workshop on Mobile entity localization and tracking in GPS-less environments, pp. 49-54, 2008.
3. J. Bisson, F. Michaud, D. Létourneau, "Relative positioning of mobile robots using ultrasounds", Intelligent Robots and Systems 2003.(IROS 2003). Proceedings. 2003 IEEE/RSJ International Conference on, pp. 1783-1788, 2003.
4. M. A. Mahammed, A. I. Melhum, F. A kochery, "Object distance measurement by stereo vision", International Journal of Science and Applied Information Technology (IJSAIT), vol. 2, no. 2, pp. 05-08, 2013.
5. D. K. Patel, P. A. Bachani, N. R. Shah, "Distance measurement system using binocular stereo vision approach", Int J Eng Res Technol, vol. 2, no. 12, pp. 2461-2464, 2013.
6. C. J. Erkelens, "Perspective Space as a Model for Distance and Size Perception", i-Perception, vol. 8, no. 6, 2017.
7. A. Joglekar et al., "Depth estimation using monocular camera", International journal of computer science and information technologies, vol. 2, no. 4, pp. 1758-1763, 2011.
8. M. N. A. Wahab, N. Sivadev, K. Sundaraj, "Target distance estimation using monocular vision system for mobile robot", Open Systems (ICOS) 2011 IEEE Conference on, pp. 11-15, 2011.
9. T. H. Wang et al., "Distance measurement using single non-metric CCD camera", Proc. 7th WSEAS Int. Conf. Signal Process. Comput. Geom. Artif. Vision, pp. 1-6, 2007.
10. M. I. Arenado et al., "Monovision-based vehicle detection distance and relative speed measurement in urban traffic", IET Intelligent Transport Systems, vol. 8, no. 8, pp. 655-664, 2014.
11. K. Hsu et al., "Development and Application of the Single-Camera Vision Measuring System", Journal of Applied Sciences, vol. 8, no. 13, pp. 2357-2368, 2008.
12. P. Paerhati, "Real-time monocular depth mapping system using variance of focal plane and pixel focus measure", PhD Thesis, 2017.
13. L. Y. Xu et al., "A new monocular vision measurement method to estimate 3D positions of objects on floor", International Journal of Automation and Computing, vol. 14, no. 2, pp. 159-168, 2017.
14. N. Yamaguti, S. Oe, K. Terada, "A method of distance measurement by using monocular camera", Proceedings of the 36th SICE Annual Conference. International Session Papers, pp. 1255-1260. 1997.
15. Jerome Gaysse, "A low cost absolute 2D position calculation system", 2006 SICE-ICASE International Joint Conference.
16. Mikhail M. Komarov, "A 2D indoor positioning system based on a wireless sensor network technology for power adjustable solutions", IEEE, 7th International Conference on Service-Oriented Computing and Applications, pp. 300-303. 2014.
17. Özsoy, K., Bozkurt, A., & Tekin, İ. "2D Indoor positioning system using GPS signals", IEEE, International Conference on Indoor Positioning and Indoor Navigation, (pp. 1-6). (2010).
18. Szeliski, R. "Computer vision: Algorithms and Applications", Springer Science & Business Media. (2010).
19. Hartley, R., & Zisserman, A. "Multiple view geometry in computer vision", Cambridge university press. (2003).
20. Zhang, Z. "A flexible new technique for camera calibration", IEEE Transactions on Pattern Analysis and Machine Intelligence, 22. (2000).

Analytical analysis on Entropy and Exergy development in adsorption refrigeration system

Mainak Bhaumik[1*], Laxmi Deepak Bhatlu M[2], Anirban Sur[3]

[1]Department of Mechanical Engineering, MGM's College of Engineering, New Mumbai - 410209, India

[2]Department of Chemical Engineering, Karpagam Academy of Higher Education, Coimbatore-641021, India

[3]Department of Mechanical Engineering, Symbiosis International Deemed University, Lavale, Pune-412115, India

[1*]mainak.bhaumik04@gmail.com

Abstract

An analytical mathematical investigation has been carried out on adsorption refrigeration system. In this analysis the entropy generation and exergy destroyed is the main focus and point of interest. Entropy generation and exergy destroyed go together. Entropy is the function of temperature. Apart from coefficient of performance (COP) of the adsorption refrigeration it is also require understanding and investigating about entropy generation and exergy destroyed phenomena in adsorption refrigeration system. A model of adsorption refrigeration of control volume is taken under consideration to know the influence of entropy and exergy in the system.

Keywords: Entropy, Exergy, adsorption refrigeration, COP

1. Introduction

An adsorption refrigeration system has been tried in fishing vessel, vehicle exhaust system etc. by various authors. Adsorption refrigeration system research and investigation is becoming popular due to use of exhaust waste heat thermal energy utilization. This system of refrigeration doesn't require any external electric power. No motor driven compressor is used. If water is used as a refrigerant it can give humidity effect [1-3]. No recycling of the refrigerant. Water is getting evaporated due to the exhaust gas energy then it's getting condensed in the

condenser and through the expansion valve passed into the economizer with cooling effect as well as humidification comfort. Such system of adsorption refrigeration can replace desert cooler, where there is instant need of motor driven electric power supply. Hence the involvement of rotary device for refrigeration system can be avoided [4-10]. The refrigeration effect can be achieved by using cheap and easily available normal domestic water which is popularly used in desert cooler. In such system of refrigeration other various refrigerants also used like ammonia, methanol, ethanol etc. In adsorption / desorption system basically uses activated carbon or silica gel, charcoal etc. to adsorbed shoot, carbon CO, CO_2 and other impurities from the waste exhaust gas. The system is quite cheaper but the COP is lesser [11-13]. The basic model on which study and investigation is to be carried out consists of an adsorption vessel or tank, condenser heat exchanger, expansion valve and economizer. The schematic diagram of the model system set up is as shown in the Fig. 1 [14-19].

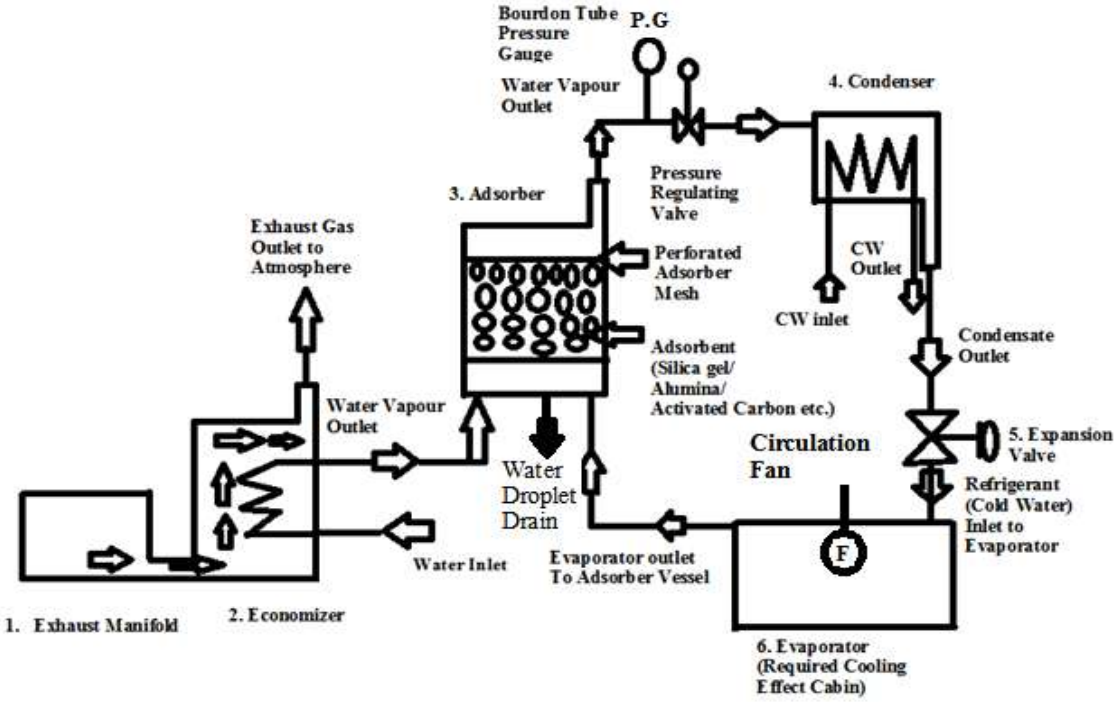

Fig. 1: Schematic diagram of Adsorption refrigeration system.

2. Problem Definition

The problem involves about the mathematical analysis of exergy and entropy influence in each individual five major components (1.Economizer 2. Adsorber 3.Condenser 4.Expansion Valve and 5.Evaporator) and the system overall COP (Co-efficient of Performance) and SOP (Specific Cooling Power). The exhaust gas of diesel engine has been considered to flow in the economizer shell side at a temperature ranging in between 250 to 550^{o}C. The atmospheric cooling water temperature ranging 25 to 45^{o}C enters into the economizer tube side for the study and analysis. The evaporator outlet water vapour enters into the adsorber bed carrying temperature ranging from 90 to 120^{o}C for study and analysis. The collected water droplets can be drained from the bottom of the adsorber vessel. The adsorber outlet vapours develops pressure more than atmospheric one. Assuming the pressure developed by the water vapours in the range of 1.5 to 3 kg/cm^2 for analysis and after achieving the minimum pressure of 1.5 kg/cm^2 , the pressure control regulating valve allows the water vapour to flow in the shell side of the condenser. Considered the atmospheric cooling water in the range of 25 to 45^{o}C has been supplied into the tube side of the condenser. Condenser cooling water outlet can be cooled using radiator fan and can be recycled. The condenser outlet admits into the thermostatic expansion valve. In the thermostatic expansion valve the pressure drops and hence temperature also drops. The temperature drop and thermal energy drop in the expansion valve is to be calculated for the expansion inlet temperature range of 30 to 35^{o}C and assuming outlet temperature range in between 20 to 28^{o}C. It is also assumed that the expansion valve inlet pressure is 1.5 to 3 kg/cm^2 and at the outlet the pressure is within the range of 1.2 to 1.5 kg/ccm^2. The expansion outlet temperature range 200 to 280^{o}C enters into the evaporator where the desired cooling effect has been experienced. Considering the temperature and heat values the COP and SCR to be determined.

3. Analytical Analysis

Economizer Section:

The analytical analysis carried out on the major units like economizer, adsorber, condenser and evaporator. Economizer is nothing but a shell and tube type heat exchanger. To find exchanger effectiveness or efficiency and other entropy and exergy values, the following relations are used,

ϵ =Actual Heat Transfer Rate / Maximum Possible Heat Transfer Rate = Q/Q_{max}.

C_c = capacity ratio = C_{min} / C_{max}

Where, ϵ = Economizer heat exchanger effectiveness or efficiency.

$Q = C_c [T_c \text{ out} – T_c \text{ in}] = C_h [T_h \text{ in} – T_h \text{ out}]$ in kW

$C_c = m_c C_{pc}$ in kW / ^oK

$C_h = m_{ch} C_{ph}$ in kW / ^oK

Q_{max} = Cmin $[T_h \text{ in} – T^c \text{ in}]$ in kW

C_{min} is the smaller valve out of C_h and C_c

This is about available energy or exergy calculation. The entropy generation can be calculated using the relation,

$S_g = (S_2 – S_1)$ in kJ/ kg K

Hence exergy destroyed can be find out using,

$X_d = (T_o \times S_g)$ in kJ / kg

Adsorption section:

The Fig. 2 shows the adsorption section with the unknowns required to find for investigation and analysis. To investigate about adsorber section the following isotherms are considered,

Freudlich Isotherm is used to find the mass of adsorption (x),

$x/m = k P^{1/n}$

Where, x = Mass of adsorbate which adsorbed

m = Mss of adsorbent

P = Pressure of adsorbate

k and n = Empirical constants for each adsorbent-adsorbate pair at given temperature.

Langmuir Isotherm is used to find the effective adsorption surface coverage of the adsorber section. The more effective adsorption phenomena depend on the higher porousness of the adsorbent. So the used Langmuir isotherm to determine the adsorption surface coverage (θ) is,

$\theta = KP / (1+ KP)$

Where, θ = Adsorption surface coverage area

P = Partial pressure of the adsorbate in the concentration.

$K = k / k^{-1}$

k= Direct rate constants

k^{-1} = Inverse rate constants

Adsorption Enthalpy:

For energy investigation of the adsorber section, it is desired to find the adsorption enthalpy development. The following relation has been used to find the adsorption enthalpy assuming that the entropy remains same,

$\Delta H_{ads.} = \Delta H_{liq.} - RT \ln c$

where, $\Delta H_{ads.}$ = Adsorption Enthalpy

$\Delta H_{liq.}$ = Enthalpy of liquefaction

R = Universal gas constant = 0.287 kJ/kg K = Assuming ideal gas.

T = Temperature of adsorbate in K.

c = Langmuir parameter for given adsorbent-adsorbate at particular temperature c = Langmuir parameter for given adsorbent-adsorbate at particular temperature.

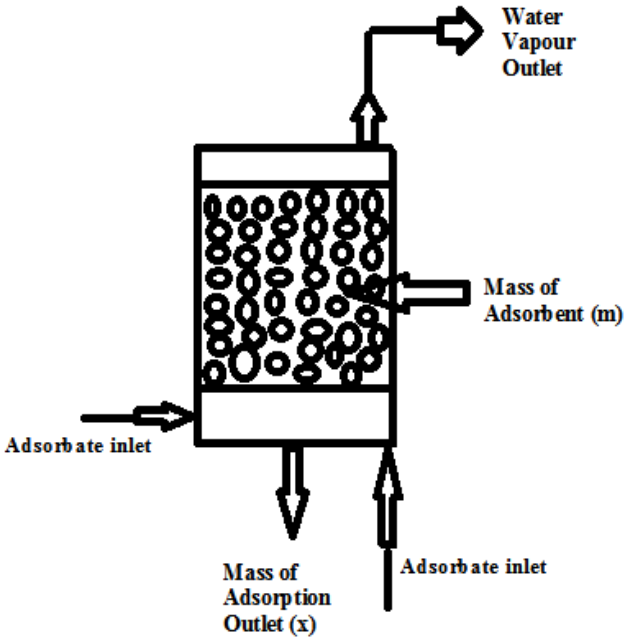

Fig. 2: Adsorber column with the notations for analysis.

Condenser:

The thermal analysis carried out in the shell and tube type surface condenser within the control volume section, to know about the successive heat transfer rate in the condenser section

to convert vapours into liquid. Fig. 3 illustrates about the condenser section control volume for thermal analysis. The mathematical relations used are as follows,

$$Q = h\ A\ [T_v - T_s]$$

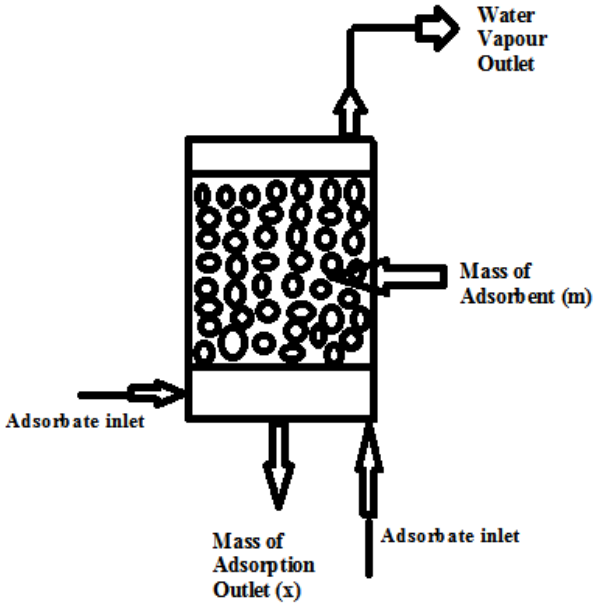

Fig. 2: Adsorber column with the notations for analysis.

Where, Q = Heat transfer rate in W

h = Average heat transfer co-efficient up to Length of tube L, in $W/m^2\ K$

from data table selected h = 9600 to 24400. The h can be calculated using relation,

$h= Z\ [(N * L\ ) / W]^{0.33}$

where, Z = Condensation co-efficient = 15413 (Taken from data table for steam at 100^0C)

N = Number of tubes

L = Length of tube

W = Weight of condensate in N/s or N/hr.

(Or) $h = 0.728\ [(k^3\rho^2 g\ hfg) / (\mu D\ (T_v - T_s))]^{0.25}$

where, k= Thermal conductivity of the liquid in W/mk

ρ = Density of fluid in kg/m^3

g= acceleration due to gravity = $9.81\ m/s^2$

h_{fg}= Latent heat of vaporization, J/kg

μ= Viscosity of liquid

L= Length of tube

D = Diameter of shell tube sheet in m.

T_v = Vapor temperature in ^oC

T_s = Condenser outlet temperature at the surface in ^oC

A = Condenser surface flow area in m^2

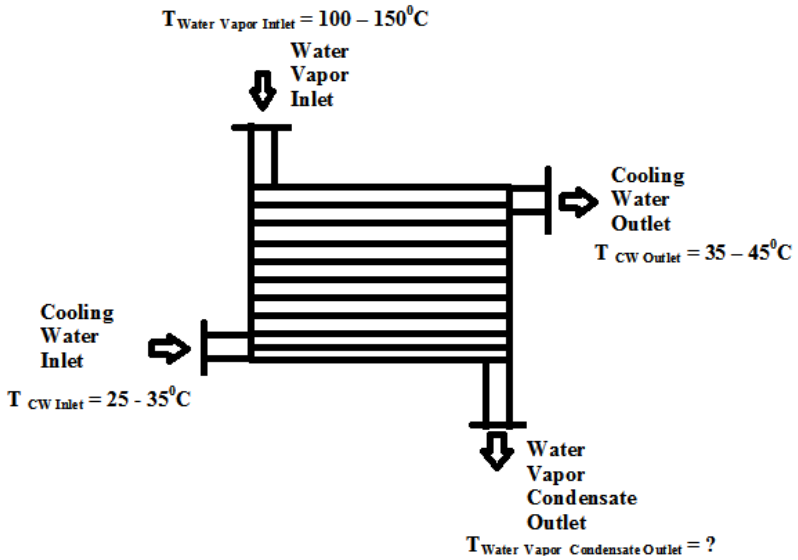

Fig. 3: Schematic Diagram of Shell and Tube type surface Condenser for study and analysis.

Expansion valve throttling:

The thermostatic expansion valve does the drop in pressure and hence temperature drops. In thermostatic expansion valve enthalpy drops takes place to give cooling effect in the evaporator section. Fig. 4 shows the schematic diagram of thermostatic expansion valve for thermal analysis. The following expressions are taken under consideration to carried out the thermal analysis in the expansion valve,

$$\Delta H = h_{inlet} - h_{outlet} \text{ in kJ/kg}$$

The entropy generation can be determined using,

$$S_g = S_{outlet} - S_{inlet} \text{ in kJ/kg K}$$

The exergy destroyed can also be determined using,

$$X_d = T_o S_g$$

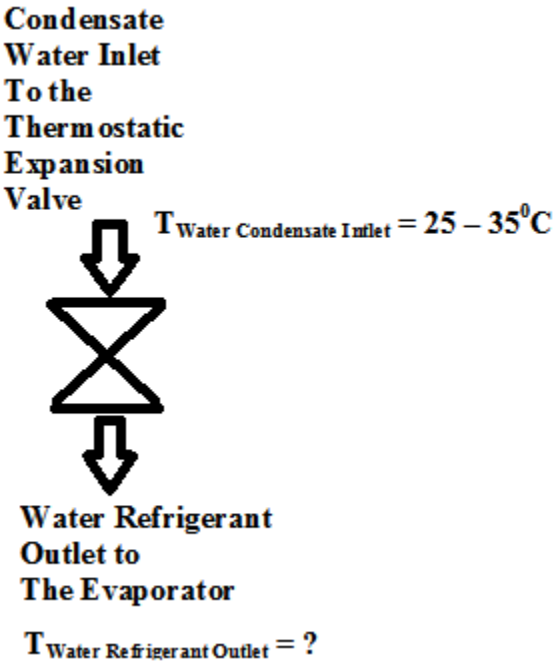

Fig. 4: Schematic Diagram of Thermostatic Expansion valve under study and analysis.

Evaporator:

The evaporator section is the place where the desired cooling effect to be achieved and maintain. The Fig. 5 shows the evaporator section considered for analysis and study. For a particular comfort temperature the evaporator performance to be determined i.e. COP of the evaporator section to be determined to understand the system performance. To determined COP the following expression is used,

$$COP = T_{inlet} / (T_{outlet} - T_{inlet})$$

Here also entropy analysis can be carried out using the relation,

$$S_g = S_{outlet} - S_{inlet} \text{ in kJ/kg K}$$

And exergy analysis uses the relation,

$$X_d = T_o S_g$$

To find the specific cooling power, SCP, it is required to use the expression as,

$$SCP = Q\ evp. / (m\ ads * T\ cycle)$$

Where, Q = Evaporative heat transfer = $m\ c_p\ \Delta T$

m ads= Mass of adsorbent

T = Cyclic time

m = mass of refrigerant (water)

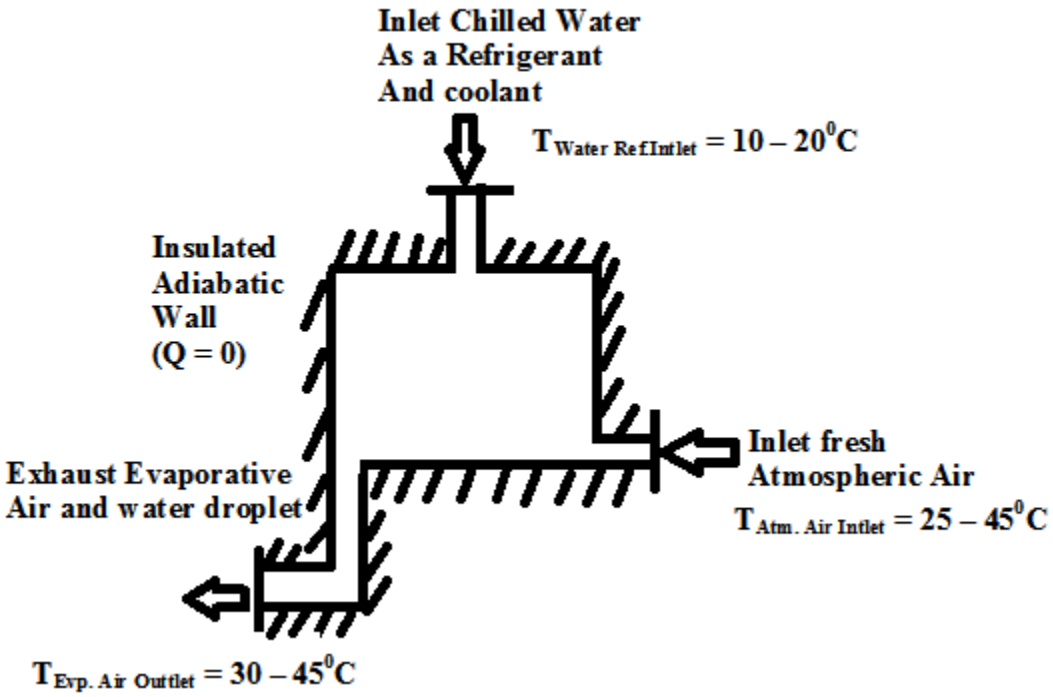

Fig. 5: Schematic Diagram of Evaporator considered for study and analysis.

4. Results and discussions

Economizer Section

In analytical analysis it is considered that there is adiabatic heat transfer from the economizer, adsorption column, condenser, expansion valve, and evaporator and of course from all the associated pipelines. It is also considered that all the heat experiencing elements are hot insulated and the cold experiencing pipelines and substances are cold insulated to avoid heat loss. Starting from economizer investigation, it is considered that the exhaust gas received from a four stroke six cylinder Truck diesel engine of Model 6BT 5.9TC(SE1613TC), available data taken from Tata Automobiles manufacturers for analysis. The engine bore is 102mm and length 120 mm and each engine volumetric capacity is 980.55 C.C. Hence total six cylinders volumetric capacity is, Vtotal =5883 C.C. The maximum given speed of engine is 2500 RPM i.e. N = 2500 RPM. To find the exhaust gas mass flow rate the considered speed is N= 2000 RPM for analysis.

The crankshaft rotates at half of the engine speed, i.e. N/2 = 2000/2 RPM and hence the exhaust stroke is 1000 per minute. Assuming uniform flow of air, we get exhaust gas mass flow rate as,

Engine Exhaust gas mass flow rate, $Q_{exhaust}$ = (Each engine capacity x Engine Exhaust stroke per minute)

$Q_{\text{ each engine exhaust}} = V_{\text{each engine}}$ x (N/2) = 980.55 x (2000/2) = 9,80,550 C.C. / min = 0.0163 m^3/sec. Approximately for analytical analysis.

Therefore total six engines exhaust volume flow rate is, $V_{total} = V_{each}$ x 6 = 0.0163 x 6 = 0.0978 m^3/sec. To determine the engine exhaust mass flow rate, here is the relation,

Density = Mass / Volume

$$\rho_{gas} = m_{gas} / V_{\text{total exhaust}}$$

Considering the density of gas at 250^0C is 0.674 kg/m^3

$$0.674 = m / 0.0978$$

Hence the exhaust hot gas mass flow rate is, m_h= 0.0659 kg/s. approximately.

Considering economizer heat exchanger is an unmixed multi-pass economizer heat exchanger for analysis. The hot exhaust gas exchanges heat with cooled atmospheric water in a 1-shell pass and 8-tube pass heat exchanger. The economizer water tubes are of thin-walled and made of copper with an internal diameter of 12 mm and external diameter of 15 mm. The length of each pass in the heat exchanger is 5 m and the tubes overall heat transfer co-efficient, U = 310 W / m^2 ^{o}C.

Let, the water flows through the tubes at a rate of, mc = 0.02 kg/s.

Considered specific heat of water at maximum atmospheric temperature 40^{o}C is ,

C_{pc} = 4.187 kJ/kg K

The exhaust hot flue gas specific heat at 250^{o}C is ,

C_{ph} = 1.038 kJ/kgK

Therefore,

$C_c = m_c C_{pc}$ = 0.02 x 4.187 = 0.0837 kW / K and

$C_h = m_h C_{ph}$ = 0.0659 x 1.038 = 0.068 kW / K

So**, $C_{min} = C_h$ =0.068** kW /K

$C_{max} = C_c$ =0.0837 kW/ K

Hence, capacity ratio c = C_{min} / C_{max} = 0.068 / 0.0837

c = 0.81

Therefore, to determine the maximum heat transfer rate Q_{max}, at Exhaust hot gas inlet temperature Th in = 250°C and at atmospheric cold water inlet temperature into the economizer pipe, Tc in = 30^0C

Q_{max}. = C_{min} ($T_h$in – $T_c$in) = 0.068 (250 – 30)

Q_{max}=14.96 kW

Using NTU method to find effectiveness and economizer shell side exhaust hot gas outlet temperature and economizer tube outlet temperature, required to use the following relations,

NTU = U As /C_{min}

Where, NTU = Number of Transfer Units

U = Economizer tubes overall heat transfer coefficient = 310 W/m^2 °C = 0.310 kW/m^2°C

As = Economizer tubes inner surface peripheral area = n (π D L)

n = No of Economizer tubes = 8

D = Economizer tubes internal diameter = 12 mm = 0.012 m

L = Economizer tubes length = 5 m.

As = 8 (π x 0.012 x 5) = 1.51 m^2

Therefore, NTU = 0.310 x 1.51 / 0.068

NTU= 6.88

From the chart of Effectiveness -1 Shell Pass, 2, 4 , 6, 8 …. Tube Passes of heat transfer and heat exchanger data table,

The effectiveness in percentage obtained is, 64%

Therefore , ϵ = 64%

ϵ= 0.64

The actual rate of heat transfer Q is,

ϵ = Q / Q_{max}

0.64 = Q / 14.96

Therefore, **Q = 9.57 kW**

Using the actual heat transfer rate relation to find out the economizer shell side outlet hot water temperature and the economizer tube side outlet water temperature, this is as follows-

Q = C_h(T_h in – T_h out) = Cc (T_c out – T_c in)

Q = C_h (T_h in – T_h out)

9.57 = 0.068 (250 – T_h out)

T_h out = 109.26 ºC

$Q = C_c (T_c \text{ out} - T_c \text{ in})$

$9.57 = 0.0837 (T_c \text{ out} - 30)$

T_c out = 144.33ºC

So it can be noted that the temperature of the atmospheric cooling water will rise from 30 to 144.33ºC and the engine exhaust flue gas temperature will reduce down from 250 to 109.26ºC during the session of heat transfer in the economizer heat exchanger with economizer effectiveness of 64%.

For different value calculations of exhaust hot gas temperature into the economizer shell and for different values of economizer tubes inlet temperatures the Qmax and Q has been calculated which has been plotted in Fig. 6. The varying heat flow v/s hot gas outlet and the cold water outlet have been plotted in the Fig. 7 and in Fig.8.

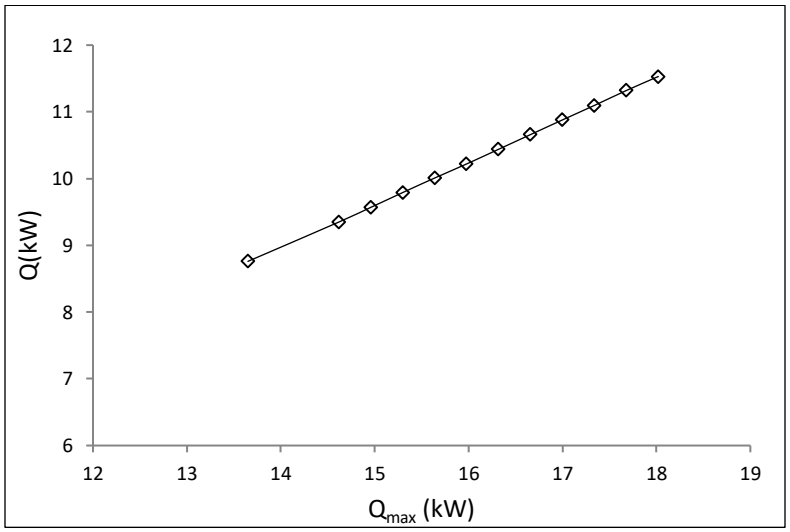

Fig. 6: Actual and maximum heat development plots for different values of temperature and for same fixed value of C_{min} and ϵ.

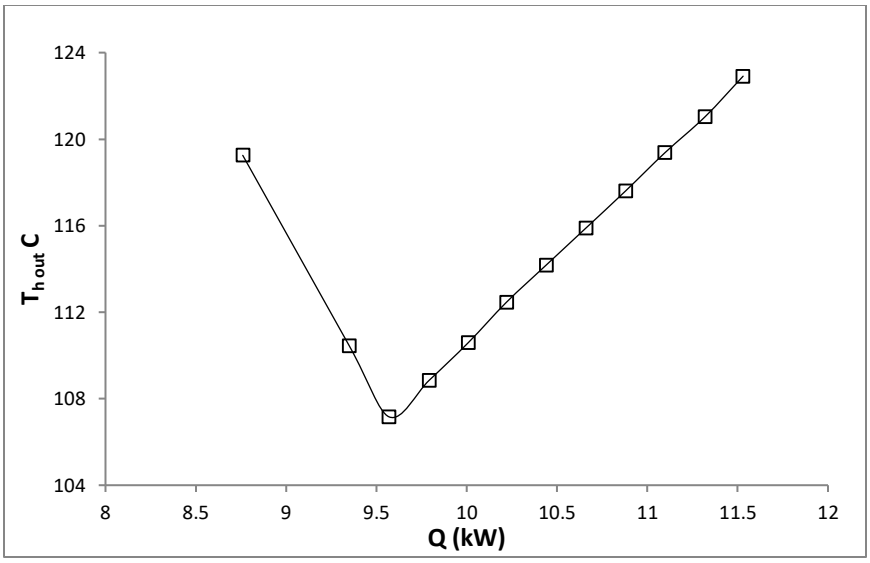

Fig. 7: The heat flow v/s hot gas outlet temperature.

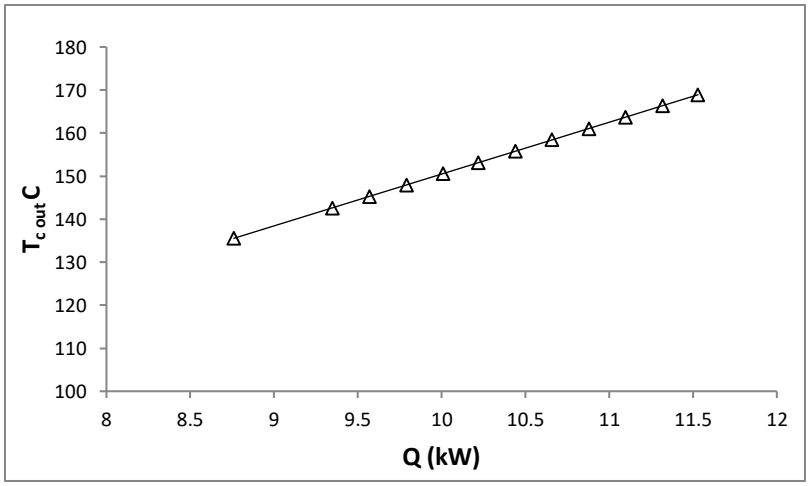

Fig. 8: The heat flow v/s cold water outlet temperature.

Now moving to find entropy generation and exergy destroyed in the economizer tubes,

By applying entropy balance in the economizer tubes,

$\Delta S = S_{in} - S_{out} + S_{generation}$

As the economizer tubes acts as an open loop system after the initial period of settlement.

Therefore for steady state mass flow $\Delta S = 0$

So, $Sg = S_{out} - S_{in}$

$Sg = (S_2 - S_1)$

From steam table, $S_1 = S_{f1} = 0.4369$ kJ / kg K at $T_1 = 30^oC$ and

$S_2 = S_{f2} = 5.0934$ kJ / kg K at $T_2 = 144^oC$ and

Therefore, Sg = (5.0934 – 0.4369)

Sg = 4.6565 kJ / kg K

Exergy destroyed due to entropy generation is given by, X_d = To Sg where $T_o = 30^0C = 303$ K

Therefore, $X_d = 303 \times 4.6565$

X_d = 1410.92 kJ / kg

The entropy generation and exergy destroyed in the economizer tube section has been calculated and the same has been plotted in the Fig.9.

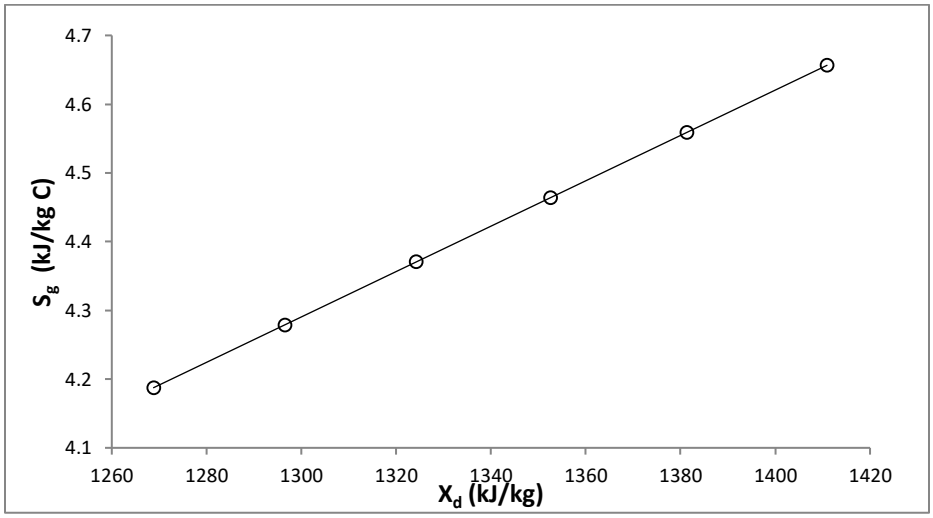

Fig. 9: Exergy v/s Entropy Generation in the economizer tube section.

By carrying out the entropy balance within the exhaust flue gas, the entropy generation within the exhaust flue gases passing through the economizer shell section can be determined for steady state open loop system. In case of open loop system the change in entropy is zero. Hence entropy generation is equal to the subtraction of entropy out and entropy in, which is as written below,

$\Delta S = S_{in} - S_{out} + S_{gen}$

Therefore, $S_{gen} = (S_{out} - S_{in})$

$S_{gen} = (Q / T_{h\,out}) - (Q / T_{h\,in})$ KW/^{o}C

The exergy is destroyed is $X_d = T_o \times S_g$ kW

The calculated values of exergy destroyed and entropy generation has been shown in Fig.10

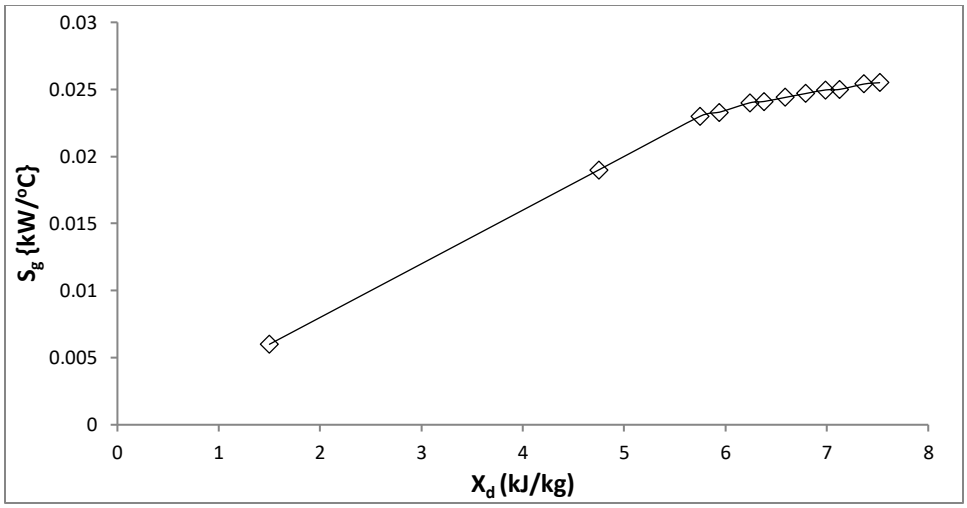

Fig. 10: Exergy destroyed (X_d) v/s Entropy generation (S_g) analysis within the exhaust hot gas.

Condenser:

It is presumed that the outlet vapour from the adsorber column enters into the condenser is of dry steam. The dry vapour steam temperature (T_v) has been taken in the range from 119 to 168°C. Atmospheric water temperature or surface temperature (Ts) has been taken from 30 to 40°C. The selected inlet vapour size of internal diameter has been taken as 50 mm. So the fixed vapour flow rate area is 0.0196 m^2. The average heat transfer co-efficient of steam has been taken as 9600 W/m^2 K. The Fig. 11 plots the condenser inlet steam temperature v/s heat transfer rate.

It is also analyzed about the entropy generation and exergy destroyed in the condenser section. The same has been plotted in the Fig. 12.

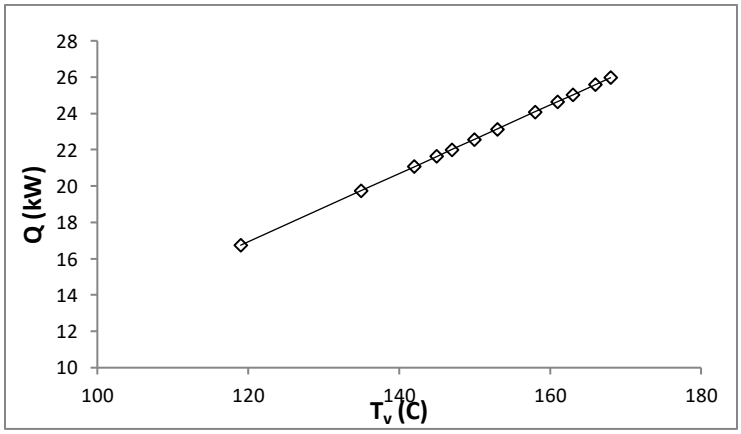

Fig.11: Vapour inlet temperature (T_v) v/s heat flow rate (Q)

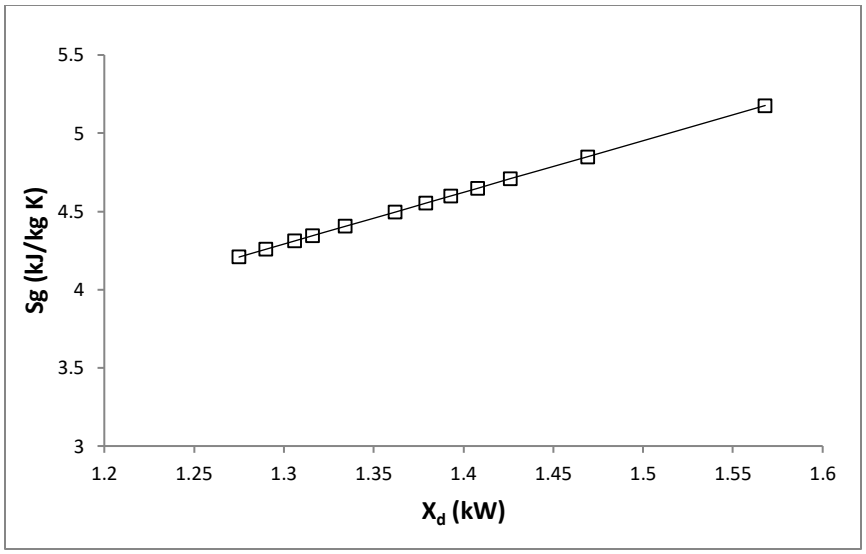

Fig.12: Condenser Exergy destroyed v/s entropy generation.

Expansion valve:

The selected expansion valve is ASB20 (American Standard Brass type material) of inlet size 1/4" (approximately 6.35 mm) ODF (Outer diameter of orifice) and outlet size of 3/8" (approximately 9.525 mm) ODF. The capacity range is from 1 to 4 with pressure drop 3 bar and outlet temperature maintaining capacity up to 10^{o}C. In our calculation it has been taken that the orifice inlet temperature is from 40 to 80^{o}C and with outlet temperature of 20^{o}C.The enthalpy values are taken from steam table for different temperature and calculations done to find enthalpy drop. The enthalpy drop v/s temperature has been plotted in the Fig. 13. Using the data from the steam table the exergy destroyed and the entropy generation within the expansion valve has been calculated. It is being plotted in the graph and shown in the Fig. 14.

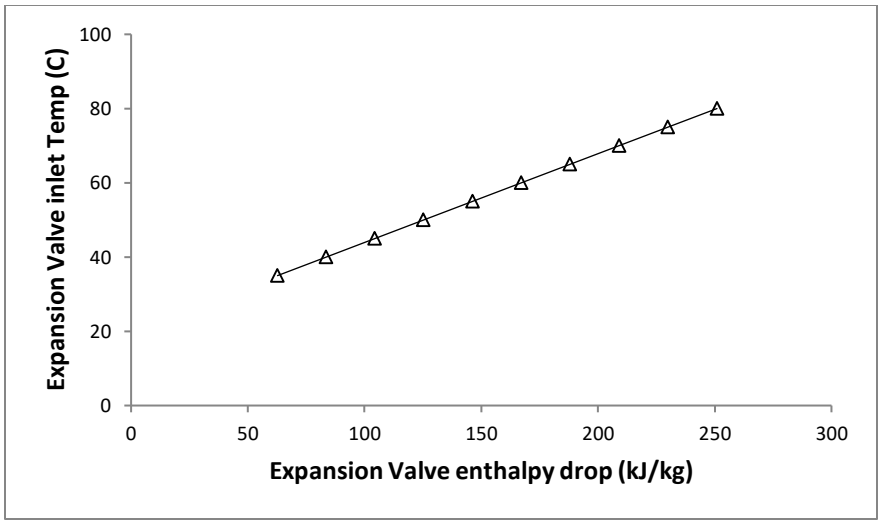

Fig.13: Expansion valve inlet temperature vs. Expansion Valve enthalpy drop

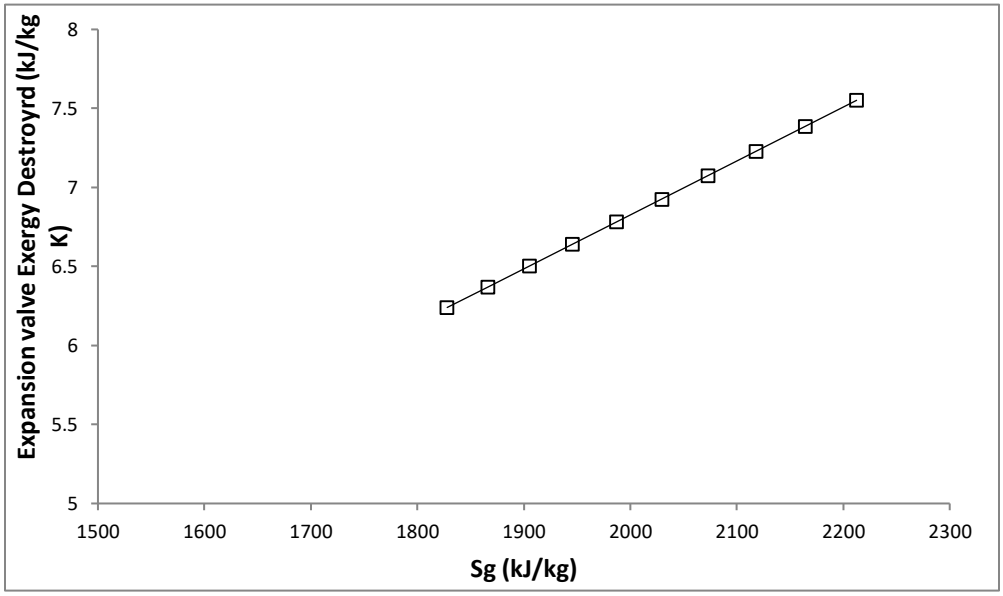

Fig.14: Expansion valve Exergy Destroyed (X_d) v/s Entropy Generation (S_g) plot.

Evaporator:

It is considered that the evaporator inlet temperature is within the range from 16 to 25^{o}C with the fixed outlet temperature of evaporator as 40^{o}C. It is observed that with the increase in inlet temperature from 160 to 250^{o}C for fixed exit temperature, the COP increases gradually. The data has been plotted and shown in the Fig. 15.

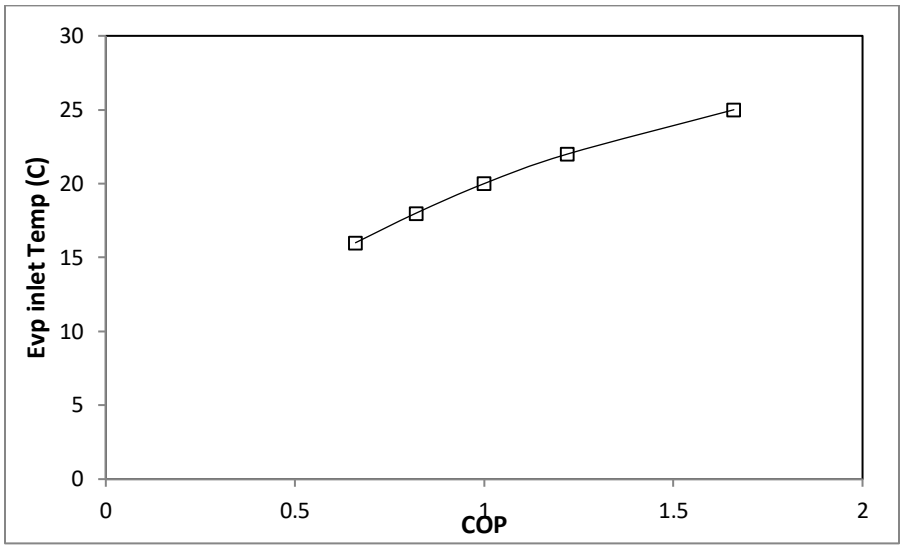

Fig. 15: Evaporator inlet temperature vs. Evaporator COP.

5. Conclusions

The analytical analysis carried out in each major section considering the control volume to find out the available energy, entropy generation, exchanger effectiveness and system COP. The analytical values can be compared with the experimental values. It was found that engine exhaust waste heat has been utilized in the economizer section with effectiveness of 0.64.The economizer exhaust heat and temperature also calculated to know the utilization of engine exhaust temperature. For the economizer minimum inlet temperature of 250^{o}C, the ΔT found is 131^{o}C. In case of evaporator and overall system performance, for evaporator minimum inlet temperature of 16^{o}C and evaporator maximum outlet temperature of 40^{o}C, the COP is 0.66. With the increase in evaporator inlet temperature from 16 to 25^{o}C, with fixed outlet temperature of the evaporator of 40^{o}C, the COP increases gradually from 0.66 to 1.66. Hence by conducting an experiment and by maintain the optimum theoretical parameters of the system the performance of the system can be checked and optimum COP can be determined.

References

[1] Sah, R. P., Choudhury, B., Das, R. K., Sur, A.: An overview of modelling techniques employed for performance simulation of low-grade heat operated adsorption cooling systems.

Renewable and Sustainable Energy Reviews, 74, 364-376 (2017). doi.org/10.1016/j.rser.2017.02.062

[2] Ambarita, H., Kawai, H.: Experimental study on solar-powered adsorption refrigeration cycle with activated alumina and activated carbon as adsorbent. Case Studies in Thermal Engineering, 7, 36-46 (2016). doi.org/10.1016/j.csite.2016.01.006

[3] Xu, S. Z., Wang, R. Z., Wang, L. W.: Temperature–heat diagram analysis method for heat recovery physical adsorption refrigeration cycle–Taking multi-stage cycle as an example. *International Journal of Refrigeration*, *74*, 254-268 (2017) doi.org/10.1016/j.ijrefrig.2016.09.021

[4] Fernandes, M. S., Brites, G. J. V. N., Costa, J. J., Gaspar, A. R., Costa, V. A. F.: Review and future trends of solar adsorption refrigeration systems. Renewable and Sustainable Energy Reviews, 39, 102-123 (2014). doi.org/10.1016/j.rser.2014.07.081

[5] Hassan, H. Z., Mohamad, A. A., Al-Ansary, H. A., Alyousef, Y. M.: Dynamic analysis of the CTAR (constant temperature adsorption refrigeration) cycle. Energy, 77, 852-858 (2014). doi.org/10.1016/j.energy.2014.09.071

[6] Alam, K. A., Sarker, M. M. A., Rouf, R. A., Saha, B. B.: Effect of mass recovery on the performance of solar adsorption cooling system. Energy Procedia, 79, 67-72 (2015). doi.org/10.1016/j.egypro.2015.11.479

[7] Li, T. X., Wang, R. Z., Kiplagat, J. K., Chen, H.: Experimental study and comparison of thermochemical resorption refrigeration cycle and adsorption refrigeration cycle. Chemical Engineering Science, 65(14), 4222-4230 (2010). doi.org/10.1016/j.ces.2010.04.022

[8] Sarbu, I., Sebarchievici, C.: Review of solar refrigeration and cooling systems. Energy and buildings, 67, 286-297 (2014). doi.org/10.1016/j.enbuild.2013.08.022

[9] Wang, L. W., Bao, H. S., Wang, R. Z.: A comparison of the performances of adsorption and resorption refrigeration systems powered by the low grade heat. Renewable Energy, 34(11), 2373-2379 (2009). doi.org/10.1016/j.renene.2009.02.011

[10] Wang, D. C., Li, Y. H., Li, D., Xia, Y. Z., Zhang, J. P.: A review on adsorption refrigeration technology and adsorption deterioration in physical adsorption systems. Renewable and Sustainable Energy Reviews, 14(1), 344-353 (2010). doi.org/10.1016/j.rser.2009.08.001

[11] Xu, X., Li, Y., Yang, S., Chen, G:. A review of fishing vessel refrigeration systems driven by exhaust heat from engines. Applied Energy, 203, 657-676 (2017). doi.org/10.1016/j.apenergy.2017.06.019

[12] Goyal, P., Baredar, P., Mittal, A., Siddiqui, A. R.: Adsorption refrigeration technology–An overview of theory and its solar energy applications. Renewable and Sustainable Energy Reviews, 53, 1389-1410 (2016). doi.org/10.1016/j.rser.2015.09.027

[13] Chekirou, W., Boukheit, N., Karaali, A.: Heat recovery process in an adsorption refrigeration machine. International Journal of Hydrogen Energy, 41(17), 7146-7157 (2016). doi.org/10.1016/j.ijhydene.2016.02.070

[14] Ma, L., Rui, Z., Wu, Q., Yang, H., Yin, Y., Liu, Z., Wang, H.: Performance evaluation of shaped MIL-101–ethanol working pair for adsorption refrigeration. Applied Thermal Engineering, 95, 223-228 (2016). doi.org/10.1016/j.applthermaleng.2015.09.023

[15] Pan, Q. W., Wang, R. Z., Wang, L. W.: Comparison of different kinds of heat recoveries applied in adsorption refrigeration system. International Journal of Refrigeration, 55, 37-48 (2015). doi.org/10.1016/j.ijrefrig.2015.03.022

[16] Watanabe, F., Akisawa, A.: Static analysis of triple-effect adsorption refrigeration with compressor. Case Studies in Thermal Engineering, 9, 90-99 (2017). doi.org/10.1016/j.csite.2017.01.002

[17] Li, W., Joshi, C., Xu, P., Schmidt, F. P.: Experimental study on adsorption refrigeration system with stratified storage–Analysis of storage discharge operation. Procedia Engineering, 146, 625-631 (2016). doi.org/10.1016/j.proeng.2016.06.416

[18] Sadeghlu, A., Yari, M., Dizaji, H. B.: Simulation study of a combined adsorption refrigeration system. Applied Thermal Engineering, 87, 185-199 (2015). doi.org/10.1016/j.applthermaleng.2015.05.009

[19] Ali, S. M., Chakraborty, A.: Thermodynamic modelling and performance study of an engine waste heat driven adsorption cooling for automotive air-conditioning. Applied Thermal Engineering, 90, 54-63 (2015). doi.org/10.1016/j.applthermaleng.2015.06.078

A Brief Perusal on Bitcoin Price Prediction using Artificial Neural Networks

Prachi Vivek Rane[1] and Sudhir N. Dhage[2]

[1] Sardar Patel Insititue of Technology, Mumbai, India
[2] prachi.rane@spit.ac.in
[3] sudhir_dhage@spit.ac.in

Abstract. According to economy metrics, Bitcoin and other cryptocurrencies has burgeoned in the financial market. Bitcoin being the first decentralized digital cryptocurrency has attracted significant growth in market over last few years. It is crucial to understand the volatility of the Bitcoin exchange price to forecast future prices. In this paper, we analyze the daily trends in Bitcoin system, user behavior, and emphasize on the dynamics showing volatility. Transaction data is collected from January 2014 to March 2019. The proposed model outperforms the machine learning technique along with timeseries statistical models. Empirical results of Bitcoin prices with utilization gives the ability to train model in predicting prices. The accuracy of the price prediction is done in USD. The parameters of prediction are compared in order to bring out the best solution to forecast prices and to improve the predictive performance of Bitcoin prices.

Keywords: Bitcoin · Bitcoin price prediction · Cryptocurrency · Machine Learning.

1 Introduction

Cryptocurrency is an another form of digital or virtual currency specifically designed as a medium of exchange to secure and verify the transactions. The prices of Bitcoin were soaring leading to increasing number of transactions involving payments, Bitcoin was the first global cryptocurrency which was introduced by Satoshi Nakamoto (a pseudonym for a person or a group whose identity is mystery) in January 2009. The Bitcoin system is completely decentralized, and all the transactions take place in peer-to-peer network. Bitcoin has topped the list of cryptocurrencies followed by Ethereum, Ripple, Bitcoin Cash, Litecoin. Bitcoin has total value of 3.069 billion. The properties of Bitcoin such as transparency and anonymity has made it topped all the charts of cryptocurrency. The popularity of Bitcoin is not just limited to online stores but rather it is being accepted by offline business as well.

A simple way to accomplish the transaction to be validated is to require proof-of-work [1], which is created with computational power. In a closed network, virtual currency is stored in a digital wallet (either in a Cloud or on Users

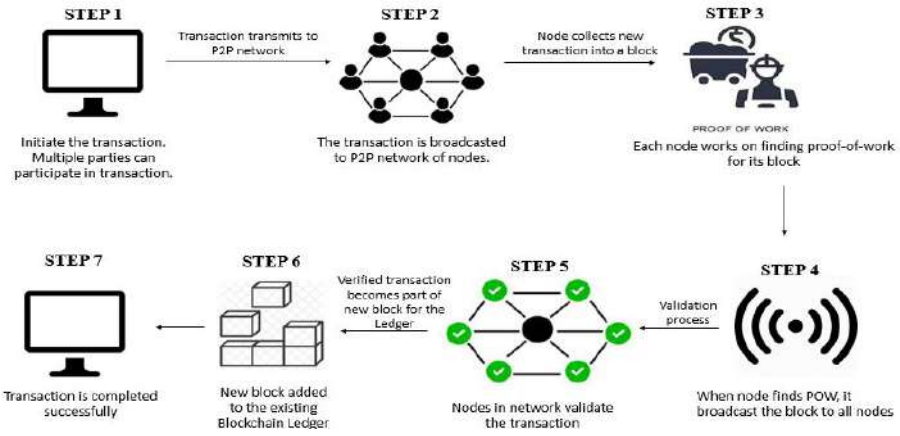

Fig. 1. Working of Bitcoin Transaction.

Computer). Bitcoin mining is done by users known as Miners. Miners [2] validate nodes in the network and record transactions. As Bitcoin accounts does not identifies miners and there is no central authority to provide details, transaction is done anonymously. Every 10 minutes these new transactions are secured, also known as hashed, into a new block. Once a miner successfully finds a hash for the block, proof-of-work is achieved then the miner broadcasts the block chain that includes addition of block to the existing blockchain public ledger. Other miners validate the authenticity of the transactions and check the hash, this new block is then added to the blockchain ledger, and the race to mine the next block begins. Computers participating in the system must solve a cryptographic puzzle to come up with a desired answer. Once they solve this puzzle, the transaction is recorded in the Blockchain. Bitcoins uniquely set payout rate which rewards miners for supporting the network with their computers also helps make it more valuable. The sender and the receiver create network, public keys are exchanged to start the transaction. The private key is exchanged to send the specific amount to the receiver. Private key generates the digital signature for authentication of sender, receiver and transaction. The Bitcoin system is capable of 7 transactions per second. Bitcoin is widely accepted by over 40 countries such as Germany, Croatia, Switzerland, Canada etc. as cryptocurrency.

The paper proceeds as follows. The next section explains literature survey. The subsequent spotlights on methodology. The following section shows the results obtained from the methodology. The last section offers concluding thoughts.

2 Literature Survey

Price is predicted using Fundamental Analysis and Technical Analysis. Fundamental Analysis observes volatility of economy and helps in decision making of

prices in cryptocurrency. Technical Analysis studies the market data for prediction of prices. [3] In paper [4], data being predicted in graph, various features are extracted to predict the value on time-frame of 1-hour, 1-day, 1-week, 1-month basis. Within the selected features the Union Find algorithm is used to remove the redundancy and to find the unique entity of a person. Machine learning algorithms such as Linear Regression, Support Vector Machine, Neural Network (Feed-Forward Neural Network), Logistic Regression are applied on the dataset. The author tried to forecast Bitcoin prices in USD, 1-hour prior along with the accuracy rate of 55%.

Latent Source Model (LSM) was developed by G. H. Chen for binary classification. [6] In this paper, Bayesian Regression is used for predicting the varying price of Bitcoin. In Bayesian Regression, data acts as proxy for Bayesian inference. The problem of unknown labels is resolved with use of training data for prediction. Latent Source Model in conjunction with Bayesian Regression examines the existing patterns in system, human behavior for prediction of prices with higher accuracy instead of doing explicitly. The average price is predicted at an interval of 10 second with the help of trading strategy which allows the user to make the decision. Using Sharpe ratio, it is observed that trading strategy performs consistently over time and yields better results during high volatility.

The relationship between Bayesian Structural Time Series Approach and various factors affecting Bitcoin prices is explained. The important feature of State Space Model (SSM) is forecast the prices into diverse components. [7] Cross-industry standard process for data mining (CRISP-DM) is processed for data mining.[8] Activation functions works best with Sandardisation for deep learning models. Here feature extraction is done with Boruta, Deep learning parameters are selected on the basis of random search, genetic algorithms and grid search.

3 Methodology

Fig. 2 explains the procedure of the implementation of proposed model. The model has three phases for the entire implementation. The Data Compilation phase collects the data from various sources to validate the data before processing. The Data Preparation phase filter the imputed values for the final processing. The final phase includes the model implementation.

3.1 Data Compilation

To accomplish the target of prediction we acquire the dataset that adequately represents the presently existing Bitcoin system, various online sources are available to obtain the data. The data is collected from Coinmarketcap. The data ranges from January 2014 to March 2019. There are total 1932 instances in the data. The transactions are verified and the parameters needed for the prediction are validated. The complete historical listing of Bitcoin prices enable us to explore various features of price prediction. The parameters that are taken into

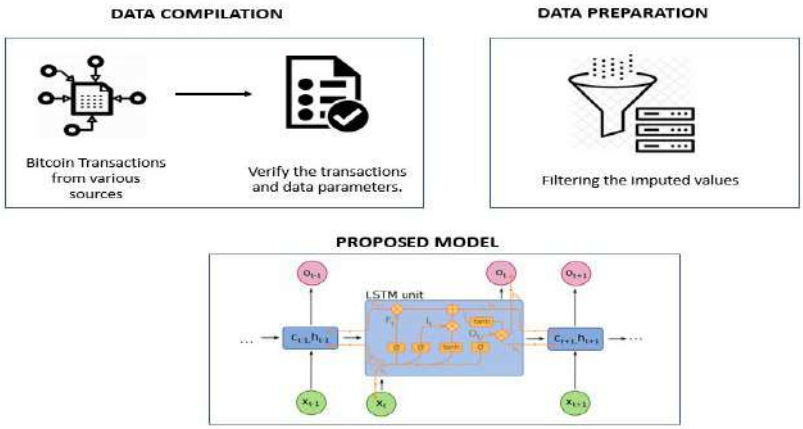

Fig. 2. Procedure of Bitcoin Price Prediction.

consideration while implementing model are Open, Volume, Close, Low, Market Cap, High. From the acquired transactions, we have computed the average price of Bitcoin and forecast on daily basis.

3.2 Data Preparation

Bitcoin Ledger has each and every record of Bitcoin transaction which uniquely analyzes the volatility in prices. The filtering phase includes the conversion of values into integers by removing commas. In next phase the values are selected by excluding the missing or incorrect values. This helps to improve the prediction more efficiently. Based on the classification of data and focus, we choose the parameters in aspect of regression in-order to gain high accuracy in prediction.

3.3 Proposed Model

Long-Short Term Memory Model is implemented to forecast the Bitcoin prices. Important parameters are used chosen for regression to predict the prices with higher precision. The parameters of each model are optimized on a daily basis to forecast the next day change in price of Bitcoin. Two evaluation metrics are used for parameter optimization: Mean Absolute Error (MAE), Root mean squared error (RMSE). MAE computes the absolute variation of test sample between predicted value and the actual value having equal weights whereas RMSE computes square root of the average of squared differences between prediction value and actual value.

Various other models based on prediction are explored and compared their performance to interpret which technique is better and to what extent. Accuracy level obtained from the models enhance to overcome the drawbacks of the existing systems.

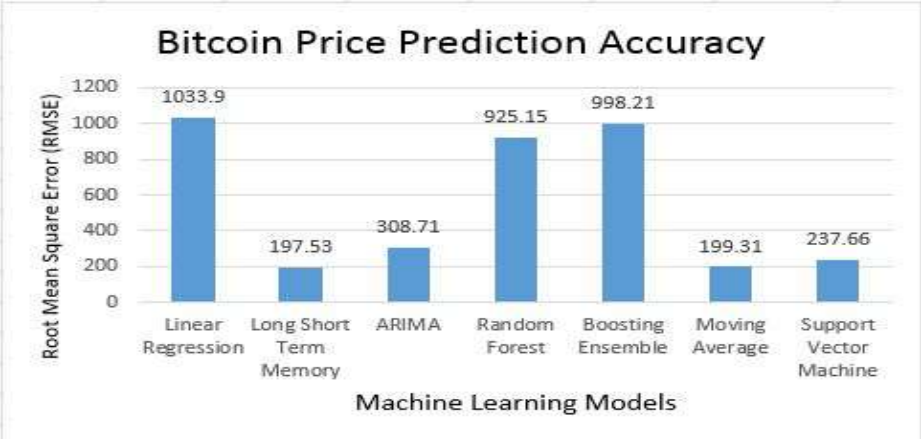

Fig. 3. Bitcoin Price Prediction Accuracy Comparison with other Machine Learning models.

4 Results

The use of Bitcoin continues to grow, despite the regulation uncertainties shared across many countries permitting its use. To increase the adoption of Bitcoin, pragmatic companies continue to deliver applications that are useful to the people. Moreover, we test to what extent market liquidity has impacted the estimated scaling exponents. According to the results, we choose to follow further modelling of values rather than intricate patterns. Although there exist a lot of volatility in the prices from the data, the tail behavior seems to be a common generality. The results derived from the proposed model show that Bitcoin price prediction can be used to enhance the growth in the industry and attract more miners to invest in the system.

Fig. 4 enables us to understand the the predicted prices and the actual prices of accuracy. The graph is so close meaning the accuracy is very sharp.

5 Conclusion

Bitcoin system demonstrates that competition in bitcoin mining done by the miners leads to a great challenge in forecasting the future prices. Due to absence of regularity in the Bitcoin market, the forecasting of the accurate prices has become a challenging task. The model was developed as a proof of concept and to demonstrate its feasibility, other functionalities can also be added to it to become a fully functional system that can be used be people. A different yet promising approach to examine cryptocurrencies such as Bitcoin system consists in quantifying the impact of effective predictors of Bitcoin, price fluctuations, market behavior. Future research might includes further exploration in the structure of Bitcoin network and how stabilize the volatility in the network.

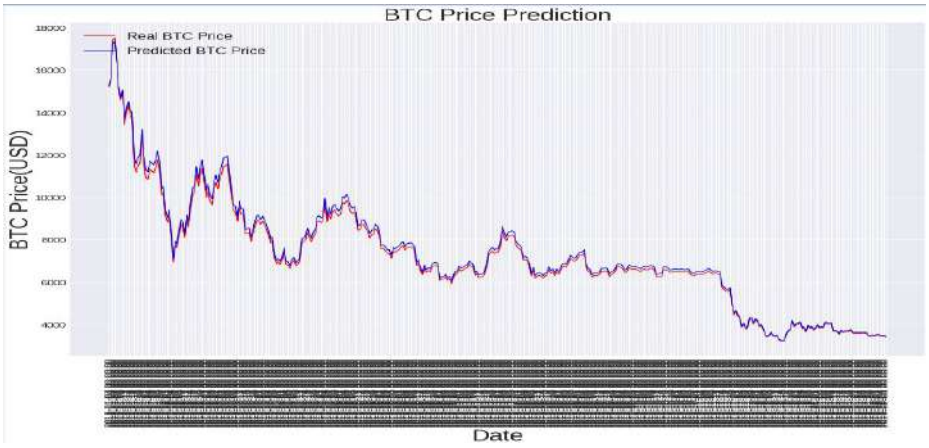

Fig. 4. Prediction of Bitcoin Prices using Long-Short Term Memory model.

This paper an overview on the fast emerging Bitcoin system highlighting mainly the volatility of prices inherent to these technologies. Broadening the current analysis of price prediction by considering other parameters of the market is a scope for future work. The aim of the paper is to explore Bitcoin system theoretically and empirically build a model from the perspective Bitcoin cryptocurrency market by predicting price with higher accuracy.

References

1. S. Nakamoto, "Bitcoin: A peer-to-peer electronic cash system",2008.
2. Luqin Wang, Yong Liu, "Exploring Miner Evolution in Bitcoin Network", NYU Polytechnic School of Engineering, Brooklyn, USA.
3. Abhyudit Bisht,Puru Agarwal, "Analysis of Bitcoin using Linear Regression and Data Mining Techniques", *International Journal of Advanced Research in Computer and Communication Engineering (IJARCCE)*, SRM University Chennai India, vol. 6, Issue 11, November 2017.
4. Alex Greaves, Benjamin Au, "Using the Bitcoin Transaction Graph to Predict the Price of Bitcoin", December 2015.
5. Tian Guo, Nino Antulov-Fantulin, "An experimental study of Bitcoin fluctuation using machine learning methods", *Association for Computing Machinery*, Zurich, Switzerland, June 2018.
6. Devavrat Shah, Kang Zhang, "Bayesian regression and Bitcoin", *IEEE Fifty-second Annual Allerton Conference, Illinois, USA*, Laboratory for Information and Decision Systems, Department of EECS, Massachusetts Institute of Technology, October 2014.
7. Obryan Poyser, "Exploring the determinants of Bitcoins price: an application of Bayesian Structural Time Series", *Thesis*, June 2017.
8. Sean McNally, Jason Roche, Simon Caton, "Predicting the Price of Bitcoin Using Machine Learning", *26th Euromicro International Conference on Parallel, Distributed, and Network-Based Processing*, Ireland, 2018.

A Fuzzy Rule Based Classification Technique by Capturing Pareto-Frontier of the Discrete Decision Space

Debjani Chakraborty
Department of Mathematics,
Indian Institute of Technology Kharagpur, West Bengal-721302, India
Email: debjani@maths.iitkgp.ac.in

* Milton Biswas
Department of Mathematics,
Indian Institute of Technology Kharagpur, West Bengal-721302, India
Email: miltonbiswas@iitkgp.ac.in

Debashree Guha
School of Medical Science and Technology,
Indian Institute of Technology Kharagpur, West Bengal-721302, India
Email: debashree@iitp.ac.in

Suman Das
Department of Mathematics,
Indian Institute of Technology Kharagpur, West Bengal-721302, India
Email: pnksmdas@gmail.com

Abstract. In this paper, we have proposed an algorithmic approach to capture the pareto-frontier of a conflicting multi-objective programming problem possessing a discrete decision space. Moreover we have incorporated this method to generate a rule-base for a classification problem. We have evaluated the obtained rule-base on a benchmark dataset available in the UCI repository and obtained expected results in terms of accuracy, applicability and versatility.

Mathematics Subject Classification: 03B52, 68T37, 94D05.

Keywords: Fuzzy rule-base · Fuzzy reasoning method · Mixed-integer linear programming · Multi-objective optimization problem.

1 Introduction

Pattern classification is a branch of machine learning and artificial intelligence emerging rapidly into almost every field of engineering sciences dealing practical problems. *Fuzzy Rule-Based Systems* (FRBSs) have been proved to be applicable to cope with this sort of classification problem. The reason is the ambiguity, irregularity and complexity present in the raw data set making conventional pattern classification techniques hard

to fit into any kind of real model. In this respect, the interpretable linguistic labeling of a FRBS makes it more practical and user-friendly as well [1,2,21]. In FRBS, a block of fuzzy rules is being extracted based on the training patterns available and then fuzzy reasoning method is deployed to classify unknown test patterns.

The application of fuzzy rule-base as a fuzzy classifier towards the classification problems had been exhibited for the first time in [1]. A fuzzy reasoning method using *Genetic Algorithm(GA)* has been developed first in [2] which considers all the extracted rules unlike the existing methods entertaining the rule with highest firing degree only. Undoubtedly, *Genetic Algorithm* is the most popular one, numerous variations and upgradations of which took place in the literature in the context of classification problems [3,4,5,6,7,8,9,10]. In the subsequent years many researchers utilized the *Fuzzy Clustering* to generate fuzzy-rule bases to address the classification problems [11,12]. *Principal component analysis* which reduces the dimension of the feature space effectively keeping the classification power intact, has been described in [13]. Apart from genetic algorithm, fuzzy classifier has been designed by many other approaches like *neural networks* [14,15,16], *support vector machines* [17,18,19] and several heuristic approaches [20]. *Mixed integer programming* has been implemented in [21,22] to generate a fuzzy rule base from data set. However in most of the cases the characteristics of a fuzzy rule base have been mathematized as a multi-objective optimization problem due to its conflicting nature and then diluted into a single objective optimization problem. But such practices may be disastrous in case of data sets possessing non-convex pareto frontier of the formulated problem and this situation may trigger the existing methods to fail [30,31]. The flip side of the simplest and perhaps the most popular method namely *weighted average method* has been detailed at [30,31]. A complete discussion on the methods, advantages, disadvantages and comparative analysis may be studied in [28,29].

Keeping those limitations in mind, in this work, we have put forward the classification problem in a different point of view carefully analyzing the characteristics of a data set and developed a set of potential rules with optimum accuracy, coverage and vagueness. For this, a multi-objective optimization problem has been formulated out of the given training patterns in a mathematically rigorous way. The feasible set of the developed multi-objective model is the entire rule set scattered in a discrete fashion. The main objective is to refrain ourselves from converting the multi-objective model holding conflicting objectives into a single objective model and in doing so the natural conflict of interest hidden within the data set has been preserved.

In the existing literature, enormous number of methods are available in order to find the evenly generated non-dominated solutions of a multi-objective optimization problem [23,24,25,26,27]. But, digging out the available literature it can be claimed that no proper method is available to solve a multi-objective decision making problem with completely discrete or totally disconnected criteria space to the best of our knowledge. This motivates us to construct a methodology to identify the Pareto-frontier as accurate as possible in case of discrete decision spaces and the same has been plugged into the proposed classification problem. It is observed that, most of the points lying on the Pareto frontier have been depicted correctly except for a negligible number of additional points due to the *knee* of the space concerned. However, we have taken care

of that issue out of the shorlisted points by pairwise comparison. In order to formulate the multi-objective optimization problem, three most vital characteristics of a rule base namely *accuracy*, *coverage capability* and the *vagueness* have been considered. As fuzzy rule antecedents, we have considered triangular fuzzy number and for the feature scaling *fuzzy c-means* algorithm [34] has been implemented. The accuracy test at the end against a benchmark data taken from UCI repository [35] presents satisfactory result with respect to the existing methods and outclasses them in terms of simplicity and domains of applicability.

The remainder of the paper has been organized as follows. Section 2 contains basic definitions and some measures related to the fuzzy rule base classification problem. Section 3 defines describes elaborately our proposed method towards finding the Pareto-frontier of the decision space. Section 4 consists of the algorithm and Section 5 presents an example of real-life application of this method to a benchmark data set. Finally, section 6 concludes the work with the scopes on possible future directions.

2 Preliminaries

Let us consider a classification problem consisting of n patterns, m classes and p features. So, a typical pattern say X can be expressed as a vector of the form $X = (x_1, x_2, ..., x_p, C_k)$, where x_i is the value of the pattern X in the i-th feature and C_k is the class of this pattern X, $i = 1, 2, ..., p$, $k = 1, 2, ..., m$.

In this paper, our objective is to construct fuzzy if-then rules of the following type:
Rule-k : If f_1 is $\tilde{F}_1$ and if f_2 is $\tilde{F}_2$ and .....and if f_p is $\tilde{F}_p$, then the Class is C_k.
Here f_i is the fuzzy variable corresponding to the i-th feature and $\tilde{F}_i$ is the triangular fuzzy number, termed as *fuzzy antecedent* corresponding to the fuzzy variable f_i, $i = 1, 2, ..., p$ and C_k is the class referred by this particular rule and termed as *consequent*.

2.1 Matching degree or Degree of Compatibility: [22]

The matching degree or the degree of compatibility of the k-th rule with the pattern X, denoted by m_k^X is defined as follows:

$$m_k^X = \prod_{i=1}^{p} \mu_{\tilde{F}_i}(x_i) \tag{1}$$

where, $\mu_{\tilde{F}_i}$ is the triangular membership function of the fuzzy set $\tilde{F}_i$ and x_i is the value of the pattern X corresponding to the i-th feature in the data set.

As we mentioned in the introduction, in the formulation of our proposed multi-objective optimization problem, we consider the characteristics namely *accuracy*, *coverage* and *vagueness* which should be possessed by an ideal rule-base, we recall those ideas and define as follows:

2.2 Accuracy or Certainty Degree of a Rule: [22]

For a given rule say k-th whose consequent is say C_k, the accuracy or certainty degree of that rule is computed in the following way,

$$\sigma_k = \frac{\sum_{X \in P_{C_k}} m_k^X}{\sum_{X \in P} m_k^X} \tag{2}$$

where P is the set of all the patterns, P_{C_k} is the set of patterns belonging to the class C_k, m_k^X is the matching degree of the pattern X with the k-th rule as described in the equation (1) This characteristic of the rule base indicates that how accurately a rule can classify an unclassified patterns belonging to the class represented by a particular rule in the consequent part.

2.3 Support or Coverage Capability of a Rule: [22]

One more characteristic is present in the literature namely *support* which takes care of the coverage capability of a rule(say k-th) towards the patterns of the class(say C_k) appearing in the consequent of this rule. It is calculated as follows,

$$\delta_k = \frac{\sum_{X \in P_{C_k}} m_k^X}{N_{C_k}} \tag{3}$$

where P_{C_k} is the set of patterns belonging to the class C_k, N_{C_k} is the number of patterns in the class C_k i.e. cardinality of the set P_{C_k}, m_k^X is the matching degree of the pattern X with the k-th rule as mentioned in the equation (1). This particular characteristic reflects the field of action of a rule supporting the patterns of the consequent class.
Along with the described two characteristics above, another significant factor namely *vagueness of a rule* has been captured and associated in our model to form the rule base, which is not yet attended and overlooked in the previous literature.

2.4 Vagueness of a Fuzzy Rule:

Let, A denotes a fuzzy set on the universe U with membership function $\mu_A(u)$ for all $u \in U$. If U is a discrete set, say, $U = \{u_1, u_2, ..., u_m\}$ and $\mu_i = \mu_A(u_i)$, then the vagueness or the fuzziness of set A is defined by,

$$E_v(A) = \quad -\frac{1}{m}\sum_{i=1}^{m}\left(\mu_i\left(ln\mu_i\right) + \left(1-\mu_i\right)\left(ln\left(1-\mu_i\right)\right)\right) \tag{4}$$

The vagueness or fuzziness of a fuzzy set can be measured by a fuzzy entropy which is similar to Shannon's entropy measure of randomness [37]. With the help of this definition we shall define the vagueness of a fuzzy rule and incorporate this concept into objective construction in the next section.

3 Identification of Representative Rules of a Data Set

Consider a data set with multiple classes and features. In order to classify the data, our purpose is to unveil the hidden similarity of patterns belonging to individual classes. Here, the target is to construct a set of rules for each of the classes and finally tie them together to form a rule base for the given set of patterns. Then rule-selecting objective functions are constructed on the basis of the rule accuracy, rule coverage capability and the rule vagueness as well. Doing so, the issue of classification problem boils down into a multi-objective optimization problem where the formulation of objectives are motivated from the must-have characteristics of a potential rule-base. This sort of classification problem is being dealt with the successful identification of the non-dominated solutions and naming them *Representative Rule* completes the rule generation step. Finally the test patterns are exploited to test the strength of the extracted rule-base based on the capability to distinguish a specific test pattern from other enemy classes and to classify them correctly. While testing, 10-fold cross validation method has been followed as a standard model validation technique.
Mathematically, let us consider a classification problem with N number of patterns, m classes and p features. So, $N = N_1 + N_2 + ... + N_m$ where N_k= Number of patterns belonging to the k-th class, ($k = 1, 2, ..., m$). Now we separate each of the classes into two parts, which are, a). Training Patterns and b). Test Patterns.

For a particular class say k-th, we consider $N_k^{train} : N_k^{test} = 90 : 10$. So we can write $N = (N_1^{train} + N_1^{test}) + (N_2^{train} + N_2^{test}) + ... + (N_m^{train} + N_m^{test}) = (N_1^{train} + N_2^{train} + ... + N_m^{train}) + (N_1^{test} + N_2^{test} + ... + N_m^{test}) = N^{train} + N^{test}$.

Then the N^{test} number of patterns have been kept aside for the test of the classifier at the end and we proceed with a fixed class say k-th, ($k = 1, 2, ..., m$). For the visual comfort, let us rename the following,
$N_k^{train} = n_k$ =number of training patterns in the k-th class.
Thus the total number of training patterns is, $N^{train} = n_1 + n_2 + ... + n_m$. So, the enumeration of the training patterns belonging to the k-th class is, $X_1^k, X_2^k, X_3^k, ..., X_{n_k}^k$, where X_s^k=s-th pattern belonging to the k-th class, where $s = 1, 2, ..., n_k$. Since each of the pattern has p numbers of features, a pattern can be expressed as a p-tuple of the form, $X_s^k = (x_{s1}^k, x_{s2}^k, ..., x_{sp}^k)$, where x_{si}^k is the numerical value of the s-th pattern of the k-th class in the i-th feature.
Let us denote the set of all patterns belonging to the k-th class as,
$P_k = \{X_1^k, X_2^k, X_3^k, ..., X_{n_k}^k\}$
Here the patterns are of the form, $X_s^k = (x_{s1}^k, x_{s2}^k, ..., x_{sp}^k)$, where $s = 1, 2, ..., n_k$.

Step-I: Clustering and Defining Fuzzy Scale: The cluster centers single out the points of congestion of the feature values available for the patterns and this is the way the benchmark fuzzy sets are constructed under the features. Here in this step, the cluster centers of the features are being computed one by one taking the patterns belonging to the k-th class. The prospective antecedents of the rules are modeled as triangular fuzzy numbers whose membership functions are computed using those developed cluster centers obtained. Let us construct the sets, $Y_i^k = (x_{1i}^k, x_{2i}^k, ..., x_{n_k i}^k)$, where $i = 1, 2, ..., p$.

Clearly, these sets hold the values of all the patterns of the class k for the features taken separately. Then we apply fuzzy c-means clustering algorithm to all Y_i^k's($i = 1, 2, ..., p$) to find the cluster centers of each of the features for the patterns belonging to the class k.
Let us fix the number of clusters to be five. So, the cluster centers for the set Y_i^k are c_{ij}^k, where $j = 1, 2, ..., 5$ and $i = 1, 2, ..., p$.
Let $min_i^k = min\{Y_i^k\} = min\{x_{1i}^k, x_{2i}^k, ..., x_{n_k i}^k\}$
and $max_i^k = max\{Y_i^k\} = max\{x_{1i}^k, x_{2i}^k, ..., x_{n_k i}^k\}$, where $i = 1, 2, ..., p$.
Therefore, the triangular fuzzy numbers corresponding to the feature say i are,

$$\tilde{F}_{ij}^k = (min_i^k, c_{ij}^k, max_i^k) \tag{5}$$

where $j = 1, \ldots 5, i = 1, \ldots, p$. Thus for the i-th feature there are 5 choices of assignments of fuzzy numbers which are $\tilde{F}_{i1}^k, \tilde{F}_{i2}^k, \tilde{F}_{i3}^k, \tilde{F}_{i4}^k, \tilde{F}_{i5}^k$.

So the number of prospective rules is 5^p, as there are p features.

While constructing the benchmarks scale of the fuzzy numbers, we have stretched those sets over the whole universe of discourse [36] with positive membership degrees. Because otherwise, the matching degree turns out to be zero for a pattern if it attains zero membership degree in any of the features.

Step-II; Computation of Membership degrees: For a pattern $X_s^k, (s = 1, 2, ..., n_k)$ belonging to the k-th class, let us compute the membership degree of that s-th pattern in the j-th fuzzy number of the i-th feature and denote by, $\mu_{sji}^k = \mu_{\tilde{F}_{ij}^k}(x_{si}^k), j = 1, \ldots, 5$ and $i = 1, \ldots, p$, where, $X_s^k = (x_{s1}^k, x_{s2}^k, ..., x_{sp}^k), s = 1, \ldots, n_k$,
$\mu_{\tilde{F}_{ij}^k}$ = membership function of the fuzzy number $\tilde{F}_{ij}^k$.
These values indicate the belongingness of a pattern in a fuzzy antecedent in fuzzy sense. Up to this point, for a particular pattern X_s^k, we get $5p$ entities representing the membership degrees corresponding to each of the fuzzy numbers of each of the features. Now let,

$$Z_{ji}^k = \sum_{s=1}^{n_k} \mu_{sji}^k, \text{ where } j = 1, \ldots, 5, i = 1, \ldots, p \tag{6}$$

Here Z_{ji}^k represents the sum of the membership degrees of all the n_k patterns belonging to the k-th class in the j-th fuzzy number of the i-th feature. This sum actually indicates the belongingness of the k-th class to a particular fuzzy antecedent out the $5p$ numbers in totality.

Step-III; Construction of the Objective Functions: Clearly a particular rule should have maximized accuracy, maximized coverage capability but a minimized vagueness which are conflicting in nature as described in the following:
First we re-look the definition of *Certainty Degree* or *Accuracy* of the k-th rule whose consequent is C_k given in the equation (2), we get,

$$\sigma_k = \frac{\sum_{X \in P_{C_k}} m_k^X}{\sum_{X \in P} m_k^X} = \frac{\sum_{X \in P_{C_k}} m_k^X}{\sum_{X \in P_{C_k}} m_k^X + \sum_{X \notin P_{C_k}} m_k^X} \tag{7}$$

Now the following inferences can be drawn from the last part of the equality (7),
a. Maximization of σ_k is tantamount to the maximization of the numerator or the minimization of the denominator or the both simultaneously.
b. But the minimization of the denominator, which itself contains the numerator, causes the conflict of the potentially considerable objectives *Support* and *Accuracy*.
c. Ultimately, minimization of the denominator is equivalent to the minimization of the quantity $\sum_{X \notin P_{C_k}} m_k^X$, i.e, minimization of the matching degrees of the enemy patterns with that specific rule.

From these observations, it is clear that, maximization of the quantity $\sum_{X \in P_{C_k}} m_k^X$ and minimization of the quantity $\sum_{X \notin P_{C_k}} m_k^X$ suffice to enhance the *Support* and the *Accuracy* of the k-th rule respectively.
Looking back the expression of *support* in the previous section we construct the objective function for the k-th class, which is to **maximize**,

$$f_1 = \sum_{i=1}^{p} \sum_{j=1}^{5} Z_{ji}^k \alpha_{ji}^k$$

subject to

$$\alpha_{ji}^k = 0 \text{ or } 1, \tag{8}$$

$$\sum_{j=1}^{5} \alpha_{ji}^k = 1 \text{ for } i = 1, \ldots, p, j = 1, \ldots, 5. \tag{9}$$

Equation (8) and (9) together ensure that exactly one fuzzy number is allowed to be assigned to a particular feature.

Now, in order to maximize the accuracy or certainty degree of the rule base we shall minimize the denominator of the definition of the *accuracy* as mentioned in the previous section. Hence, our objective here is to **minimize** the following,

$$f_2 = \sum_{k'=1,2,\ldots,m,\, k' \neq k} \sum_{i=1}^{p} \sum_{j=1}^{5} Z_{ji}^{k'} \alpha_{ji}^k \tag{10}$$

subject to

$$\alpha_{ji}^k = 0 \text{ or } 1,$$

$$\sum_{j=1}^{5} \alpha_{ji}^k = 1 \text{ for } i = 1, \ldots, p, j = 1, \ldots, 5.$$

$k' \neq k$ indicates that we need to consider the enemy patterns and minimize the effect of those patterns in the extraction of optimal rule.

Let us represent the vagueness of an arbitrary rule whose i-th feature contains say j-th fuzzy antecedent for a fixed class say k-th as the following definition,

$$\lambda_k = \sum_{i=1}^{p} \sum_{j=1}^{5} v_{ji}^k, \tag{11}$$

where, $v_{ji}^k = -\frac{1}{N_k^{train}} \sum_{s=1}^{N_k^{train}} \left(\mu_{sji}^k \left(ln\mu_{sji}^k\right) + \left(1-\mu_{sji}^k\right)\left(ln\left(1-\mu_{sji}^k\right)\right)\right)$ and μ_{sji}^k =membership degree of the s-th pattern of the k-th class at the j-th fuzzy value of the i-th feature. Now, at this point, our aim is also to **minimize** the vagueness of the resultant rule base is,

$$f_3 = \sum_{i=1}^{p}\sum_{j=1}^{5} v_{ji}^k \alpha_{ji}^k \tag{12}$$

subject to

$$\alpha_{ji}^k = 0 \text{ or } 1,$$
$$\sum_{j=1}^{5} \alpha_{ji}^k = 1 \text{ for } i = 1, \ldots, p, j = 1, \ldots, 5.$$

There are few other objectives that could have been taken into consideration while making the rule-base for a classification problem for instance interpretability and relevance.

Step-IV; Formulating Multi-Objective Optimization Problem: In the previous step, we have broadly discussed the cause of conflict of the major characteristics of a rule base namely *support or coverage* and *accuracy* and hence the existence of the trade-off within the corresponding objective functions f_1 and f_2 as constructed in the step-III. We feel too that, a proper rule-base should bear minimum vagueness as much as possible in the antecedent part. Thus the ultimate issue boils down to the solution of the following tri-objective optimization problem,

$$\text{maximize } f_1 = \sum_{i=1}^{p}\sum_{j=1}^{5} Z_{ji}^k \alpha_{ji}^k$$
$$\text{minimize } f_2 = \sum_{k'=1,2,\ldots,m,\, k'\neq k} \sum_{i=1}^{p}\sum_{j=1}^{5} Z_{ji}^{k'} \alpha_{ji}^k$$
$$\text{minimize } f_3 = \sum_{i=1}^{p}\sum_{j=1}^{5} v_{ji}^k \alpha_{ji}^k$$

subject to

$$\alpha_{ji}^k = 0 \text{ or } 1 \text{ i.e. binary variables},$$
$$\sum_{j=1}^{5} \alpha_{ji}^k = 1 \text{ for } i = 1, \ldots, p, j = 1, \ldots, 5.$$

We find the Pareto frontier of the above tri-objective optimization problem using modified *Ideal Cone(IC)* method for the discrete decision space [38]. This method is based on the exhaustive translation and rotation of an ideal cone throughout the decision space. Geometrically a ideal cone starts moving towards a fixed direction and

declares the point to be a Pareto solution which the cone meets first(for a minimization problem). As the direction changes this method generates almost all the non-dominated solutions lying on the Pareto-frontier except for a few number of additional dominated points(due to the possible existence of knees in the decision space). To get rid of these, we determine the original one from the shortlisted solutions manually comparing one another and finally form the intended rule base. The formal way to pose this method is, move θ and ϕ starting from 0 to $\frac{\pi}{2}$ with a very small step length and
minimize z
subject to

$$\begin{aligned} z\sin\theta\cos\phi &\geq -f_1 \\ z\sin\theta\sin\phi &\geq f_2 \\ z\cos\theta &\geq f_3 \\ \alpha_{ji}^k &= 0 \text{ or } 1 \text{ i.e. binary variables,} \\ \sum_{j=1}^{5}\alpha_{ji}^k &= 1 \text{ for } i=1,\ldots,p, j=1,\ldots,5. \end{aligned}$$

Each of the solutions of the above mixed integer linear programming problem corresponds to a representative rule for the k-th class in consideration. We repeat these steps(I to III) for the m number of classes and store the rules together and this is the required rule-base of the classification problem. Finally we take N^{test} test patterns and find the matching degree of each of these patterns with all the rules and the consequent of the rule with highest matching degree for a test pattern is being assigned to that unclassified patterns.

4 Algorithm

The proposed classification procedure can be put into the following algorithmic structure:

Algorithm 1 Main Algorithm

Require: Data set $\mathbf{X}$; Number of classes m; Number of attribute p; Number of cluster c; Class size vector $[s_i]_{1\times m}$

Separate test data $\mathbf{X}_{test}$ and training data $\mathbf{X}_{train}$ from $\mathbf{X}$
# *Representative selection*
for class $i = 1$ to m **do**
    Calculate the co-efficient matrix A_f and A_g
    Solve the Optimization **Problem-1**
    Obtain set of rules R_i for i^{th} class
end for
Store the rules R_i in $\mathbf{R}$
# *Accuracy test*
for test data 1 to $\mid \mathbf{X}_{test} \mid$ **do**
    for rule 1 to size of $\mathbf{R}$ **do**
        Find the firing degree d_{ij} of i^{th} test data to j^{th} rule
    end for
    Find k, such that $d_{ik} = max\{d_{ij}\}$
    Assign test data x_i to the class of which is represented by j^{th} rule
end for

5 Numerical Result

To validate the effectiveness of the proposed algorithm, we examined it on a benchmark data set, namely "new-thyroid.data" obtained from the UCI (University of California at Irvine) Machine Learning Repository [35]. In the computation of accuracy, 10-fold *Cross Validation* technique has been adopted. The numerical result has been shown in following table:

Table 1: New-thyroid data and its classification

1	Number of data	215
2	Class	3
3	Feature	5
4	Division of data in classes	(150,35,30)
5	Training data	193=(135,31,27)
6	Test data	22=(15,4,3)
7	Number of rules obtained	(5,3,3)
8	Accuracy of the classification	86.36%

6 Conclusion

In this paper, we have captured the Pareto-frontier of a multi-objective optimization problem by introducing a new methodology which stands upon the rigid platform of the optimization theory. The obtained frontier then has been employed to construct a fuzzy rule-base which in turn demonstrated its expected performance for a benchmark data set obtained from UCI repository. This algorithm is fast and simple but robust in nature. In this scenario, our model should play a crucial rule in the decision making strategy and machine learning. In future, the antecedents of the rules may be considered as type-2 fuzzy numbers for better training flexibility. Also, many other aspects which we left, like interpretability, relevance may be deployed as deciding factors to choose the optimal rule base and the individual contribution of these objectives may be justified in formulating the final rule base.

References

1. Ishibuchi, H., Nozaki, K. and Tanaka, H., 1992. Distributed representation of fuzzy rules and its application to pattern classification. Fuzzy sets and systems, 52(1), pp.21-32.
2. Cordón, O., del Jesus, M.J. and Herrera, F., 1999. A proposal on reasoning methods in fuzzy rule-based classification systems. International Journal of Approximate Reasoning, 20(1), pp.21-45.
3. Aydogan, E.K., Karaoglan, I. and Pardalos, P.M., 2012. hGA: Hybrid genetic algorithm in fuzzy rule-based classification systems for high-dimensional problems. Applied Soft Computing, 12(2), pp.800-806.
4. Alcalá, R., Alcalá-Fdez, J., Herrera, F. and Otero, J., 2007. Genetic learning of accurate and compact fuzzy rule based systems based on the 2-tuples linguistic representation. International Journal of Approximate Reasoning, 44(1), pp.45-64.
5. Gómez-Skarmeta, A.F., Valdés, M., Jiménez, F. and Mar??n-Blázquez, J.G., 2001. Approximative fuzzy rules approaches for classification with hybrid-GA techniques. Information Sciences, 136(1-4), pp.193-214.
6. Hu, Y.C., 2005. Finding useful fuzzy concepts for pattern classification using genetic algorithm. Information Sciences, 175(1-2), pp.1-19.
7. Ishibuchi, H., Yamamoto, T. and Nakashima, T., 2005. Hybridization of fuzzy GBML approaches for pattern classification problems. IEEE Transactions on Systems, Man, and Cybernetics, Part B (Cybernetics), 35(2), pp.359-365.
8. Li, M. and Wang, Z., 2009. A hybrid coevolutionary algorithm for designing fuzzy classifiers. Information Sciences, 179(12), pp.1970-1983.
9. Zhou, E. and Khotanzad, A., 2007. Fuzzy classifier design using genetic algorithms. Pattern Recognition, 40(12), pp.3401-3414.
10. Alcala-Fdez, J., Alcala, R. and Herrera, F., 2011. A fuzzy association rule-based classification model for high-dimensional problems with genetic rule selection and lateral tuning. IEEE Transactions on Fuzzy systems, 19(5), pp.857-872.
11. Abe, S. and Thawonmas, R., 1997. A fuzzy classifier with ellipsoidal regions. IEEE Transactions on fuzzy systems, 5(3), pp.358-368.
12. Lee, C.Y., Lin, C.J. and Chen, H.J., 2007. A self-constructing fuzzy CMAC model and its applications. Information Sciences, 177(1), pp.264-280.
13. Ravi, V., Reddy, P.J. and Zimmermann, H.J., 2000. Pattern classification with principal component analysis and fuzzy rule bases. European Journal of Operational Research, 126(3), pp.526-533.

14. Chakraborty, D. and Pal, N.R., 2004. A neuro-fuzzy scheme for simultaneous feature selection and fuzzy rule-based classification.
15. Lin, C.T. and Lee, C.S.G., 1991. Neural-network-based fuzzy logic control and decision system. IEEE Transactions on computers, 40(12), pp.1320-1336.
16. Nauck, D. and Kruse, R., 1997. A neuro-fuzzy method to learn fuzzy classification rules from data. Fuzzy sets and Systems, 89(3), pp.277-288.
17. Castro, J.L., Flores-Hidalgo, L.D., Mantas, C.J. and Puche, J.M., 2007. Extraction of fuzzy rules from support vector machines. Fuzzy Sets and Systems, 158(18), pp.2057-2077.
18. Chiang, J.H. and Hao, P.Y., 2004. Support vector learning mechanism for fuzzy rule-based modeling: a new approach. IEEE Transactions on Fuzzy systems, 12(1), pp.1-12.
19. Ren, Y., Liu, X. and Cao, J., 2011. A parsimony fuzzy rule-based classifier using axiomatic fuzzy set theory and support vector machines. Information Sciences, 181(23), pp.5180-5193.
20. Belacel, N., Raval, H.B. and Punnen, A.P., 2007. Learning multicriteria fuzzy classification method PROAFTN from data. Computers & Operations Research, 34(7), pp.1885-1898.
21. Derhami, S. and Smith, A.E., 2014, July. Iterative mixed integer programming model for fuzzy rule-based classification systems. In 2014 IEEE International Conference on Fuzzy Systems (FUZZ-IEEE) (pp. 2079-2084). IEEE.
22. Derhami, S. and Smith, A.E., 2017. An integer programming approach for fuzzy rule-based classification systems. European Journal of Operational Research, 256(3), pp.924-934.
23. Hwang, C., Masud, A. and Paidy, S. (1979). Multiple objective decision making, methods and applications: a state-of-the-art survey, Springer-Verlag, Berlin.
24. Pascoletti, A. and Serafini, P., 1984. Scalarizing vector optimization problems. Journal of Optimization Theory and Applications, 42(4), pp.499-524.
25. Helbig, S., 1990. An interactive algorithm for nonlinear vector optimization. Applied Mathematics and Optimization, 22(1), pp.147-151.
26. Das, I. and Dennis, J.E., 1998. Normal-boundary intersection: A new method for generating the Pareto surface in nonlinear multicriteria optimization problems. SIAM Journal on Optimization, 8(3), pp.631-657.
27. Ghosh, D. and Chakraborty, D., 2015. A direction based classical method to obtain complete Pareto set of multi-criteria optimization problems. Opsearch, 52(2), pp.340-366.
28. Marler, R.T. and Arora, J.S., 2004. Survey of multi-objective optimization methods for engineering. Structural and multidisciplinary optimization, 26(6), pp.369-395.
29. Li, D., Yang, J.B. and Biswal, M.P., 1999. Quantitative parametric connections between methods for generating noninferior solutions in multiobjective optimization. European journal of operational research, 117(1), pp.84-99.
30. Koski, J., 1985. Defectiveness of weighting method in multicriterion optimization of structures. Communications in applied numerical methods, 1(6), pp.333-337.
31. Das, I. and Dennis, J.E., 1997. A closer look at drawbacks of minimizing weighted sums of objectives for Pareto set generation in multicriteria optimization problems. Structural optimization, 14(1), pp.63-69.
32. Athan, T.W. and Papalambros, P.Y., 1996. A note on weighted criteria methods for compromise solutions in multi-objective optimization. Engineering Optimization, 27(2), pp.155-176.
33. Martínez, M., Sanchis, J. and Blasco, X., 2007. Global and well-distributed Pareto frontier by modified normalized normal constraint methods for bicriterion problems. Structural and Multidisciplinary Optimization, 34(3), pp.197-209.
34. Bezdek, J.C., Ehrlich, R. and Full, W., 1984. FCM: The fuzzy c-means clustering algorithm. Computers & Geosciences, 10(2-3), pp.191-203.
35. Dua, D. and Graff, C. (2019). UCI Machine Learning Repository [http://archive.ics.uci.edu/ml]. Irvine, CA: University of California, School of Information and Computer Science.

36. Chakraborty, D., Guha, D. and Dutta, B., 2016. Multi-objective optimization problem under fuzzy rule constraints using particle swarm optimization. Soft Computing, 20(6), pp.2245-2259.
37. Shannon, C., 1948. A mathematical theory of communication, bell System technical Journal 27: 379-423 and 623?656. Mathematical Reviews (MathSciNet): MR10, 133e, 20.
38. Ghosh, D. and Chakraborty, D., 2014. Ideal cone: a new method to generate complete Pareto set of multi-criteria optimization problems. In Mathematics and Computing 2013 (pp. 171-190). Springer, New Delhi.

A hybrid TOPSIS-AHP in Multi-Criteria Decision Making using Interval Type-2 Fuzzy Sets

Abhay Sobhanan
Department of Mathematics, NIT Agartala, Tripura, India.
Email: abhay.sobhanan@gmail.com

Apu Kumar Saha
Department of Mathematics, NIT Agartala, Tripura, India.
Email: apusaha_nita@yahoo.co.in

Ravi Shankar Kumar
Department of Mathematics, NIT Agartala, Tripura, India.
Email: ravikhushi4120@yahoo.co.in

Abstract. Multi-criteria decision making (MCDM) methods mostly rely on the accuracy of the individual or collective judgments provided by the decision-makers. We use the concept of Interval type-2 fuzzy numbers in MCDM as they account for the broader range of vagueness present in the proposed data. This paper presents a new decision-making technique using AHP and TOPSIS in the type-2 fuzzy environment. We also execute the signed distance approach to achieve the ranking of the alternatives, which simplifies the computational difficulty of otherwise complex type-2 fuzzy numbers. Finally, the proposed fuzzy MCDM technique is verified using a practical example.

Mathematics Subject Classification: 60B10, ...

Keywords: AHP· TOPSIS· MCDM· Type-2 fuzzy sets· Signed distance

1 Introduction

Decision making is a crucial selection procedure which forms an integral part of various management procedures, research analysis, financial predictions, engineering applications, etc. More often, it becomes difficult for decision-makers to choose the best solution from the seemingly equivalent alternatives of the data set. Mathematical procedures can reduce the complexity of such situations while optimizing the solution.

The main goal of Multi-Criteria Decision Making/Analysis (MCDM/MCDA) involves the selection of an alternative option for a specific objective by explicitly evaluating a set of criteria. Popular MCDM methods used in engineering are Analytical Hierarchy Process (AHP), Technique for Order of Preference by Similarity to Ideal Solution (TOPSIS), Elimination et Choice Translation Reality (ELECTRE), Preference ranking organization method for enrichment of evaluations (PROMETHEE), etc [17]. A comparison study on some of these methods is present in [8]. It is highly probable

that the decision proposed by the decision-makers contains uncertainty. Thus, it is also essential to account fuzziness in rational decision making for an adequate evaluation of the problem. A large number of studies which made the mathematical analysis of MCDM was carried out using the Fuzzy Set Theory [7] developed by Zadeh in 1965.

In this paper, we integrate the two most popular and highly used MCDM methods such as AHP and TOPSIS, to form an effective decision-making technique. To account for the imprecision and uncertainty present in the real world problems, we develop the proposed method in Type-2 fuzzy environment, which is much more effective compared to the type-1 fuzzy set theory. Defuzzification of type-2 fuzzy numbers usually involves tedious calculation procedures which make its implementation inconvenient. Chen proposed the signed distance method for a powerful and effective evaluation of the fuzzy numbers [1].

The first part of this paper contains the literature review of different fuzzy MCDA methods. The MCDA methods such as AHP and TOPSIS are briefly explained in the next section. The fuzzy set theory is also discussed further. Later, the proposed method of Fuzzy MCDA is presented and followed by a suitable example for verification. The paper finally concludes with some ideas for future research and development.

2 Literature Review

The type-2 fuzzy set was proposed by Zadeh [11] in 1975 to include the more considerable uncertainty and impreciseness, which slowly started to gain popularity after two decades [12]. Later, the Interval Type-2 Fuzzy Sets (IT2FSs) turned out to be the most commonly used type-2 fuzzy sets due to its easiness in representation and computational procedures [10]. Several models and industrial applications were developed using IT2FSs as they could handle more noisy data. A brief review of various MCDM techniques on IT2FSs is available in [9].

Cheng and Hwan proposed fuzzy TOPSIS [16] by integrating the existing TOPSIS method with fuzzy set theory. Later, it found valuable applications for a variety of problems such as supplier evaluation and selection in Supply Chain Management [13], public transportation [14], robot selection [15], etc. Fuzzy AHP procedure was developed where the pairwise comparisons and scores were estimated using fuzzy numbers. This powerful method of mathematical simplicity is one of the widely used fuzzy MCDM procedures.

3 Research Methodology

In this section, we will layout the procedures of TOPSIS and AHP methods and then review some fundamentals of fuzzy set theory as a literary introduction.

3.1 Technique for Order of Preference by Similarity to Ideal Solution (TOPSIS)

TOPSIS [2], proposed by Hwang and Yoon, is one of the most widely familiar MCDA methods. It chooses an optimal alternative based on its proximity to a Positive Ideal Solution (PIS) while maximizing the remoteness to the Negative Ideal Solution (NIS). The procedure of TOPSIS is explained as follows

1. Let there be k decision-makers, n alternatives $A_1, A_2, ..., A_n$ which need to be evaluated against m criteria $C_1, C_2, ..., C_m$. Each decision-maker creates a decision matrix $D_{n\times m}$ which contains the performance rating for each alternative with respect to all given criteria, denoted as x_{ij} where $i = 1, 2, ..., n$ and $j = 1, 2, ..., m$.

$$\begin{array}{c} \\ A_1 \\ A_2 \\ \vdots \\ A_n \end{array} \begin{array}{c} \begin{array}{cccc} C_1 & C_2 & \cdots & C_m \end{array} \\ \begin{bmatrix} x_{11} & x_{12} & \cdots & x_{1m} \\ x_{21} & x_{22} & \cdots & x_{2m} \\ \vdots & \vdots & \vdots & \\ x_{m1} & x_{m2} & \cdots & x_{nm} \end{bmatrix} \end{array}$$

2. The $D_{n\times m}$ matrices are converted into $R_k = (r_{ij})_{n\times m}$ by normalization. $r_{ij} = \frac{x_{ij}}{\sqrt{\sum_{i=1}^{n} x_{ij}^2}}$, $i = 1, 2, ..., n$, $j = 1, 2, ..., m$
3. The evaluation criteria are given weights by the decision makers depending on their respective level of influence. If $w_j (j = 1, 2, ..., m)$ denotes the criteria weight vector, then the weighted normalized decision matrix $T = (t_{ij})_{n\times m} = (w_j r_{ij})_{n\times m}$ where $i = 1, 2, ..., n$.
4. Let J_+ denote the set of benefit criteria (the more, the better) and similarly J_- denotes the set of negative criteria (the less, the better). Now PIS and NIS are calculated with the best and worst level of attributes respectively.
   $PIS_i = \{min(t_{ij}|i = 1, 2, ..., n)|j \in J_-, max(t_{ij}|i = 1, 2, ..., n)|j \in J_+\}$
   $NIS_i = \{max(t_{ij}|i = 1, 2, ..., n)|j \in J_-, min(t_{ij}|i = 1, 2, ..., n)|j \in J_+\}$
5. The distance of each alternative from PIS and NIS is calculated.

$$d_{iPIS} = \sqrt{\sum_{j=1}^{m}(t_{ij} - PIS_{ij})^2} \quad i = 1, 2, ..., n$$

$$d_{iNIS} = \sqrt{\sum_{j=1}^{m}(t_{ij} - NIS_{ij})^2} \quad i = 1, 2, ..., n$$

6. Find the relative proximity of each alternative on a measure with respect to the best alternative.

$$s_i = \frac{d_{iNIS}}{d_{iNIS} + d_{iPIS}} \quad i = 1, 2, ..., n$$

   It can be deduced that the i-th solution is the PIS when $s_i = 1$ or the NIS when $s_i = 0$. The alternatives are ranked according to their s_i values.

3.2 Analytical Hierarchy Process (AHP)

Saaty developed AHP [6] to determine the relative importance of alternatives and criteria in MCDM. It involves the construction of a hierarchy where the goal is at the top, criteria of the problem in the intermediate levels, and the decision alternatives belongs to the bottom. The next step is the priority setting, where the relative importance of criteria at each level are determined. The pairwise comparison of elements are made on a

linguistic scale of $1-9$; 1 being equally essential and 9 being most important. A matrix A of order $m \times m$ is built by the pairwise comparisons of m criteria.

$$\begin{array}{c} \\ C_1 \\ C_2 \\ \vdots \\ C_m \end{array} \begin{array}{c} \begin{array}{cccc} C_1 & C_2 & \cdots & C_m \end{array} \\ \begin{bmatrix} a_{11} & a_{12} & \cdots & a_{1m} \\ a_{21} & a_{22} & \cdots & a_{2m} \\ \vdots & \vdots & \ddots & \vdots \\ a_{m1} & a_{m2} & \cdots & a_{mm} \end{bmatrix} \end{array},$$

where $a_{ii} = 1, a_{ij} = \frac{1}{a_{ji}}$ for $a_{ij} \neq 0$.

Normalize the comparison matrix by dividing each element by the sum of all elements in the respective column. The criteria vector w, an $m \times 1$ vector, is determined by averaging the entries on each row of the normalized matrix.

$$w_j = \frac{\sum_{l=1}^{m} \bar{a}_{jl}}{m}$$

As explained in [5], the $n \times m$ matrix S of option scores is calculated where n is the number of decision alternatives. Each element s_{ij} of S represents the score of i-th alternative with j-th criterion. In order to achieve this, a pairwise comparison $n \times n$ matrix $B^{(j)}$ is built for each criterion in the same way as before. On applying AHP again, we obtain the score vectors $s^{(j)}, j = 1, 2, ..., m$ and $S = [s^{(1)} \quad s^{(2)} \quad ... \quad s^{(m)}]$. Finally, the ranking is achieved by $v = Sw$ and v_i corresponds to the global score evaluated by the AHP to the i-th alternative.

3.3 Fuzzy Set Theory

The application of traditional set theory worked well for definite and well-distinguished situations. However, there are many cases in real life where the elements of a set are not precisely definite or not distinguishable. The invention of the fuzzy set theory acted as a solution to this problem. The elements of a fuzzy set possess a grade of membership value. Reference [3] presents the following definitions for fuzzy set theory. Since the concept of Interval fuzzy sets is used throughout this paper, some preliminary knowledge regarding the same is listed as in [1].

Definition 1. *Let x be an arbitrary element of a set X, then a fuzzy set $\tilde{A}$ in X is a set of ordered pairs:*

$$\tilde{A} = \{(x, \mu_{\tilde{A}}(x)) | x \in X\}$$

where $\mu_{\tilde{A}}(x) \in [0, 1]$ is called the membership of x.

Definition 2. *A type 2 fuzzy set is a fuzzy set whose membership values are type 1 fuzzy sets on $[0, 1]$ and is denoted as*

$$\tilde{A} = \{((x, u), \mu_{\tilde{A}}(x, u)) | \forall x \in X, 0 \leq u, \mu_{\tilde{A}}(x, u) \leq 1\}$$

Definition 3. *Let Int*$([0,1])$ *represent the set of all closed subintervals of* $[0,1]$ *and* X *be any finite non-empty set. An Interval Type-2 Fuzzy Set (IT2FS)* $\tilde{A}$ *in* X *is* $\tilde{A} = \{(x, \mu_{\tilde{A}}(x)) | x \in X\}$ *where the function* $\mu_{\tilde{A}} : X \rightarrow$*Int*$(0,1)$ *defines the degree of membership of an element* x *to* $\tilde{A}$ *such that,*$x \rightarrow \mu_{\tilde{A}} = [\mu^{-}_{\tilde{A}}(x), \mu^{+}_{\tilde{A}}(x)]$.

Definition 4. *Let* A^L *and* A^U *represent two generalized trapezoidal fuzzy numbers. Let* h^L_A *and* h^U_A *denote the heights of* A^L *and* A^U *respectively, where the height of a generalized fuzzy number is between zero and one. Let* $a^L_1, a^L_2, a^L_3, a^L_4, a^U_1, a^U_2, a^U_3$, *and* a^U_4 *be real values. An Interval Type-2 Trapezoidal Fuzzy Number (IT2TrFN)* $\tilde{A}$ *defined on the universe of discourse* X *is depicted as:*

$$A = [A^L, A^U] = [(a^L_1, a^L_2, a^L_3, a^L_4; h^L_A), (a^U_1, a^U_2, a^U_3, a^U_4; h^U_A)]$$

where $a^L_1 \leq a^L_2 \leq a^L_3 \leq a^L_4$, $a^U_1 \leq a^U_2 \leq a^U_3 \leq a^U_4$, $0 \leq h^L_A \leq h^U_A \leq 1$, $a^U_1 \leq a^L_1$, *and* $a^L_4 \leq a^U_4$. *Also,* $A^L = (a^L_1, a^L_2, a^L_3, a^L_4; h^L_A)$, $A^U = (a^U_1, a^U_2, a^U_3, a^U_4; h^U_A)$ *and* $A^L \subset A^U$. *The membership functions of* A^L *and* A^U *are given as follows:*

$$A^L(x) = \begin{cases} h^L_A(x - a^L_1)/(a^L_2 - a^L_1) & \text{for } a^L_1 \leq x \leq a^L_2, \\ h^L_A & \text{for } a^L_2 \leq x \leq a^L_3, \\ h^L_A(a^L_4 - x)/(a^L_4 - a^L_3) & \text{for } a^L_3 \leq x \leq a^L_4, \\ 0 & \text{otherwise;} \end{cases}$$

$$A^U(x) = \begin{cases} h^U_A(x - a^U_1)/(a^U_2 - a^U_1) & \text{for } a^U_1 \leq x \leq a^U_2, \\ h^U_A & \text{for } a^U_2 \leq x \leq a^U_3, \\ h^U_A(a^U_4 - x)/(a^U_4 - a^U_3) & \text{for } a^U_3 \leq x \leq a^U_4, \\ 0 & \text{otherwise.} \end{cases}$$

The arithmetic operations on IT2TrFN can be referred from [1]. Here, we use the concept of signed distance extended over IT2TrFNs to achieve the ranking of the alternatives as proposed in [1].

Definition 5. *Consider an IT2TrFN 'A' on the universe of disclosure* X *and let* $A = [A^L, A^U] = [(a^L_1, a^L_2, a^L_3, a^L_4; h^L_A), (a^U_1, a^U_2, a^U_3, a^U_4; h^U_A)]$, *where* $0 < h^L_A \leq h^U_A \leq 1$. *Let* $\tilde{1}_1$ *represents a level 1 fuzzy number corresponding to the y-axis at* $x = 1$. *The signed distance from* A *to* $\tilde{1}_1$ *is defined as:*

$$d(A, \tilde{1}_1) = \tfrac{1}{8}(a^L_1 + a^L_2 + a^L_3 + a^L_4 + 4a^U_1 + 2a^U_2 + 2a^U_3 + 4a^U_4 + 3(a^U_2 + a^U_3 - a^U_1 - a^U_4)\tfrac{h^L_A}{h^U_A} - 16)$$

4 The Proposed Method

As discussed before, the following algorithm is an efficient integration of TOPSIS and AHP to handle uncertain environments.

1. Express the ratings of alternative A_i with respect to each criterion C_j as IT2TrFNs.

2. Construction of Fuzzy weight vector The pairwise comparisons of criteria are made as follows:

$$\begin{array}{c} \\ C_1 \\ C_2 \\ \vdots \\ C_m \end{array} \begin{array}{c} \begin{array}{cccc} C_1 & C_2 & \cdots & C_m \end{array} \\ \begin{bmatrix} a_{11} & a_{12} & \cdots & a_{1m} \\ a_{21} & a_{22} & \cdots & a_{2m} \\ \vdots & \vdots & \ddots & \vdots \\ a_{m1} & a_{m2} & \cdots & a_{mm} \end{bmatrix} \end{array}$$

where each a_{ij} is an interval type-2 fuzzy number.
Normalize the matrix by converting each entry of the above matrix as:

$$\bar{a}_{ij} = \frac{a_{ij}}{\sum_{i=1}^{m} a_{ij}}$$

Now, the criteria vector is obtained as:

$$\tilde{w}_j = \frac{\sum_{i=1}^{m} \bar{a}_{ij}}{m}$$

3. Form the decision matrix of alternatives with criteria by averaging the values given by decision makers.
4. Determine the weighted decision matrix

$$T = (t_{ij})_{n\times m} = (w_j r_{ij})_{n\times m}$$

for $i = 1, 2, ..., n$ and $j = 1, 2, ..., m$.
5. Compute the signed distance of each IT2FN component of the weighted decision matrix T.
$d(A, \tilde{1}_1) = \frac{1}{8}(a_1^L + a_2^L + a_3^L + a_4^L + 4a_1^U + 2a_2^U + 2a_3^U + 4a_4^U + 3(a_2^U + a_3^U - a_1^U - a_4^U)\frac{h_A^L}{h_A^U} - 16)$
When $0 < h_A^L = h_A^U \leq 1$, use the following for faster calculation

$$d(A, \tilde{1}_1) = \frac{1}{8}(a_1^L + a_2^L + a_3^L + a_4^L + a_1^U + 5a_2^U + 5a_3^U + a_4^U - 16)$$

6. Form the matrix $M = (m_{ij})_{n\times m}$ of signed distance values.
7. If required, normalize the matrices M.
8. Identify A^+ and A^- for the matrix M
$A^+ = (p_1^+, p_2^+, ..., p_m^+)$ is the PIS.
$A^- = (p_1^-, p_2^-, ..., p_m^-)$ is the NIS.
where

$$p_j^+ = \begin{cases} \max\limits_i p_{ij} & \text{if } p_{ij} \in J^+ \\ \min\limits_i p_{ij} & \text{if } p_{ij} \in J^- \end{cases}$$

$$p_j^- = \begin{cases} \min\limits_i p_{ij} & \text{if } p_{ij} \in J^+ \\ \max\limits_i p_{ij} & \text{if } p_{ij} \in J^- \end{cases}$$

J^+ and J^- are the sets of benefit and cost criteria respectively.

9. Calculate the Euclidean distances of each A_i

$$d_i^+ = \sqrt{\sum_{j=1}^{n}(p_j^+ - p_{ij})^2} \quad i = 1, 2, ..., m$$

$$d_i^- = \sqrt{\sum_{j=1}^{n}(p_j^- - p_{ij})^2} \quad i = 1, 2, ..., m$$

10. The relative closeness with respect to the Positive Ideal Solution is obtained as:

$$\xi(A_i) = \frac{d_i^-}{d_i^+ + d_i^-}$$

11. Form a vector G combining the results obtained from the above step.

$$\text{G} = \begin{bmatrix} \xi(M_1) \\ \vdots \\ \xi(M_m) \end{bmatrix}$$

12. Ranking of Alternatives
    (a) If $\xi(M_i) > \xi(M_j) \implies A_i > A_j$
    (b) If $\xi(M_j) > \xi(M_i) \implies A_j > A_i$
    (c) else if $\xi(M_i) = \xi(M_j) \implies A_i \approx A_j$

5 Case Study

We use an example of car selection [4] based on four attributes "Safety", "Price", "Appearance", and "Performance" to evaluate the proposed MCDM method. Assume there are three decision-makers D_1, D_2 and D_3 to evaluate the cars x_1, x_2 and x_3 based on their given attributes. The linguistic terms and their corresponding fuzzy values are used to form the decision matrix. Similar measures are used to evaluate the average weights of the attributes proposed by the decision-makers.

1. Averaging the decision values given by the decision-makers in [4], we get the average decision matrix as

$$\begin{array}{c} \\ \text{Safety} \\ \text{Price} \\ \text{Appearance} \\ \text{Performance} \end{array} \begin{array}{c} \begin{array}{ccc} x_1 & x_2 & x_3 \end{array} \\ \begin{bmatrix} \tilde{f}_{11} & \tilde{f}_{12} & \tilde{f}_{13} \\ \tilde{f}_{21} & \tilde{f}_{22} & \tilde{f}_{23} \\ \tilde{f}_{31} & \tilde{f}_{32} & \tilde{f}_{33} \\ \tilde{f}_{41} & \tilde{f}_{42} & \tilde{f}_{43} \end{bmatrix} \end{array}$$

   where the values are given in 1.

Table 1: Average decision matrix values

$\tilde{\mathbf{f}}_{\mathbf{ij}}$	**Corresponding IT2TrFN Value**
$\tilde{f}_{11}$	$((0.57, 0.77, 0.77, 0.93; 1, 1), (0.67, 0.77, 0.77, 0.85; 0.9, 0.9))$
$\tilde{f}_{12}$	$((0.63, 0.83, 0.83, 0.97; 1, 1), (0.73, 0.83, 0.83, 0.9; 0.9, 0.9))$
$\tilde{f}_{13}$	$((0.7, 0.87, 0.87, 0.97; 1, 1), (0.78, 0.87, 0.87, 0.92; 0.9, 0.9))$
$\tilde{f}_{21}$	$((0.77, 0.93, 0.93, 1; 1, 1), (0.85, 0.93, 0.93, 0.97; 0.9, 0.9))$
$\tilde{f}_{22}$	$((0.7, 0.87, 0.87, 0.97; 1, 1), (0.78, 0.87, 0.87, 0.92; 0.9, 0.9))$
$\tilde{f}_{23}$	$((0.83, 0.97, 0.97, 1; 1, 1), (0.9, 0.97, 0.97, 0.98; 0.9, 0.9))$
$\tilde{f}_{31}$	$((0.77, 0.93, 0.93, 1; 1, 1), (0.85, 0.93, 0.93, 0.97; 0.9, 0.9))$
$\tilde{f}_{32}$	$((0.83, 0.97, 0.97, 1; 1, 1), (0.9, 0.97, 0.97, 0.98; 0.9, 0.9))$
$\tilde{f}_{33}$	$((0.43, 0.63, 0.63, 0.83; 1, 1), (0.53, 0.63, 0.63, 0.73; 0.9, 0.9))$
$\tilde{f}_{41}$	$((0.77, 0.93, 0.93, 1; 1, 1), (0.85, 0.93, 0.93, 0.97; 0.9, 0.9))$
$\tilde{f}_{42}$	$((0.83, 0.97, 0.97, 1; 1, 1), (0.9, 0.97, 0.97, 0.98; 0.9, 0.9))$
$\tilde{f}_{43}$	$((0.77, 0.93, 0.93, 1; 1, 1), (0.85, 0.93, 0.93, 0.97; 0.9, 0.9))$

Table 2: Average criteria weights

$\tilde{\mathbf{w}}_{\mathbf{ij}}$	**Corresponding IT2TrFN Value**
$\tilde{w}_1$	$((0.83, 0.97, 0.97, 1; 1, 1), (0.9, 0.97, 0.97, 0.98; 0.9, 0.9))$
$\tilde{w}_2$	$((0.83, 0.97, 0.97, 1; 1, 1), (0.9, 0.97, 0.97, 0.98; 0.9, 0.9))$
$\tilde{w}_3$	$((0.43, 0.63, 0.63, 0.83; 1, 1), (0.53, 0.63, 0.63, 0.73; 0.9, 0.9))$
$\tilde{w}_4$	$((0.77, 0.93, 0.93, 1; 1, 1), (0.85, 0.93, 0.93, 0.97; 0.9, 0.9))$

2. We can get the average weighting matrix $\tilde{W}$ by averaging the criteria weight values proposed. Table 2 represents the elements of $\tilde{W}$.

$$\tilde{W} = \begin{matrix} Safety & Price & Appearance & Performance \end{matrix} \\ \begin{bmatrix} \tilde{w}_1 & \tilde{w}_2 & \tilde{w}_3 & \tilde{w}_4 \end{bmatrix}$$

3. Get the weighted decision matrix as

$$\tilde{Y}_w = \begin{matrix} & x_1 & x_2 & x_3 \end{matrix} \\ \begin{matrix} \text{Safety} \\ \text{Price} \\ \text{Appearance} \\ \text{Performance} \end{matrix} \begin{bmatrix} \tilde{Y}_{11} & \tilde{Y}_{12} & \tilde{Y}_{13} \\ \tilde{Y}_{21} & \tilde{Y}_{22} & \tilde{Y}_{23} \\ \tilde{Y}_{31} & \tilde{Y}_{32} & \tilde{Y}_{33} \\ \tilde{Y}_{41} & \tilde{Y}_{42} & \tilde{Y}_{43} \end{bmatrix}$$

Table 3: Weighted decision matrix values

$\tilde{\mathbf{Y}}_{\mathbf{ij}}$	**Corresponding IT2TrFN Value**
$\tilde{Y}_{11}$	$((0.47, 0.74, 0.74, 0.93; 1), (0.6, 0.74, 0.74, 0.84; 0.9))$
$\tilde{Y}_{12}$	$((0.53, 0.81, 0.81, 0.97; 1), (0.66, 0.81, 0.81, 0.89; 0.9))$
$\tilde{Y}_{13}$	$((0.58, 0.84, 0.84, 0.97; 1), (0.71, 0.84, 0.84, 0.9; 0.9))$
$\tilde{Y}_{21}$	$((0.64, 0.9, 0.9, 1; 1), (0.77, 0.9, 0.9, 0.95; 0.9))$
$\tilde{Y}_{22}$	$((0.58, 0.84, 0.84, 0.97; 1), (0.71, 0.84, 0.84, 0.9; 0.9))$
$\tilde{Y}_{23}$	$((0.69, 0.93, 0.93, 1; 1), (0.81, 0.93, 0.93, 0.97; 0.9))$
$\tilde{Y}_{31}$	$((0.33, 0.59, 0.59, 0.83; 1), (0.45, 0.59, 0.59, 0.71; 0.9))$
$\tilde{Y}_{32}$	$((0.36, 0.61, 0.61, 0.83; 1), (0.48, 0.61, 0.61, 0.72; 0.9))$
$\tilde{Y}_{33}$	$((0.19, 0.4, 0.4, 0.69; 1), (0.28, 0.4, 0.4, 0.54; 0.9))$
$\tilde{Y}_{41}$	$((0.59, 0.87, 0.87, 1; 1), (0.72, 0.87, 0.87, 0.93; 0.9))$
$\tilde{Y}_{42}$	$((0.59, 0.87, 0.87, 1; 1), (0.72, 0.87, 0.87, 0.93; 0.9))$
$\tilde{Y}_{43}$	$((0.64, 0.9, 0.9, 1; 1), (0.77, 0.9, 0.9, 0.95; 0.9))$

4. Calculate the signed distance of each element of the above matrix.
5. Form the corresponding matrix of signed distance values as

$$M = \begin{matrix} & x_1 & x_2 & x_3 \end{matrix} \\ \begin{matrix} \text{Safety} \\ \text{Price} \\ \text{Appearance} \\ \text{Performance} \end{matrix} \begin{bmatrix} -4.2667 & -3.2067 & -2.7367 \\ -1.8133 & -2.7367 & -1.3433 \\ -6.5933 & -6.2833 & -9.5067 \\ -2.2900 & -2.2900 & -1.8133 \end{bmatrix}$$

6. Find PIS and NIS
   Since the greater magnitude of signed distance (with a negative sign) implies larger

deviation from certainty, we select the smallest magnitude for benefit criteria and greatest magnitude for cost criteria in case of PIS. With the similar logic, NIS is obtained.

$$x^+ = \begin{bmatrix} -2.7367 \\ -2.7367 \\ -6.2833 \\ -1.8133 \end{bmatrix} \quad x^- = \begin{bmatrix} -4.2667 \\ -1.3433 \\ -9.5067 \\ -2.2900 \end{bmatrix}$$

7. Calculate the euclidean distances of each alternative from PIS and NIS.
   $d_1^+ = 1.8753 \quad d_1^- = 2.9511$
   $d_2^+ = 0.6694 \quad d_2^- = 3.6682$
   $d_3^+ = 3.5117 \quad d_3^- = 1.6025$
8. The relative closeness with respect to the PIS are:
   $\xi(x_1) = 0.6114$
   $\xi(x_2) = 0.8457$
   $\xi(x_3) = 0.3133$
9. Thus the order of preference of alternatives is $x_2 > x_1 > x_3$.

Since the relative closeness of all the alternatives are different, a clear alternative ranking is achieved with respect to the given criteria set.

6 Conclusion

In this paper, we discussed the basic concepts of Multi-criteria decision making procedures and Fuzzy set theory with more focus on Interval type-2 fuzzy sets. It was observed that type-2 fuzzy membership associates with more real situations compared to type-1 fuzzy set and its membership. Thus, we have integrated the fuzzy TOPSIS method in decision making, with the fuzzy AHP method implemented for weight factor evaluation. The proposed method has been developed in a type-2 fuzzy environment using trapezoidal fuzzy numbers, and the alternatives are then ranked using the signed distance approach. The method has been verified by using an example from the existing literature. The proposed method gives a powerful method of classifying the alternatives, with highly valuable computational simplicity. The next course of action is to conduct a detailed sensitivity analysis to improvise the method for large problems.

References

1. Chen, Ting-Yu. "An integrated approach for assessing criterion importance with interval type-2 fuzzy sets and signed distances." Journal of the Chinese Institute of Industrial Engineers 28, no. 8 (2011): 553-572.
2. Hwang, Ching-Lai, and Kwangsun Yoon. "Methods for multiple attribute decision making." In Multiple attribute decision making, pp. 58-191. Springer, Berlin, Heidelberg, 1981.
3. Zimmermann, Hans-Jürgen. Fuzzy set theory—and its applications. Springer Science & Business Media, 2011.
4. Lee, Li-Wei, and Shyi-Ming Chen. "Fuzzy multiple attributes group decision-making based on the extension of TOPSIS method and interval type-2 fuzzy sets." In 2008 International Conference on Machine Learning and Cybernetics, vol. 6, pp. 3260-3265. IEEE, 2008.

5. Mocenni, Chiara. "The analytic hierarchy process." University of Siena, Department of Information Engineering and Mathematics (2016).
6. Saaty, Thomas L. "Decision making with the analytic hierarchy process." International journal of services sciences 1, no. 1 (2008): 83-98.
7. Zadeh, L. A. "Information and control." Fuzzy sets 8, no. 3 (1965): 338-353.
8. Zanakis, Stelios H., Anthony Solomon, Nicole Wishart, and Sandipa Dublish. "Multi-attribute decision making: a simulation comparison of select methods." European journal of operational research 107, no. 3 (1998): 507-529.
9. Celik, Erkan, Muhammet Gul, Nezir Aydin, Alev Taskin Gumus, and Ali Fuat Guneri. "A comprehensive review of multi criteria decision making approaches based on interval type-2 fuzzy sets." Knowledge-Based Systems 85 (2015): 329-341.
10. Mendel, Jerry M. "Advances in type-2 fuzzy sets and systems." Information sciences 177, no. 1 (2007): 84-110.
11. Zadeh, L. A. "The concept of a linguistic variable and its application to approximate reasoning—I." Information sciences 8, no. 3 (1975): 199-249.
12. John, Robert, and Simon Coupland. "Type-2 fuzzy logic: A historical view." IEEE computational intelligence magazine 2, no. 1 (2007): 57-62.
13. Chen, Chen-Tung, Ching-Torng Lin, and Sue-Fn Huang. "A fuzzy approach for supplier evaluation and selection in supply chain management." International journal of production economics 102, no. 2 (2006): 289-301.
14. Awasthi, Anjali, Satyaveer S. Chauhan, and Hichem Omrani. "Application of fuzzy TOPSIS in evaluating sustainable transportation systems." Expert systems with Applications 38, no. 10 (2011): 12270-12280.
15. Chu, T-C., and Y-C. Lin. "A fuzzy TOPSIS method for robot selection." The International Journal of Advanced Manufacturing Technology 21, no. 4 (2003): 284-290.
16. Chen, Shu-Jen, and Ching-Lai Hwang. "Fuzzy multiple attribute decision making methods." In Fuzzy multiple attribute decision making, pp. 289-486. Springer, Berlin, Heidelberg, 1992.
17. Sangaiah, A.K., Gopal, J., Basu, A. et al. Neural Comput & Applic (2017) 28: 111. https://doi.org/10.1007/s00521-015-2040-7 .

Evaluation of Interaction Pattern of Estrogen Receptor alpha and beta with Available Drugs for Breast Cancer through Computational Analysis

Prashant Bhardwaj
Department of Coputer Science and Engineering, NIT Agartala, 799046, India
Email: cse.pbh@gmail.com

Biswanath Bhunia
Department of BioEngineering, NIT Agartala, 799046, India
Email: bbhunia@gmail.com

Abstract. Breast cancer is the leading cancer in women, both in developed and developing countries. The survival rate is more in developed countries compared to the developing countries. Breast cancer is a malignant tumour that develops in breast tissues. The cancer cells start from breast ducts and spread to lymph nodes, and in course of time spreads to different parts of the body. The biologist have attributed the cause of cancer to the imbalance of Estrogen Receptors(ER) , progesterone receptors(PR) and human epidermal growth factor receptor(HER). The aim of this manuscript is to evaluate the Interaction Pattern of Estrogen Receptor alpha and beta with available drugs for Breast Cancer through computational analysis. The protein samples with RCSB code 5W9C And 2FSZ were considered as a template for Estrogen Receptor alpha and beta respectively. The interaction study was carried out with commercially available 30 drugs with theses receptors using CDOCKER tool of Discovery Studio 4.1. Doxorubicin Hydrochloride and Lapatinib Ditosylate showed maximum energy among 30 molecules and reported as 54.02 KJ/ and 54.76 KJ/ for ER alpha and ER beta respectively. It is suggested that Doxorubicin Hydrochloride and Lapatinib Ditosylate may be the best blocker for breast cancer disease.

Mathematics Subject Classification: 92C75, 97M60, 92B05, 62P10

Keywords: Breast Cancer · Estrojen Receptor · Molecular Docking · CDOCKER.

1 Introduction

Breast cancer is the leading cancer in Women all over the world. The mutation in DNA of the breast cell is the main cause of the Breast Cancer. Some cases of breast cancer inherited genetically, others are caused by unhealthy life styles and environmental pollution. Breast cancer can be cate- gorised in five types depending on the molecular subtype signatures: Luminal A, Luminal B, Normal Like, Basal Like and ERBB2[2]. Among the different types of breast cancer, Human Epidermal Growth Factor Receptor (HER) and Estrogen receptor(ER) plays a major role. Most of the breast cancer

cases are ER-positive in women today[1]. Breast cancer exhibit different behavioural and pathological features; hence the treatment needs to be specific. The motivation to write this paper is based on the fact that approximately 85% breast cancer is caused by over expression of ER.

About 5 to 10% Breast cancer cases are attributed to genetic inheritance from the person's parents including BRCA1 and BRCA2 mutations. The survival rates for breast cancer depends on the type and extent of mutation and age of the patient. Survival in the developed nations, are higher compared to the developing countries[3][4][5]. The developed countries have better medical diagnosis facilities and there is awareness among the general population; The survival rate in the developing countries is is poor due to the lack of awareness and adequate medical facilities among the wide population [6]. The first perceptible sign of breast cancer include a lump in the breast, that feels different from the rest of the breast tissue. In the later stages, the breast cancer cases become metastatic and the cancer cells spread to bone, liver, lung and brain[7]. Thus in general cases breast cancer is manifested via symptoms of other disease such as Bone or joint pains, jaundice, unexplained weight loss or neurological symptoms when it becomes metastatic. It has been observed that smoking tobacco appears to elevate the risk of breast cancer, with direct proportions to the amount smoked and inversely proportional to the age at which smoking began[8]. The breast cancer for long-time chain smokers ticks at an increased rate of 35% to 50. In the women the use of hormonal birth control I also related to the development of premenopausal breast cancer[9][10] . There are many diet related factors that affect the possible endocrine disorder. The amount of alcohol intake [11] plays a role in endocrine malfunctioning. Obesity is another major risk factor [12] for breast cancer. The risk increases by 7% with a unit of alcohol, and as the intake intake increases, the risk increases in linear fashion[11]. Section 2 emphasizes on the relation between Estrogen and Breast Cancer. Section 3 introduces the concept of Molecular docking. Section 4 presents the data and processing of the protein and ligands. Section 5 concludes with a discussion.

2 Estrogen Receptor and Breast Cancer

We know that ovaries produce the estrogen which affects normal growth of our body and its effect is mostly discussed as a promoter of sexual characteristics of a human being. Estrogen plays an important role in growth and development of sexual organs of female. Estrogen plays a major role to regulate the menstrual cycle and reproduction. Estrogen interacts with the receptors, estrogen receptor ER and ER and modulate the gene expression of elements in the promoter region resulting in the biological effects of estrogen. Breast cancers can be ER positive or ER negative. ER positive cancer have higher survival rate than ER negative [13]. Around 85% of sub types of Breast Cancer are breast Cancer positive , hence estrogen play a major role in promoting the propagation of both the normal and the neoplastic breast epithelium. The relation between dose of estrogen and duration of exposure is a factor in breast cancer risk. The women experiencing early menarche and late menopause are at a greater risk to suffer by breast cancer, whereas the women having late menarche and early menopause suffer with less risk of breast cancer. With the increasing age, the production of estrogen in the ovaries

decreases and increase the risk of breast cancer [14][15][16]. The biological activities such as not having child, having late child and breast feeding patterns are also associated with the risk of breast cancer [17]. The study of estrogen and other hormones during the pregnancy and breast feeding gives us very useful insights into the relation of the estrogen production and risk of breast cancer. The very high release of estrogen and progesterone during pregnancy reduces the risk of breast cancer in long term by promoting growth of the mammary epithelium differentiation of epithelial [18][19]. Thus each birth reduces the risk of breast cancer[20][21]. The breast cancer risk vary with the estrogen receptor level of an individuals[22][23]. Estrogen Receptor levels vary with age, menopausal status and race [24][25]. The balance between ER and ER receptor determine the acceptability of estrogen by breast tissue.Generally ER has a lower affinity for estrogen but it may affect the sensitivity of ER to estrogen [26].

3 Molecular Docking

Molecular docking is a computational tool to predict possibilities of complex formation between two molecules, it might be protein-protein or protein-ligand. Molecular Docking considers the chemical structure of the combining molecules and compare all the possible orientation of molecules that could bind to each other. Docking aims to classify appropriate poses of ligands in the binding pocket of a protein and predict interaction energy around those poses. The strength of the association or binding affinity between two molecules is predicted using scoring functions. Docking is most frequently used tool for in-silico prediction of the successful binding of two molecules. Pharmaceutical research has benefited a lot by the molecular docking technologies. The orientation of drug candidates can be easily tested to interact with their target protein in order to predict the affinity and activity of the small molecule before in-vitro testing. There are numerous possible poses of interaction for a protein structure, every pose is accessed for interaction with the other molecule and the pose with the lowest energy score is predicted as best match . Since the revolutionary Kuntz et.al. [27] substantial advancement has been made in research of molecular docking to aggravate the computational speed and accuracy. The protein-ligand docking has seen major developments because of its economic and social impact on the research techniques compared to the in vitro research for structure-based drug design [28][29] A protein-ligand algorithm works in two stages: sampling and scoring. Sampling refers to the searching of the ligand binding orientations near binding pockets of a protein. Scoring is the prediction of the interaction/ binding energy of the ligand for various poses in the binding orientations pocket employing empirical energy function[30]. The scoring functions can be grouped into three category: force field, empirical, and knowledge-based scoring. CDOCKER tool of Discovery studio has been used for present study. CDOCKER is a CHARMM (Chemistry at HARvard Macromolecular Mechanics)-based docking algorithm gives highly accurate docked poses. CHARMM is built on a conventional molecular mechanics force field algorithm[31].

4 Material and Method

4.1 Simulation Environment

All simulations were performed on Dell Precision M4800 workstation having Intel® Core (TM) i7-4910MQ, Quad Core, 2.90 GHz, 3.90 GHz Turbo, 8MB cache, with HD Graphics 4600, Mobile Intel® QM87 Chipset, 16 GB RAM operating on 64-bit operating system.The Docking procedure was carried using CDOCKER tool of Discovery Studio 4.1.

4.2 Selection of Drug structure for docking

The pdb structures of the Estrogen receptors were downloaded from the RCSb website. The resolution and R-free value of the crystallographic structure was considered as a deciding factor to select the template for docking study. Among the 258 ER alpha structures available, we have chosen the one with the highest resolution for our study. The list of 55 breast cancer drugs was collected from the cancer website [cancer website reference] . The 3 Dimensional structures of the drugs were downloaded from the pubchem website. Among the list of the drugs available,9 compounds were found to act upon the same constituent compound. The 3 dimensional Conformer generation for 12 drugs could not be possible in pubchem since they had too many atoms. The details of 7 drug compumnds was not available in the puchem database. The conformation of 24 distinct drug molecules could be downloaded from puchem database, rest were either redundant chemicals or could not be downloaded since the 3D structure could not be found in the pubchem website.

4.3 Selection of Drug structure for docking

For Estrogen Alpha 5W9C structure and for Estrogen Beta 2FSZ was opened in Discovery studio 4.1. The water, hetam and ligand groups were removed. Polar hydrogen was added to the molecule to balance the charge. Valence electron was added to the molecule to simulate the natural environment. There were 4 chains in the crystallographic structure of 5W9C: A, B, C and D The structure of 2FSZ contained 2 chains: A and B. The redundant chains were removed and only A chain was kept for docking in both the structures. ER alpha protein fetched 45 binding sites after applying the binding site prediction algorithm. ER beta fetched 15 sites for docking. The biggest pocket with radius 9.4 Å was chosen for ER alpha and pocket with radius 16.1 Å. Was chosen for 2FSZ. One by one, 24 every available ligand was docked using CDOCKER algorithm.

5 Result

The docking results of the protein and the ligands were very positive. All the 24 drug templates showed high interaction energy when docking to the ER and ER candidates.There was not a major difference in binding energy in most of the cases. The difference between the docking energy of ER and ER with the 24 drug samples varied

by and amount of 5KCal/mol. Doxorubicin Hydrochloride reports highest CDOCKER Energy (54.02 K.Cal.) with ER , Lapatinib Ditosylate shows highest CDOCKER Energy (54.76 K.Cal.) with ER . The binding energy of the ER and ER with the drug templates is shown in Fig 1.

S.No.	Breast Cancer Drug	CDOCKER Energy with 5W9C	CDOCKER Energy with 2FSZ
1	Fluorouracil Injection	10.66	15.8
2	Thiotepa	26.056	20.09
3	Gemcitabine Hydrochloride	26.77	27.07
4	Exemestane	27.032	29.138
5	Cyclophosphamide	28.695	23.288
6	Aredia (Pamidronate Disodium)	30.489	26.132
7	Femara (Letrozole)	30.59	24.57
8	Letrozole	30.593	24.57
9	Anastrozole	32.82	30.03
10	Fulvestrant	37.003	49.22
11	Faslodex (Fulvestrant)	37.006	49.22
12	Fareston (Toremifene)	37.56	37.52
13	Lynparza (Olaparib)	38.469	44.132
14	Trastuzumab	38.789	33.71
15	Xeloda (Capecitabine)	38.79	43.56
16	Megestrol Acetate	38.864	34.8
17	Lapatinib Ditosylate	42.291	54.76
18	Ixabepilone	42.559	47.48
19	Ibrance (Palbociclib)	45.535	43.51
20	Verzenio (Abemaciclib)	46.483	48.3
21	Trexall (Methotrexate)	48.199	50.07
22	Kisqali (Ribociclib)	48.733	45.35
23	Ellence (Epirubicin Hydrochloride)	51.548	51.22
24	Doxorubicin Hydrochloride	54.02	53.24

Table 1: Binding Energy of ER and ER with various breast cancer drugs

It was observed that 7 Hydrojen bond and 8 hydrophobic bonds were involved in bonding of ER with Doxorubicin Hydrochloride . The amino acid involved in the binding were ARG394, GLU353, ASN532, VAL533, MET343, THR347, MET421, LEU346, ALA350, LEU387, LEU391, ALA350 and LEU525 as shown in table 2.

S. No	Name	Distance	Category	Type
1	A:ARG394:HH22 - A:OHT601:O4	2.05932	Hydrogen Bond	Conventional Hydrogen Bond
2	A:OHT601:H1 - A:GLU353:OE2	1.80813	Hydrogen Bond	Conventional Hydrogen Bond
3	A:OHT601:H23 - A:VAL533:O	2.43039	Hydrogen Bond	Carbon Hydrogen Bond
4	A:OHT601:H24 - A:ASN532:O	2.44379	Hydrogen Bond	Carbon Hydrogen Bond
5	A:OHT601:H26 - A:ASN532:O	2.57131	Hydrogen Bond	Carbon Hydrogen Bond
6	A:OHT601:H26 - A:VAL533:O	1.53184	Hydrogen Bond	Carbon Hydrogen Bond

7	A:OHT601:H28 - A:VAL533:O	2.47115	Hydrogen Bond	Carbon Hydrogen Bond
8	A:MET343:SD - A:OHT601	5.82032	Other	Pi-Sulfur
9	A:LEU346:C,O;THR347:N - A:OHT601	4.43128	Hydrophobic	Amide-Pi Stacked
10	A:OHT601 - A:MET421	5.11026	Hydrophobic	Pi-Alkyl
11	A:OHT601 - A:LEU346	5.43238	Hydrophobic	Pi-Alkyl
12	A:OHT601 - A:ALA350	4.54716	Hydrophobic	Pi-Alkyl
13	A:OHT601 - A:LEU387	4.66688	Hydrophobic	Pi-Alkyl
14	A:OHT601 - A:LEU391	5.46062	Hydrophobic	Pi-Alkyl
15	A:OHT601 - A:ALA350	3.84301	Hydrophobic	Pi-Alkyl
16	A:OHT601 - A:LEU525	5.24319	Hydrophobic	Pi-Alkyl

Table 2: Types of bond between ER and Doxorubicin Hydrochloride

2 hydrogen bond and 8 hydrophobic bonds were involved in the bond formation between ER sample and Lapatinib Ditosylate . The amino acid involved in the binding were ASP303, PHE356, ILE376, LEU476, ALA302, LEU339, LEU343 and ALA302 as shown in table 3.

S. No	**Name**	**Distance**	**Category**	Type
1	A:OHT101:H19 - A:ASP303:OD1	3.02855	Hydrogen Bond	Carbon Hydrogen Bond
2	A:OHT101:H23 - A:ASP303:OD2	2.64418	Hydrogen Bond	Carbon Hydrogen Bond
3	A:PHE356 - A:OHT101	5.21964	Hydrophobic	Pi-Pi T-shaped
4	A:OHT101 - A:ILE376	5.3386	Hydrophobic	Pi-Alkyl
5	A:OHT101 - A:LEU476	5.32394	Hydrophobic	Pi-Alkyl
6	A:OHT101 - A:ALA302	4.63397	Hydrophobic	Pi-Alkyl
7	A:OHT101 - A:LEU339	4.72706	Hydrophobic	Pi-Alkyl
8	A:OHT101 - A:LEU343	5.12577	Hydrophobic	Pi-Alkyl
9	A:OHT101 - A:ALA302	3.88815	Hydrophobic	Pi-Alkyl
10	A:OHT101 - A:LEU476	4.95293	Hydrophobic	Pi-Alkyl

Table 3: Types of bond between ER and Lapatinib Ditosylate

Fig 1a and 1b shows the binding poses of the ER with Doxorubicin Hydrochloride and ER with Lapatinib Ditosylate

6 Conclusion

Estrogen plays an important role in the metabolism of women. The physical and sexual development of women body is also dependent on the secretion of Estrogen. On the contrary the overexpresion of Ertrogen receptor has been observed in early stages of breast cancer. It has been reported that some specific ERalpha gene promoter are found to be responsible for increased transcription of the gene.The study of the function and working of Estrogen receptor is very important for development of new diagnosis and medication techniques for prevention of breast cancer. Molecular Docking is

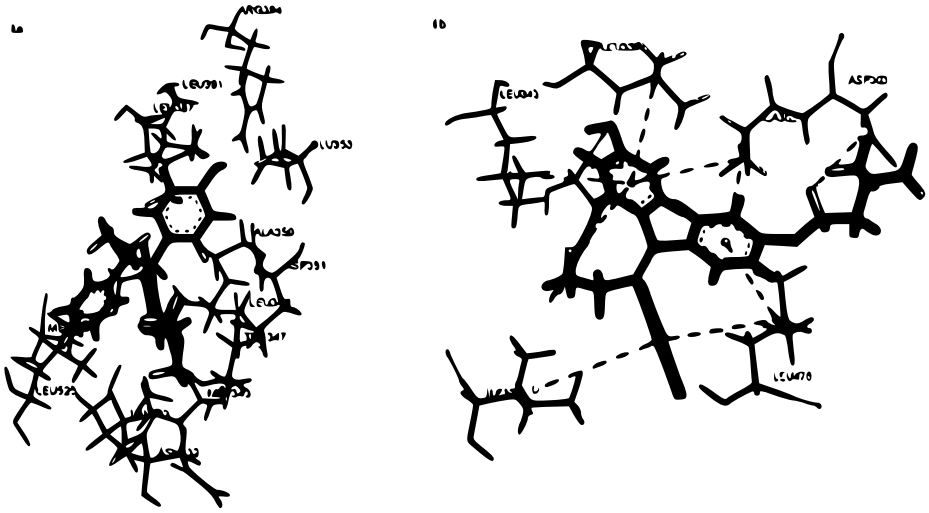

Fig. 1: 1a.Binding Pose of ER and Doxorubicin Hydrochloride, 1b. Binding Pose of ER and Lapatinib Ditosylate

very promising technique for providing insights into the functioning of the protein gene mechanism. It provides the fast and cost effective approach to make an approximation about the binding patterns of different macromolecules. Finally, the present study has suggested that the estrogen receptor alpha and beta both play a crucial role in the breast cancer. Later molecular dynamics studies should be performed to access the stability of the compounds formed after docking. Further studies are needed to solve the riddle of Estrogen receptor and Breast cancer association. Further elucidation of the estrogen dependent cancer will be very beneficial for clinical assessment of the responses to the endocrine therapy for cancer.

References

1. Spitale A, Mazzola P, Soldini D, Mazzucchelli L and Bordoni A. Breast cancer classification according to immunohistochemical markers: clinicopathologic features and short-term survival analysis in a population-based study from the South of Switzerland. Ann Oncol 2009; 20: 628-635.
2. ”Intrinsic molecular signature of breast cancer in a population-based cohort of 412 patients”, Breast Cancer Res. 2006;8(4):R34.
3. ”World Cancer Report” (PDF). International Agency for Research on Cancer. 2008. Archived (PDF) from the original on 20 July 2011. Retrieved 26 February 2011.
4. ”Cancer Survival in England: Patients Diagnosed 2007–2011 and Followed up to 2012” (PDF). Office for National Statistics. 29 October 2013. Archived (PDF) from the original on 29 November 2014. Retrieved 29 June 2014.
5. ”SEER Stat Fact Sheets: Breast Cancer”. NCI. Archived from the original on 3 July 2014. Retrieved 18 June 2014.

6. World Cancer Report 2014. World Health Organization. 2014. pp. Chapter 5.2. ISBN 92-832-0429-8.
7. Lacroix M (December 2006). "Significance, detection and markers of disseminated breast cancer cells". Endocrine-Related Cancer. Bioscientifica. 13 (4): 1033–67. doi:10.1677/ERC-06-0001. PMID 17158753
8. Johnson KC, Miller AB, Collishaw NE, Palmer JR, Hammond SK, Salmon AG, Cantor KP, Miller MD, Boyd NF, Millar J, Turcotte F (Jan 2011). "Active smoking and secondhand smoke increase breast cancer risk: the report of the Canadian Expert Panel on Tobacco Smoke and Breast Cancer Risk (2009)". Tobacco control. 20 (1): e2. doi:10.1136/tc.2010.035931. PMID 21148114.
9. Hayes,, James; Ricahrdson, Ann; Frampton, Chris (15 November 2013). "Population attributable risks for modifiable lifestyle factors and breast cancer in New Zealand women". IMJ. 43 (11): 1198–1204. doi:10.1111/imj.12256. PMID 23910051.
10. Kahlenborn C, Modugno F, Potter DM, Severs WB (Oct 2006). "Oral contraceptive use as a risk factor for premenopausal breast cancer: a meta-analysis". Mayo Clinic Proceedings. 81 (10): 1290–302. doi:10.4065/81.10.1290. PMID 17036554.
11. Collaborative Group on Hormonal Factors in Breast Cancer: Alcohol, tobacco and breast cancer: collaborative reanalysis of individual data from 53 epidemiological studies, including 58,515 women with breast cancer and 95,067 women without the disease. Br J Cancer 2002, 87:1234-1245.
12. International Agency for Research on Cancer: Weight Control and Physical Activity. Lyon, France: IARC Press; 2002.
13. Roger P, Sahla ME, Makela S, Gustafsson JA, Baldet P, Rochefort H: Decreased expression of estrogen receptor beta protein in proliferative preinvasive mammary tumors. Cancer Res 2001, 61:2537-2541.
14. Endogenous Hormones and Breast Cancer Collaborative Group: Endogenous sex hormones and breast cancer in postmenopausal women: reanalysis of nine prospective studies. J Natl Cancer Inst 2002, 94:606-616.
15. Collaborative Group on Hormonal Factors in Breast Cancer: Breast cancer and hormone replacement therapy: collaborative reanalysis of data from 51 epidemiological studies of 52,705 women with breast cancer and 108,411 women without breast cancer. Lancet 1997, 350:1047-1059.
16. Eerola H, Aittomaki K, Asko-Seljavaara S, Nevanlinna H, von Smitten K: Hereditary breast cancer and handling of patients at risk. Scand J Surg 2002, 91:280-287.
17. Key TJ, Verkasalo PK, Banks E: Epidemiology of breast cancer. Lancet Oncol 2001, 2:133-140.
18. Russo J, Wilgus G, Russo IH: Susceptibility of the mammary gland to carcinogenesis: I. Differentiation of the mammary gland as determinant of tumor incidence and type of lesion. Am J Pathol 1979, 96:721-736.
19. Liu Q, Wuu J, Lambe M, Hsieh SF, Ekbom A, Hsieh CC: Transient increase in breast cancer risk after giving birth: postpartum period with the highest risk (Sweden). Cancer Causes Control 2002, 13:299-305.
20. Collaborative Group on Hormonal Factors in Breast Cancer: Breast cancer and breastfeeding: collaborative reanalysis of individual data from 47 epidemiological studies in 30 countries, including 50302 women with breast cancer and 96973 women without the disease. Lancet 2002, 360:187-195.
21. Ewertz M, Duffy SW, Adami HO, Kvale G, Lund E, Meirik O, Mellemgaard A, Soini I, Tulinius H: Age at first birth, parity and risk of breast cancer: a meta-analysis of 8 studies from the Nordic countries. Int J Cancer 1990, 46:597-603.
22. Clemons M, Goss P: Estrogen and the risk of breast cancer. N Engl J Med 2001, 344:276-285.

23. Khan SA, Rogers MA, Obando JA, Tamsen A: Estrogen receptor expression of benign breast epithelium and its association with breast cancer. Cancer Res 1994, 54:993-997.
24. Lawson JS, Field AS, Champion S, Tran D, Ishikura H, Trichopoulos D: Low oestrogen receptor alpha expression in normal breast tissue underlies low breast cancer incidence in Japan. Lancet 1999, 354:1787-1788.
25. Shoker BS, Jarvis C, Sibson DR, Walker C, Sloane JP: Oestrogen receptor expression in the normal and pre-cancerous breast. J Pathol 1999, 188:237-244.
26. Hall JM, McDonnell DP: The estrogen receptor beta-isoform (ERbeta) of the human estrogen receptor modulates ERalpha transcriptional activity and is a key regulator of the cellular response to estrogens and antiestrogens. Endocrinology 1999, 140:5566-5578.
27. Kuntz, I.D.; Blaney, J.M.; Oatley, S.J.; Langridge, R.; Ferrin, T.E. A geometric approach to macromolecule-ligand interactions. J. Mol. Biol. 1982, 161, 269-288.
28. Kitchen, D.B.; Decornez, H.; Furr, J.R.; Bajorath, J. Docking and scoring in virtual screening for drug discovery: Methods and applications. Nat. Rev. Drug Discov. 2004, 3, 935-948.
29. Rajamani, R.; Good, A.C. Ranking poses in structure-based lead discovery and optimization: Current trends in scoring function development. Curr. Opin. Drug. Discov. Devel. 2007, 10, 308-315.
30. Gilson, M.K.; Zhou, H.X. Calculation of protein-ligand binding affinities. Annu. Rev. Biophys. Biomol. Struct. 2007, 36, 21-42.
31. Brooks BR, Bruccoleri RE, Olafson BD, States DJ, Swaminathan S, Karplus M. CHARMM—a programm for macromolecular energy, minimization, and dynamics calculations. J Comput Chem 1983;4:187–217.

Feasibility Analysis and Realization of a Microcontroller Based Low Cost ECG Instrument

Dwipjoy Sarkar*[1], Ajay Das[1], Nabajit Debnath[1], Martish Sarkar[1], Panchali Paul[1] and Priyanka Das[1]

[1] Department of Electronics & Communication Engineering
Tripura Institute of Technology, Narsingarh, Tripura (W)
{dwipjoysarkar@gmail.com, ajaywindows64@gmail.com, nabajitdebnath005@gmail.com, martishsarkar9436@gmail.com, paulpanchali877@gmail.com, priyankadas2024@gmail.com}

Abstract. This paper exhibits the feasibility of a simple and efficient ECG cum heart rate measurement system using ATmega16 microcontroller. A low cost and portable device is proposed to measure the heart rate and ECG signal using 3 lead electrodes. The proposed device incorporates an improved algorithm which minimizes the data transmission time between microcontroller and PC with better synchronization. The output signal from instrumentation amplifier is suppressed using an active low pass filter, which is then applied to the A/D converter port of ATmega16 microcontroller for pre and post processing with the help of python based software module.

Keywords: Feasibility, ECG, AT-Mega16, AD8232, RS-232

1 INTRODUCTION

The heart rate of a body describes the health condition of the human body. With the help of heart rate, it is possible to recognize whether the health condition is proper or poor. There are many ways to detect the ECG signal available in biomedical science but in this paper, the main objective is to design a microcontroller based biomedical instrument having better synchronization with the host device using Atmega16 microcontroller. In [1], a PIC18F4550 microcontroller based ECG & measurement system was proposed. After the signal conditioning stage, the output is applied to microcontroller & viewed in CRO & PC. Articles [2-4] depict several other microcontrollers and/or Arduino based ECG signal detection systems which utilize some other host device such as PC or android based cell phone for post-processing of the ECG data. In [5], the accuracy between two microcontrollers based embedded R wave detection methods for heart rate variability analysis is compared. [6] Is a computer-based heart rate monitoring system where the signal is collected from the fingertip and applied to an IR sensor for eliminating noise using an active low pass filter. The processed signal is displayed using a computer through the audio jack. [7] is a heart rate monitoring system where two stages of active low pass filter are used for responding during emergencies via Bluetooth and cellular communication. The article [8] presents a portable wireless ECG monitoring terminal for using in the mobile application in a personal healthcare scenario which can detect real-time signals. [9] Depicts an Atmel 89C51 microcontroller based real-time heart rate measurement from the ECG signal. In the article [10], an ECG bedside monitor based on STC89C52RC microcontroller is proposed which is integrated with the functions of sampling, analysis, storage, displaying and transmitting of the ECG signal.

Although a huge amount of research work is done for the implementation of low-cost ECG and heart rate estimation system in the past decade, most of the low-cost devices transmit data

*Corresponding author
Email id: dwipjoysarkar@gmail.com

in real time using RS-232 port of microcontroller to the host device (PC or mobile) for post-processing and further analysis. The baud rate of RS-232 varies from 9600 bps (bits per second) to 115200 bps, where the error rate increases with the increase of baud rate. This problem is not treated by most of the works. In this paper, an improved algorithm is proposed which uses an adaptive data array in RS-232 data chunk, thereby reducing the overall time of data transmission. This method results in better accuracy of the received signal. The proposed algorithm is simulated in Proteus circuit simulator and implemented using the Atmega16 microcontroller board and AD8232 instrumentation amplifier.

2 CONVENTIONAL METHOD

A conventional 3 lead-based ECG measurement system is shown in Fig.1. The amplitude of an ECG signal lies in between 0.4 mV to 1.2 mV. Fig.2 and Fig. 3 depict a clean ECG (PQRST) and a noisy ECG signal. The added 50 Hz power line noise from the noisy ECG signal of Fig. 3 must be filtered out before final analysis.

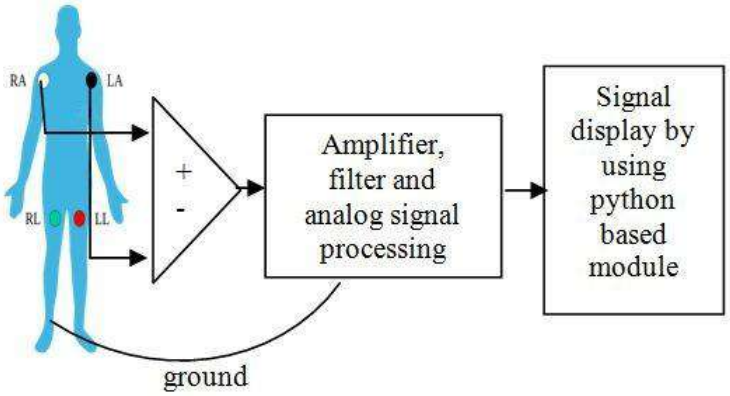

Fig. 1. 3 lead ECG signal acquisition method

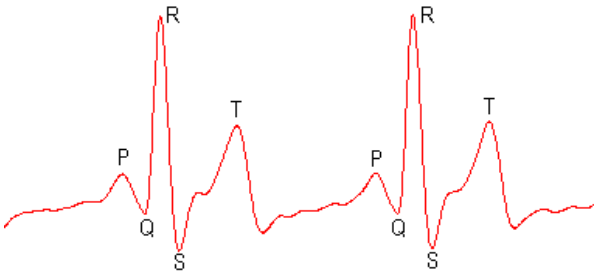

Fig. 2. A normal ECG signal

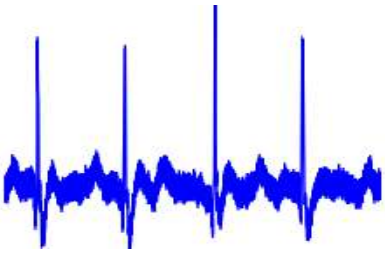

Fig. 3. ECG signal added with 50Hz power line noise

The system mentioned above is implemented in hardware using AD8232 based instrumentation amplifier and AT-Mega16 developer board which is depicted in Fig.4. The AD8232 module contains a specialized instrumentation amplifier (IA), an operational amplifier (A1), a right leg drive amplifier (A2), and a mid-supply reference buffer (A3) circuit to provide clean ECG analog output [11]. A two pole highpass filter in AD8232 IC is used to eliminate the motion artifacts whereas a three-pole low-pass filter is utilized to remove additional noise from the ECG signal. Fig. 5(b) depicts the digital oscilloscope output of the AD8232 module, which is obtained from a test person. It is evident from Fig. 5(b) that the extent of ECG signal loss due to filtering of power line noise is minimal and can be neglected. The detailed working of the AD8232 instrumentation amplifier along with the circuit diagram of the amplifier module can be found from its technical datasheet [11].

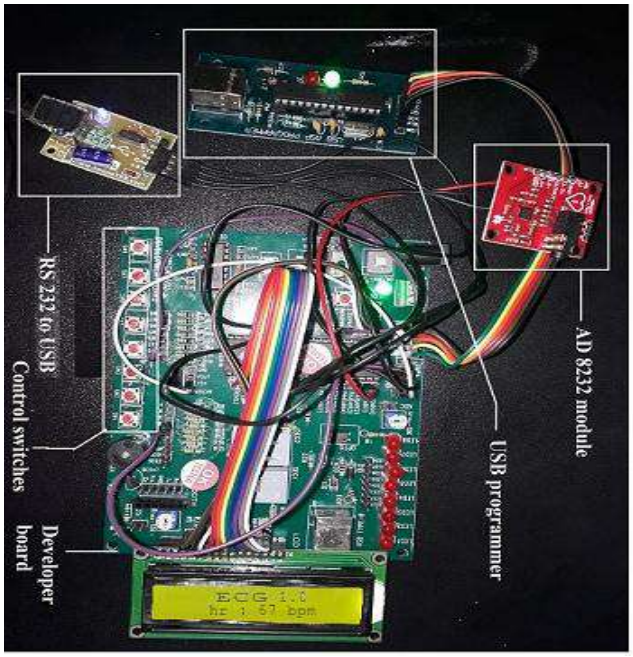

Fig. 4. Photograph of the hardware module

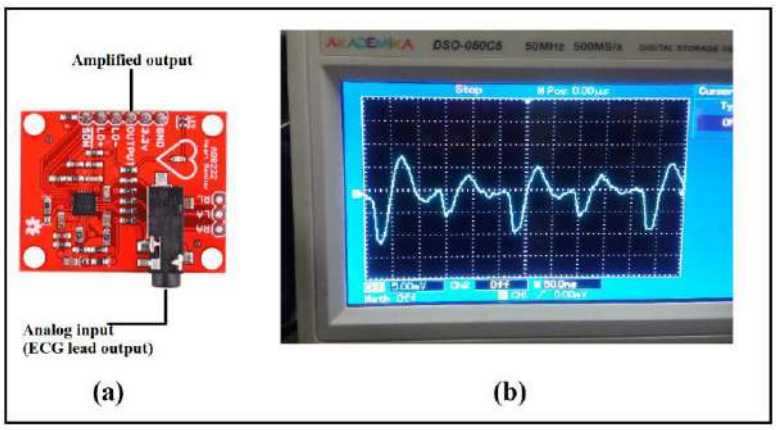

Fig. 5 (a) AD8232 module; (b) ECG signal in the DSO from AD8232 output

The amplified output from the AD8232 module is applied to the AT-Mega16 A/D converter channel-0 for further processing. The heartbeat rate per minute is easily detected by counting the number of peaks in the signal for the one-minute duration. This is realized by using the timer counter overflow interrupt of AT-Mega16, where the numbers of peaks are displayed in the overflow interrupt service routine which is triggered after one minute.

3 PROPOSED METHOD

The main problem in the conventional method arises in the post-processing stage when the A/D converter readings are serially transmitted to PC in real time by RS-232 port of AT-Mega16. This can be understood by observing the real-time plot obtained using Python software, which is shown in Fig. 6. From Fig.6 it can easily be predicted that some synchronization problem is present in this method.

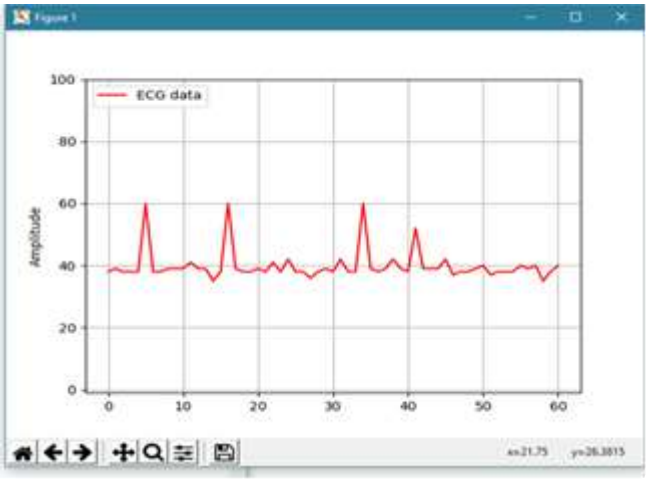

Fig. 6. ECG signal plotted in Python software

The minimum sampling frequency of the AT-Mega16 ADC should be at least 60 Hz as the useful component of ECG signal lies in between 0 – 30 Hz. In this work, the ADC sampling frequency is approximately set to 9.61 KHz with a 16 MHz crystal oscillator. The maximum supported RS-232 baud rate of AT-Mega 16 is about 115200 bps. The number of bits in a particular reading affects its transmission time and the increase of bits in that reading may result in missing of data at the host device due to comparatively higher ADC conversion rate of AT-Mega16. The above effect can also be observed from Fig. 6.

The transmission time, t_s of a sample can be found as:

$$t_s = \frac{b_{nS}}{b_{rr}} \qquad (1)$$

Where, b_{nS} is the number of bits representing the sample and b_{rr} is the baud rate in bps.

The problem mentioned above is treated in this work. Fig.7 shows a typical RS-232 data frame. It incorporates a start bit, stop bit, a parity bit and a data chunk of 5 to 9 bit. In this work, the data bytes are sent in ASCII mode, which is of 7-bit size. Therefore, the total data frame is of 10-bit size.

Fig. 7. A typical RS-232 frame

The A/D converter of AT-Mega16 is of 10-bit size which provides the readings in the range of 0 to 1023 respectively. In the conventional method, this data is usually scaled down by a constant number to decrease its size which can be easily sent to the host device. However, the fixed scaling coefficient in the above method results in samples of the same size as shown in equation (1) for each reading of the ADC channel which requires to be transmitted by the serial port.

In the currently proposed method, the data type of the variable which is used to transmit the ADC reading is changed for every reading. For example, if zero voltage appears in the ADC reading, only a single bit is sent to the serial port as a sample. Likewise, for smaller readings, less number of bits are used and for larger readings, more bits are used. The transmission time, $t_{\text{var\_}s}$ of a sample of variable bit size $\text{var\_}b_{nS}$ can be found as:

$$t_{\text{var\_}s} = \frac{\text{var\_}b_{nS}}{b_{rr}} \qquad (2)$$

It is clearly evident from equation (2) that the transmission time of a particular sample can be fairly reduced by reducing the number of bits in a particular sample. This is achieved by using unsigned char data size selection library components (uint2_t, uint4_t, uint8_t, uint16_t, etc.) of WinAVR GNU-GCC compiler. The received ECG signal in Python software with the currently proposed method is depicted in Fig.8 which clearly shows the betterment of signal reception in the host device compared to the conventional method.

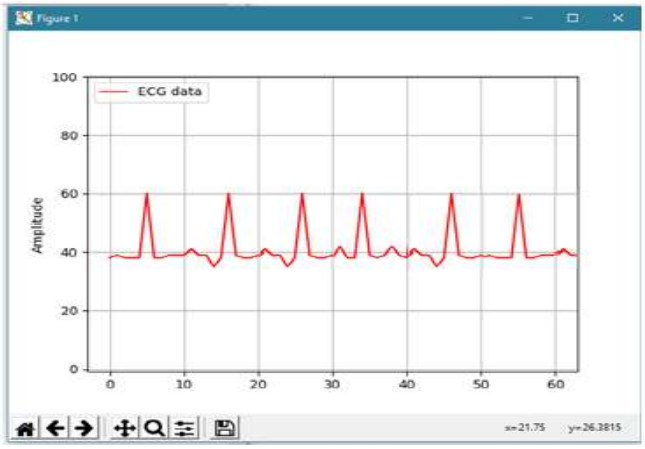

Fig. 8. Improved ECG signal plotted in Python software

4 CONCLUSION

In this work, the feasibility of a simple and efficient ECG cum heart rate measurement system using an ATmega16 microcontroller and AD8232 instrumentation amplifier is studied. A low cost and portable device with an improved algorithm is also proposed here to measure the ECG and heart rate of a human being using a microcontroller and PC based 3-lead ECG acquisition method.

5 REFERENCES

1. Sarkar, D., Choudhury, A.: Low cost and efficient ECG measurement system using PICI8F4550 Microcontroller. In: IEEE- International Conference on Electronic Design. Computer Networks & Automated Verification (EDCAV), 29-30 Jan. 2015, Shillong, pp.6-11 (2015).

2. Yener, S.C., & Mutlu, R.: A microcontroller-based ECG signal generator design utilizing microcontroller PWM output and experimental ECG data. In: Electric Electronics, Computer Science, Biomedical Engineerings' Meeting (EBBT), 18-19 April 2018, Istanbul, Turkey (2018).

3. Lichtman, A., & FUCHS, P.: Hardware and software design for one channel ECG measurement using MSP430 microcontroller. In: Cybernetics & Informatics (k & I), pp.1-5 (2018).

4. Wu, M.-J.,Shieh, S.-F., Liao,Y.-L., & Chen,Y.-C.: ECG Measurement System Based on Arduino and Android Devices. In: International Symposium on Computer, Consumer and control (IS3C), pp. 690-693 (2016).

5. Yamakawa, T., Kinoshita, R., Fujiwara, K., Kano, M., Miyajima, M., Sakata, T., & Ueda, Y.: Accuracy comparision between two microcontroller –embedded R wave detection methods for heart –Heart rate variability analysis. In: Asia Pacific signal and information processing Association Annual summit and Conference (APSIPA), Hong Kong, 2015, pp. 1010-1013 (2015).

6. Mohammad Abu, Raihan Miah, Saikat Basak, Md. Rafiul Huda and Apartim Roy: Low cost Computer Based Heart Rate Monitoring System using Fingertip and Microphone Port. In: International Conference on Informatics, Electronics and Vision (ICIEV), 17-18 May 2013, Dhaka, pp.1-4 (2013).

7. Saikh Anowarul Fatteh et al.: Wrist card:PPG Sensor based Wrist Wearable Unit for Low Cost Personalized Cardio Healthcare System. In: Sens Technol (ICST), 2013 Seventh Int. Conf., pp.627-631 (2013).

8. F. Wang et al: Design of a Portable Wireless ECG Monitoring Terminal. In: IEEE-2011 International Workshop on Complexity and Data Mining (IWCDM), pp.56-59 (2011).

9. Chatterjee, H.K., Gupta, R., and Mitra, M.: A microcontroller based system for real-time heart rate estimation from ECG signal. In: IEEE-2012 Annual IEEE India Conference (INDICON), pp.1020-1025 (2012).

10. Segura-Jucirez, J.J., Cuesta-Frau, D., and SamblasPena, L.: A microcontroller-based portable electrocardiograph system. In: 10th IEEE International Conference on Electronics, Circuits and Systems (ICECS), vol. 2, pp.922-925 (2003).

11. Analog.com. (2019). [online] Available at: https://www.analog.com/media/en/technical-documentation/data-sheets/AD8232.pdf [Accessed 6 Apr. 2019].

Heat Kernel approximation using N-degree Taylor polynomial used in community detection

Tapesh Mandal[1] and W. Wilfred Godfrey[2]

[1] Robotics Laboratory
ABV-IIITM Gwalior, India
tapesh.mandal@gmail.com
[2] Robotics Laboratory
ABV-IIITM Gwalior, India
godfrey@iiitm.ac.in, godwil@gmail.com

Abstract. Graph diffusion is of particular interest in the field of network analysis. Heat kernel is a graph diffusion technique which finds its origin in physics. The expression used for heat propagation in a network is the solution of the popular heat equation and it has been modified in the lines of PageRank diffusion. It finds its usage in community detection, with the flow of heat starting from a seed node. The expression to be evaluated eventually is a Taylor series with the practical constraint of summing up to infinite terms. The most practical way to solve this problem is to use a Taylor polynomial of N terms which acts as an approximation for the above. Our work determines the value of N for a given t, such that the error in approximation does not exceed a certain ϵ. This work aims to find an alternative to an existing formula for determining the value of N.

Keywords: Graph kernels · Graph Diffusion · Taylor series · Community detection · Graph theory

1 Introduction

Kernels are functions in discrete mathematics that compare two inputs. In network science, kernels are used to compare two graphs given as input and are known as graph kernels[1][2][3]. Kernels are not just used to compare graphs but also to throw light on comparison of nodes [4]. The graph kernel chosen in this case is *Heat Kernel*. From mathematical point of view, the solution for the heat equation is the heat kernel. In the field of mathematical physics it is used for spectrum analysis of laplacian operaters. Heat kernel as the name suggests deals with the evoulution of temperature in a region bounded by fixed temperature. It begins with a particular quantity of heat at time t=0 and tracks how the heat flows at every instance of time. Note that the parameter t used in the rest of paper is not time but a parameter of heat kernel. In terms of network science diffusion is flow of some material from one node to the neighboring nodes. In [5], the authors provide an estimate of diffusion using Monte Carlo method. The beginning nodes are known as seeds. The seeds are assumed to possess some material, which theoretically is some value or weight which represents the heat in our case. The process of diffusion finds its application in the field of community detection. The heat diffusion if

calculated in the nearby nodes of the seed node helps in identifying communities near the seed node. Many algorithms have been devised to implement the above process. The use of such algorithms is to detect communities by determining the flow of heat from the seed nodes. The algorithm in context solves a linear system resulting in a matrix exponential. The whole process is inspired by personalized PageRank diffusion. In [6] a study of communities resulting out of personalized PageRank diffusion is studied. It can be seen that the heat kernel process of community detection performs much better than PageRank.

2 Background

Diffusion has been well studied by Chung et al [7].They came up with a Cheeger inequality in the process of estimating the expression for heat diffusion. To begin with, it is essential to define notations to be used. $G(V, E)$ is a simple undirected graph, where the number of vertices is given by the cardinality of the set of vertices, $n = |V|$. Each vertex has numeric identity, from 1 to n. For each vertex $v \in V$, the degree of v is represented by d_v. The adjacency matrix of G is given by **A**. **D** represents the diagonal degree matrix, where every diagonal element d_i represents the degree of the vertex i. The object of main interest is the random walk transition matrix **R**. The definition as given in [8] is as follows,

$$R = (D^{-1}A)^T = AD^{-1} \tag{1}$$

Equation **(1)** can be understood from the properties of tranposition of matrices. $(D^{-1}A)^T = A^T D^{-1^T}$. Since both the matrices are symmetric. $A^T = A$ and $D^{-1^T} = D^{-1}$. s_i is the seed vector with 1 at i-th position and s is the vector of all ones.

2.1 Conductance

Conductance measure to detect communities is a popular approach[9][10][11]. Volume of a subset S_V, $S_V \subset V$ is given by :-

$$vol(S_V) = \sum_{i \in S_V} d_i \tag{2}$$

$\delta(S_V)$ represents is the *edge-boundary*. The edge-boundary is the set of all vertices that are adjacent to a vertex in S but are not an element of S. By adjacent it is meant that there is an edge between the two vertices. Mathematically,

$$\delta(S_V) = \{u \in V - S_V | (u, v) \in E, v \in S_V\} \tag{3}$$

Thus conductance of a set S_V is given by :-

$$\phi(S_V) = \frac{|\delta(S_V)|}{min(S_V, V - S_V)} \tag{4}$$

The conductance $\phi(S_V)$ represents the probability with which a one hop random walk which started randomly from within S_V will land outside of S_V.

2.2 Identifying communities through conductance by diffusion

Graph diffusion can be expressed as following :-

$$C = \sum_{n=0}^{\infty} \alpha_n R^n s \tag{5}$$

$\sum \alpha_n = 1$. In the present context, the diffusion from single nodes is considered. Therefore in this case $s = s_i$. s is the beginning point of heat/material flow from the seed node to its neighbors. Since s is a stochastic vector, s is also written as $\sum_{i \in S_V} s_i/|S_V|$. If the diffusion C, is known for a seed, it is possible to detect community around the seed node.

2.3 PageRank diffusion

For personalized Pagerank diffusion, Equation **(5)** is modified slightly. For $\alpha \in (0, 1)$,

$$P = (1 - \alpha) \sum_{n=0}^{\infty} \alpha_n R^n s \tag{6}$$

2.4 Heat Kernel diffusion

The equation for heat kernel diffusion comes with some modifications in Equation **(6)**. α_n is replaced with $\frac{t^n}{n!}$

$$H = e^{-t}(\sum_{n=0}^{\infty} \frac{t^n}{n!} R^n)s = exp\{-t(I - R)\}s \tag{7}$$

Comparing α^n and $\frac{t^n}{n!}$ growth rates shows that $\frac{t^n}{n!}$ decays faster than α^n. Finding h involves evaluating Equation **(7)** which is an exponential matrix expression,Higham [12]. Evaluation of matrix exponential is an active area of research [13]. Some of the recent works in this field includes [14][15][16].This process requires dividing by the degree of each node of the graph in the end. That is we are trying to find $X \approx H$ such that,

$$\|D^{-1} exp\{-t(I - R)\}s - D^{-1}X\|_\infty < \varepsilon$$

Applying the standard properties of matrix exponential, the following can be easily obtained

$$exp\{-t(I - R)\} = e^{-t}e^{tR}$$

Multiplying throughout e^t, the scaled equation is as following

$$\|D^{-1}e^{tR}s - Y\|_\infty < e^{-t}\varepsilon$$

2.5 Taylor polynomial of degree-N

The Taylor series expansion of $exptR$ is given by

$$\sum_{n=0}^{\infty} \frac{t^n}{n!} R^n \approx \sum_{n=0}^{N} \frac{t^n}{n!} R^n = T_N(tR)$$

The task here is to calculate $exp(tR)s$, where t, P, s are all non-negative. Practically evaluating the above equation is not possible. Hence the Taylor series is approximated till N terms, giving rise to a N-degree Taylor polynomial.

2.6 Existing derivation for N

N is chosen such that

$$\|D^{-1}exp\{-t(I-R)\}s - D^{-1}T_N(tR)s\|_\infty < \varepsilon/2$$

$T_N(tR)s \approx Y$ is calculated. And the resulting inequality is

$$\|D^{-1}T_N(tR)s - D^{-1}Y\|_\infty < \varepsilon/2$$

Now applying triangle inequality,

$$\|D^{-1}exp\{-t(I-R)\}s - D^{-1}Y\|_\infty < \varepsilon$$

which is equal to the original estimation made. From the properties of matrix it can be noted that,

$$\frac{F(x)}{D} = F(x)D^{-1} = D^{-1}F(x)$$

Therefore,

$$\|D^{-1}exp\{tR\}s - D^{-1}T_N(tR)s\|_\infty = \\ \|exp\{tR^T\}D^{-1}s - T_N(tR^T)D^{-1}s\|_\infty$$

Also,

$$\|exp\{tR^T\}D^{-1}s - T_N(tR^T)D^{-1}s\|_\infty < \\ \|exp\{tR^T\} - T_N(tR^T)\|_\infty \|D^{-1}s\|_\infty$$

Since s is a stochastic vector and $\|D^{-1}\|_\infty < 1$, $\|D^{-1}s\|_\infty < 1$

From the proofs on approximation of Taylor series in [17], it is concluded that,

$$\frac{\|tR^T\|_\infty^{N+1}}{(N+1)!}\frac{(N+2)}{(N+2-t)} < \frac{t^{N+1}}{(N+1)!}\frac{(N+2)}{(N+2-t)} < \varepsilon/2$$

3 Objective

Since for a given dataset D and A are constant,it can be easily inferred that R^T is constant. So the objective is to estimate the value of N for different values of t.

4 Methodology

Taylor's theorem and Lagrange's remainder theorem provide a different insight for estimating the value of N by helping in choosing t.

4.1 Taylor's theorem(Lagrange's remainder form)

$$F(t) - T_N(t) = \frac{F^{N+1}(z)t^{N+1}}{(N+1)!} \tag{8}$$

z lies in the domain of t and is chosen in such a way that $F^{N+1}(z)$ is maximum. In the present context $F(t) = e^{R^T t}$ and t is taken to be in the range of 1 to 20. In this case, z is between 0 and t always. Please note, in this case the taylor polynomial is centred around 0.

4.2 Chebyshev's distance, L_∞ norm

$\|.\|_\infty$ has been used throughout this paper while calculating the error in approximation of the Taylor series. For the proposed methodology, the following definition is of major importance.

$$\|A\|_\infty = \max_i \sum_{j=0}^{n} |a_{ij}| \tag{9}$$

A is any square matrix. It is clear from the expression that $\|A\|_\infty$ evaluates to the maximum of all rowsums of matrix A.

4.3 Proposed derivation for N

$$\|f(t) - T_N(t)\|_\infty = \max_i \sum_{j=0}^{n} |f(t) - T_N(t)|$$

$$\|exp\{tR^T\}D^{-1}s - T_N(tR^T)D^{-1}s\|_\infty < \|exp\{tR^T\} - T_N(tR^T)\|_\infty$$

From now on,$F(t) = e^{R^T t}$.

From Taylor's theorem, Equation **(8)**,

$$\|F(t) - T_N(t)\|_\infty = \|\frac{F^{N+1}(z)t^{N+1}}{(N+1)!}\|_\infty \tag{10}$$

$$F^{N+1}(z) = F(z)R^{T^{N+1}}$$

Substituting the above in Equation **(10)**

$$\|F(t) - T_N(t)\|_\infty = \|\frac{F(z)R^{T^{N+1}}t^{N+1}}{(N+1)!}\|_\infty \tag{11}$$

According to properties of norms on matrix,$\|Ak\| = \|A\|k$, $\|AB\| < \|A\|\|B\|$

Applying these properties in Inequality **(11)**,

$$\|\frac{F(z)R^{T^{N+1}}t^{N+1}}{(N+1)!}\|_\infty < \|F(z)\|_\infty \|R^{T^{N+1}}\|_\infty \frac{t^{N+1}}{(N+1)!} \tag{12}$$

$\|R^{T^k}\|_\infty$ **is seen to be equal to 1.**

Therefore,

$$\|F(z)\|_\infty \|R^{T^{N+1}}\|_\infty \frac{t^{N+1}}{(N+1)!} = \|F(z)\|_\infty \frac{t^{N+1}}{(N+1)!} \tag{13}$$

Substituting the value of $F(z)$ and using $\|A+B\| < \|A\| + \|B\|$ in Inequality **(13)**,

$$\|F(z)\|_\infty \frac{t^{N+1}}{(N+1)!} < (1 + \frac{\|R^T\|_\infty z}{1!} + \frac{\|R^{T^2}\|_\infty z^2}{2!}...)\frac{t^{N+1}}{(N+1)!}$$

$$= (1 + \frac{z}{1!} + \frac{z^2}{2!}...)\frac{t^{N+1}}{(N+1)!}$$

Since

$$e^z = 1 + \frac{z}{1!} + \frac{z^2}{2!} + \frac{z^3}{3!}...$$

From Inequality **(11),(12),(13)**,

$$\|F(t) - T_N(t)\|_\infty < e^z \frac{t^{N+1}}{(N+1)!} < \epsilon/2 \tag{14}$$

5 Experimentation and Results

The experiments were performed on Intel Core-i3, 2.00GHz $\times$ 4 (64 bit), Ubuntu 14.04 LTS. The experiments were implemented in python(2.7.6) using igraph library [18]. The $R^T = D^{-1}A$, transpose of R was raised to the power of N=1,2,3..etc. and its chebyshev norm $\|R^{T^N}\|_\infty = 1$ always. This was performed on four datasets Zachary's Karate Club, Dolphin Social Network, Copperfield Word Adjacencies, American College Football [19][20][21][22] , as mentioned in Table **1**.

The theoretical estimation for the number of terms for the N-term Taylor polynomial which is an approximation for infinite sum Taylor series is done by taking a Taylor

Table 1: Details about each dataset

Sr.no.	Dataset	no.of nodes
1	karate	34
2	dolphins	62
3	adjnoun	112
4	football	115

polynomial for a given R^T of 100 terms which is considered to be $F(t)$. This consideration is valid since 100 terms is good enough to be treated as infinity in this case. Accordingly the value of N is calculated for $T_N(t)$ by evaluating the difference between the two and taking its chebyshev norm. The value for N is chosen such that the chebyshev distance between $F(t)$ and $T_N(t)$ is less than $\epsilon/2$. In this case ϵ is taken as 0.05 for 95 percent confidence. The values obtained for N for each value of t, which was found to be independent of dataset as $\|R^T\|_\infty = 1$, is presented in Table **2**

Table 2: The values of N for each value of t, $\epsilon = 0.05$

t(1-10)	N	t(11-20)	N
1	4	11	31
2	7	12	34
3	9	13	36
4	12	14	39
5	15	15	42
6	17	16	44
7	20	17	47
8	23	18	50
9	25	19	52
10	28	20	55

The value of z in Inequality **(14)** was determined to be 0.41 by experimentation until the output was equal to the theoretical value. The value of z was found to be equal to 0.41, if t is desired to be in the range of 1-20. So Inequality **(14)** can now be rewritten as,

$$\|F(t) - T_N(t)\|_\infty < e^{0.41} \frac{t^{N+1}}{(N+1)!} < \epsilon/2 \tag{15}$$

The difference between the expression above and the one in [14], shown at the end of literature review section is that now $\frac{(N+2)}{(N+2-t)}$ has been replaced by a constant $e^{0.41}$.

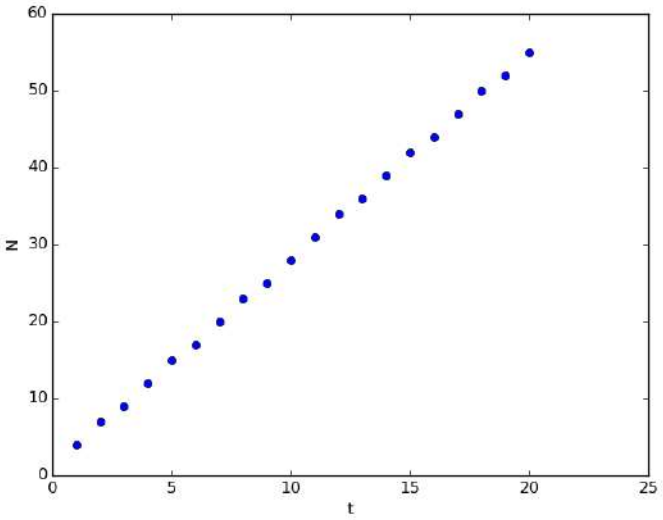

Fig. 1: Values of N for corresponding values of t

6 Conclusion

Through experimentation the value for z in Inequality **(14)** has been determined and the finally the expression stands as is represented by Inequality **(15)**. The previous inequality used in [14] involves a term $\frac{(N+2)}{(N+2-t)}$ along with $\frac{t^N}{(N+1)!}$. Though the second part of the expression remains same but $\frac{(N+2)}{(N+2-t)}$ has been replaced by $e^{0.41}$. Another important conclusion to be noted is the value of $z = 0.41$. As Lagrange's remainder theorem clearly states that z should lie between a, around which the polonomial curve is centered. So 0.41 perfectly fulfills the above criteria by being between 0 (which is the value of a in this case) and all the values of t, t=1,2,3,...,20. This results in an alternative formula for determining N.

7 Future work

Currently, the proposed formula works fine for the values of t in range 1 to 20. So, the next step would be to improve the proposed formula so that it works for any value of t. The time taken to determine N in the existing as well as the proposed formula for any t is in the order of microseconds. So it leaves very little scope of improvement.

References

1. S.V.N. Vishwanathan, Nicol N. Schraudolph, Risi Kondor, Karsten M. Borgwardt (2010). *Graph kernels*. Journal of Machine Learning Research. **11**: 1201–1242.

2. L. Ralaivola, S. J. Swamidass, S. Hiroto, P. Baldi (2005). *Graph kernels for chemical informatics*. Neural Networks. **18**: 1093–1110. doi:10.1016/j.neunet.2005.07.009.
3. Risi Imre Kondor, John Lafferty (2002). *Diffusion Kernels on Graphs and Other Discrete Input Spaces*. Proc. Int'l Conf. on Machine Learning (ICML).
4. B. Schölkopf and A. J. Smola. *Learning with Kernels*. MIT Press,Cambridge, MA, 2002.
5. F. Chung and O. Simpson. *Solving linear systems with boundary conditions using heat kernel pagerank*. In Algorithms and Models for the Web Graph, pages 203–219. Springer, 2013.
6. R. Andersen, F. Chung, and K. Lang. *Local graph partitioning using PageRank vectors*. In FOCS, 2006.
7. F. Chung. *A local graph partitioning algorithm using heat kernel pagerank.* Internet Mathematics, **6(3)**:315–330, 2009.
8. Kloster K, Gleich DF. *Heat kernel based community detection*. In Proceedings of the 20th ACM SIGKDD international conference on Knowledge discovery and data mining 2014 Aug 24 (pp. 1386-1395). ACM.
9. S. E. Schaeffer. *Graph clustering*. Computer Science Review, **1(1)**:27–64, 2007.
10. J. Leskovec, K. J. Lang, A. Dasgupta, and M. W. Mahoney. *Community structure in large networks: Natural cluster sizes and the absence of large well-defined clusters*. Internet Mathematics, **6(1)**:29–123, September 2009.
11. I. S. Dhillon, Y. Guan, and B. Kulis. *Weighted graph cuts without eigenvectors a multilevel approach*. IEEE Trans. Pattern Anal. Mach. Intell., **29(11)**:1944–1957, November 2007.
12. N. J. Higham. *Functions of Matrices: Theory and Computation*. SIAM, 2008.
13. A. H. Al-Mohy and N. J. Higham. *Computing the action of the matrix exponential, with an application to exponential integrators*. SIAM J. Sci. Comput., **33(2)**:488–511, March 2011.
14. J. Sastre, J. Ibánez, Emilio Defez, and P. Ruiz. *New scaling-squaring Taylor algorithms for computing the matrix exponential*, SIAM Journal on Scientific Computing 37, no. 1 (2015): A439-A455.
15. M. Caliari, and F. Zivcovich. *On-the-fly backward error estimate for matrix exponential approximation by Taylor algorithm*, Journal of Computational and Applied Mathematics 346 (2019): 532-548.
16. David F. Gleich, and Kyle Kloster. *Sublinear column-wise actions of the matrix exponential on social networks*, Internet Mathematics 11, no. 4-5 (2015): 352-384.
17. M. Liou. *A novel method of evaluating transient response*.Proceedings of the IEEE, **54(1)**:20–23, 1966.
18. Gabor Csardi and Tamas Nepusz, *The igraph software package for complex network research*, InterJournal ,Complex Systems, pp. 1695, 2006,
19. W. W. Zachary, *An information flow model for conflict and fission in small groups*, Journal of Anthropological Research **33**, 452-473 (1977).
20. D. Lusseau, K. Schneider, O. J. Boisseau, P. Haase, E. Slooten, and S. M. Dawson, Behavioral Ecology and Sociobiology **54**, 396-405 (2003).
21. M. Girvan and M. E. J. Newman, Proc. Natl. Acad. Sci. USA **99**, 7821-7826 (2002).
22. M. E. J. Newman, Phys. Rev. **E 74**, 036104 (2006).

Investigation of Band Gap Tailoring Phenomenon in In NP and TiO_2 NW Heterostructure

Vinit Kumar Yadav
Department of ECE, NIT Agartala, 799046, India
Vinod Yadav
Department of ECE, NIT Agartala, 799046, India
Rahul Raman
Department of ECE, NIT Agartala, 799046, India
* Mitra Barun Sarkar
Department of ECE, NIT Agartala, 799046, India
Email: vinityadav94@gmail.com

Abstract. Investigation of noble metal nanoparticles (NPs) qualities is developing out as a fascinating area of research in Nanoscience because of their wide dimension of uses in single- electron devices; medicate conveyance, sensors, photocatalysis and so on. Glancing angle deposition (GLAD) technique was employed to synthesize both Indium (In) NPs and Titania (TiO_2) nanowire (NW) heterostructure under controlled chamber parameter using e-beam evaporator technique. The Optical absorption and transmission measurement were investigated on both the samples. A 1.5 fold enhancement in absorption was observed due to In NPs incorporation. Bandgap calculations were done using the Tauc plot and subsequent band tailoring was also observed due to various sub-bandgap transition.

Keywords: TiO_2 nanowire, GLAD, Nanoparticle, Energy bandgap.

1 Introduction

Now a day's metal nanoparticles have been extensively used for wideband detection. Among several noble metals, In has drawn enormous attention due to their wider absorption in selective plasmon resonance frequency [1,2,3]. In this paper, a GLAD technique has been employed to fabricate In NP and TiO_2 NW heterostructure and subsequent comparison was made between both the samples to investigate the changes in the absorption spectra and band tailoring effect in the detection of UV-Vis light. Two separate structures of Si (P-type)/ 70nm (TiO_2) TF / 150 nm (TiO_2) NW and Si (P-type)/ 70nm (TiO_2) TF / 150nm (TiO_2) NW/ 5nm In NP were proposed and fabricated that are shown below in Fig. 1(a) & (b) respectively.

2 Experimental

Firstly, the cleaning process of the Si wafer has been done with help of different chemical solutions i.e. methanol, acetone and DI (deionization) water followed by quick deep

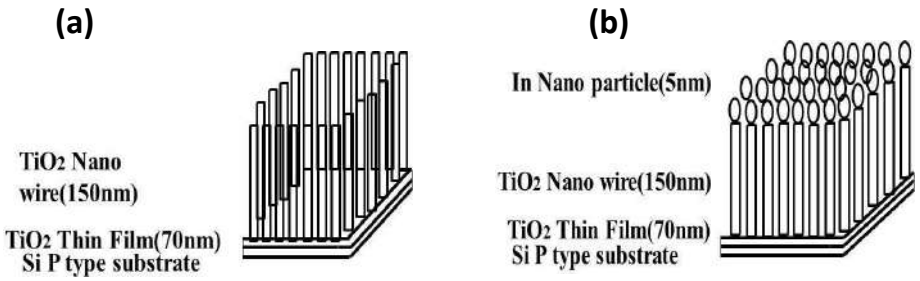

Fig. 1: (a) Proposed structure of TiO2 NW. (b) Proposed structure of TiO_2 NW incorporation In (NP)

into the mixture of HF (hydrofluoric) acid and DI water (1:50 ratio) in the ultrasonicator. After that, deposition has been done inside e-beam evaporator to deposit the TiO_2 thin film of 70 nm thickness on P-Type silicon substrate at a base pressure of 2×10^{-5} mbar followed by synthesis of 150 nm TiO_2 NW using a GLAD technique. Thereafter, In NPs of 5nm have been deposited on top of the NW. NWs and NPs both have been deposited with the help of GLAD technique that is depicted in Fig. 2. In both the cases, the tilt of GLAD was kept above 80^o and rpm (rotation per minute) of GLAD was kept below 500 rpm with a very small duration for NP whereas longer time duration has been maintained in case of NW synthesis. The involved fabrication steps (step1 to step5) are elaborately depicted in Fig. 2. Thereafter, the optical absorption and transmission measurement were investigated on the samples by a UV Spectrophotometer (Lamda950, Perkin Elmer) using a specular reflection method. In this set up a pre-aligned tungsten-halogen source was used as a light source. This light was entered into a dispersion device through an entrance slit. While coming out from the device the impinging light split into different colour and fall on the sample through an exit slit. A detector detects the output signal; i.e. the amount of the radiation transmitted at each wavelength was measured and plotted against the wavelength to obtain the spectrum.

3 Results and Discussion

Room temperature optical absorption experiment was gone up against the In NPs/(TiO_2) NW sample and as deposited (TiO_2) NW synthesised on the P-Si Substrate and the relevant absorption spectra has been depicted in Fig.3 (a). A 1.5 fold improvement was seen in UV–Vis region for In NPs-implanted (TiO_2) NW compared to bare (TiO_2) NW sample. The enhancement below 370 nm was observed because of absorption of light caused by the excitation of electrons from the valence band to the conduction band i.e. for fundamental band change of (TiO_2)[4,5,6,7]. The absorption edge of In NPs demonstrates a blue shift when contrasted with the (TiO_2) NW which obviously shows the impact of surface texturing. Subsequently, the energy band gap was calculated by the Tauc plot. Fig.3 (b) demonstrate the plot of $(\alpha h\nu)^2$ vs photon energy(eV) curve for both In NP and (TiO_2) NW where $h\nu$ refers to photon energy and α is absorp-

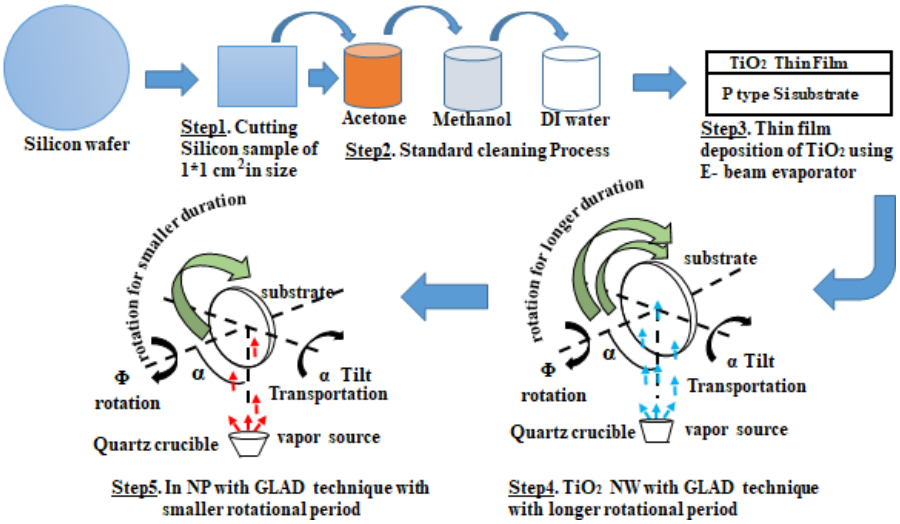

Fig. 2: Steps involved in the fabrication of the proposed structure

tion coefficient (a.u.).[1] The absorption coefficient was calculated from the measured transmission coefficient (T) with the help of equation (1).

$$\alpha = 2.303 \log(\frac{T}{d}) \tag{1}$$

Where d is the thickness of the sample. Extrapolation of the linear part of the curve to the energy (eV) axis yields the band gap value at various wavelengths. A bandgap near 3.4 eV was observed corresponds to the main band gap of TiO_2. Another bandgap near 3.1eV was seen because of oxygen deformity related sub-band change [6]. Inset Fig.3 (b) demonstrates the energy band diagram and corresponding carrier transition in Indium NP on TiO_2 NW[7]. In reality, two types of sub-bandgap transition have occurred. One is related to trap assisted transition from Ti^{3+} to the conduction band and the second one is a sub-bandgap transition from In (5p) to the conduction band due to In NPs incorporation into the NW sample, which magnifies the optical absorption in visible region [1].

4 Conclusion

In conclusion, In NPs and TiO_2 Nanowire on TiO_2 thin film upon p-type silicon substrate have been successfully fabricated by e-beam evaporator using a GLAD technique. The incident photon on the NWs was trapped and dispersed inside the device. A 1.5 fold enhancement in overall absorption was observed due to In NPs incorporation into the NW sample. Incorporation of In NP into the NW sample yields larger surface states which lead to the further reduction in bandgap due to distinct sub-bandgap transitions. Therefore, In NPs on (TiO_2) NW structure can be used as a promising visible photosensor.

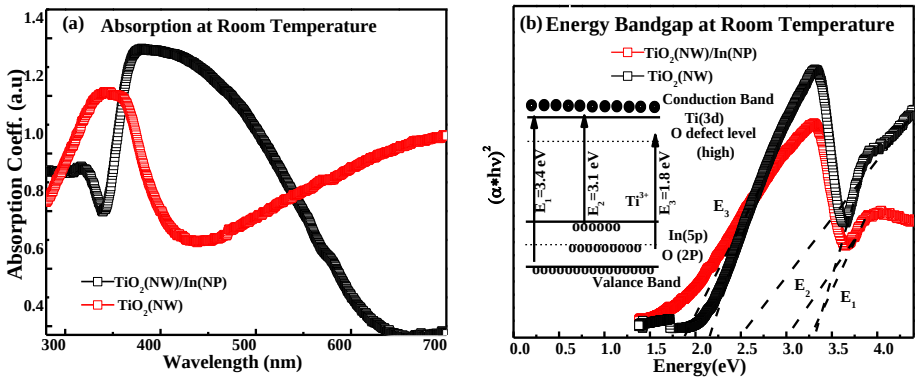

Fig. 3: (a) Absorption spectra of In NP and TiO_2 NW (b) $(\alpha h\nu)^2$ vs E curve for In NP and TiO_2 NW. Energy band diagram corresponding to carrier transition in In deposited Nanoparticle on TiO_2 NW

References

1. Sarkar,M.B., Mondal, A., Choudhuri, B., : Presence of capacitive memory in indium doped TiO_2 alloy thin film, *Journal of Alloys and Compounds* **654**, 529-533, (2016).
2. Yadav,V.K., Nath,A., Das,A., Mazumder, T.M., Sarkar,M.B., Indium Nanoparticles Capped TiO_2 Nanowire Array for Boosted Photosensing Adoption, *IEEE Electron Device Letters* **42**, 192-195, (2021).
3. Lee, S.Y., Park, S.J., : TiO2 photocatalyst for water treatment applications; *Journal of Industrial and Engineering Chemistry.* **19**, 1761–1769 (2013)
4. Pathak, P., Mallick,D., : Size-Dependent Magnetization Switching in Magnetoelectric Heterostructures for Self-Biased MRAM Applications, *IEEE Transactions on Electron Devices* **68**, 4418-4424, (2021).
5. Mukherjee, D., Mallick, D., : Magnetoelectric Wireless Power Transfer System for Biomedical Implants, *IEEE International Midwest Symposium on Circuits and Systems (MWSCAS)*, 356-359, (2021).
6. Lahiri, R., Ghosh, A., Choudhuri, B., Mondal, A., : Investigation on improved performance of Erbium doped TiO_2 nanowire based UV detector, *Materials Research Bulletin* **103**, 259-267, (2018).
7. Talukdar, J., Rawat,G., Choudhuri,B., Singh,K., Mummaneni,K.,: Device physics based analytical modeling for electrical characteristics of single gate extended source tunnel FET (SG-ESTFET), *Superlattices and Microstructures* **148**, 106725, (2020).

Large Eddy Simulation of Flow Over A Prismatic Building

Rohit Kumar
Deptt. Of Mechanical Engg. NIT Agartala
rksinghrathore13579@gmail.com
Dr. Bibhab Kumar Lodh
Deptt. Of Mechanical Engg. NIT Agartala
bibhab123@rediffmail.com
Dr. Ajoy K. Das
Deptt. Of Mechanical Engg. NIT Agartala
akdas_72@yahoo.com

Abstract— A numerical investigation of turbulent flow over a prismatic building is being carried out in the present study. The numerical analysis is carried out using LES(large eddy simulation) model. The FVM (Finite Volume Method) based CFD code 'ANSYS FLUENT' is used for numerical simulation and Ansys Design Modeler for generation of geometry and meshing. A 2-D model of NIT Agartala Administration Block of the dimension 40m×66m at high Reynolds Number, R_e = 10800, 21600, 32400, 43200 and 54000 are considered in the present study. Numerical simulation results are represented in form of Stream lines, Pressure Contours, Velocity Contours, time history of drag and lift forces, pressure coefficients. From simulation results a huge vortex formation has been recorded at two sites in the fluid domain which have a considerably large pressure load on the building.

Index Terms—*Ansys Fluent, FVM(Finite Volume Method), LES(Large Eddy Simulation).*

1. Introduction:

The outside stream past a feign body is an intriguing theme from crucial perspective of the flow physics (hazards, bifurcations) just as application parts of liquid elements (forces, heat transfer and temperamental impacts like vortex shedding). Flow over high-rise buildings, bridges, chimneys, cooling towers, tube banks in heat exchangers and many more things are the engineering applications of such flows. These flows have been the subject of excessive research, mainly pertaining to the engineering importance of structural design, and flow-induced vibrations.

A body encounters a drag compel, which is typically separated into two segments at whatever point liquid passes over it: frictional drag and pressure drag. Frictional drag is the friction between the fluid and the surface over which it is flowing. Pressure drag is the eddy formation that are developed in the fluid when passing over a body. Basically both types of drag are due to viscosity, but the distinction is needful because the two types of drag are due to different phenomena of flow.

Frictional drag is prominent in attached flows (where there is no separation). Pressure drag is prominent in separated flows. The stream over a prismatic structure comprises a comparative arrangement to examine the stream over feign bodies aside from extremely low Reynolds number. The asymmetric generation of vortices into the wake induces forces on the building leading to structural vibration. This is Vortex-Induced Vibration (VIV). Hence, the flow over a prismatic building is a similar test-case of great interest not only to study

vortex induced vibration phenomenon but also the aerodynamics of bluff bodies.

1.2 TURBULENCE:

In liquid elements, choppiness or violent stream is the example of smooth movement which are described by disordered unsettling influences in stream speed and weight. It is rather than a laminar stream routine, which happens when the liquid streams into parallel layers, without intrusions between those layers. Turbulence is commonly seen in everyday phenomena such as rapidly flowing rivers, undulating storm or chimney smoke.
Disturbance is caused because of exorbitant dynamic vitality in parts of a liquid stream, which surpasses the hosing impact of liquid consistency. It is expected this reason, choppiness is less demanding to create in low consistency liquids, however it is progressively troublesome in high thickness liquids. In general terms, in the turbulent flow, the unstable vortexes appear of many sizes interacting with each other, therefore the drag due to the friction effects increases [1].

The outside stream over each kind of vehicles, for example, autos, planes, ships and submarines are instances of violent stream. The approaching of turbulence can be anticipated by the Reynolds number, which is the proportion of inertia force to viscous force inside a liquid. The relative movement between liquid layers produces liquid erosion, which is a factor for advancement of fierce stream. The liquid consistency which increments, continuously hinders disturbance, as progressively thick liquid retains increasingly active vitality. This capacity to anticipate the approaching of choppiness in the stream is an essential plan apparatus for gear, for example, flying machine wings or channeling frameworks. The role played by friction drag (also called viscous drag) and pressure drag (also called form drag or profile drag) can be seen by considering an airfoil at different angles of attack, just gentle weight inclinations are experienced by the limit layers on the best and base surface at little approach, and they stay appended along nearly the whole length. The drag is commanded by the thick erosion inside the limit layers and the wake is little. As the approach builds, the pressure angles on the airfoil increases in like manner. The negative weight slope on the best back bit of the airfoil may wind up sufficiently able to cause a stream partition. This detachment will result in increment of the extent of the wake, and the weight misfortunes in the wake because of arrangement of vortex. Therefore the pressure drag increases. At a high assault edge, an extensive volume of the stream super surface may get isolated, and the airfoil is said to be blocked. At this stage, the viscous drag is much lesser than the pressure drag. At the point when the thick drag is predominant, we state the body is streamlined, and when the weight drag is overwhelming, we state the body is feign. Regardless of whether the stream is commanded by gooey drag or weight drag depends altogether on the state of the body. For a feign body, the weight drag is the predominant wellspring of drag. For a given speed and frontal territory, a streamlined body will dependably have a lower opposition than a feign body.

1.3 CFD ANALYSIS:

Computational Fluid Dynamics is a part of fluid mechanics that uses data structures and numerical examination to deal with and look at the issues drew in with fluid stream. With the assistance of PCs computations important to reenact the association of fluids and gases with surfaces characterized by form conditions are performed. With high speed supercomputers

better results can be accomplished.

At first the exploratory approval of such programming is finished utilizing a breeze passage and afterward the last approval comes in full scale tests. Practically all CFD issues are in a general sense dependent on the Navier-Stokes conditions. These conditions can be rearranged by disregarding terms that depict the gooey activities to deliver Euler's conditions. Greater simplification, by neglecting the terms that describe the vorticity, produces all potential equations. At last, for little Disturbances in subsonic and supersonic transitions.

These equations can be linearized to produce the potential amplifiers equations. At the time of preprocessing, you can define the geometry and the physical limits of the problem. From that point, the information can be handled and the volume of liquid (or liquid area) is separated. The Volume of the liquid is isolated into discrete cells. The mesh might be uniform or non-uniform, unstructured or organized. Limit conditions are characterized. This involves feeding all necessary properties and values. The arrangement of conditions are done iteratively as a relentless state or transient once the reproduction is begun lastly with the assistance of post-processor investigation and representation of the subsequent arrangement is finished.

1.4 SIGNIFICANCE OF DIMENSIONLESS NUMBER:

Reynolds Number:

It is defined as a dimensionless number which is the proportion of inertia forces to viscous forces and further evaluates the relative significance of the two types of forces for given stream conditions.

$$Re = \rho Dv/\mu$$

- Essentially used to examine diverse stream routines to be specific laminar, violent or both.
- When viscous forces are prevailing it is a laminar flow & at the point when inertial forces are prevailing it is a Turbulent stream.
- The change from laminar to fierce stream relies upon the surface harshness, geometry, stream speed and kind of liquid.

II. METHODOLOGY

LARGE EDDY SIMULATION

Large eddy simulation is a numerical model for choppiness utilized in computational liquid elements. It was at first proposed in 1963 by Joseph Smagorinsky to mimic environmental air flows, and first investigated by Deardorff (1970). LES discovers application in a wide assortment of building applications, including ignition, and reenactments of the climatic limit layer [2]. The iterative computation of fierce streams by numerically tackling the Navier–Stokes conditions requires fathom a wide scope of time and length scales, all of which influence the stream field. Such an immovability can be acquired with direct numerical reenactment (DNS), yet DNS is computationally over the top expensive, and its cost breaking points recreation of useful building frameworks with complex geometry or stream courses of action, for example, siphons, vehicles tempestuous, flies, and landing gears. LES

is based on the thought that the little fierce structures are more general in nature than the extensive vortexes. Therefore, the idea is to compute the contributions of the large, energy-carrying edifice to energy transfer and momentum and to model the effects of the small edifice, which are not settled by the numerical plan. Due to the more homogeneous and universal character of the small scales, we may expect that the so called subgrid-scale models can be kept much simpler than the turbulence models for the RANS equations [3] [4].

III. GOVERNING EQUATIONS

Continuity equations:

$$\frac{\partial u_i}{\partial x_i} = 0$$

Navier-Stokes Equations:

$$\frac{\partial u_i}{\partial t} + u_j \frac{\partial u_i}{\partial x_j} = -\frac{1}{\rho}\frac{\partial p}{\partial x_i}\frac{\mu}{\rho}\frac{\partial}{\partial x_j}\left(\frac{\partial u_i}{\partial x_j}\right)$$

Energy Equations:

$$\rho c \frac{\partial T}{\partial t} + \rho c u_i \frac{\partial T}{\partial x_i} = \lambda \frac{\partial}{\partial x_j}\left(\frac{\partial T}{\partial x_j}\right)$$

IV. GRID INDEPENDENCY TEST

Grid independence is inspected to guarantee the precision and unwavering quality of the numerical techniques. Grid convergence is the term used to depict the improvement of results by utilizing progressively littler cell sizes for the estimations. A count should approach the right answer as the mesh ends up better, henceforth the term grid convergence. The typical CFD system is to begin with coarse sized mesh and step by step refine it until the progressions saw in the outcomes are littler than a pre-characterized satisfactory mistake. A touchy report was done so as to decide the impact of Grid refinement on the recreation results. The results are summarized in Table 1. Grid of 67000 nodes is found to meet the requirement of the mesh independent limit.

Table 1 Effect of grid on Cd_{avg} and Cl_{rms}

Grid	Nodes	Δt	Re	Cd_{avg}	Cl_{rms}
1.	65000	0.05	10800	6.42	3.26
2.	67000	0.05	10800	6.435	3.287
3.	69000	0.05	10800	6.433	3.288

V. RESULTS AND DISCUSSION

Large eddy simulations were performed to study the fluid flow over a prismatic building at higher values of Reynolds number. The simulation was carried out at five different values of Reynolds number from 10.8×10^3 to 54×10^3. The hydrodynamic forces, pressure contour,

streamline contour, velocity contour were computed.

5.1 Calculation of Drag and Lift:

The drag coefficient per unit length is defined as Cd = 2Fx/ρU2D, where Fx is the force acting in the direction of the fluid flow at the boundary of the obstacle and ρ = 1. The lift coefficient per unit length is defined as Cl = 2Fy/ρU2D. The unsteady lift and drag coefficient gradually increases with time and oscillates periodically between a range of maximum and minimum value. This range of periodic oscillation goes on decreasing with time or number of iterations. The drag and lift using the LES model for flow over the prismatic building at Re=54×10^3 was calculated in fluent itself. The value of drag force is 174447.27N which tremendously high for the front face in contrast to lift force which is of the value 84.733325N. Thereby the ratio of drag force upon lift force comes out to be 2058.7799 which clearly shows the correctness of results from aerodynamics point of view.
This work was conducted to find the effect of Reynolds number on the prismatic building by changing the velocity of air keeping other parameters of simulation same.

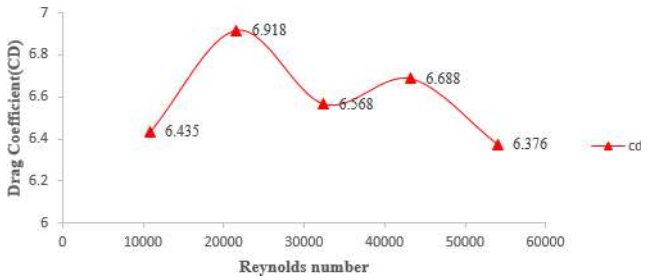

Figure 1: Variation of drag coefficient (CD) with Reynolds number

Above plot clearly depicts that there are certain range for which CD decreases.

5.2Pressure Contour:

Pressure distribution is important in the study of flow around bluff bodies. In the region of the bodies Pressure changes are seen with the movement of vortices. Stream partition happens over structure with sharp corners, for example, the main edge and trailing edge of a square area [5], [6]. This introduces periodic forces on the body due to changes in the pressure. This situation is most important in flow involving fluid and structure interaction such as the flow over a tall building or long spanned bridge. Forces on the bodies swaddled in the flow are generated due to Vortex formation and progression. A negative pressure deficit area adjacent to the surface is created where vortex progresses. Thus it is important to study pressure distribution for the analysis of the aerodynamic forces over a structure. Fig. 2, 3, 4, 5, 6 shows the contour maps of mean pressure for flow over the prismatic building for Reynolds number varying between10.8×10^3 to 54×10^3.

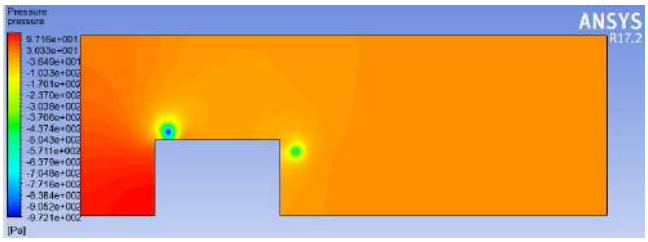

Figure 2: Pressure contour at Re=10.8×10^3

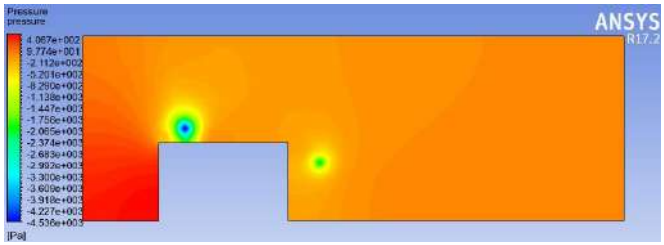

Figure 3: Pressure contour at Re= 21.6×10^3

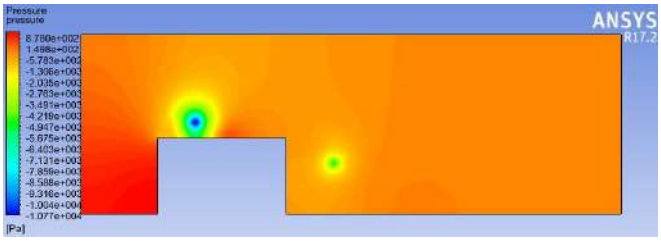

Figure 4: Pressure contour at Re= 32.4×10^3

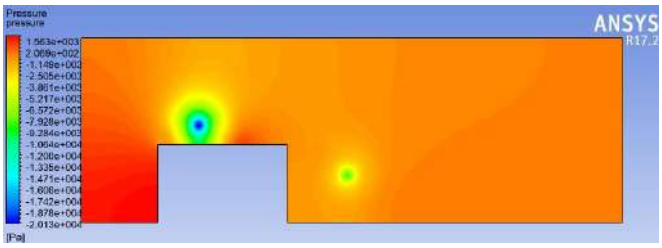

Figure 5: Pressure contour at Re= 43.2×10^3

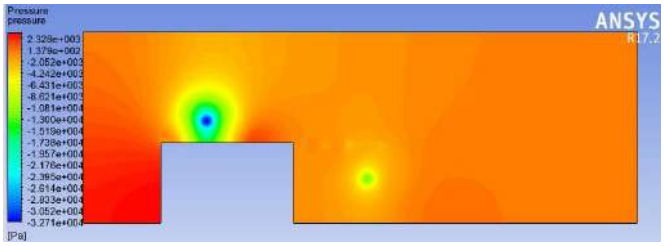

Figure 6: Pressure contour at Re= 54×10^3

5.3 Pressure Coefficient Calculation:

Figured pressure coefficient of mean surface pressure on the prismatic structure is depicted in

the graph underneath Fig. 7. There is by and large great understanding among processed and estimated values. The reference velocity for figuring of pressure coefficient is taken as velocity of moving toward stream at the stature of structure.

The position on the graphs are taken as the distance through x axis and y axis for front face and for top face of the prismatic body and is plotted against the pressure coefficient Cp throughout the internal surface of the geometric domain

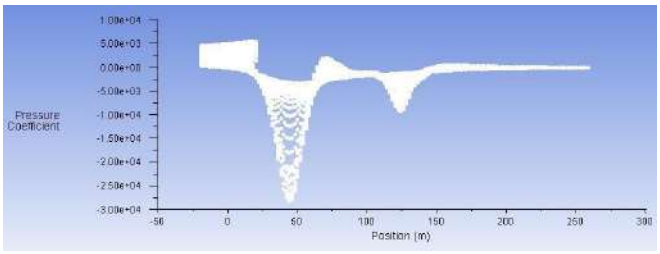

Figure 7: Plot for pressure coefficient (Cp)

5.4 Velocity Contours:

Fig. 8, 9, 10, 11 and 12 shows the mean flow pattern over the prismatic building for Re = 10.8×10^3 to Re= 54×10^3. The figure shows that the flow separates from the top and a vortex originates at the top and back of the building

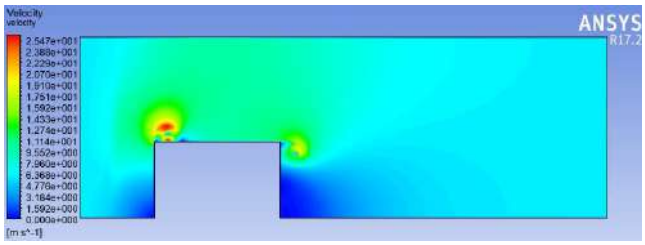

Figure 8: Velocity contour at Re=10.8×10^3

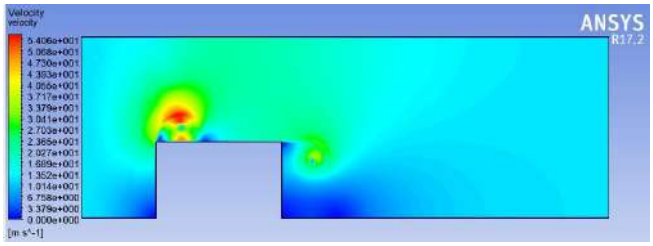

Figure 9: Velocity contour at Re= 21.6×10^3

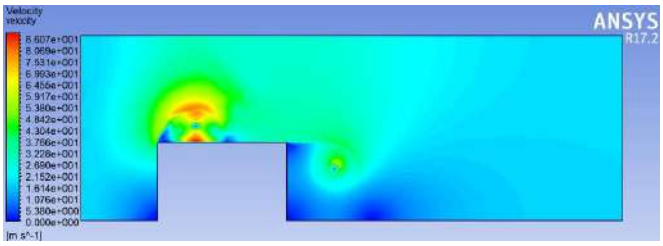

Figure 10: Velocity contour at Re= 32.4×10^3

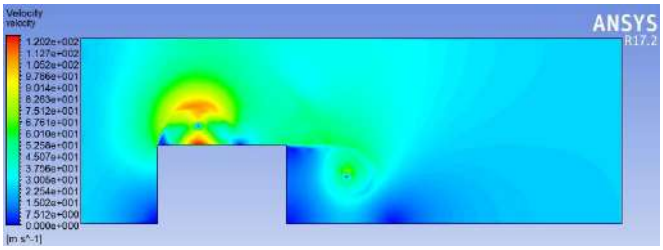

Figure 11: Velocity contour at Re= 43.2×10^3

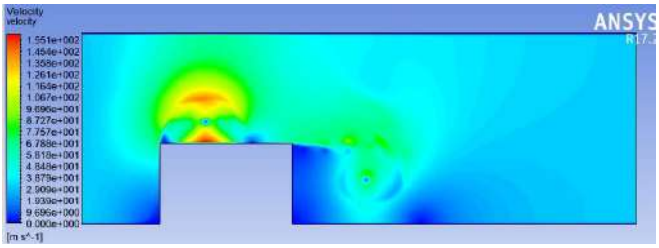

Figure 12: Velocity contour at Re= 54×10^3

5.5 Streamline Contours:

The eddies are formed at the top and back of the prismatic building in the downstream. These eddied grow larger with the passage of the flow time. There are two sites of high vorticity which can be seen from the

figure below. The wake with pair of vortices in the recirculation region is observed. Fig. 13, 14, 15, 16 and 17 shows the streamlines of flow for Re = 10.8×10^3 to Re= 54×10^3

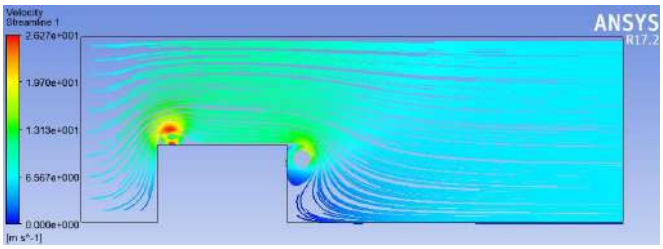

Figure 13: Streamlines at Re= 10.8×10^3

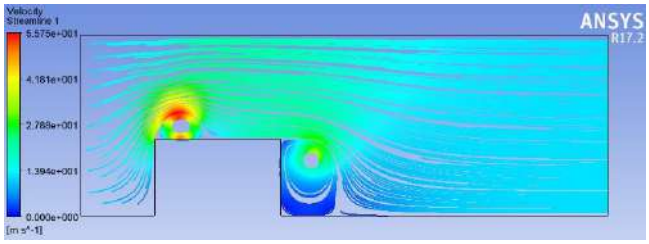

Figure 14: Streamlines at Re= 21.6×10^3

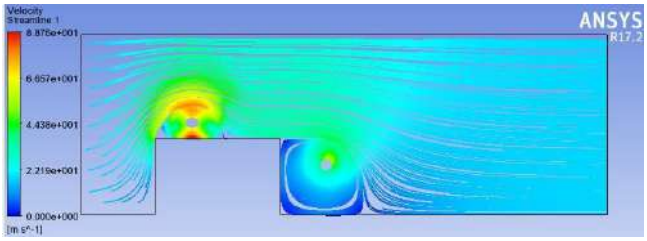

Figure 15: Streamlines at Re= 32.4×10^3

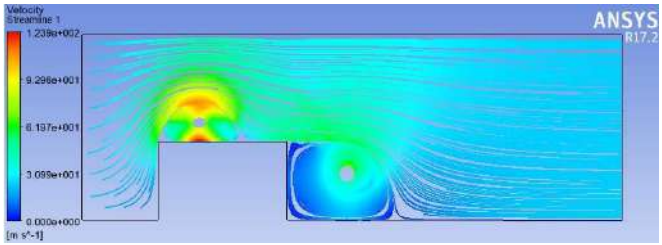

Figure 16: Streamlines at Re= 43.2×10^3

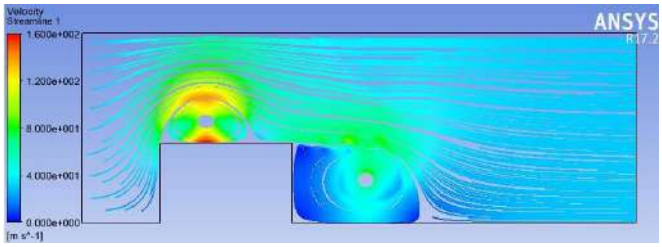

Figure 17: Streamlines at Re= 54×10^3

CONCLUSION

This work was conducted using Large eddy simulation smagorinsky model in ANSYS 17.2 taking NIT Agartala administrative block as model of the study. The study was performed at Reynolds number ranging from lower to higher values keeping other parameters constant. It is clear from the results that increasing wind speed results in formation of larger and larger sized vortex region at the development sites which ultimately indicates increasing drag force with increasing Reynolds number.

REFERENCES

[1] Lee, B. E. "The effect of turbulence on the surface pressure field of a square prism." Journal of Fluid Mechanics 69.2 (1975): 263-282.
[2] Boileau, M., Duchaine, F., Jouhaud, J. C. and Sommere, Y., (2013). Large -eddy simulation of heat transfer around a square cylinder using unstructured grids. AIAA journal, 51(2), 372-385.
[3] Rodi, W. "Comparison of LES and RANS calculations of the flow around bluff bodies." Journal of wind engineering and industrial aerodynamics 69 (1997): 55-75.
[4] Sohankar, A. "Flow over a bluff body from moderate to high Reynolds numbers using large eddy simulation." Computers & fluids 35.10 (2006): 1154-1168.
[5] Sohankar, Ahmad, Lars Davidson, and Christopher Norberg. "Large eddy simulation of flow past a square cylinder: comparison of different sub grid scale models." Journal of Fluids Engineering 122.1 (2000): 39-47.
[6] Rodi, W. "On the simulation of turbulent flow past bluff bodies." Computational Wind Engineering 1. 1993. 3-19.

L^r Version of inequalities in polar derivative of a polynomial with s-fold zeros at the origin

Barchand Chanam
Department of Mathematics
National Institute of Technology, Manipur, Langol 795004, India
Email: barchand_2004@yahoo.co.in

Abstract. Suppose $f(z)$ is a polynomial of degree n and α be any real or complex number. The polar derivative of $f(z)$, denoted by $D_\alpha f(z)$, is defined by $D_\alpha f(z) = nf(z) + (\alpha - z)f^{'}(z)$. If all the zeros of $f(z)$ lie in $|z| \leq t, t \leq 1$ with a zero of multiplicity s at the origin. Then for each real or complex numbers α with $|\alpha| \geq t$, β with $|\beta| < t^{n-s}$ and for each $r > 0$, we prove

$$\left\{\int_0^{2\pi} \left|D_\alpha \left\{f(e^{i\theta}) + \tfrac{m}{t^n}\beta e^{is\theta}\right\}\right|^r d\theta\right\}^{\frac{1}{r}} \geq$$
$$(|\alpha| - t)\left(\tfrac{n+st}{1+t}\right)\left\{\int_0^{2\pi} \left|f(e^{i\theta}) + \tfrac{m}{t^n}\beta e^{is\theta}\right|^r d\theta\right\}^{\frac{1}{r}},$$

where $m = \min_{|z|=t} |p(z)|$.
Our result improves and generalizes other known inequalities.

Mathematics Subject Classification: 30C10, 30C15

Keywords: Polynomial · Polar Derivative · Integral Mean · Maximum Modulus.

1 Introduction

Throughout this paper, we denote by $F_t(z)$ the class of all polynomials of degree n with all its zeros lying in $|z| \leq t, t \leq 1$ and $M(f,t) = \max_{|z|=t} |f(z)|$. And as usual, $\mathbb{C}$ denotes the set of complex numbers.

If $f \in F_1(z)$, the famous result of P. Turán [12] is

$$M(f^{'}, 1) \geq \frac{n}{2} M(f, 1). \tag{1}$$

Inequality (1) is sharp and equality occurs for those polynomials with all zeros on $|z| = 1$.

Malik [8] generalised inequality (1) by considering the class $F_t(z)$, Malik [8] generalised inequality (1) as

$$M(f^{'}, 1) \geq \frac{n}{1+t} M(f, 1). \tag{2}$$

Aziz and Shah [4] gave another generalization of (2) and proved that if $f \in F_t(z)$, with a zero of multiplicity s at the origin, then

$$M(f^{'},1) \geq \frac{n+st}{1+t} M(f,1). \tag{3}$$

Equality occurs in (3) for $f(z) = z^s(z+t)^{n-s}, 0 \leq s \leq n$.

Suppose $f(z)$ be a polynomial of degree n and $\alpha \in \mathbb{C}$ then the polar derivative of $f(z)$, denoted by $D_\alpha f(z)$, is defined as

$$D_\alpha f(z) = nf(z) + (\alpha - z)f^{'}(z). \tag{4}$$

It is evident that $D_\alpha f(z)$ is a polynomial of degree at most $n-1$ and it gives a generalization of the ordinary derivative $f^{'}(z)$ of $f(z)$ in the following sense

$$\lim_{\alpha \to \infty} \frac{D_\alpha f(z)}{\alpha} = f^{'}(z).$$

Different names, e.g., the "émanant" of $f(z)$, the "derivative of $f(z)$ with respect to the point α" and "the polar derivative of $f(z)$" are given respectively by Laguerre [7], Pólya and Szegö [10] and Marden [9].

Shah [11] extended Turán's inequality (1) to polar derivative.

Theorem 1. *If $f \in F_1(z)$, and $\alpha \in \mathbb{C}$ with $|\alpha| \geq 1$,*

$$M(D_\alpha f,1) \geq \frac{n}{2}(|\alpha|-1)M(f,1). \tag{5}$$

Inequality (5) is best possible for $f(z) = (z-1)^n$, $\alpha \geq 1$.

Aziz and Rather [1] obtained the polar version of (2) as

Theorem 2. *If $f \in F_t(z)$, and $\alpha \in \mathbb{C}$ with $|\alpha| \geq t$,*

$$M(D_\alpha f,1) \geq n\frac{|\alpha|-t}{1+t} M(f,1). \tag{6}$$

Equality holds for $f(z) = (z-t)^n$ with $\alpha \geq t$.

It is of interest to obtain L^r version for the polar derivative. Aziz et al. [2] proved

Theorem 3. *If $f \in F_t(z)$, and $\alpha \in \mathbb{C}$ with $|\alpha| \geq 1$, and $r \geq 1$,*

$$\left(\int_0^{2\pi} \left|D_\alpha f(e^{i\theta})\right|^r d\theta\right)^{\frac{1}{r}} \leq n(|\alpha|+t)G_r \left(\int_0^{2\pi} \left|f(e^{i\theta})\right|^r d\theta\right)^{\frac{1}{r}}, \tag{7}$$

where

$$G_r = \left(\frac{2\pi}{\int_0^{2\pi} |t+e^{i\theta}|^r \, d\theta}\right)^{\frac{1}{r}}.$$

In the limiting case when $r \to \infty$, inequality (7) becomes equality for $p(z) = (z+t)^n$ with $0 \leq \alpha \leq 1$.

Dewan et al. [5] presented results on L^r analogues and these generalize respectively inequalities (5) and (6) and (3).

Theorem 4. *If $f \in F_t(z)$, and $\alpha \in \mathbb{C}$ with $|\alpha| \geq t$, and for each $r > 0$,*

$$n(|\alpha| - t)\left(\int_0^{2\pi} \left|f(e^{i\theta})\right|^r d\theta\right)^{\frac{1}{r}} \leq \left(\int_0^{2\pi} \left|1 + te^{i\theta}\right|^r d\theta\right)^{\frac{1}{r}} \max_{|z|=1} |D_\alpha f(z)|. \quad (8)$$

When $r \to \infty$, (8) attains equality for $f(z) = (z - k)^n, \alpha \geq t$.

Theorem 5. *If $f \in F_t(z)$ and it has a zero of multiplicity s at the origin, $\alpha \in \mathbb{C}$ with $|\alpha| \geq t$, and for each $r > 0$,*

$$\left(\int_0^{2\pi} \left|D_\alpha f(e^{i\theta})\right|^r d\theta\right)^{\frac{1}{r}} \geq \frac{(|\alpha| - t)(n + ts)}{1 + t}\left(\int_0^{2\pi} \left|f(e^{i\theta})\right|^r d\theta\right)^{\frac{1}{r}}. \quad (9)$$

2 Main Theorem

By involving $m = \min_{|z|=t} |p(z)|$, we obtain generalization as well an improvement of inequality (9) due to Dewan et al. [5].

Theorem 6. *If $f \in F_t(z)$ and it has a zero of multiplicity s at the origin, $\alpha, \beta \in \mathbb{C}$ with $|\alpha| \geq t$, $|\beta| < t^{n-s}$ and for each $r > 0$,*

$$\left\{\int_0^{2\pi} \left|D_\alpha\left\{f(e^{i\theta}) + \tfrac{m}{t^n}\beta e^{is\theta}\right\}\right|^r d\theta\right\}^{\frac{1}{r}} \geq$$
$$(|\alpha| - t)\left(\tfrac{n+st}{1+t}\right)\left\{\int_0^{2\pi} \left|f(e^{i\theta}) + \tfrac{m}{t^n}\beta e^{is\theta}\right|^r d\theta\right\}^{\frac{1}{r}}, \quad (10)$$

where $m = \min_{|z|=t} |p(z)|$.

Remark 1. If we let $r \to \infty$ on both sides of (10) we obtain a result recently obtained by Khojastehnezhad and Bidkham [6].

Corollary 1. *If $f \in F_t(z)$ and it has a zero of multiplicity s at the origin, $\alpha, \beta \in \mathbb{C}$ with $|\alpha| \geq t$, $|\beta| < t^{n-s}$,*

$$\max_{|z|=1}\left|D_\alpha f(z) + \frac{m}{t^n}\beta z^s\right| \geq (|\alpha| - t)\left(\frac{n + st}{1 + t}\right)\max_{|z|=1}\left|f(z) + \frac{m}{t^n}\beta z^s\right| \quad (11)$$

where $m = \min_{|z|=t} |p(z)|$.

Remark 2. When we divide both sides of (10) by $|\alpha|$ and take limit as $|\alpha| \to \infty$, it reduces to a result due to Dewan et al. [5, Corollary 1.2].

Corollary 2. *If $f \in F_t(z)$ and it has a zero of multiplicity s at the origin, then for every $\beta \in \mathbb{C}$ with $|\beta| < t^{n-s}$ and for each $r > 0$,*

$$\left\{\int_0^{2\pi} \left|f^{'}(e^{i\theta}) + \frac{m}{t^n}\beta s e^{i(s-1)\theta}\right|^r d\theta\right\}^{\frac{1}{r}} \geq \left(\frac{n+st}{1+t}\right)\left\{\int_0^{2\pi} \left|f(e^{i\theta}) + \frac{m}{t^n}\beta e^{is\theta}\right|^r d\theta\right\}^{\frac{1}{r}}, \tag{12}$$

where $m = \min_{|z|=t} |p(z)|$.

As mentioned earlier, when we put $\beta = 0$ in Corollary 2, we obtain an inequality of Dewan et al. [5, Corollary 1.2].

Remark 3. Further, if $r \to \infty$ on both sides of (12), we have

$$\max_{|z|=1}\left|f^{'}(z) + \frac{m}{t^n}\beta s z^{s-1}\right| \geq \left(\frac{n+st}{1+t}\right)\max_{|z|=1}\left|f(z) + \frac{m}{t^n}\beta z^s\right|. \tag{13}$$

Now

$$\left|f^{'}(z) + \frac{m}{t^n}\beta s z^{s-1}\right| \leq |f^{'}(z)| + \frac{m}{t^n}|\beta| s |z|^{s-1}$$

which for $|z| = 1$ becomes

$$\left|f^{'}(z) + \frac{m}{t^n}\beta s z^{s-1}\right| \leq |f^{'}(z)| + \frac{m}{t^n}|\beta| s,$$

which further gives

$$\max_{|z|=1}\left|f^{'}(z) + \frac{m}{t^n}\beta s z^{s-1}\right| \leq \max_{|z|=1}|f^{'}(z)| + \frac{m}{t^n}|\beta| s. \tag{14}$$

Combining (13) and (14), we have

$$M(f^{'},1) + \frac{m}{t^n}|\beta| s \geq \left(\frac{n+st}{1+t}\right)\max_{|z|=1}\left|f(z) + \frac{m}{t^n}\beta z^s\right|. \tag{15}$$

Let z_0 on $|z| = 1$ be such that $M(f,1) = |f(z_0)|$, then, in particular, (15) gives

$$M(f^{'},1) + \frac{m}{t^n}|\beta| s \geq \left(\frac{n+st}{1+t}\right)\left|f(z_0) + \frac{m}{t^n}\beta z_0^s\right|. \tag{16}$$

When suitable choice of the argument of β in (16) is made such that

$$\left|f(z_0) + \frac{m}{t^n}\beta z_0^s\right| = |f(z_0)| + \frac{m}{t^n}|\beta| = M(f,1) + \frac{m}{t^n}|\beta|. \tag{17}$$

From (16) and (17), it follows that

$$M(f^{'},1) + \frac{m}{t^n}|\beta| s \geq \left(\frac{n+st}{1+t}\right)\left\{M(f,1) + \frac{m}{t^n}|\beta|\right\},$$

or

$$M(f^{'},1) \geq \left(\frac{n+st}{1+t}\right)M(f,1) + \frac{m}{t^n}|\beta|\left\{\frac{n+st}{1+t} - s\right\}$$

or

$$M(f^{'},1) \geq \left(\frac{n+st}{1+t}\right)M(f,1) + \frac{m}{t^n}|\beta|\left(\frac{n-s}{1+t}\right). \tag{18}$$

Finally, letting $|\beta| \to t^{n-s}$ in (18), it reduces to

Corollary 3. *If $f \in F_t(z)$ and it has a zero of multiplicity s at the origin, then*

$$M(f^{'},1) \geq \left(\frac{n+st}{1+t}\right) M(f,1) + \frac{m}{t^n}|\beta| \left(\frac{n-s}{1+t}\right), \tag{19}$$

where $m = \min_{|z|=t} |p(z)|$.
As in the above cases equality occurs for $f(z) = z^s(z+t)^{n-s}$, $0 \leq s \leq n$.

This corollary improves upon inequality (3) due to Aziz and Shah [4].

3 Lemma

For the proof of the theorem, we require the following lemma.

Lemma 1. *If $f \in F_t(z)$ then for $|z| = 1$*

$$t|f^{'}(z)| \geq |g^{'}(z)|, \tag{20}$$

where

$$g(z) = z^n \overline{f\left(\frac{1}{\bar{z}}\right)}.$$

The above lemma is a particular case of a result due to Aziz and Shah [3].

4 Proof of the Main Theorem

Proof of Theorem 6: Since all the zeros of $f(z)$ lie in $|z| \leq t, t \leq 1$ and $f(z)$ has a zero of multiplicity s at the origin, it can be written

$$f(z) = z^s h(z),$$

where $h(0) \neq 0$ and $h(z)$ is of degree $n-s$ with all the zeros in $|z| \leq t, t \leq 1$.
If $\beta \in \mathbb{C}$ such that $|\beta| < t^{n-s}$, then applying Rouché's theorem to the polynomial $f(z) + \frac{m}{t^n}\beta z^s$, where $m = \min_{|z|=t} |p(z)|$, it is precise that all the zeros of
$F(z) = z^s \left\{h(z) + \frac{m}{t^n}\beta\right\}$ lie in $|z| \leq t, t \leq 1$.

Hence, it is claimed that $F(z)$ has a zero of multiplicity s at the origin, for which it is required to verify that at the origin,

$$h(z) + \frac{m}{t^n}\beta \neq 0.$$

If $m = 0$, then the claim follows trivially, since $h(0) \neq 0$. Thus we assume $m \neq 0$.
Now

$$m = \min_{|z|=t} |f(z)| = \min_{|z|=t} |z^s h(z)| = t^s \min_{|z|=t} |h(z)|,$$

i.e.,

$$\frac{m}{t^s} = \min_{|z|=t} |h(z)| \leq |h(z)| \quad \text{for} \quad |z| = t. \tag{21}$$

Since $|\beta| < t^{n-s}$, (21) implies

$$\left|\beta\frac{m}{t^n}\right| = |\beta|\frac{m}{t^n} < \frac{m}{t^s} \leq |h(z)| \quad \text{for} \quad |z| = t.$$

i.e.,

$$\left|\beta\frac{m}{t^n}\right| < |h(z)| \quad \text{for} \quad |z| = t. \tag{22}$$

Thus, it is concluded that every zero of $h(z)+\beta\frac{m}{t^n}$ lies in the region i.e. in the punctured disc $0 < |z| < k$, and this implies that $h(0) + \beta\frac{m}{t^n} \neq 0$.

Also

$$F^{'}(z) = sz^{s-1}\left\{h(z) + \beta\frac{m}{t^n}\right\} + z^s h^{'}(z),$$

which implies

$$\frac{zF^{'}(z)}{F(z)} = s + \frac{z\frac{d}{dz}\left\{h(z) + \beta\frac{m}{t^n}\right\}}{h(z) + \beta\frac{m}{t^n}}.$$

If $z_1, z_2, ..., z_{n-s}$ are the zeros of $h(z) + \beta\frac{m}{t^n} = H(z)$ (say), then none of them is zero and $|z_k| \leq t, t \leq 1$ for all $k = 1, 2, ..., n-s$ and we have for each θ, $0 \leq \theta < 2\pi$,

$$Re\left\{\frac{e^{i\theta}F^{'}(e^{i\theta})}{F(e^{i\theta})}\right\} = s + Re\left\{\frac{e^{i\theta}H^{'}(e^{i\theta})}{H(e^{i\theta})}\right\}$$

$$= s + \sum_{k=1}^{n-s}\frac{e^{i\theta}}{e^{i\theta} - z_k}$$

$$\geq s + \sum_{k=1}^{n-s}\frac{1}{1 + |z_k|}$$

$$\geq s + \frac{n-s}{1+t} = \frac{n+st}{1+t}.$$

For those points $e^{i\theta}$, $0 \leq \theta < 2\pi$, except the zeros of $F(z)$.
Hence

$$|F^{'}(e^{i\theta})| \geq \frac{n+st}{1+t}|F(e^{i\theta})|, \tag{23}$$

for points $e^{i\theta}$, $0 \leq \theta < 2\pi$, except the zeros of $F(z)$. Further, (23) follows for those points $e^{i\theta}$, $0 \leq \theta < 2\pi$, as well-those zeros of $F(z)$ and we are implied for $|z| = 1$,

$$|F^{'}(z)| \geq \frac{n+st}{1+t}|F(z)|. \tag{24}$$

Since $F(z)$ has all its zeros in $|z| \leq t, t \leq 1$, therefore by the Lemma 1, we have

$$t|F^{'}(z)| \geq |G^{'}(z)|, \quad \text{for} \quad |z| = 1, \tag{25}$$

where

$$G(z) = z^n\overline{F\left(\frac{1}{\bar{z}}\right)}.$$

For $\alpha \in \mathbb{C}$, by the definition of polar derivative

$$D_\alpha F(z) = nF(z) + (z-\alpha)F^{'}(z),$$

from which, we have for $|z| = 1$,

$$\begin{aligned} |D_\alpha F(z)| &= |nF(z) + (z-\alpha)F^{'}(z)| \\ &\geq \|\alpha||F^{'}(z)| - |nF(z) - zF^{'}(z)\| \\ &= \|\alpha||F^{'}(z)| - |G^{'}(z)\|. \end{aligned} \tag{26}$$

Since for $|z| = 1$, $|G^{'}(z)| = |nF(z) - zF^{'}(z)|$.
Using (25), we have

$$|\alpha||F^{'}(z)| - |G^{'}(z)| \geq (|\alpha| - t)|F^{'}(z)|.$$

Since $|\alpha| \geq t$, (26) on using the above inequality gives

$$|D_\alpha F(z)| \geq (|\alpha| - t)|F^{'}(z)| \quad \text{for} \quad |z| = 1. \tag{27}$$

For $|\alpha| \geq k$, combining (24) and (27), we obtain

$$|D_\alpha F(z)| \geq (|\alpha| - t)\frac{n+st}{1+t}|F(z)|, \quad \text{for} \quad |z| = 1.$$

i.e.,

$$\left|D_\alpha\left\{f(z) + \frac{m}{t^n}\beta z^s\right\}\right| \geq (|\alpha| - t)\frac{n+st}{1+t}\left|f(z) + \frac{m}{t^n}\beta z^s\right|, \quad \text{for} \quad |z| = 1. \tag{28}$$

Note that each $r > 0$, and for each θ, $0 \leq \theta < 2\pi$, (28) equivalently gives

$$\left|D_\alpha\left\{f(e^{i\theta}) + \frac{m}{t^n}\beta e^{is\theta}\right\}\right|^r \geq (|\alpha| - t)^r\left(\frac{n+st}{1+t}\right)^r\left|f(e^{i\theta}) + \frac{m}{t^n}\beta e^{is\theta}\right|^r. \tag{29}$$

Performing integration throughout for $\theta \in [0, 2\pi]$, the main theorem is led.

Acknowledgements

The author is very grateful to the reviewer for his valuable suggestions.

References

1. Aziz, A., Rather, N. A.,: A refinement of a theorem of Paul Turán concerning polynomials, *J. Math. Ineq. Appl.* **1**, 231-238, (1998).
2. Aziz, A., Rather, N. A., Aliya, Q.,: L^q norm inequalities for the polar derivative of a polynomia, *Math. Inequal. Appl.* **10(4)**, 733-744, (2007).
3. Aziz, A., Shah, W. M.,: An integral mean estimate for polynomials, *Indian J. Pure and Appl. Math.* **28**, (1997).

4. Aziz, A., Shah, W. M.,: Inequalities for a polynomial and its derivative, *Math. Inequal. Appl.* **7(3)**, 379-391, (2004).
5. Dewan, K. K., Abdullah Mir., Naresh Singh., Bhat, A. A.,: Some inequalities for polar derivative of a polynomial, *Southeast Asian Bulletin of Math.* **34**, 69-77, (2010).
6. Khojastehnezhad, E., Bidkham, M.,: Inequalities for the polar derivative of a polynomial with S-fold zeros at the origin, *Bull. Iranian Math. Soc.* **43(7)**, 2153-2167, (2017).
7. Laguerre, E.,: "Oeuvres", *1 Gauthier-villars, Paris.* (1898).
8. Malik, M. A.,: On the derivative of a polynomial, *J. London Math. Soc.* **1**, 57-60, (1969).
9. Marden, M.,: Geometry of the zeros of polynomials in a complex variable, *Math. Surveys, No.3. Amer. Math. Soc.* providence, R.I., (1949).
10. Pólya, G., Szegö, G.,: Aufgaben and Lehratze ous der Analysis, *Springer-Verlag, Berlin.* (1925).
11. Shah, W. M.,: A generalization of a theorem of Paul Turán, *J. Ramunujan Math. Soc.* **1**, 67-72, (1996).
12. Turán, P.,: Über die ableitung von polynomen, *Compositio Math.* **7**, 89-95, (1939).

Modified E-VIKOR method for decision making problem based on hesitant fuzzy set

Biplab Singha[1,2] Mausumi Sen[1] and Nidul Sinha[1]

[1] National Institute of Technology Silchar, India
[2] sbiplab217@gmail.com

Abstract. VIKOR method is applied in decision making problems to assign the ranks of the alternatives. VIKOR method is based on compromise programming method where decision makers are unable to decide which is the best solution of a particular situation. Then the decision makers come out with two best solutions using VIKOR method which are said to be the compromise solutions of the problem. Since these two best solutions are going to be accepted for the particular problem so the compromise solutions should come together whenever ranking is concerned. Modified E-VIKOR method is introduced which overcomes the limitations and have shown that in any situation compromise solutions always come together with a satisfactory result.

Keywords: Fuzzy set · Hesitant Fuzzy Set · VIKOR method · Modified E-VIKOR method.

1 Introduction

VIKOR method is very effective tool to deal with the situations where decision makers face problems and can not reach to a final solution. VIKOR method helps experts to obtain a compromise solution and this solution is considered to be the final consideration. This method is based on ranking of the alternatives and from this ranking the top alternatives are considered to be the compromise solution. VIKOR method a ranking based method and also in MCDM problems with great interest. The extension of VIKOR method is studied by many researchers and applied in many directions with successful results. Opricovic and Tzeng [7] compared TOPSIS and VIKOR method. VOKOR method is extended by Sayadi et. al. [5] using interval numbers. Sanayei et. al. [9] developed a new method of supply chain system using fuzzy VIKOR method. Chen and Wang [8] used this method to get best solution. After that Vahdani [6] developed interval-valued fuzzy VIKOR method. Torra and Narukawa [2] and Torra [3] contributed hesitant fuzzy set where experts assign more than one membership values. Zhang and Wei [4] extended VIKOR method in MCDM problems.
In this paper we have extended the paper presented by Zhang and Wei [4] and have shown that the proposed method can easily handle the compromise solutions. In real life some situations are arose where decision makers fail to achieve the best alternative, so they prefer to choice the compromise solution. The earlier VIKOR methods are complicated and lots of calculations are required to achieve a compromise solution. To avoid this complex calculation the modified E-VIKOR method is developed so that

one can attain the compromise solution easily. Through the proposed method we have shown that the compromise solutions are always come together with less calculations. We organize the paper using the following sections: Section 2 consists of the preliminaries idea of hesitant fuzzy set theory and the VIKOR method. In section 3, the proposed modified E-VIKOR method is studied with application. Section 4 concludes the paper.

2 Preliminaries

Definition 1 *[2]*

Let Y be s set of universe, if each and every element of Y has a set of membership values between $[0, 1]$ through a function then mathematically we define a hesitant fuzzy set A as

$$A = \{< x, h_A(x) > |x \in X\}.$$

where $h_A(x)$ defines hesitant fuzzy elements.

Example 1

Let $Y = \{y_1, y_2, y_3\}$ be a set of three students under consideration. Also let $h_A(y_1) = \{.4, .5, .6\}$, $h_A(y_2) = \{.2, .3, .5\}$, $h_A(y_3) = \{.7, .8, .9\}$ denote the membership degree sets of $y_i(i = 1, 2, 3)$ according to their height to the set A respectively. Consider the membership value of the height 6 ft is $\{1\}$ and that of the value 5 ft is $\{0\}$. Then A is an HFS, namely

$$A = \{< y_1, \{.4, .5, .6\} >, < y_2, \{.2, .3, .5\} >, < y_3, \{.7, .8, .9\} >\}.$$

2.1 VIKOR method

The VIKOR method is a ranking based method where the decision makers fail to achieve a final result, so they prefer a compromise solution using L_p- metric from which the VIKOR method is developed.

$L_{p,i} = \{\sum_{j=1}^{n} [\frac{w_j(k_j^* - k_{ij})}{k_j^* - k_j^-}]^p\}^{1/p}$; $1 \leq p \leq \infty$

where S_i and R_i are $L_{1,i}$ and $L_{\infty,i}$ respectively, j^{th} criterion functional value is k_{ij} for the alternative E_i and total criteria is n [4].

3 Modified E-VIKOR method

VIKOR method helps decision makers to reach the best solution of a problem effectively. Through VIKOR method decision makers get a compromise solution of that problem and with the help of that compromise solution they can able to attain the result easily. Nian Zhang et. al. [4] have shown that compromise solution may not always come together whenever ranking is concerned. In this paper, E-VIKOR method is modified to handle the compromise solution accurately and have shown that in any situation

Table 1: Decision Matrix

Alternative	Criteria			
E_i	G_1	G_2	...	G_n
E_1	g_{11}	g_{12}	...	g_{1n}
E_2	g_{21}	g_{22}	...	g_{2n}
...	...	...	...	...
E_m	g_{m1}	g_{m2}	...	g_{mn}

compromise solution always come together. The following decision matrix in Table 1 gives the idea to solve the problem comfortably:

where $E_1, E_2, ..., E_m$ and $G_1, G_2, ..., G_n$ are possible alternatives and criteria respectively. g_{ij} is the hesitant fuzzy elements of alternative E_i with respect to criteria G_j. Also $g_{ij} = (g_{E(x)})_{ij}$ and w_j is the weight of criterion G_j.

3.1 Algorithm of modified E-VIKOR method

The modified E-VIKOR method consists of the following steps:
Step 1. Positive ideal solution (PIS) and the negative ideal solution (NIS) are defined as:

$E^* = \{g_1^*, g_2^*, ..., g_n^*\}$,

where $g_j^* = \bigcup_{i=1}^{m} g_{ij} = \bigcup_{\gamma_{1j} \in g_{1j}, \gamma_{2j} \in g_{2j}, ..., \gamma_{mj} \in g_{mj}} \max\{\gamma_{1j}, \gamma_{1j}, ..., \gamma_{1j}\};\ j = 1, 2, ..., n$

$E^- = \{g_1^-, g_2^-, ..., g_n^-\}$,

where $g_j^- = \bigcap_{i=1}^{m} g_{ij} = \bigcup_{\gamma_{1j} \in g_{1j}, \gamma_{2j} \in g_{2j}, ..., \gamma_{mj} \in g_{mj}} \min\{\gamma_{1j}, \gamma_{1j}, ..., \gamma_{1j}\};\ j = 1, 2, ..., n$

Step 2. In this step, compute S_i and R_i as below:

$$S_i = \sum_{j=1}^{n} \frac{w_j(g_j^* - g_{ij})}{g_{ij} + g_j^-},\ i = 1, 2, ..., m$$

$$R_i = \max_j \frac{w_j(g_j^* - g_{ij})}{g_{ij} + g_j^-} \times \min_j \frac{w_j(g_j^* - g_{ij})}{g_{ij} + g_j^-}\ i = 1, 2, ..., m.$$

Step 3. Compute the values $Q_i (i = 1, 2, ..., m)$, by the following relations:

$$Q_i = t\frac{S_i - S^*}{S^- + S^*} + (1 - t)\frac{R_i - R^*}{R^- + R^*}$$

where $S^* = \min_i S_i, \quad S^- = \max_i S_i.$

$R^* = \min_i R_i, \quad R^- = \max_i R_i.$

here "the majority of criteria" in terms of weight is t , suppose $t = 0.5$.
Step 4: S, R and Q are arranged in decreasing order and ranking is done according to their values.
Step 5. The compromise solution E' and E'' are always come together, where E' and

E'' are the best and second best ranked by the measure Q and also E'' must be the best ranked by S or/and R.
When $t > 0.5$, "majority supports", $t = 0.5$, it is "consensus" and when $t < 0.5$, it is "veto".

3.2 Numerical Example: [4]

Table 2: Hesitant Fuzzy Decision Matrix

Alternatives	G_1	G_2	G_3	G_4
E_1	{0.2, 0.4, 0.7}	{0.2, 0.6, 0.8}	{0.2, 0.3, 0.6, 0.7, 0.9}	{0.3, 0.4, 0.5, 0.7, 0.8}
E_2	{0.2, 0.4, 0.7, 0.9}	{0.1, 0.2, 0.4, 0.5}	{0.3, 0.4, 0.6, 0.9}	{0.5, 0.6, 0.8, 0.9}
E_3	{0.3, 0.5, 0.6, 0.7}	{0.2, 0.4, 0.6}	{0.3, 0.5, 0.7, 0.8}	{0.2, 0.5, 0.6, 0.7}
E_4	{0.3, 0.5, 0.6}	{0.2, 0.4}	{0.5, 0.6, 0.7}	{0.8, 0.9}

Using modified E-VIKOR method, the following steps give the solution of the problem:
Step 1. Positive ideal solution and the negative ideal solution is to be defined as follows:
$E^* = \{g_1^*, g_2^*, ..., g_n^*\}$ = $\{0.900, 0.800, 0.900, 0.900\}$
$E^- = \{g_1^-, g_2^-, ..., g_n^-\}$ = $\{0.200, 0.100, 0.200, 0.200\}$

Step 2. In this step, compute S_i and R_i as below:

$$S_1 = \frac{w_1(g_1^* - g_{11})}{g_{11} + g_1^-} + \frac{w_2(g_2^* - g_{12})}{g_{12} + g_2^-} + \frac{w_3(g_3^* - g_{13})}{g_{13} + g_3^-} + \frac{w_4(g_4^* - g_{14})}{g_{14} + g_4^-} = 0.519,$$

$S_1 = 0.519$, $S_2 = 0.616$, $S_3 = 0.606$, $S_4 = 0.578$

$$R_1 = \max_4[\frac{w_1(g_1^* - g_{11})}{g_{11} + g_1^-}, \frac{w_2(g_2^* - g_{12})}{g_{12} + g_2^-}, \frac{w_3(g_3^* - g_{13})}{g_{13} + g_3^-}, \frac{w_4(g_4^* - g_{14})}{g_{14} + g_4^-}] \times \min_4[\frac{w_1(g_1^* - g_{11})}{g_{11} + g_1^-}, \frac{w_2(g_2^* - g_{12})}{g_{12} + g_2^-}, \frac{w_3(g_3^* - g_{13})}{g_{13} + g_3^-}, \frac{w_4(g_4^* - g_{14})}{g_{14} + g_4^-}] = 0.012$$

$R_1 = 0.012$, $R_2 = 0.026$, $R_3 = 0.015$, $R_4 = 0.006$
Step 3. Let $v = 0.5$, compute the values $Q_i (i = 1, 2, 3, 4)$:
$Q_1 = 0.094$, $Q_2 = 0.355$, $Q_3 = 0.179$, $Q_4 = 0.026$
Step 4. According to the values of S, R and Q rank the alternatives in decreasing order, which is given in Table 3.
Step 5. $@_1, @_4$ is the compromise solution and always come together whenever ranking is concerned.
Rank the alternatives $E_i (i = 1, 2, 3, 4)$ according to the values S_i, R_i and Q_i as the weight t changes, which is depicted in Table 4, along with compromise solution.

Table 3: The ranking and the compromise solutions

	E_1	E_2	E_3	E_4	Ranking	Compromise solution
S	0.519	0.616	0.606	0.578	$@_1 > @_4 > @_3 > @_2$	$@_1, @_4$
R	0.012	0.026	0.015	0.006	$@_4 > @_1 > @_3 > @_2$	$@_4, @_1$
$Q(t = 0.5)$	0.094	0.355	0.179	0.026	$@_4 > @_1 > @_3 > @_2$	$@_4, @_1$

Table 4: S, R and $Q(t_i)$ values obtained by the weight t changes and the compromise solutions

	v	E_1	E_2	E_3	E_4	Ranking	Compromise solution
S		0.519	0.616	0.606	0.578	$@_1 > @_4 > @_3 > @_2$	$@_1, @_4$
R		0.012	0.026	0.015	0.006	$@_4 > @_1 > @_3 > @_2$	$@_4, @_1$
	0	0.188	0.625	0.281	0	$@_4 > @_1 > @_3 > @_2$	$@_4, @_1$
	0.1	0.169	0.571	0.261	0.005	$@_4 > @_1 > @_3 > @_2$	$@_4, @_1$
	0.2	0.150	0.517	0.240	0.010	$@_4 > @_1 > @_3 > @_2$	$@_4, @_1$
	0.3	0.132	0.463	0.220	0.016	$@_4 > @_1 > @_3 > @_2$	$@_4, @_1$
	0.4	0.113	0.409	0.199	0.021	$@_4 > @_1 > @_3 > @_2$	$@_4, @_1$
$Q(t)$	0.5	0.094	0.355	0.179	0.026	$@_4 > @_1 > @_3 > @_2$	$@_4, @_1$
	0.6	0.075	0.301	0.159	0.031	$@_4 > @_1 > @_3 > @_2$	$@_4, @_1$
	0.7	0.056	0.247	0.138	0.036	$@_4 > @_1 > @_3 > @_2$	$@_4, @_1$
	0.8	0.038	0.193	0.118	0.042	$@_1 > @_4 > @_3 > @_2$	$@_1, @_4$
	0.9	0.019	0.139	0.097	0.047	$@_1 > @_4 > @_3 > @_2$	$@_1, @_4$
	1	0	0.085	0.077	0.052	$@_1 > @_4 > @_3 > @_2$	$@_1, @_4$

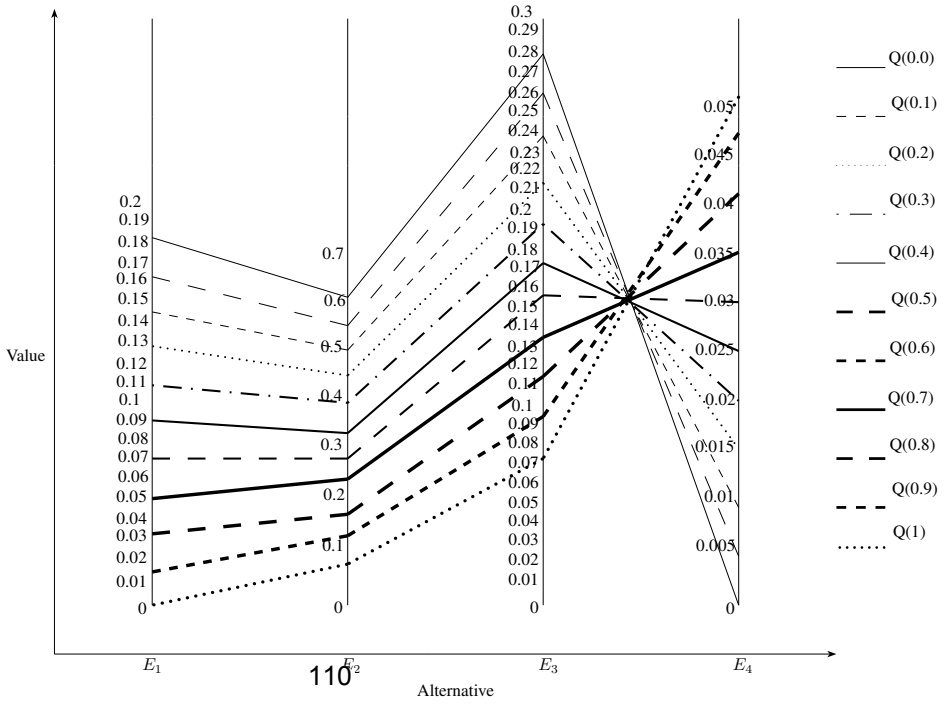

Fig 1. gives the idea of same distribution when $t \leq 0.5$ or $t \geq 0.5$ and when t increases the $Q(t_i)$ values change with same rate.
Modified E-VIKOR method is defined in such a way that the compromise solution never go beyond of each other i.e. compromise solution always come together.

4 CONCLUSION

Hesitant fuzzy set is an effective tool for the situation when decision makers are in hesitant mood. VIKOR method is developed when decision makers are unable to reach to a definite solution. This method helps us to get a compromise solution so that at least an approximate solution can be achieved comfortably. In this paper modification of E-VIKOR method is done and have shown that compromise solution always come together whenever ranking is considered. Since compromise solution gives the final result of the problem that is why their position should be the best or second best in the ranking list. At last with the help of an example, alternatives are ranked and have shown that compromise solution come together whenever "the maximum group utility" is considered in a hesitant situation.

References

1. K. Atanassov, Intuitionistic fuzzy sets, Fuzzy Sets Syst, 20 (1) 87-96 (1986).
2. V. Torra, Y. Narukawa, On hesitant fuzzy sets and decision, The 18th IEEE International Conference on Fuzzy Systems Jehu Island, Korea, 1378-1382 (2009).
3. V. Torra, Hesitant fuzzy sets, International Journal of Intelligent Systems, 25 529-539 (2010).
4. N. Zhang, G. Wei, Extension of VIKOR method for decision making problem based on hesitant fuzzy set, Applied Mathematical Modelling, 37 4938-4947 (2013).
5. M. K. Sayadi, M. Heydari, K. Shahanaghi, Extension of VIKOR method for decision making problem with interval numbers, Appl. Math. Model, 33 2257-2262 (2009).
6. B. Vahdani, H. Hadipour, J. S. Sadaghiani, M. Amiri, Extension of VIKOR method based on interval-valued fuzzy sets, Int. J. Adv. Manuf. Technol., 47 1231-1239 (2010).
7. S. Opricovic, G. H. Tzeng, Compromise solution by MCDM methods: a comparative analysis of VIKOR and TOPSIS, Eur. J. Oper. Res., 156 445-455 (2004).
8. L. Y. Chen, T. C. Wang, Optimizing partners' choice IS/IT outstanding projects: the strategic decision of fuzzy VIKOR, Int. J. Prod. Econ., 120 233-242 (2009).
9. A. Sanayei, S. Farid Mousavi, A. Yazdankhah, Group decision making process for supplier selection with VIKOR under fuzzy environment, Expert Syst. Appl., 37 24-30 (2010).
10. J. San Cristobal, Multi-criteria decision-making in the selection of a renewable energy project in Spain: the VIKOR method , Renew. Energy, 36 498-502 (2011).
11. M. Xia, Z. Xu, Hesitant fuzzy information aggregation in decision making, International Journal of Approximate Reasoning, 52 395-407 (2011).
12. Z. Xu, Hesitant Fuzzy Sets Theory, (2014).
13. L. Zadeh, Fuzzy Sets, Inf.Control, 8 338-353 (1965).

Modelling of Permeability and Clogging Retention in Pervious Concrete Pavement

Abhay Kandpal*, Barnali Debnath!, and Partha Pratim Sarkar$
Department of Civil Engineering, NIT Agartala, Agartala, India - 799046
Email: *abhaykandpal95@gmail.com, !brnali540@gmail.com, and
$ ps_partha@yahoo.com

Abstract. — Pervious concrete pavement has large pores or interconnected voids which gives it an ability to pass water through it. Due to its open porous structure, the stormwater can be drained off directly to the groundwater and thus pervious concrete act as a sustainable urban drainage system and an eco-friendly pavement option. However, these overall benefits get badly hampered due to the clogging of the exposed pores in the pervious concrete which simultaneously reduces the infiltration rate. Clogging in pervious concrete mainly occurs due to the contaminant of stormwater with dirt, debris or organic materials which get trapped into the pores and hinders the flow of water. This study mainly aims to find out a mathematical relationship between the permeability and the percentage of clogging retention in pervious concrete mixes made with over burnt brick aggregate. Due to the unavailability of natural stone aggregate, the locally available brick aggregate is chosen in this study to check its suitability as an alternate pavement material. Different sizes of aggregates were used in this study showing three different aggregate gradation such as G-1 (12.5 mm - 9.5 mm), G-2 (9.5 mm - 4.75 mm), and G-3 (13.2 mm – 12.5 mm). Water to cement (w/c) ratio of 0.3 and 0.32 was chosen from a variety of other w/c ratios for the optimum result. Clogging material such as silty sand, sand and clay was added at a percentage of 20, 40, 60, 80 and 100 by weight to the casted samples. Permeability was evaluated using a falling head permeability set up, and the clogging retention was obtained by estimating the change of mass of the specimens before and after testing. The outliers were removed from the obtained results, and the final results were used for the statistical analysis. Two-way ANOVA test was performed to check the statistical significance among the variables. Then the regression analysis was performed to obtain the relationship between the permeability and clogging retention. The proposed equation will be helpful to facilitate proper maintenance and de-clogging of existing pervious concrete pavement. The results also showed that clay has an austere impact on the permeability of pervious concrete than that of silty sand and sand.

Keywords: ANOVA · clogging · pervious concrete · regression.

1 Introduction

Pavement system constituting about 30-40 percent of the total urban fabric have converted pervious natural ground into an impervious system which has created a negative

impact on the environment. These impacts can be broadly categorized into hydrological aspect, environmental aspect, and temperature in the surrounding ambiance. About the hydrological aspects, the existing dense pavement system, being impervious in nature, reduce the groundwater recharge and increase the quantity of runoff which may create flood like situation in low lying areas. About the temperature in the surrounding ambiance, impervious pavement system act as a heat storage media that store heat and release it back to the atmosphere, increasing ambient temperature by 2-6 degree Celsius compared to surrounding rural temperature. This has created a phenomenon termed urban heat island (UHI) [1]. The Conventional pavement was designed for the vehicular purpose but to reduce the effect of urbanization on pavement related issues; there is a definitive need to adopt environmentally sustainable strategies that can serve both road user and the environment. For solving this, pervious pavement is intentionally designed such that a network of the interconnected void has existed and this can be done by gap grading the coarse aggregate and either eliminating or minimizing the fine aggregate in the concrete mix which allows the fluid to pass through the concrete structure. Pervious pavement fundamentally used in car parks, pedestrian footpath, cycle path, and other low traffic areas. The porosity of pervious pavement is typically 15-25%, and the permeability is typically about 2-6 cm/s [2] [3]. This results in the reduction of runoff volume and peak flow rates[4]. For example, annual runoff volume reductions of 50% to 100% have been observed[4] [5]. Further, the rough surface texture provides a good skid resistance riding surface even in the wet condition, reducing the surrounding urban air temperature by various mechanisms of heat transfer that may become future UHI mitigation strategy, it makes project economical (no need to provide side drainage). Impermeability is the major concern of the pervious pavement which is majorly due to the influx of the contaminated stormwater containing debris, dirt and organic matters. These foreign matters trapped in the pores of the structure leads to gradual reduction of drainage capacity of the pavement over the period. Hence such pavement required intermittent and frequent cleaning and maintenance. An in-situ infiltration rate test showed approximately 87% reduction of permeability after 3 years of construction [4]. A pervious concrete may be impractical for public streets under a load of clogging materials, and a good strategy may be feasible to minimize the surface clogging by suitable structural design, proper site locating and protecting the pavement using periodical maintenance[6]. It is found in previous researches that clogging of voids is independent upon the maximum aggregate size and design void in the mixture, but depends on the distribution and structure of the voids in the mix[7]. The pore structure features and porous behavior have a very substantial role in the pervious pavements as these pavements are expected to assist as a bi-functional pavement system – structural function and hydrological function. Moreover, the efficacy of the hydrological functioning of pervious pavements is getting abridged due to continuous clogging. The clogging in the permeable pavement can be addressed as physical clogging, chemical clogging and biological clogging [8]. The process of clogging is time-dependent in nature, and this can be attributed as a slow siltation process which includes cyclic deposition of clogging material and rapid siltation process which is caused by sudden slump deposition or landslide[9]. Xinzhuang et al.[10] have developed a real-time simulation system for clogging and reported that the clogging process completes in three phases viz. quick

clogging, temporary mitigation of clogging and progressive clogging. Many types of research have been conducted on both pervious concrete and porous asphalt pavements to accumulate in-situ clogging behavior and the variability of hydraulic conductivity with different clogging materials. Permeability prediction with sand and very fine sand shows that clogging relatively reduces the infiltration rate[2], but in another study, it has seen that clay (montmorillonite) causes approximately ten times more clogging than sand per mass [12]. Another study was carried out with bentonite and kaolinite clay under extreme conditions and results obtained after a series of clogging cycles indicated that the surface layer became a nearly impenetrable barrier[11]. Kevern et al. [13]However, most of the previous researches were based on the mechanism of clogging, type of clogging or type of clogging materials. A research was done to find the mechanism of sediment clogging in the pores of pervious concrete pavement under surface runoff. Previous studies suggest that the retention of sand-sized materials does not result in significant clogging [14] [15]. In contrast, retention of fines (i.e., silt and clay size materials) is a far greater concern [11] [16]. This study mainly aims to find out a mathematical relationship between the permeability and the percentage of clogging retention in pervious concrete mixes made with over burnt brick aggregate. This mathematical relationship will help in identifying the period afterward maintenance for the pavement is required, and the life of the pervious concrete pavement can be enhanced.

2 Experimental Program

In this section, we recall some related definitions as ready references for the present work.

2.1 Materials Due to the unavailability of natural stones in North-Eastern India, over burnt brick aggregate (OBBA) is used in this study as a replacement of stone aggregate. Three single sizes aggregate grading were used in this study as shown in Table I. The physical properties of OBBA is shown in Table II. Locally available sand of zone IV[17] is also added with coarse aggregate at a percentage of 10% by weight of the coarse aggregate. The binding material used in this study was ordinary Portland cement (OPC) of 43 grade conforming to[18].

Table 1: Different Size of aggregate used.

Grade Designation	*Range of Size*
G-1	12.5mm - 9.5mm
G-2	9.5mm - 4.75mm
G-3	13.2mm - 12.5mm

Table 2: Physical index of OBBA.

Test	*Result*
Specific Gravity	1.9
Water Absorption(%)	7.3
Impact Value(%)	36.6
Crushing Value(%)	38.7
Abrasion Value(%)	43.95
Flakiness Index(%)	41.4
Elongation Index(%)	36.4

2.2 Sample Preparation Cylindrical Mould of height 200 mm and 100 mm diameter was used to prepare the samples of pervious concrete pavement. Another perfect cube mould of dimensions 150 mm was used to find the compressive strength of pervious pavement. The OBBA used for casting was properly washed by water and air dried before mixing so that the fines attached over the surface were washed out. The optimum water-cement ratio of (0.3, 0.32) obtained from the various test was used for the preparation of samples. The samples were demoulded after 24 hrs and placed in curing tank for 28 days. Similarly, the above method was used for preparation 90 samples of pervious pavement.

2.3 Clogging Materials In order to analysis, the effect of clogging retention on pervious concrete mix, three different types of soil samples were used in this study. Clayey soil, silty sand, and sandy soils were collected from the locally available field which was treated as the clogging materials. The grain size distribution of three types of soils is shown in Fig. 1.

2.4 Evaluation of Permeability Permeability is the ability of any system by which the system is to allow the fluid to flow through itself. Variable head permeability method was used to determine the hydraulic conductivity of the pervious concrete specimens. The detailed of the test apparatus was shown in Fig. 2. In this test, freeflowing water was allowed to flow through the pervious pavement. The samples coated with duct tape and the joints between the sample and the mould were sealed with a locally available sealant to prevent any leakage of water. The water head was noted before and after the test. The time taken for the head to become h2 from h1 was noted by stopwatch. The coefficient of permeability (k) was calculated using Darcy's law as (1),

$$k = 2.303 \, \frac{al}{At} \, log_{10} \frac{h_1}{h_2} \tag{1}$$

where, a = area of water tube, A = area of the sample, l = length of the sample, h1 = initial head, h2 = final head, t = time taken to reach water level from h1 to h2.

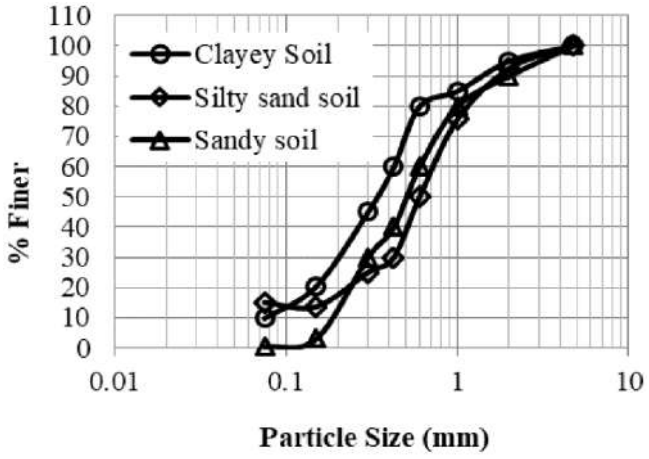

Fig. 1: Grain size distribution of Clogging Material.

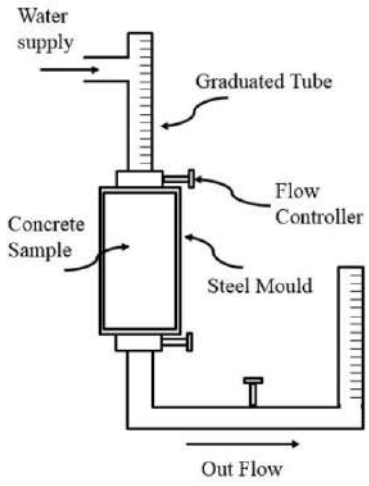

Fig. 2: Schematic diagram of the permeability test setup.

3 Result And Discussion

3.1 Effect of gradation on permeability and clogging retention The permeability of pervious pavement is proportional to the size of the flow passage and porosity of the pervious medium. The size of flow passage and porosity depends upon the structural arrangement of the aggregate. Different gradation (G-1, G-2, G-3) having size 9.5 mm to 12.5 mm, 4.75 mm to 9.5 mm, 13.2 mm to 12.5 mm, respectively used for preparing samples. The nature of permeability changes as the gradation size varies. Smaller aggregate size cause to restrict the water flow through the flow passage, hence permeability gets decreased due to the increase in the resistance offered against the surface

of small size aggregate (having high specific surface area) as shown in Fig. 4 (a)-(b) Clogging retention increases due to the small size of the flow channel which causes to easily trap the soil grain present in the influx of contaminated water.

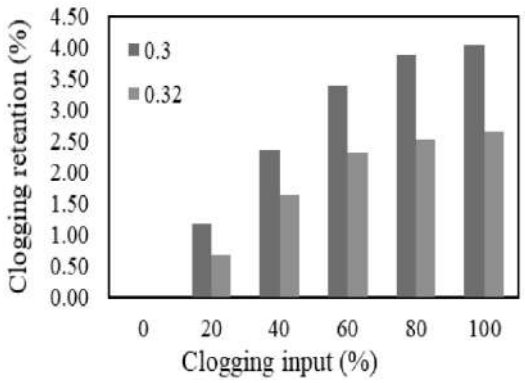

Fig. 3: Variation of clogging retention with different w/c ratio.

3.2 Effect of water/cement ratio on permeability and clogging retention Lesser the w/c ratio more resistance will be offered by the aggregate when compacting and thus it causes to have more pores due to which the permeability is high, but the compressive strength is comparatively low. As the w/c ratio is increased, it improves the workability of the pervious pavement due to excess water present in the mix which caused to ease the compaction, subsequently causing a reduction in the permeability and increase in the compressive strength. A series of compressive strength tests were performed in cube samples with various water-cement ratio ranging from 0.28 to 0.35. From the tests, an optimum range of water-cement ratio was selected (w/c = 0.3 and 0.32). The clogging tests were performed for every aggregate and soil gradation at a water-cement ratio of 0.3 and 0.32. The nature of percentage clogging retention was increased with increase in percentage clogging input, but the increase of clogging retention at w/c ratio of 0.3 was comparatively more than w/c ratio of 0.32 (Fig. 3).

3.3 Effect of clogging materials on permeability and clogging retention Three different clogging material was used in this study. Silty sand, sandy soil and clayey soils were put in the samples at various percentages, and the permeability and the clogging retention were checked. Fig. 4-6 is showing the changes in the permeability and clogging retention in different clogging materials for silty sand, sand and clay, respectively. It has been observed from the figure that the finer material exhibits deeper penetration and shows higher clogging retention compared to the coarse-grained soil.

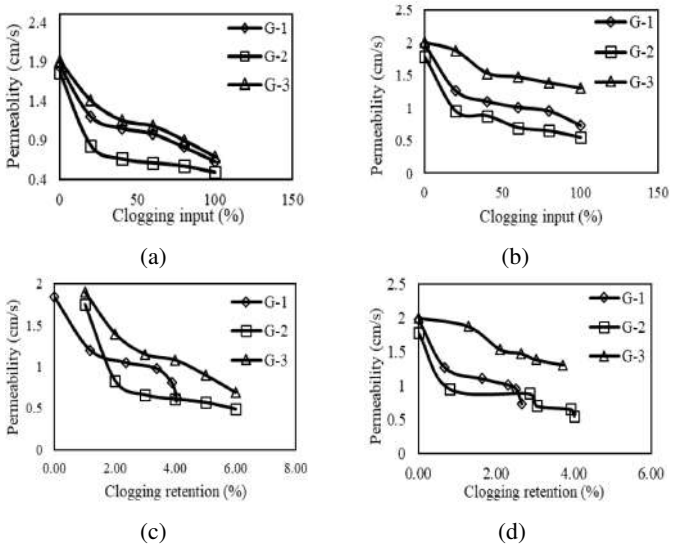

Fig. 4: Clogging material is silty sand: Permeability vs Clogging input (a) 0.3w/c ratio; (b) 0.32 w/c ratio; Permeability vs clogging retention (c) 0.3 w/c ratio; (d) 0.32 w/c ratio.

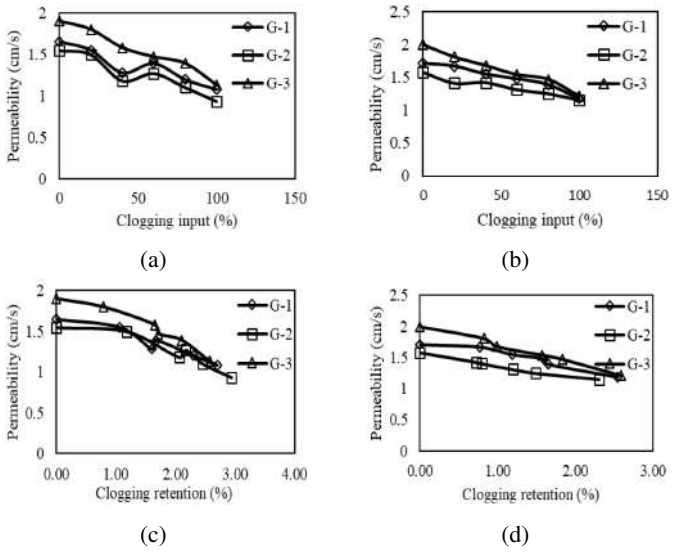

Fig. 5: Clogging material is sand: Permeability vs Clogging input (a) 0.3w/c ratio; (b) 0.32 w/c ratio; (c) Permeability vs clogging retention (c) 0.3 w/c ratio; (d) 0.32 w/c ratio.

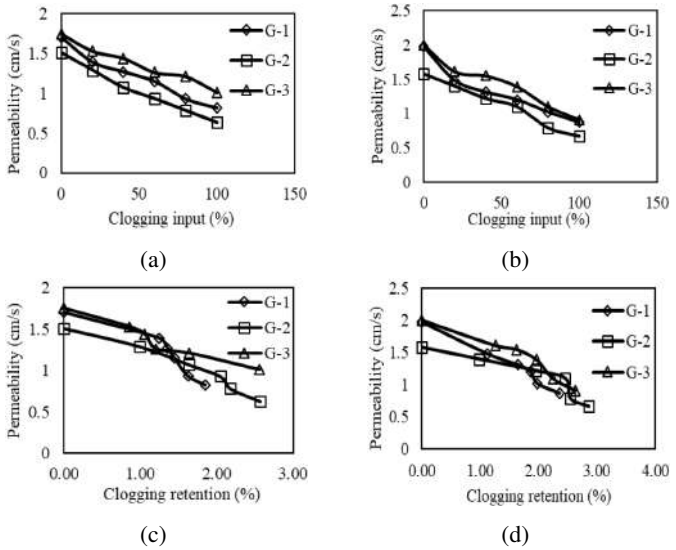

Fig. 6: Clogging material is clay: (a) Permeability vs Clogging material of 0.3w/c ratio; (b) 0.32 w/c ratio; (c) Permeability vs clogging retention of 0.3 w/c ratio; (d) 0.32 w/c ratio.

4 Mathmatical Modelling

The data collected from the experimental tests are utilized for the statistical analysis. After the collection of data, integrity and consistency were checked, and the outliers were removed. Outliers are those data that show an extreme deviation from the mean of the sample data which may arise due to systematic/non-systematic errors. Several methods are there to detect the outliers such as boxplot, Z-score or clustering. In this study, the boxplot method was adopted for finding out the outliers. Once the data are finalized, the statistical significance between the coefficient of permeability and clogging retention was checked through one-way ANOVA test for 95% confidence level. Table III shows that the null hypotheses expressing the equality of the mean of permeability associated with clogging retention were rejected, i.e., the p-value is less than 0.05. In order to develop the mathematical relationship between permeability and clogging retention, regression analysis was performed. For each type of soils, different regression equations are obtained, and the relationship between the permeability and clogging retention is developed. The relation between permeability and clogging retention for various types of soils are tabulated in Table IV. Fig. 7-9 is showing the variation of the predicted model and the calculated permeability results. The figures depict that the predicted model for the permeability fitted well with the experimental test results.

Table 3: One-way ANOVA for different clogging material.

Type of Soil	*Sum of Squares*		*Df*	*Mean Square*	*F*	*Sig.*
Clayey soil	Between groups	3.960	29	0.137	3.907	0.041
	Within groups	0.999	6	0.035		
	Total	4.169	35			
Sandy Soil	Between groups	2.074	29	0.094	2.83	0.047
	Within groups	0.183	6	0.026		
	Total	2.256	35			
Sandy Silt	Between groups	7.314	30	0.244	23.84	0.001
	Within groups	0.051	5	0.01		
	Total	7.365	35			

Table 4: One-way ANOVA for different clogging material.

Type of soil	*Predicated equations*	
Sandy silt	k = 1.88 - 0.367 x C_R	$R^2 = 0.963$
Sandy soil	k = 1.93 - 0.327 x C_R	$R^2 = 0.952$
Clayey soil	k = 1.77 - 0.352 x C_R	$R^2 = 0.984$

5 Conclusion

This study mainly deals with the clogging potential of pervious concrete pavement. In this study, the influence of different mix variables on the permeability and clogging retention are checked. Moreover, then a mathematical relationship is drawn between the permeability and clogging retention of pervious concrete pavement. Based on the experimental tests, it is found that the size of aggregate has a drastic effect on clogging retention and permeability. Smaller size aggregate produces a smaller flow channel and hence clogging retention increases due to the small size of the flow channel which causes to easily trap the soil grain present in the influx of contaminated water. In the case of the water-cement ratio, the. The clogging retention at w/c ratio of 0.3 was comparatively more than that of w/c ratio of 0.32. The effect of the different size of clogging materials indicates that the finer the clogging material, more will be the clogging retention. From the statistical analysis, predicted equations are developed for every type of clogging materials. The proposed equation will be helpful to facilitate proper maintenance and de-clogging of existing pervious concrete pavement.

References

1. Golden, J. S., Kaloush, K. E.: Mesoscale and microscale evaluation of surface pavement impacts on the urban heat island effects. *International Journal of Pavement Engineering*, **7(1)**, 37–52, (2006).

2. Dean, S. W., Montes, F., Valavala, S., Haselbach, L. M.: A new test method for porosity measurements of Portland cement pervious concrete. *Journal of ASTM International*, **2(1)**, 12931, (2005).
3. Tennis, P.D., Leming, M.L. and Akers, D.J.: Pervious Concrete Pavements. Technical Report, EB30202. Portland Cement Association, Skokie, and National Ready Mixed Concrete Associated, Silver Spring, (2004).
4. Abbott, C. L., Comino-Mateos, L.: In-situ hydraulic performance of a permeable pavement sustainable urban drainage system. *Water and Environment Journal: The Journal*, **17(3)**, 187–190, (2003).
5. Legret, M., Colandini, V.: Effects of a porous pavement with reservoir structure on runoff water: Water quality and fate of heavy metals. *Water Science and Technology: A Journal of the International Association on Water Pollution Research*, **39(2)**, 111–117, (1999).
6. Schwartz, S. S.: Effective curve number and hydrologic design of pervious concrete storm-water systems. *Journal of Hydrologic Engineering*, **15(6)**, 465–474, (2010).
7. Król, J. B., Khan, R., Collop, A. C.: The study of the effect of internal structure on permeability of porous asphalt. *Road Materials and Pavement Design*, **19(4)**, 935–951, (2018).
8. Yong, C. F., McCarthy, D. T., Deletic, A.: Predicting physical clogging of porous and permeable pavements. *Journal of Hydrology*, **481**, 48–55, (2013).
9. Reiser, D. W., Ramey, M. P., Wesche, T. A.: Flushing Flows. In *Alternatives in Regulated River Management* (pp. 91–135). CRC Press, (2018).
10. Cui, X., Zhang, J., Huang, D., Tang, W., Wang, L., Hou, F.: Experimental simulation of rapid clogging process of pervious concrete pavement caused by storm water runoff. *International Journal of Pavement Engineering*, **20(1)**, 24–32, (2019).
11. Haselbach, L. M.: Potential for clay clogging of pervious concrete under extreme conditions. *Journal of Hydrologic Engineering*, **15(1)**, 67–69, (2010).
12. Coughlin, J. P., Campbell, C. D., Mays, D. C.: Infiltration and clogging by sand and clay in a pervious concrete pavement system. *Journal of Hydrologic Engineering*, **17(1)**, 68–73, (2012).
13. Kevern, J. T., Schaefer, V. R., Wang, K.: Evaluation of pervious concrete workability using gyratory compaction. *Journal of Materials in Civil Engineering*, **21(12)**, 764–770, (2009).
14. González-Angullo, N., Castro, D., Rodríguez-Hernández, J., Davies, J. W.: Runoff infiltration to permeable paving in clogged conditions. *Urban Water Journal*, **5(2)**, 117–124, (2008).
15. Haselbach, L. M., Valavala, S., Montes, F.: Permeability predictions for sand-clogged Portland cement pervious concrete pavement systems. *Journal of Environmental Management*, **81(1)**, 42–49, (2006).
16. Siriwardene, N. R., Deletic, A., Fletcher, T. D.: Clogging of stormwater gravel infiltration systems and filters: insights from a laboratory study. *Water Research*, **41(7)**, 1433–1440, (2007).
17. IS: 383 (2016). Coarse and Fine Aggregate for Concrete — specification, 3rd revision.
18. IS: 8112 (2013). Ordinary Portland Cement, 43 grade — specification, 2nd revision.

Multiscale Complexity Analysis of Cardiac Arrhythmia using Approximate Entropy and Recurrence Quantification Analysis

Vikramjit Singh[1][0000-0003-4843-0985], Dr. Amit Gupta[2] and Dr. J. S. Sohal[3]

[1] Research Scholar, Department of Electronics and Communication Engineering, I K G Punjab Technical University, Jalandhar
vikramkang@gmail.com

[2] Assistant Professor, Department of Electronics and Communication Engineering, I K G Punjab Technical University, Jalandhar

[3]Director, Ludhiana College of Engineering and Technology, Ludhiana, Punjab, India

Abstract. This paper evaluates the cardiac arrhythmia using an integrated approach based on approximate entropy (ApEn) and recurrence quantification analysis (RQA). The paper highlights the appropriate use of tolerance threshold, r_{opt} and embedding dimension, m of ApEn and RQA for the quantification of heart rate variability (HRV) of healthy and diseased patients. The paper uses publicly available MIT-BIH arrhythmic dataset along with normal sinus rhythm database for the study. It is found that (i) Mean RR of arrhythmic and healthier subjects appears to be similar and statistically insignificant ($p>0.05$) whereas SDNN significantly ($p<0.05$) and clearly stratifies the two groups of subjects, (ii) complexity quantified by ApEn appears to be lower in arrhythmic patients with value of 1.203±0.16 (mean ±SD) and 1.316 ± 0.31 (mean ± SD) respectively for arrhythmic patients and healthy subjects, with a p value <0.05, (iii) other ApEn indices such as R_{min} and R_D also significantly classifies arrhythmic and healthier subjects whereas R_{max} fails to provide such significant classification, (iv) % Recurrence appears to be 6% higher for normal sinus rhythm and is also statistically significant ($p<0.05$) (iv) Similar significant classification is provided other RQA indices like % determinism and % laminarity (v) Overall, in general, it is concluded in case of arrhythmia, complexity of HRV is reduced due to which non-linear ApEn and RQA based indices show significantly different results.

Keywords: Arrhythmia, Approximate Entropy, Recurrence quantification analysis, Heart rate Variability, Normal sinus rhythm

1 Introduction:

Cardiovascular system is a complex mechanism that work meticulously within a feedback loop known as baroreflex feedback. In this system, numerous subsystems interact

with each other at multiple temporal scales to keep the cardiovascular standards within safe thresholds. For the diagnosis and prognosis of this vital biological process, it is extremely important to study the underlying dynamics of the system. Autonomic nervous control system (ANS), which is responsible for the overall control of cardiovascular system [1–4], creates a balance between parasympathetic and sympathetic drives to so as to regulate the rate with which the heart beats. An index known as heart rate variability (HRV) has emerged as one of the most important non-invasive way to quantify the health of any individual[5–7]. The strength of the feedback involved in cardiovascular mechanism, known as Baroreflex sensitivity (BRS) provides the ability of cardiovascular system to adapt as per requirements[8–10]. The heart rate of the healthy individual is not purely regular and depends upon numerous factors such as exercise, mental stress, disease etc. Moreover, the beat-to-beat intervals also fluctuate due to respiration, thermoregulation, renin angiotensin system, blood pressure and many other hidden factors[11, 12]. Therefore, HRV of a healthy person is highly complex and hence high complexity is considered as marker of good cardiac health[13, 14].

Arrhythmia is the problem in the rhythm with which the heart beats. In Arrhythmia, the heart either beats slowly or very rapidly or follows an irregular pattern. Enhanced sympathetic drive or reduced parasympathetic drive leads to increase in the heart rate, whereas reduced sympathetic drive and enhanced parasympathetic drive decreases the heart rate. Overall in ANS, the inputs from both SNS and PNS, regulate the local atrial and ventricular function of the heart. So, suppression of control of any one of these nervous system controls may lead to irregular heart-beats or Arrhythmia. It is therefore very important to understand the behavior that the ANS plays in case of arrhythmia pathogenesis so as to prevent and treat the case of Arrhythmias[6, 17]

In past, researchers have used numerous non-linear methods such as approximate entropy (ApEn) [18, 19], sample entropy (SampEn) [20–22] and Recurrence quantification analysis (RQA)[23, 24] to quantify the HRV for healthy and diseased subjects. In this paper, a hybrid approach comprising of ApEn and RQA indices is used to quantify the complexity of HRV. The parameters such as tolerance threshold, r_{opt}, embedding dimension, m and data length, N, required to accurately compute ApEn and RQA are carefully chosen to avoid the biasness in the computation. The paper uses MIT-BIH Arrhythmia database[25–27] and normal sinus rhythm[28] database available at physionet.org[23, 28] to compute the ApEn and RQA indices.

2 Materials and methods

2.1 The MIT BIH Dataset

The MIT-BIH Arrhythmia database of arrhythmic inpatients (60%) and outpatients (40%) was recorded by Beth Israel Hospital Arrhythmia Laboratory between 1975 and 1979. The database contains ECG recording of 48 subjects each of about 30 minutes

duration. The recoded subjects include 26 men aged 32 to 89 years, and 22 women aged 23 to 89 years. Originally, the database was recoded in analog format and was later digitized at a sampling frequency of 360 samples per second per channel with 11-bit resolution over a 10mV range. Fig. 1 shows the HRV signal of a typical arrhythmic subject (100) from MIT-BIH dataset.

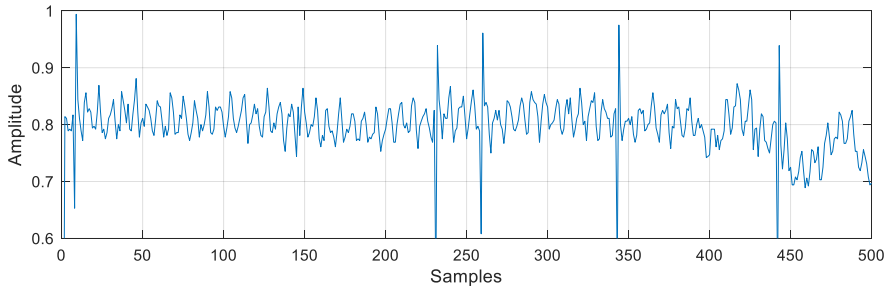

Fig. 1. HRV of typical arrhythmic subject (Record 100 of MIT-BIH dataset)

2.2 The normal sinus rhythm dataset

This database, available at physionet.org, consists 54 long term ECG recordings of subjects having no significant Arrhythmia that includes recording of 30 men aged 28.5 to 76, and 24 women, aged 58 to 73. The original recordings were in analog format which were later digitized at a sampling frequency of 128 samples per second.

2.3 Approximate entropy

Approximate entropy (ApEn), a method used to quantify similarity of the time series, is governed by input factors like tolerance threshold (r), embedding dimension (m) and data length (N). The calculation involves template matching derived from the given time series, $\{u(n): 1 \leq n \leq N\}$, where m is the derived template length, and r is the tolerance mismatch among various templates.

First, from the given series, templates, $v_1^m, v_2^m \cdots, v_{N-m+1}^m$ are created, where:

$$v_n^m = \{u(n), u(n+t), \ldots, u(n+(m-1))\} \text{ for } n = 1, 2, \ldots, N\text{-}m+1 \quad (1)$$

Then, the distance parameter (S), which defines the maximum norm distance, $\|.\|$, between two such templates, lying within r is computed as:

$$S_{np} = r \geq \|v_n^m - v_p^m\| \quad (2)$$

From this distance parameter, conditional entropy, $E_n^m(r)$ is formulated as

$$E_n^m(r) = {}^{S_{np}}/_{N+1-m} \quad (3)$$

ApEn is computed according to the equation;

$$\mathrm{ApEn}(m,r) = \left(\sum_{n=1}^{N-m+1} \ln\left(\frac{E_n^m(r)}{N-m+1}\right) \Big/ N-m+1\right) - \left(\sum_{n=1}^{N-m} \ln\left(\frac{E_n^{m+1}(r)}{N-m}\right) \Big/ N-m\right) \quad (4)$$

In this paper, r is optimally chosen as a value which corresponds to maximum approximate entropy ($ApEn_{max}$) [29] of the time series, as shown in Fig. 2, and is denoted as r_{opt}. The value of m is chosen as 2 [2] and N =300 [24] for appropriate computation of ApEn. Moreover, in this study, the biasness of ApEn, introduced due to self-matching templates, is reduced by excluding the self matches and as a correction strategy, the resultant indeterminate conditional probability $E_n^m(r)$ is substituted as 0.5 [2]

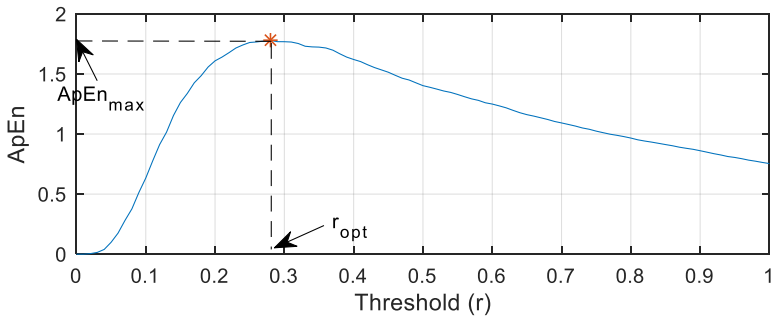

Fig. 2. ApEn calculated for range of tolerance threshold, r. r_{opt} corresponds to maximum ApEn, $ApEn_{max}$

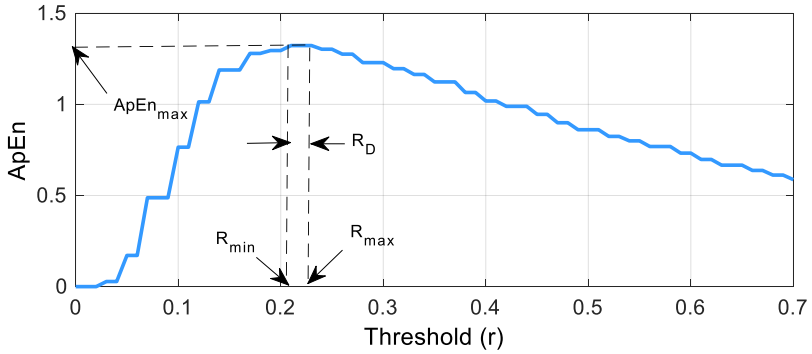

Fig. 3. Computation of R_D from HRV time series

While calculating ApEn of HRV, the r_{opt} often corresponds to the range of values within which $ApEn_{max}$ lies. This uncertainty plateau of r, in the computation of $ApEn_{max}$, is called as Radius differential (R_D) [24]. This paper utilizes R_D, minimum value of optimum threshold (R_{min}) and maximum value of optimum threshold (R_{max}) for the

classification of normal sinus rhythm and arrhythmic subjects. Fig. 3 shows the process of computation of R_D from HRV of an arrhythmic subject.

2.4 Recurrence quantification analysis

This technique is based on analysis of state space trajectory for the quantification of recurrence of events or samples in a system[30, 31]. The first step in RQA is the extension of S_{np} to two dimensional $M \times M$ matrix by expanding both n and p from 1 to M=N-m+1, to create a recurrence plot (RP). Fig. 4 shows the recurrence plot of HRV time series. The diagonal line shows the matching among same templates.

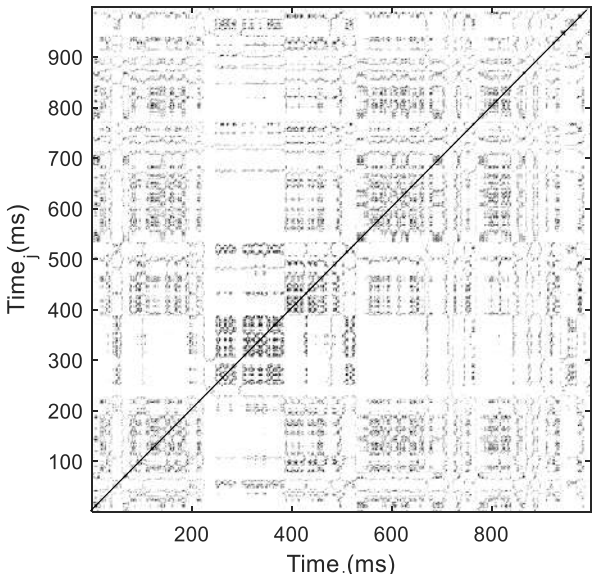

Fig. 4. Recurrence plot of HRV series. Diagonal line signifies self matches

Later the recurrence quantification analysis is performed over RP by calculating various indices such as percentage recurrence (%REC), percentage determinism (%DET), percentage laminarity (%LAM), and vertical line entropy (VEntr) etc. %REC is defined as density of recurrent points in RP, whereas %DET gives the ratio of such recurrent points that form diagonal lines. %DET quantifies the deterministic nature of the signal. Similarly, %LAM computes the ratio of recurrent points that form vertical lines and is used to measure randomness of the time series. Since, RQA is an extension to S_{np}, it also requires input parameters (r, m & N), like ApEn, to be fixed before computation of output indices. This paper uses same values of input parameters as fixed for ApEn

for the computation of RQA indices. This data driven strategy for computing r, ensures appropriate computation of RQA indices and restricts aberration.

3 Results and Discussion

This paper evaluates the effect of cardiac Arrhythmia on HRV using various standardized indices including descriptive and non-linear indices. Table 1 presents the mean and standard deviation (SD) of all such indices computed from arrhythmic and healthy subjects with normal sinus rhythm. Further, to assess the validity of results, statistical analysis test is performed for every index with a significance level of 0.05. Results indicate that the descriptive index, mean RR is statistically insignificant ($p>0.05$) to stratify the arrhythmic and healthy subjects whereas standard deviation of beat-to-beat interval (SDNN) significantly ($p<0.05$) classifies the problematic cases from healthy subjects. This is due to the fact, in case of arrhythmic subjects, autonomic control and baroreflex control reduces thus restricting the beat-to-beat variations, measured as SDNN.

Table 1. Mean and SD of various indices of Arrhythmia and normal sinus rhythm datasets

Measure	Arrhythmia		Normal Sinus rhythm (Healthy)		p-value
	Mean	SD	Mean	SD	
Mean RR	0.751	0.222	0.734	0.115	0.287
SDNN	0.083	0.074	0.135	0.252	<0.05
$ApEn_{max}$	1.203	0.160	1.366	0.313	<0.05
R_{min}	0.165	0.065	0.126	0.084	<0.05
R_{max}	0.190	0.080	0.201	0.113	0.210
R_D	0.025	0.0328	0.075	0.105	<0.05
%REC	2.737	0.864	2.919	1.387	<0.05
%DET	27.904	15.961	34.112	10.360	<0.05
%LAM	13.832	19.149	26.384	12.183	<0.05

For the calculation of ApEn and RQA related indices, m=2 and N=300 is used. The ApEn indices ($ApEn_{max}$, R_{min}, R_{max} and R_D) computed for arrhythmic and normal sinus rhythm is tabulated next to descriptive indices, in Table 1. Mean and SD of each of these indices along with their p values are depicted. Mean of $ApEn_{max}$ is lower for arrhythmic subjects than healthier subjects, indicating lower complexity. This also indicates the loss of baroreflex control in arrhythmic subjects thus making heart beat at a regular rhythm[32, 33].

These results can also be confirmed from Fig. 5, which shows box and whisker plot of the computed indices. Mean value of R_{min}, in comparison, appears higher for arrhythmic subjects and is statistically significant ($p<0.05$), whereas averaged R_{max} shows no difference among arrhythmic and normal sinus rhythm and is also statistically insignificant ($p>0.05$). Parameter R_D has a prominently higher mean value for the normal sinus rhythm and appears to be statistically significant. The stratifications provided by these ApEn indices highlight the changes in the underlying dynamics in arrhythmic subjects in comparison to their healthier counterparts.

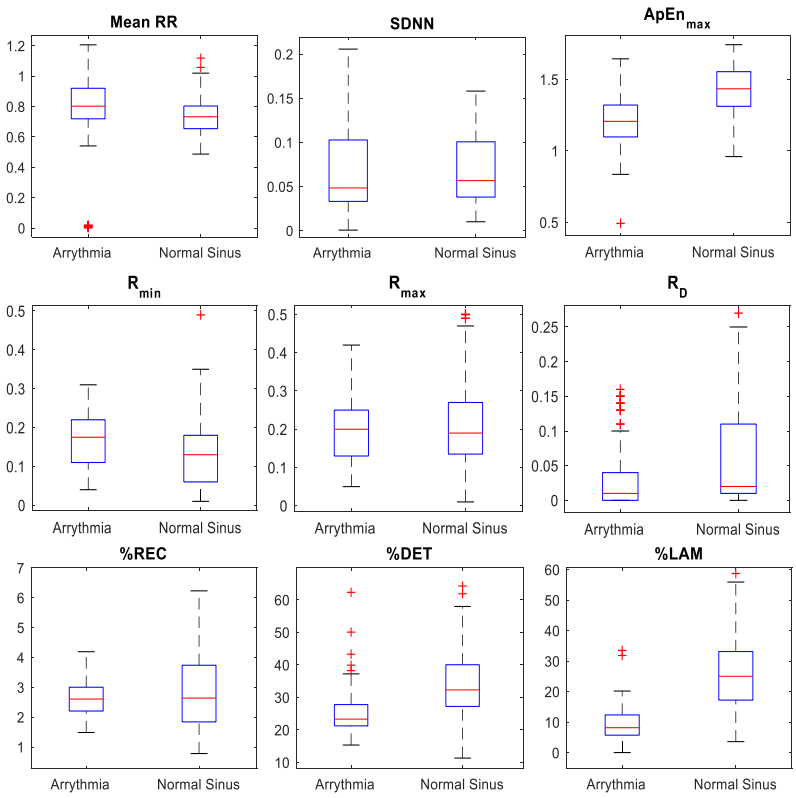

Fig. 5. Indices computed for HRV of Arrhythmia and normal sinus rhythm database

Further the RQA based indices are also computed for the two set of subjects. % REC appears to be 6% higher for healthier subjects than arrhythmic subjects and is also statistically significant. % DET shows a slight difference among healthier and arrhythmic subjects but results appear statistically significant. %LAM appear to be almost double for normal sinus rhythm than arrhythmic subjects and appear to be most prominent

marker among all indices. Overall RQA indices appear to be reliable classifiers to stratifying arrhythmic subjects.

4 Conclusion

The non-linear control mechanisms of ANS required to regulate the heart rate in the healthy human being. The paper uses linear descriptive indices along with non-linear ApEn and RQA indices to quantify the cardiovascular changes in the healthy and arrhythmic subjects. It is concluded that enhanced classification accuracy can be achieved by using non-linear indices, computed by optimal choice of tolerance threshold, r_{opt}. Non-linear indices such as, $ApEn_{max}$, R_{min}, $R_{D,}$ %REC, %DET, and %LAM significantly classify arrhythmic subjects whereas R_{max} fails to provide significant stratification. In future, these optimized non-linear indices can be used to diagnose and prognose cardiac health issues through intelligent machine learning algorithms.

5 Acknowledgements

The authors would like to thank the Department of Electronics and Communication Engineering, Inder Kumar Gujral Punjab Technical University, Jalandhar for its extended support that was helpful in compilation of this study.

References

1. Saini BS, Singh D, Uddin M, Kumar V (2008) Improved Power Spectrum Estimation for RR-Interval Time Series. Int J Electr Comput Eng 2:2108–2112
2. Singh A, Saini BS, Singh D (2016) An alternative approach to approximate entropy threshold value (r) selection: application to heart rate variability and systolic blood pressure variability under postural challenge. Med Biol Eng Comput 54:723–732. https://doi.org/10.1007/s11517-015-1362-z
3. Gierałtowski J, Hoyer D, Tetschke F, et al (2013) Development of multiscale complexity and multifractality of fetal heart rate variability. Auton Neurosci Basic Clin 178:29–36. https://doi.org/10.1016/j.autneu.2013.01.009
4. Hoyer D, Pompe B, Herzel H, Zwiener U (1998) Nonlinear Coordination of Cardiovascular Autonomic Control. IEEE Eng Med Biol Mag 17–21. https://doi.org/10.1109/51.731315
5. Singh M, Singh B, Banga VK, et al (2014) Effect of ECG Sampling Frequency on Approximate Entropy based. Int J Bio-Science Bio-Technology 6:179–186
6. Hohnloser SH, Klingenheben T, Zabel M, Yi Gang Li (1997) Heart rate variability used as an arrhythmia risk stratifier after myocardial infarction. PACE - Pacing Clin Electrophysiol 20:2594–2601. https://doi.org/10.1111/j.1540-8159.1997.tb06109.x
7. Sassi R, Cerutti S, Lombardi F, et al (2015) Advances in heart rate variability signal

analysis : joint position statement by the e-Cardiology ESC Working Group and the European Heart Rhythm Association co-endorsed by the Asia Pacific Heart Rhythm Society. Europace 17:1341–1353. https://doi.org/10.1093/europace/euv015

8. Orini M, Laguna P, Mainardi LT, Bailón R (2012) Assessment of the dynamic interactions between heart rate and arterial pressure by the cross time-frequency analysis. Physiol Meas 33:315–331. https://doi.org/10.1088/0967-3334/33/3/315
9. Laude D, Baudrie V, Elghozi JL (2009) Tuning of the sequence technique. IEEE Eng Med Biol Mag 28:30–34. https://doi.org/10.1109/MEMB.2009.934630
10. Laude D, Elghozi J-L, Girard A, et al (2004) Comparison of various techniques used to estimate spontaneous baroreflex sensitivity (the EuroBaVar study). Am J Physiol Regul Integr Comp Physiol 286:R226–R231. https://doi.org/10.1152/ajpregu.00709.2002
11. Arcentales A, Giraldo BF, Caminal P, et al (2011) Recurrence quantification analysis of heart rate variability and respiratory flow series in patients on weaning trials. In: 2011 Annual International Conference of the IEEE Engineering in Medicine and Biology Society. IEEE EMBS, Boston, USA, pp 2724–2727
12. Iyengar N, Peng CK, Morin R, et al (1996) Age-related alterations in the fractal scaling of cardiac interbeat interval dynamics. Am J Physiol 271:R1078-84
13. Porta A, Guzzetti S, Montano N, et al (2000) Information domain analysis of cardiovascular variability signals: Evaluation of regularity, synchronisation and co-ordination. Med Biol Eng Comput 38:180–188. https://doi.org/10.1007/BF02344774
14. Costa M, Goldberger AL, Peng CK (2005) Multiscale entropy analysis of biological signals. Phys Rev E - Stat Nonlinear, Soft Matter Phys 71:1–18. https://doi.org/10.1103/PhysRevE.71.021906
15. Buijs RM (2013) The autonomic nervous system : a balancing act. In: Autonomic Nervous System, 1st ed. Elsevier B.V., pp 1–11
16. Akselrod S, Gordon D, Ubel F, et al (1981) Power spectrum analysis of heart rate fluctuation: a quantitative probe of beat-to-beat cardiovascular control. Science (80-) 213:220–222. https://doi.org/10.1126/science.6166045
17. Franciosi S, Perry FKG, Roston TM, et al (2017) The role of the autonomic nervous system in arrhythmias and sudden cardiac death. Auton Neurosci Basic Clin 205:1–11. https://doi.org/10.1016/j.autneu.2017.03.005
18. Pincus SM (1991) Approximate entropy as a measure of system complexity. Proc Natl Acad Sci 88:2297–2301. https://doi.org/10.1073/pnas.88.6.2297
19. Li X, Yu S, Chen H, et al (2015) Cardiovascular autonomic function analysis using approximate entropy from 24-h heart rate variability and its frequency components in patients with type 2 diabetes. J Diabetes Investig 6:227–235. https://doi.org/10.1111/jdi.12270
20. Richman JS, Lake DE, Moorman JR (2004) Sample Entropy. Methods Enzymol 384:172–184. https://doi.org/10.1016/S0076-6879(04)84011-4
21. Singh B, Singh D (2012) Effect of Threshold Value r on Multiscale Entropy based Heart Rate Variability. Cardiovasc Eng Technol 3:211–216. https://doi.org/10.1007/s13239-012-0082-x
22. Marwaha P, Sunkaria RK (2017) Exploring total cardiac variability in healthy and pathophysiological subjects using improved refined multiscale entropy. Med Biol Eng Comput 55:191–205. https://doi.org/10.1007/s11517-016-1476-y
23. Ding H, Crozier S, Wilson S (2007) A new heart rate variability analysis method by

means of quantifying the variation of nonlinear dynamic patterns. IEEE Trans Biomed Eng 54:1590–1597. https://doi.org/10.1109/TBME.2007.893495

24. Singh V, Gupta A, Sohal JS, Singh A (2018) A unified non-linear approach based on recurrence quantification analysis and approximate entropy: application to the classification of heart rate variability of age-stratified subjects. Med Biol Eng Comput Online Fir:1–15. https://doi.org/10.1007/s11517-018-1914-0
25. Pan J, Willis J (1985) A Real-Time QRS Detection Algorithm. IEEE Trans Biomed Eng 32:230–236
26. Patil PB, Chavan MS (2012) A wavelet based method for denoising of biomedical signal. Int Conf Pattern Recognition, Informatics Med Eng 278–283. https://doi.org/10.1109/ICPRIME.2012.6208358
27. Manikandan MS, Soman KP (2012) A novel method for detecting R-peaks in electrocardiogram (ECG) signal. Biomed Signal Process Control 7:118–128. https://doi.org/10.1016/j.bspc.2011.03.004
28. Rawal K, Saini BS, Saini I (2015) Adaptive correlation dimension method for analysing heart rate variability during the menstrual cycle. Australas Phys Eng Sci Med 38:509–523. https://doi.org/10.1007/s13246-015-0369-y
29. Richman JS, Moorman JR, Physiol AJ, Circ H (2008) Physiological time-series analysis using approximate entropy and sample entropy. 2039–2049
30. Webber CL, Zbilut JP (2005) Recurrence Quantification Analysis of Nonlinear Dynamical Systems. In: Tutorials in contemporary nonlinear methods for the behavioral sciences. pp 26–94
31. Webber CL, Marwan N (2015) Recurrence Quantification Analysis

Plancherel formula for finite generalized Hankel transform of third kind

V. R. Lakshmi Gorty
Department of Basic Science and Humanities, SVKM's NMIMS, MPSTME-400056.
India
Email: vr.lakshmigorty@nmims.edu

SVKM's NMIMS, MPSTME

Abstract. The variant of the finite generalized Hankel transform is defined and inversion is stated. Also Plancherel equality for the generalized Fourier-Bessel type series expansion is developed in this study.

Mathematics Subject Classification: 44A20; 46F12.

Keywords: Plancherel formula · finite generalized Hankel transform of third kind · generalized Fourier-Bessel type series expansion · operator · translation.

1 Introduction

In [4] the finite generalized Hankel transform (FGHT) defined by

$$\left(\hbar_{\alpha,\beta,\nu,\mu} f\right)(n) = F_{\alpha,\beta,\nu,\mu}(n) = \nu^2 \beta^2 \int_0^a x^{2\nu-2\alpha-1} \jmath_{\alpha,\beta,\nu,\mu}(\lambda_n x) f(x) dx, \tag{1}$$

$\jmath_{\alpha,\beta,\nu,\mu}(x) = x^{\alpha} J_{\mu}(\beta x)^{\nu}$, $J_{\alpha,\beta,\nu,\mu}(x)$ as defined in [6].
In this paper, form Dorta [1] the study is extended to FGHT of third kind.

2 Main Results

For FGHT the Sturm-Liouville problem [10] can be designed as

$$\left(\Delta_{\alpha,\beta,\nu,\mu} + \lambda^2\right) y = 0, a \leq x \leq b, \tag{2}$$

$$a_1 y(a) + a_2 y'(a) = 0, b_1 y(b) + b_2 y'(b) = 0 \tag{3}$$

where $\Delta_{\alpha,\nu,\mu} = x^{-\mu\nu+\alpha+1-2\nu} D x^{2\mu\nu+1} D x^{-\mu\nu-\alpha}$.
The general solution of the (2) is

$$y = \phi_{\lambda}(x) = A(\lambda) \jmath_{\alpha,\beta,\nu,\mu}(\lambda x) + B(\lambda) \Upsilon_{\alpha,\beta,\nu,\mu}(\lambda x)$$

or

$$y = \phi_{\lambda_n}(x) = A(\lambda_n)\,\mathcal{J}_{\alpha,\beta,\nu,\mu}(\lambda_n x) + B(\lambda_n)\,\Upsilon_{\alpha,\beta,\nu,\mu}(\lambda_n x) \tag{4}$$

where $\mathcal{J}_{\alpha,\beta,\nu,\mu}(x) = x^{\alpha} J_{\mu}(\beta x^{\nu}), \Upsilon_{\alpha,\beta,\nu,\mu}(x) = x^{\alpha} Y_{\mu}(\beta x^{\nu})$.
Let $y = \phi_n(x)$ be eigenfunctions of (2) (3), corresponding to non-zero eigenvalues λ_n.
The orthogonality gives

$$\beta^2\nu^2 \int_0^a x^{2\nu-2\alpha-1}\phi_m(x)\,\phi_n(x)\,dx = 0; \text{ if } m \neq n.$$

$$\beta^2\nu^2 \int_a^b x^{2\nu-2\alpha-1}\mathcal{J}_{\alpha,\beta,\nu,\mu}(ax)\,\mathcal{J}_{\alpha,\beta,\nu,\mu}(ax)\;dx$$

$$= \frac{b^{-2\alpha}\mathcal{J}^2_{\alpha,\beta,\nu,\mu}(a\lambda_n) - a^{-2\alpha}\mathcal{J}^2_{\alpha,\beta,\nu,\mu}(b\lambda_n)}{2\nu\pi^2\lambda_n{}^{4-2\alpha}\mathcal{J}^2_{\alpha,\beta,\nu,\mu}(b\lambda_n)}; \text{ if } m = n. \tag{5}$$

$$\beta^2\nu^2 \int_a^b x^{2\nu-2\alpha-1}\mathcal{J}_{\alpha,\beta,\nu,\mu}(ax)\,\mathcal{J}_{\alpha,\beta,\nu,\mu}(ax)\;dx = 0; \tag{6}$$

if , $m \neq n$.
The differential operator as in [2] given as

$$\Delta_{\alpha,\beta,\nu,\mu} = x^{-\mu\nu+\alpha+1-2\nu} D x^{2\mu\nu+1} D x^{-\mu\nu-\alpha}$$

$$= x^{2-2\nu}D^2 + (1-2\alpha)\,x^{1-2\nu}D - x^{-2\nu}\left\{(\mu\nu)^2 - \alpha^2\right\}. \tag{7}$$

Since $\Delta_{\alpha,\beta,\nu,\mu}$ is not self adjoint, , the operator

$$\Delta^*{}_{\alpha,\beta,\nu,\mu} = x^{-\alpha-\nu\mu} D x^{2\mu\nu+1} D x^{-\mu\nu+\alpha+1-2\nu}$$

$$= x^{2-2\nu}D^2 + (4\nu - 2\alpha - 3)x^{1-2\nu}D - x^{-2\nu}\left\{(\mu\nu)^2 - (\alpha+1-2\nu)^2\right\}. \tag{8}$$

$\Delta^*{}_{\alpha,\beta,\nu,\mu}$ is called the adjoint operator of $\Delta_{\alpha,\beta,\nu,\mu}$.
The main differentiation formulas for J_μ analogous to [7] follows as

$$\frac{d}{dx}\left\{(\lambda_m x)^{(\mu\nu+\nu)} J_{\mu+1}(\beta(\lambda_m x)^{\nu})\right\}$$

$$= \nu\beta(\lambda_m x)^{(\mu\nu+2\nu)} x^{-1} J_{\mu}(\beta(\lambda_m x)^{\nu}). \tag{9}$$

$$\frac{d}{dx}\left\{(\lambda_m x)^{(-\mu\nu)} J_{\mu}(\beta(\lambda_m x)^{\nu})\right\}$$

$$= -\nu\beta(\lambda_m x)^{(-\mu\nu+\nu)} x^{-1} J_{\mu+1}(\beta(\lambda_m x)^{\nu}) \tag{10}$$

for $x, y > 0$. By combining (9) and (10), it can be easily inferred

$$\Delta_{\alpha,\beta,\nu,\mu,x}\, \mathcal{J}_{\alpha,\beta,\nu,\mu}\left(\lambda_m x\right) = -\lambda_m^2\, \mathcal{J}_{\alpha,\beta,\nu,\mu}\left(\lambda_m x\right) \tag{11}$$

for $x > 0$.

$$\mathcal{J}_\mu(x) \approx \left(\frac{2}{\pi x}\right)^{1/2} [P - Q]. \tag{12}$$

Here

$$P = \cos\left(x - \frac{1}{2}\mu\pi - \frac{1}{4}\pi\right) \sum_{m=0}^{\infty} \frac{(-1)^m\,(\mu, 2m)}{(2x)^{2m}}$$

and

$$Q = \sin\left(x - \frac{1}{2}\mu\pi - \frac{1}{4}\pi\right) \frac{(-1)^m\,(\mu, 2m+1)}{(2x)^{2m+1}}.$$

$\phi_{\lambda_n}(x)$

$$= \mathcal{J}_{\alpha,\beta,\nu,\mu}\left(\lambda_n x\right) \mathcal{Y}_{\alpha,\beta,\nu,\mu}\left(\lambda_n a\right) - \mathcal{J}_{\alpha,\beta,\nu,\mu}\left(\lambda_n a\right) \mathcal{Y}_{\alpha,\beta,\nu,\mu}\left(\lambda_n x\right). \tag{13}$$

3 FGHT of third kind

From [3] and by virtue of (6), the following Fourier-Bessel expansion is given by

$$f(x) = \sum_{n=1}^{\infty} a_n\, \phi_{\lambda_n}(x) \tag{14}$$

where

$$a_n = \frac{2\nu\lambda_n^{4-2\alpha}\pi^2 \mathcal{J}^2_{\alpha,\beta,\nu,\mu}\left(b\lambda_n\right)}{b^{-2\alpha}\mathcal{J}^2_{\alpha,\beta,\nu,\mu}\left(a\lambda_n\right) - a^{-2\alpha}\mathcal{J}^2_{\alpha,\beta,\nu,\mu}\left(b\lambda_n\right)} \beta^2\nu^2 \int_a^b x^{2\nu-2\alpha-1} \phi_{\lambda_n}(x)\, f(x) dx. \tag{15}$$

The convergence of the series (14) is straight forward and follows from [1].
Proposition 3.1. Expression (14) and (15) suggest to introduce the integral transform

$$F_{\alpha,\beta,\nu,\mu}(n) = \int_a^b x^{2\nu-2\alpha-1} \phi_{\lambda_n}(x)\, f(x)\, dx \tag{16}$$

called as FGHT of third kind [5].
Then the inversion formula is given by

$$f(x) = \sum_{n=1}^{\infty} \frac{2\nu{\lambda_n}^{4-2\alpha}\pi^2\beta^2\nu^2 \mathcal{J}^2_{\alpha,\beta,\nu,\mu}\left(b\lambda_n\right) F_{2,\alpha,\beta,\nu,\mu}(n)\, \phi_{\lambda_n}(x)}{\left[b^{-2\alpha}\mathcal{J}^2_{\alpha,\beta,\nu,\mu}\left(a\lambda_n\right) - a^{-2\alpha}\mathcal{J}^2_{\alpha,\beta,\nu,\mu}\left(b\lambda_n\right)\right]};$$

(17)

for $n = 1, 2, 3, \cdots$.
Considering

$$\mathcal{J}'_{\alpha,\beta,\nu,\mu}(x\lambda_n)\,\mathcal{Y}_{\alpha,\beta,\nu,\mu}(a\lambda_n) - \mathcal{Y}'_{\alpha,\beta,\nu,\mu}(x\lambda_n)\,\mathcal{J}_{\alpha,\beta,\nu,\mu}(a\lambda_n)$$

$$= \left[-\frac{2}{\pi(x\lambda_n)^{1-2\alpha}}\right]\frac{\mathcal{J}_{\alpha,\beta,\nu,\mu}(a\lambda_n)}{\mathcal{J}_{\alpha,\beta,\nu,\mu}(x\lambda_n)}. \tag{18}$$

Let

$$\phi_{\lambda_n}(h) = (\nu\beta)^4 h^{(2\nu-2\alpha-1)n}\mathcal{J}_{\alpha,\beta,\nu,\mu}(\lambda_n h). \tag{19}$$

The following operational rule satisfies for $f(x) \in C^2(a,b)$, the differential equation as in [5]

$$\hbar_{\alpha,\beta,\nu,\mu}[\phi_{\lambda_n}(h)] = (\nu\beta)^4\lambda_n^{2\nu}(\hbar_{\alpha,\beta,\nu,\mu})\,f(\lambda). \tag{20}$$

To define the FGHT convolution, we need to introduce FGHT translation.
Define

$$D_{\alpha,\beta,\nu,\mu}(x) = \int_0^1 t^{-\mu\nu-\alpha}\left\{\nu\beta t^{-1-2\alpha+2\nu}\mathcal{J}_{\alpha,\beta,\nu,\mu}(\lambda_n x)\right\}dt. \tag{21}$$

Lemma 3.2. Property of the kernel $D_{\alpha,\beta,\nu,\mu}(x)$: Following analogous study [9] is established.
For $x > 0$ and $0 \le t < 1$, we have

$$\int_0^1 \nu\beta t^{\mu\nu+\alpha} z^{-1-2\alpha+2\nu}\mathcal{J}_{\alpha,\beta,\nu,\mu}(\lambda_n x)\,D_{\alpha,\beta,\nu,\mu}(x,t)\,dt$$

$$= (\nu\beta)^2(xt)^{-1-2\alpha+2\nu}\mathcal{J}_{\alpha,\beta,\nu,\mu}(\lambda_n x). \tag{22}$$

Proof. Here

$$D_{\alpha,\beta,\nu,\mu}(x,t) = t^{-\mu\nu-\alpha}\hbar_{\alpha,\beta,\nu,\mu}\left\{(\nu\beta)^2(xt)^{-1-2\alpha+2\nu}\mathcal{J}_{\alpha,\beta,\nu,\mu}(\lambda_n x)\right\}. \tag{23}$$

$$\hbar^{-1}_{\alpha,\beta,\nu,\mu}\left\{t^{\mu\nu+\alpha}D_{\alpha,\beta,\nu,\mu}(x,t)\right\} = (\nu\beta)^2(xt)^{-1-2\alpha+2\nu}\mathcal{J}_{\alpha,\beta,\nu,\mu}(\lambda_n x). \tag{24}$$

Proposition 3.3. The Plancherel formula for every $f \in L_2(I)$,

$$\int_I |f(x)|^2\nu^4\beta^4 x^{4\nu-4\alpha-2}dx = \int_I |\hbar_{\alpha,\beta,\nu,\mu}f(\lambda_n)|^2 d_{\alpha,\beta,\nu,\mu}(\lambda_n). \tag{25}$$

Define the generalized translation operator T^p, $p \ge 0$ by the relation

$$T^{p}f\left(x\right)=p^{\mu\nu+\alpha}D_{\mu,\alpha,\beta,\nu}\left(x\right). \tag{26}$$

$$\hbar^{-1}_{\alpha,\beta,\nu,\mu}\left\{p^{\mu\nu+\alpha}D_{\mu,\alpha,\beta,\nu}\left(\lambda_{n}\right)\right\}$$

$$=\left(\nu\beta\right)^{2}(\lambda_{n}p)^{-1-2\alpha+2\nu}(\lambda_{n}p)^{\alpha}J_{\mu}\left[\beta(\lambda_{n}p)^{\nu}\right]. \tag{27}$$

$$p^{\mu\nu+\alpha}D_{\mu,\alpha,\beta,\nu}\left(\lambda_{n}\right)$$

$$=\hbar_{\alpha,\beta,\nu,\mu}\left(f\right)\left(\lambda_{n}\right)\left\{\left(\nu\beta\right)^{2}(\lambda_{n}p)^{-1-2\alpha+2\nu}\mathcal{J}_{\alpha,\beta,\nu,\mu}\left(\lambda_{n}p\right)\right\}. \tag{28}$$

$$\hbar_{\alpha,\beta,\nu,\mu}\left(T^{p}f\right)\left(\lambda\right)=\phi_{\lambda}\left(p\right)\hbar_{\alpha,\beta,\nu,\mu}\left(f\right)\left(\lambda\right). \tag{29}$$

$$\hbar_{\alpha,\beta,\nu,\mu}\left(\Delta_{\alpha,\beta,\nu,\mu}f\right)\left(\lambda\right)$$

$$=\left(-1\right)\left(\nu\beta\right)^{4}\left(\lambda_{n}^{2\nu}\right)\left(\hbar_{\alpha,\beta,\nu,\mu}\right)\left(f\right)\left(\lambda\right). \tag{30}$$

4 Plancherel equality and results

Lemma 4.1. For $f\in W_{\varphi}^{r}\left(\Delta_{\alpha,\beta,\nu,\mu}\right)$;

$$\left\|T^{p}\left(\Delta_{\alpha,\beta,\nu,\mu}f\right)\left(x\right)-p^{(2\nu-2\alpha-1)n}\left(\Delta_{\alpha,\beta,\nu,\mu}f\right)\left(x\right)\right\|^{2}_{2,\alpha,\beta,\nu,\mu,n}$$

$$=\int_{0}^{1}\left(\nu\beta\right)^{2}p^{2(2\nu-2\alpha-1)n}|\mathcal{J}_{\alpha,\beta,\nu,\mu}\left(\lambda_{n}p\right)-1|^{2}\hbar_{\alpha,\beta,\nu,\mu}\left(f\right)\left(\lambda_{n}\right)d\left(\lambda_{n}\right) \tag{31}$$

where $r=0,1,2,\cdots$.
Proof. From (30), we obtain

$$\hbar_{\alpha,\beta,\nu,\mu}\left(\Delta_{\alpha,\beta,\nu,\mu}f\right)\left(\lambda\right)=\left(-1\right)\left(\nu\beta\right)^{4}\left(\lambda_{n}^{2\nu}\right)\left(\hbar_{\alpha,\beta,\nu,\mu}\right)\left(f\right)\left(\lambda\right). \tag{32}$$

By using (20) and (29), we conclude that

$$\hbar_{\alpha,\beta,\nu,\mu}\left(T^{p}f-\Delta_{\alpha,\beta,\nu,\mu}f\right)\left(\lambda\right)$$

$$=\left\{\phi_{\lambda}\left(p\right)+\left(\nu\beta\right)^{4}\left(\lambda_{n}^{2\nu}\right)\right\}\left(\hbar_{\alpha,\beta,\nu,\mu}\right)\left(f\right)\left(\lambda\right). \tag{33}$$

$$\hbar_{\alpha,\beta,\nu,\mu}\left(T^{p}f-\Delta_{\alpha,\beta,\nu,\mu}f\right)\left(\lambda\right)$$

$$=\left(\nu\beta\right)^{4}h^{(2\nu-2\alpha-1)n}\left\{\mathcal{J}_{\alpha,\beta,\nu,\mu}\left(\lambda_{n}h\right)-1\right\}\left(\hbar_{\alpha,\beta,\nu,\mu}\right)\left(f\right)\left(\lambda\right). \tag{34}$$

Now by (30) and (34) and Plancherel equality, we have the results.

5 Applications

For a finite interval, application of FGHT of third kind is demonstrated.

$$x^{2-2\nu}\frac{\partial^2 v}{\partial x^2}+(1-2\alpha)\,x^{1-2\nu}\frac{\partial v}{\partial x}-x^{-2\nu}\left\{(\mu\nu)^2-\alpha^2\right\}v-\kappa\frac{\partial v}{\partial t}=0, \tag{35}$$

$a<x<b, t>0$ from [4].
Here consider $V(n,t)=\hbar_{\alpha,\beta,\nu,\mu}(v(x,t))$.
Now (35) becomes

$$\Delta_{\alpha,\beta,\nu,\mu}v-\kappa\frac{\partial v}{\partial t}=0. \tag{36}$$

By applying $\hbar_{\alpha,\beta,\nu,\mu}$ to (36)

$$-(\nu\beta)^4{\lambda_n}^{2\nu}V(n,t)-\kappa\frac{\partial}{\partial t}V(n,t)=0,$$

whose solution is

$$V(n,t)=\hbar_{\alpha,\beta,\nu,\mu}(n)\,e^{-\frac{(\nu\beta)^4{\lambda_n}^{2\nu}t}{\kappa}}, \tag{37}$$

λ_n represents the n^{th} positive zeros of the (37).

$$\mathcal{J}_{\alpha,\beta,\nu,\mu}(\lambda_n b)\mathcal{Y}_{\alpha,\beta,\nu,\mu}(\lambda_n a)-\mathcal{J}_{\alpha,\beta,\nu,\mu}(\lambda_n a)\mathcal{Y}_{\alpha,\beta,\nu,\mu}(\lambda_n b)=0.$$

We may now invoke the inversion formula (17) gives as

$$v(x,t)$$
$$=\sum_{n=1}^{\infty}\frac{\left\{\mathcal{J}_{\alpha,\beta,\nu,\mu}(b\lambda_n)\right\}^2 2\nu\lambda_n^4\beta^2\nu^2 e^{-\frac{(\nu\beta)^4{\lambda_n}^{2\nu}t}{\kappa}}\hbar_{\alpha,\beta,\nu,\mu}(n)\left\{\phi_{\lambda_n}(x)\right\}}{\left[b^{-2\alpha}\mathcal{J}^2_{\alpha,\beta,\nu,\mu}(a\lambda_m)-a^{-2\alpha}\mathcal{J}^2_{\alpha,\beta,\nu,\mu}(b\lambda_m)\right]}. \tag{38}$$

References

1. Dorta Diaz, J. A. and Mèndèz Pèvèz, J. M. R.: Dini's series expansions and the finite Hankel-Clifford transformations, *Jour. Inst. Math. & Comp. Sci., (Math. Ser.)*, **5**(1), 1–17 (1992).
2. Malgonde, S. P.: Generalized Hankel-Clifford transformation of certain spaces of distributions, *Rev. Acad. Canaria Cienc.* , **XII** (1-2), 51–73 (2000).
3. Titchmarsh, E. C.: A class of expansions in series of Bessel functions, *Proc. London Math. Soc.* **2**(22), xiii–xvi (1924).
4. Malgonde, S. P. and Lakshmi Gorty, V. R.: Orthogonal series expansions of generalized functions and the finite generalized Hankel-Clifford transformation of distributions, *Rev. Acad. Canaria Cienc.* **XX (1-2)**, 49–61 (2008).
5. Sneddon, I. N.: The use of integral transforms, *Tata McGraw-Hill*, New-Delhi (1979).
6. Watson, G. N.: A treatise on the theory of Bessel functions, *Cambridge Univ. Press*, London (1958).
7. Zemanian, A. H.: Orthogonal series expansions of certain distributions and distributional transform calculus, *J. Math. Anal. Appl.* **14** (1966).

8. Zemanian, A. H.: Generalized integral transformations, *Interscience publishers*, (New-York, Republished by Dover, N. Y. (1978).
9. Lakshmi Gorty, V. R.: Continuous Hankel-Clifford wavelet transformation, *Journal of Wavelet Theory and Applications*, **7** (1), 45–55 (2013).
10. Al-Gwaiz, Mohammed.: Sturm-Liouville Theory and its Applications, *Springer-Verlag*, London (2008).

Rainfall Runoff Simulation of Tlawng Sub Watershed using Geo-informatics and HEC-HMS Modeling

*Lal Hmingliana
Department of Computer Engineering, Mizoram University, 796004, India
Email: lalhmingliana@mzu.edu.in

Ch.Udaya Bhaskara Rao
Department of Geography and Resource Management,Mizoram University, 796004, India
Email: chegondiu@yahoo.co.in

Goutam Saha
Department of Information Technology, N.E.H.U, Shillong, 793022, India
Email: dr.goutamsaha@gmail.com

Abstract. In order have a better understanding of hydrological processes and the availabil-ity of water resources, different hydrological modeling have been appied to sim-ulate River Basin across the world. This paper presents the simulation of rainfall runoff of Tlawng river sub-basin using remote sensing data, ArcGIS 10.3 and HEC-HMS modeling. Estimation of runoff has become an important issue for proper management of watershed since water becomes scarce day-by-day due to climate change and change in the environment. Surface runoff relies heavily on rainfall, soil type and land use characteristics. The SCS-CN method was applied to obtain curve number for the area of interest, which depends on soil type and land use characteristics. Thematic layers such as soil map, drainage map, slope map, flow accumulation map and land use/land cover (LULC) were generated in GIS environment. HEC-HMS 4.2.1 was used to simulate the runoff. In the past, the sub-basin under study has caused flood in Sairang which is near to Aizawl (capital of Mizoram) and thus understanding the hydrological process in this sub-basin has become very important.

Keywords: HEC-HMS, SCS-CN, flow direction, flow accumulation, GIS

1 Introduction

Rainfall-runoff model plays a significant role in watershed management and provide better understandability of hydrological behavior for which different models have been developed with varying parameters. Hydrological modeling is the most frequently used tool for estimating and assessing the basin's hydrologi-cal response. It enhances and provide a better insight of hydrologic response to various watershed management prac-tices [1]. HEC-HMS model simulates rain fall-runoff relation for dendritic watershed

in space and time [2]. HEC-HMS model have been applied successfully for watershed modeling of different River basins [3] [4] Remote sensing has provided valuable datasets to examine hydrolog-ical variables and morphological changes over large regions at different spatial and temporal scales (e.g. MSR-E, TRMM, GSMAP, ASTER, SAR and several others). Many researchers over the past 20 years have focused on satellite image-ry applications in hydrology [5] [6] [7] [8] [9].

A GIS is a tool for collecting, storing, and analysing spatial and non- spatial data [10]. Various thematic layers can be generated by applying spatial analysis with GIS software. These layers can then be integrated for identifying suitable sites for dam. In 2008, GIS and remote sensing techniques were applied by Forzieri et al.[7] to assess the suitability of sites for the installation of small dams for the purpose of water harvesting in arid areas. The Soil Conservation Service (SCS) method is the most widely used approach for estimating surface runoff from small catchments after a rainfall event [11]. It considers the relationship between land cover and hydrologic soil group, which together makeup the curve number [12] [13]. Number of researchers applied the Soil Conservation Service (SCS) with Curve Number (CN) method, focusing on how much runoff could be generated from a runoff area [14]. Several hydrological models in-corporate the SCS-CN method for estimating storm runoff, including TOPMODEL [15], watershed modelling system [16], KINEROS [17], and SWAT [18]. Integrating these models/methods with advanced tools such as RS and GIS can enhance the accuracy and precision of runoff prediction.

In this study, we use remote sensing data, ArcGIS and HEC-HMS model to simulate runoff in Tlawng basin. The basin is divided into a number of smaller sub-basins and we considered only one of the Tlawng watershed as the numbers of sub-basins were many. We assigned a curve number to the selected basin using SCS-CN method.

2 Description of the study area

Tlawng river basin spreads in Kolasib, Mamit, Aizawl, Serchhip and Lunglei districts in the state of Mizoram, India. The river flows in north – south direc-tion between 92° 32' 10" – 92° 50' 23" east longitudes and 22°49'58" – 24°07'18" north latitudes (Fig.1) with an area of about 1732.72 km^2. It origi-nates in Zopuii hill near Zobawk village in Lunglei districts at an elevation of about 1395 m above MSL (Fig.2). The river flows in north-south direction over a length of about 234 km in Mizoram and joins the Barak river in Cachar dis-trict of Assam state and has Tut and Teirei as the its major tributaries. The area enjoys moist tropical climate with an average annual rainfall of about 250cm.

3 Material and Method

Topographic map at the scale of 1:50000 prepared by Survey of India (SOI) were used for delineation of Tlawng watershed. The watershed code is 3C2A8 as per watershed Atlas of India. Satellite image (IRS P6, LISS IV, MX, Geocoded) ASTER DEM was

Fig. 1: Elevation map

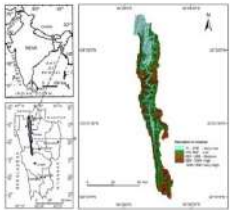

Fig. 2: Slope map

used to generate LU/LC and hydrological soil group was ob-tained from LU/LC. ArcGIS 10.3 was used to delineate the catchment area and this area has been divided into 46 sub-basins based on an automatic delineation procedure. A stream network was generated from DEM and digitized the LU/LC. Soil map of the catchment was rectified in ERDAS Imagine 9.1 and the boundary of the different soil texture was digitized in ArcGIS. In this study only one type of soil (loamy) which comes under the hydrologic soil group B is found in the sub-basin. At the beginning of rainfall event, the relative saturation of the soil is measured by Antecedent Moisture Condition (AMC) and plays an important role in runoff process, it influences the infiltration process. In this study AMC II (average condition) was considered. Rainfall data were collected from Department of Agriculture, Government of Mizoram for the period 1986-2017 out of which only the rainfall which causes flood was considered (1st – 14th June 2017). Curve number (CN) was obtained using SCS-CN method. These curve numbers along with rainfall data were input into the HEC-HMS model to simu-late rainfall-runoff.

3.1 HEC-HMS

The Hydraulic Engineering Center - Hydrologic Modeling System (HEC-HMS) is a semi -distributed hydrological model and provides run off simulation. The input data to this model includes precipitation, evapotranspiration, runoff flow of the basin (for calibration and validation), and geographical information of the basin, the model then produced the simulated runoff. HEC-HMS model consists of a basin model, meteorological model, control specifications, and input data (time series data). The Basin model for instance, contains the sub-basin and several other hydrologic elements and their

connectivity that represent the movement of water through the drainage system. The meteorological component is also the first computational element by means of which precipitation in-put is spatially and temporally distributed over the river basin [2].

The SCS curve number method was chosen as infiltration loss model. The SCS (Soil Conservation Service) unit hydrograph method was chosen for modeling the transformation of precipitation excess into direct surface runoff. Baseflow method was not employed and put Null. To model the reaches, the Muskingum routing model was employed.

3.2 Climatic condition

Mizoram experiences moist tropical climate, the temperature in summer ranges from 20 to 29°C (68 to 84°F) and gets warmer, most probably due to climate change, with summer temperatures crossing 30°C and winter temperatures ranging from 7 to 22°C (45 to 72°F). During monsoon, the region received heavy rainfall mostly from May to September with little rain in the dry (cold) season. The climate pattern is moist tropical to moist sub-tropical, with average state rainfall 254 centimeters (100 in) per annum. The capital of Mizoram (Aizawl), rainfall is about 215 centimeters (85 in) and in Lunglei, another major centre, about 350 centimeters (140 in).

Tlawng river has very good network of streams though 1st and 2nd order streams flow at higher degree of slopes of about 15° – 30° and above at higher elevations. In the Tlawng watershed the drainage density ranges between 7.77 to 10.38 km/km^2.

4 Result and Discussion

In this study, the soil conservation service (SCS), design storm (Type II distri-bution) was used for simulation of rainfall event. To calculate runoff for the study area (Sairang), SCS Curve Number Loss method was used which com-putes incremental precipitation during a storm by recalculating the infiltration volume for each time interval. The SCS Unit Hydrograph method was used as a transform method where the hydrograph is scaled by the lag time to produce unit hydrograph. The curve number obtained using SCS-CN method was 69.

The total area of the sub-basin (Sairang) under study was found to be 5.28 sq. Km and other physical parameters are mentioned in Table (1).

5 Conclusion

Tlawng sub-basin was modeled using HEC-HMS and ArcGIS for determining the hydrologic parameters and to compute peak discharge by using SCS-CN method.

This paper presents a method for computing the CN values by integrating soil map and

Table 1

Sl.No	Parameter	Measurement
1	Perimeter	32.09 km
2	length	9 km
3	Mainstream length	10.07 km
4	Total stream length	464.78 km
5	Stream gradient	0.007 m/m
6	Slope	0.05 m/m
7	Drainage density	88 km/km^2

land use characteristics. The determination of the CN values plays a significant role to the successful SCS-CN modeling. To establish the effective-ness of this approach, runoff is simulated under 70 mm precipitation for the study area. The result demonstrated that the SCS-CN method is effective and ef-ficient. The date of peak discharge happens to be the starting date of flood and thus SCS-CN with HEC-HMS is effective and reliable.

References

1. K. Choudhari, B. Panigrahi and J.C. Paul: Simulation of rainfall-runoff process using HEC-HMS model for Balijore Nalawatershed, Odisha, India, *Int. J of Geomatics and Geosciences* **5**, 253-265, (2014).
2. A.D. Feldman: Hydrologic Modeling System HEC-HMS. Technical Reference Manual. US Army Corps of Engineers (USACE), *Hydro Engg Center, HEC. Davis, CA, USA*(2000).
3. C. McColl and G. Aggett: Land-use forecasting and hydrologic model integration for improved land-use decision support, *J Environ Manage***84**,494-512, (2007).
4. Z. Yusop, CH. Chan and A. Katimon: Runoff characteristics and application of HEC-HMS for modelling stormflow hydrograph in an oil palm catchment, *Water Sci Technol***56**,41-48, (2007).
5. G. W. Kite and A. Pietroniro: Remote sensing applications in hydrological modeling, *Hydrol Sci***41**,563-591, (1996).
6. J. Liu, J.M. Chen, J. Cihlar: Mapping evapotranspiration based on remote sensing: An application to Canada's landmass, *Water Resour Res***39**,1189, (2003).
7. G. Forzieri, M. Gardenti, F. Caparrini, F. Castelli: A methodology for the pre-selection of suitable sites for surface and under-ground small dams in arid areas: A case study in the region of Kidal, *Physics and Chemistry of the Earth***33**,74-85, (2008).
8. E. Abushandi, B. Merkel: Rainfall estimation over the Wadi Dhuliel arid catchment, Jordan from GSMaP MVK, *Hydrol. and Earth Syst Sci***8**,1665-1704, (2011).
9. S. Mahmoud:Investigation of rainfall-runoff modeling for Egypt by using remote sensing and GIS integration, *CATENA***120**,111-121, (2014).
10. B. Mati, T. De Bock, M. Malesu, E. Khaka, A. Oduor, M. Nyabenge and V. Oduor:Mapping the potential of rainwater harvesting technologies in Africa:A GIS overview on development domains for the continent and ten selected countries, *ICRAF***7**,(2007).
11. K.K. Gupta, J. Deelstra and K.D. Sharma:Estimation of water harvesting potential for a semi arid area using GIS and re-mote sensing, *IAHS***242**,52-62, (1997).

12. D. Ramakrishnan, A. Bandyopadhyay and K.N. Kusuma:SCS-CN and GIS based approach for identifying potential water harvesting sites in the Kali Watershed, Mahi River Basin, *India J Earth Syst Sci***118**,355-368, (2009).
13. A.K. Kadam, S.S. Kale,N.J. Pawar, R.N. Sankhua and N.J. Pawar:Identifying potential rain water harvesting sites of a semi-arid, basaltic region of Western India, using SCS-CN method, *Water Res. Mangmnt***26**,2537–2554, (2012).
14. G.B Senay and J.P. Verdin:Developing index maps of water harvest potential in Africa, *Applied Engg. in Agri.***20**,789–799, (2004).
15. K. Warrach, M. Stieglitz, H.T. Mengelkamp and E. Raschke:Advantages of a topographically controlled runoff simulation in a soil vegetation atmosphere transfer model, *J of Hydrometeorology***3**,131–148, (2002).
16. HEC-1, Hydrologic Engineering Center 2001 Hydrologic Modeling System, HEC-HMS: differences between HEC-HMS and HEC-1:US Army Corps of Engineers, CPD-74B, Mississippi, USA.
17. D.A. Woolhiser, R.E. Smith and D.C. Goodrich:KINEROS: a kinematic runoff and erosion model: documentation and user manual, *US Department of Agriculture, Agricultural Research Service*(1990).
18. J.G. Arnold, J.R. Williams, R. Srinivasan and K.W. King:The Soil and Water Assessment Tool(SWAT) user's manual, *Temple, TX.* (2000).

SECURING PATIENTS INFORMTION IN IOT ENVIRONMENT

Shruti Sawardekar[1], Prof.Renuka Pawar[1]
shruti.sawardekar@spit.ac.in
renuka_pawar@spit.ac.in
Sardar Patel Institute of technlogy, Andheri

Abstract. The growth of internet has introduced different types of services which includes actuators and sensors proving remarkable and outstanding performances. It is found that the greatest current issue in IoT field is to obtain an easy and a safe access control scheme for the large amount of data that is being managed in the IoT services. The main fundamental features of security used in the web applications and internet are Authorization and Authentication. By providing the appropriate security functionality level to the IoT environment proves to be a logical improvement and also it decreases the possibility of illegal access to private information. So, a study of adaptation of previously established as well as systematic authorization along with authentication techniques is worth examining. This study describes how the machine learning approach of data masking along with the User Managed Access (UMA) can be proved useful for securing patient's medical information in an IoT environment.

Keywords: Security, Iot, Data masking, Encryption

1 Introduction

The Internet of Things also known as IoT is an encouraging model that integrates several communication and technical solutions. The IoT is defined as a field in which each physical object is to be connected at anytime and at any place with the help of internet and to be able in identifying these devices to other devices. In the current era there have been remarkable advances in the field of IoT. According to a survey which estimated that there is an increase in connected devices over the years and the results are surprising. It is listed in the table as follows.

YEAR	NUMBER OF CONNECTED DEVICES
1990	0.3 million
1999	90.0 million
2010	5.0 billion
2013	9.0 billion
2025	1.0 trillion

Figure 1. Rise in the number of connected devices over the years.

In the recent days, as information technology is developing, it is making rapid improvements in the branch of medical study. Paper based systems are no longer of use and are now taken place by computerized techniques. Taking into consideration the improvement in medical research, large amounts of medical data needs to be managed

transparently and cost-effectively.[5].With the rapid improvement in the field of medical research, there are new emerging technologies to help work faster with large amounts of data. Such data includes patient's medical records, treatment factors and diagnosis having security risks associated with it.

The various security issues discussed so far in the recent years are, in 2016 it was observed that the health data of about 35,000 people in a pathology laboratory in the state of Maharashtra was leaked. The data notably included the EMRs (electronic medical records). Similarly in 2017 at the Augusta University Medical Centre the organization has been hit with a successful phishing attack for the second time. From the year 2017 of April up to the year 2018 of June about total of twenty two thousands of Indian websites consisting of one hundred and fourteen portals of government were being hacked, according to government data. The figure below depicts the different security challenges. [10].

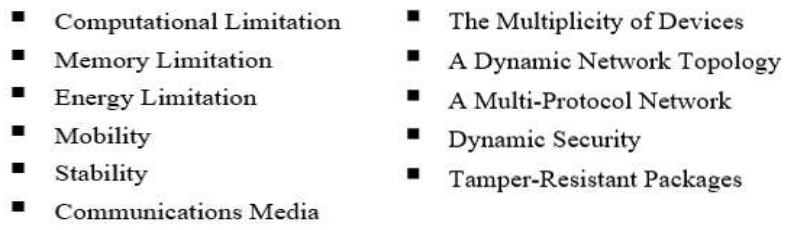

Figure 2. Security challenges

In the whole electronic health and electronic related health care use cases, a huge improved and well developed advantages are brought for the encouraging Internet of Medical Things that is IoMT also known as the Internet of Health care Things (IoHT). It is estimated that the duration from the year 2017 until the year 2022 shall be most significant before 2020. From the year 2017 up to the year 2022, improvement in applications of health care in internet of things is definitely assured for accelerating as the Internet of Things is a basic concept in the transformation of the digital world of industry related to health care and different stake holders are improving efforts on large scale. Internet of things ranks third in the development of implementation, a total of about sixty percent of the institutes introduced the internet of things connected devices.[3]. There are a lot many IoT applications and within those health care system is considered as one of the most significant challenges in the present world. The various IoT health care services and applications are listed as below.

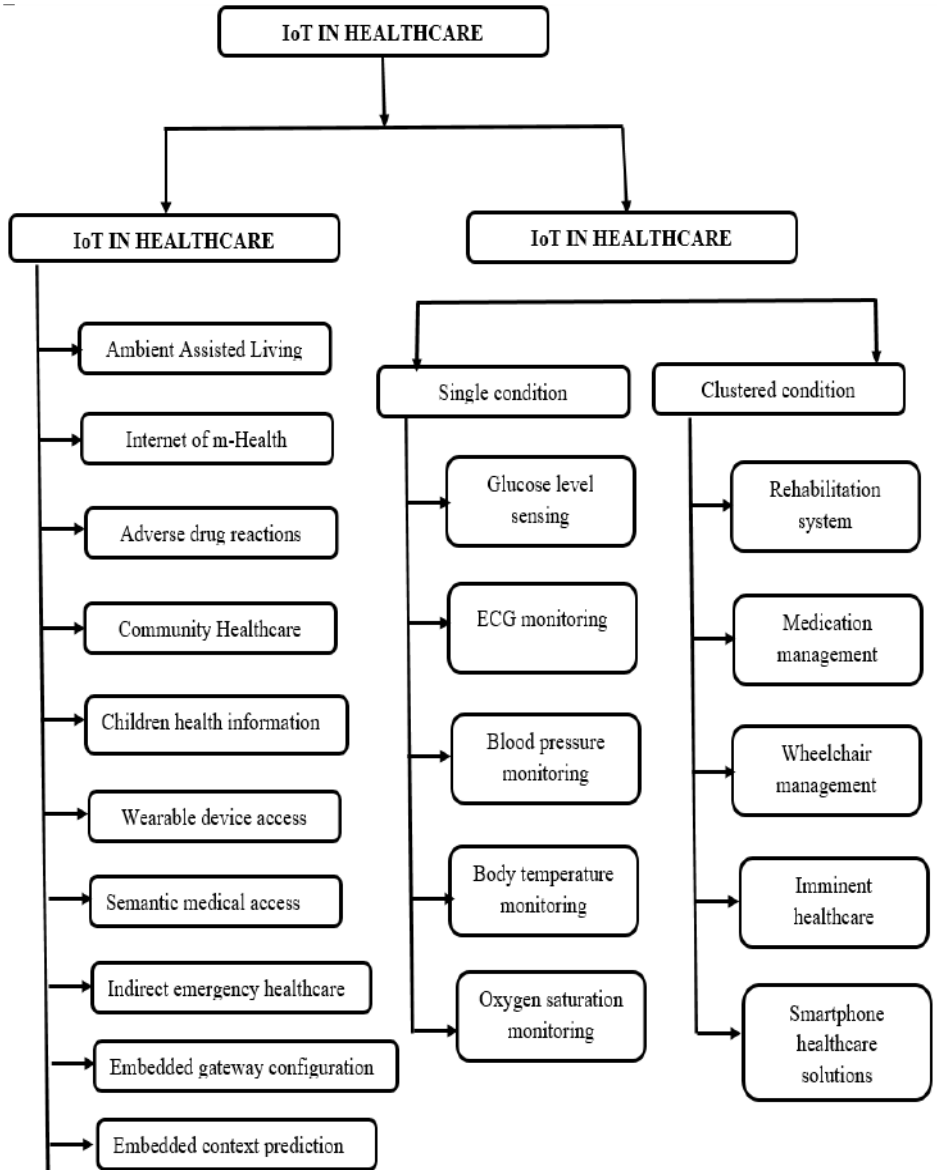

Figure 3. IoT healthcare services and applications

2 Related Work

(AAL) framework is designed which is one among the huge applications in internet of things. The main aim of this framework is to focus the challenges and issues so as to provide security and safety while accessing sensitive health data. The AAL framework considers privacy preservation and multi-level access. The framework designed focuses on two major points- (a) Data collection from biometric sensors and ambient sensors for performing recognizing of activity at top level(b) Securing the collected private health care data with the help of effective access control[1].On the basis of smartphone monitoring of pressure of blood pressure application is developed and evaluated. The technique developed is based on the measurement of the time when the valve of aortic opens and pulse after arriving a particular site of arterial. Seismo used here is based on Seismo cardiography (SCG) which makes use of the vibration that is caused by the movement of valve activities and the blood as the beating of heart occurs which allows for the accurate measuring of aortic valve opening time [2].

The proposed system integrates devices of IoT in a system of control of access that is being developed for services on basis of web by designing some internet of things communication components. The protocol used is transport of telemetry of queuing of message (MQTT) protocol. The scheme of control of access is user managed access system on that tests have been carried out. The energy consumption overhead is finally evaluated [3]. A novel access control architecture is being proposed for improving management of policy authentication in a huge system of health care by decreasing the number of policies by giving access control of fine grained manner. Fine grained access control architecture is developed combining RBAC, ABAC, and CapBAC with all their advantages gathered and attributes are being used for role membership, evaluating conditions in permissions and capability parameterisation [4].

The health related data are gathered from different monitoring medical devices. Also some of the data is taken from the patients itself. Finally the sensitive data is then secured by encryption for the purpose of transmission ad it also provided with the prevention of security attacks and threats and also for secured transmission [5]. A secure and smart health care information system is being designed using advanced security mechanisms and machine learning for handling big data of medical industry. Masking of data of data security and primary layer provides confidentiality of data by carrying out encryption [6].

Security provided and light network of sensor of body weight is proposed on basis of IoT for the purpose of cloud health care surroundings so as to mark weaknesses that are found in the schemes investigated previously. The proposed system of network of body area consists of four main parties in the scheme as senor of body, reader that is personal, reader that is medical and server of cloud related to medical [7]. The proposed system mainly focuses on securing health care personal data by making of a fog computing facility in a cloud environment. The DMBD are being utilized by honey pot and stored in fog. The OMBD are being stored privately in cloud [8].

The various security requirements are analyzed that are being used in a number of different health care system [9]. It proposes a smart gateway that provides protection to the entire system by making use of changed protocol of identity of host for exchange of diet (HIPDEX) which is a protocol for exchange of key. Due to the need of storage of data IBM Bluemix was used for clouding [10]. The proposed work is based on the

comparison of AES and MASK algorithm. It is compared in the number of times of encryption that takes place, confusion, scattering and attack that are statistical. The results are obtained using Xilinx Virtex 5 xc5vlx50t FPGA [11]. In the proposed system, the protocol of authorization of web (OAuth) is used combing accompanied by the user managed access (UMA). It may prove useful internet of things environment for the purpose of bringing WebScale authorization services in the IoT World. The entities described here are the owner of resource, server of resource, server of authorization, requesting party and of client. It centralizes the administration of entire process in a service of cloud [12].

A system is developed that protects privacy of patients and their data by non removal of sensitive attributes. It is also allowing for the analysis of top level of data using the data that is masked. Here, single values of level of record are changed [13].

3 Proposed Work

Handling large amounts of medical records of patient can be a difficult task for the large organizations. Also these sensitive information can be leaked and manipulated for various illegal and promotional purposes by the malicious users. So there's a need that the sensitive information should be properly managed and controlled by the patient as well as trusted entities in order to avoid such circumstances. As well as patient and other assigned authorities should be able to give authority to other users of the organization so that the patients may not face any issues in their treatment even in future when they are not the part of the particular organization. Also it will be helpful in future to other patients who needs to use the approach to keep themselves secure. Using data masking technique the sensitive data needs to masked appropriately as well as UMA approach needs to be designed in such a way that allows proper defined user access and overcome the existing security attacks by finally presenting the resulted outcomes by performing data visualization and analysis.

For this purpose, we need to apply data masking to secure sensitive information. A system needs to be designed for centralizing the authorization process for distributed resources. The system should be designed in such a way to meet the design principles. On the data appropriate data visualisation and analysis should be performed by using statistical graphs. There must be improved clinical decision making.

In the figure below we represent our proposed system architecture. It is simulated on Cooja which is the Contiki network simulator. Contiki is an open operating system. It uses Contiki programming language. Instant Contiki is an Ubuntu Linux Virtual Machine and it runs in VMWare player which consists of the Contiki and all the compilers, simulators and development tools that is used in Contiki development installed. It is composed of the following components, a blood pressure monitoring device named Omron HEM-7124 BP Monitor, creating database file for gathered information, and an authentication protocol named Needham Schroeder. The architecture is divided into three phases. It is as follows.

Phase I- The first phase is of data collection. The blood pressure monitoring device named Omron HEM-7124 BP monitor is used for collecting patients' data which records systolic blood pressure, diastolic blood pressure and the pulse rate. It is an upper arm BP monitor device, has a LCD display, number of batteries required are four. It

has Minimum Pressure Measurement Range 0 mmHg, Maximum Pressure Measurement Range 299 mmHg, Minimum Pulse Measurement Range 40 beats/min, Maximum Pulse Measurement Range 180beats/min, Pulse Measurement Accuracy plusmn 5% of reading, Pressure Measurement Accuracy plusmn 3 mmhg. The data of seven patients is collected including patients' ID, Diastolic Blood Pressure, Systolic Blood Pressure and pulse rate. The data collected is stored in contiki files of each patient separately.

Phase II- The second phase consists of securing the data and storing it. The gathered data is first masked using algorithm of data masking named kd tree algorithm. The values are swapped using pseudo code for swapping. It is as follows.

```
set a 89     #day 1 original DP of first patient
set b 74     #day 1 swapped DP of first patient
swap a b
puts "a is $a b is $b"
```

The dataset is as follows which contains both the original as well as swapped values.

ID	AGE	WEIGHT	DAY 1 DP (ORIGINAL)	DAY 1 DP (SWAPPED)	ALL DAYS DP (ORIGINAL)	ALL DAYS DP (SWAPPED)
1	27	130	89	74	88	76
2	61	134	103	74	103	75
3	26	101	74	87	76	83
4	27	145	87	89	83	88
5	56	190	94	86	94	96
6	55	114	74	103	75	103
7	56	162	86	94	96	94

Table 1. Dataset

The data partitioning of the values after applying pseudo code is shown below.

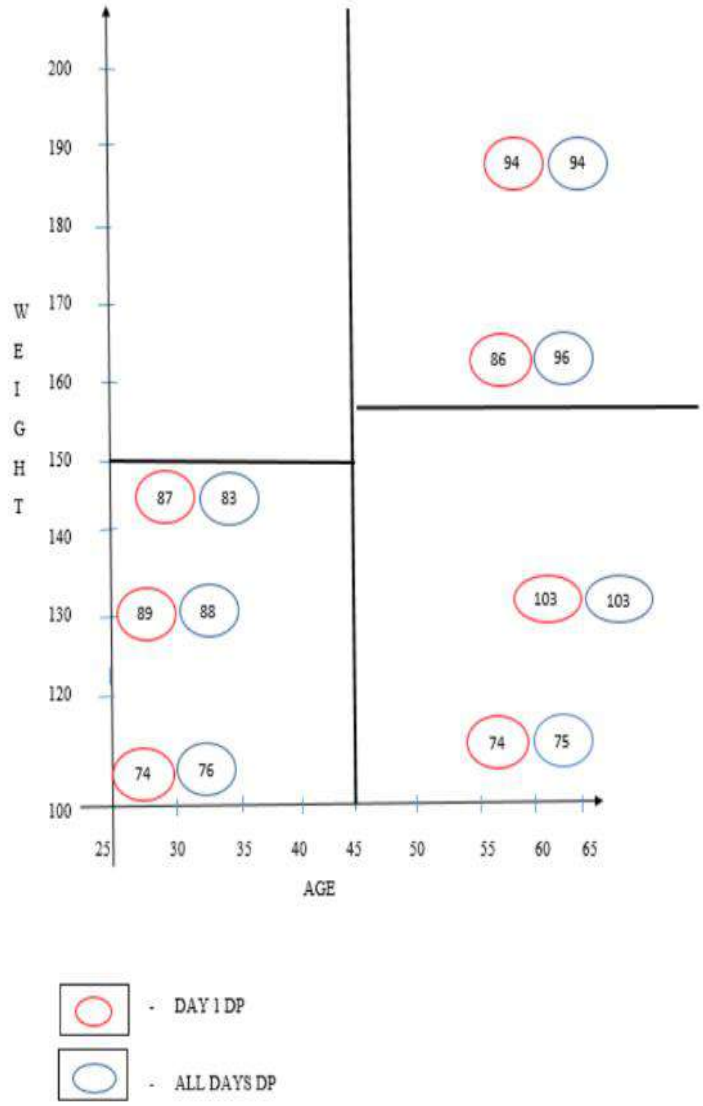

Fig 4. Data Partitioning

After the values are swapped it is again stored in contiki files of individual patient. Further it is being encrypted using AES algorithm . The masked data is being stored on the database file which is secured with username and password. On this data authorization and authentication is being carried out with the help of Needham Schroeder Protocol.

Phase III- The third phase consists of authentication and authorization roles for accessing information. Needham Schroeder Protocol is used for this purpose. The roles are being assigned for different entities. The role of entities includes such as patients, doctor and specialist . This protocol is based on the symmetric key encryption and it is the basis of Kerberos protocol. The aim of this protocol is establishing a session key between two parties on a network for protecting further communication. It is based on the public key cryptography and for providing mutual authentication between two parties communicating on a network. For the purpose of communicating between doctors and specialists, there is trusted middle man server S. If the doctor want to have a communication with the specialist, then he needs to communicate with the middle man server named as S stating that I wants to communicate with the specialist. A =Doctor, B = Specialists, sk (AS) = symmetric key recognizable by the doctor and the middle man server "S", sk (BS) = symmetric key recognizable by the specialist and the middle man server "S", non (A) = Nonce created by Doctor, non (B) = Nonce created by Specialist, sk(S) =symmetric key or session key created by the server named "S" for both the doctors and the specialists. Nonce is an arbitrarily created string that has validation for limited period of time. For preventing the replay attacks use of nonce is done in protocols used for encryption. Considering an example, if a person captures a packet while communication is being taken place between a shopping website and me, he or she can again send the packet without carrying any decryption process on it, in such a way that the server accepts the packet and carries out operations on it. In order to prevent this the arbitrarily generated value called as nonce is being added to the data making it convenient for the server to check whether the nonce is expired or is valid for some time. Symmetric keys of both the specialist and doctor are being shared with the middle man server named "S". Also symmetric keys of any other entity present in the network is also being shared with the middle man server "S". The communication is carried out in following manner.

Message (1): Firstly Doctor wants to communicate with the Specialist so he sends the message to server stating I want to communicate with the specialist. A⟶ S [This message consists of non (A) as well as A and B]. Message (2): Message 2 containing sk(S) is sent back to Doctor by the Server "S", along with it also one copy of sk(S) that is being encrypted with sk (BS) is being sent by Doctor to Specialist. Message (3): Doctor then forwards to Specialist the copy of sk(S) and then the Specialist can decrypt it with the help of the key as it was being encrypted by the middle man server with the help of Specialist's symmetric key sk (BS). Message (4): At this stage, Specialist sends a nonce value back to the Doctor that is being encrypted with sk(S) in order to provide confirmation that he is having the symmetric key or the session key that is being provided by the middle man server. Message (5): Doctor conducts on the nonce an easy experiment that is being given by the Specialist and sends it again to the Specialist just to verify Doctor has the key. The overall operation is carried out in the following manner.

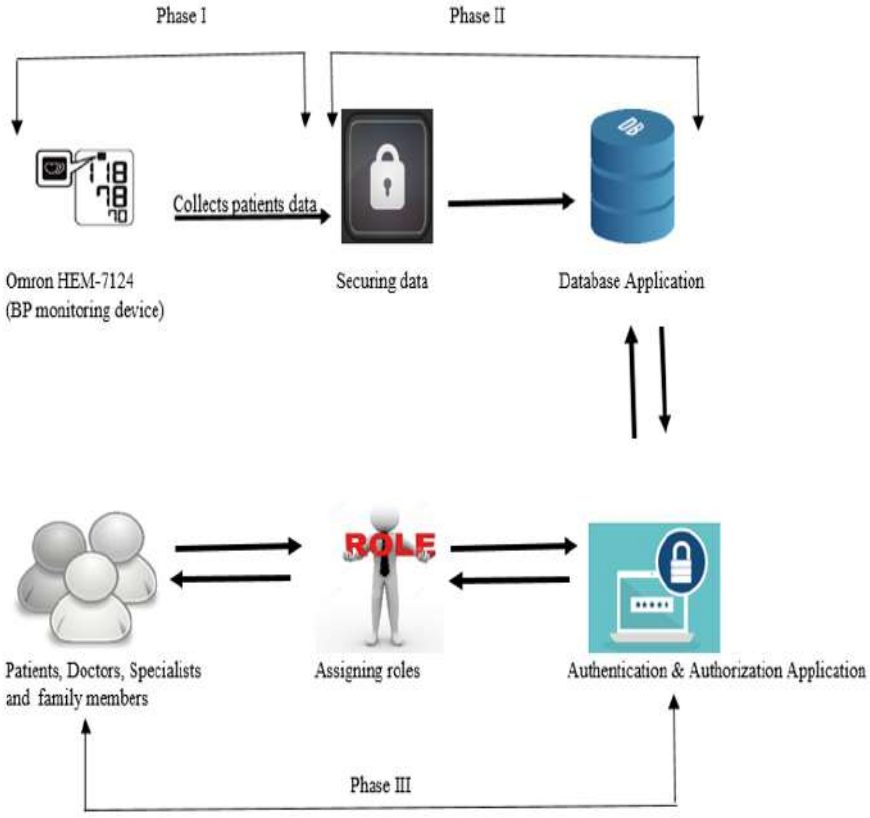

Fig 5. System Architecture

-Securing data- Apply kd tree data masking algorithm and AES (Advanced Encryption Standard) algorithm.
-Database application- Database file created which stores all the patients data.
-Authentication & Authorization application- Needham Schroeder protocol used for assigning roles to entities and grant permissions.
-Assigning Roles- Roles are assigned as Patients, Doctor and Specialist.

Conclusion

The IoT in Health care is proving tremendous growth. It is are remarkably increasing across different specific Internet of Things use cases. It is also observed that use cases of IoT are increasing tremendously as well as the reality connecting health care is moving rapidly although the obstacles exist. This paper discusses about IoT health care scenarios. The various techniques are addressed along with their limitations. Data masking technique is used here for protecting patient's medical information and a User Managed Access approach is designed for defining various rights of accessing the personal information.

References

[1] Usama Salama , Lina Yao and Hye-young Paik , “An Internet of Things Based Multi-Level Privacy-Preserving Access Control for Smart Living”, Informatics (Basel), 3 May 2018.
[2] Edward Jay Wang, Junyi Zhu1, Mohit Jain, Tien-Jui Lee, Elliot Saba, Lama Nachman, and Shwetak N.Patel , “Seismo: Blood Pressure Monitoring using Built-in Smartphone Accelerometer and Camera”, Proceedings of the 2018 CHI Conference on Human Factors in Computing Systems, no. 425, April 2018.
[3] Cruz-Piris L, Rivera D, Marsa-Maestre I, de la Hoz E, and Velasco JR. “Access Control Mechanism for IoT Environments Based on Modelling Communication Procedures as Resources”, Sensors (Basel) , 20 March 2018.
[4] Shantanu Pal , Michael Hitchens, Vijay Varadharajan, and Tahiry Rabehaja, “Fine-Grained Access Control for Smart Healthcare Systems in the Internet of Things”, EAI Endorsed Transactions on Industrial Networks and Intelligent Systems, vol. 4, no. 13, 20 March 2018.
[5] M.Prabhu ,G.Seethalakshmi, and Gollapudi Anisha, “SECURED HEALTHCARE SYSTEM IN IoT”, International Journal of Pure and Applied Mathematics, vol. 118, no. 20, 2018
[6] Prableen Kaura, Manik Sharmab, and Mamta Mittalc , “Big Data and Machine Learning Based Secure Healthcare Framework”, International Conference on Computational Intelligence and Data Science (ICCIDS 2018) , 2018.
[7] Yong-Yuan Deng , Chin-Ling Chen , Woei-Jiunn Tsaur , Yung-Wen Tang and Jung-Hsuan Chen , “Internet of Things (IoT) Based Design of a Secure and Lightweight Body Area Network (BAN) Healthcare System ”, Sensors (Basel), 15 Dec 2017.
[8] Hadeal Abudulaziz Al Hamid, SK MD Mizanur Rahman , M. Shamim Hossain , Ahmad Almogren , and Atif Alamri,“A Security Model for Preserving the Privacy of Medical Big Data in a Healthcare Cloud Using a Fog Computing Facility With Pairing-Based Cryptography ”,IEEE , 28 September 2017.
[9] Sejal Patel, Narendra Singh, and Sharnil Pandya , “IoT based Smart Hospital for Secure Healthcare System ”, International Journal on Recent and Innovation Trends in Computing and Communicat, vol. 5, Issue :5, May 2017.
[10] Binu P. K., Karun Thomas, and Nithin P. Varghese ,“Highly Secure and Efficient Architectural Model for IoT Based Health Care Systems”, International Conference on Advances in Computing, Communications and Informatics (ICACCI), 2017.
[11] Heera G. Walia and Nalini C. Iyer, “Modified MASK Algorithm for Image Encryption”, International Conference on Information Security Privacy (ICISP2015), December 2015.
[12] H. Tschofenig, E. Maler, E. Wahlstroem and S. Erdtman, “Authentication and Authorization for Constrained Environment Using OAuth and UMA”, Tschofenig, 2015.
[13] Luvai Motiwalla and Xiao-Bai Li, “Developing privacy solutions for sharing and analysing healthcare data”, Int. J. Business Information Systems, vol. 13, No. 2, 2013.

Some Results on Intuitionistic Fuzzy Sets

Jaydip Bhattacharya
Department of Mathematics, Bir Bikram Memorial College, Agartala,
West Tripura,Pin-799004, India
Email: jay73bhatta@gmail.com

*

Abstract. Many operations so far are defined in intuitionistic fuzzy sets since its inception. Some new operations are introduced in this paper and their properties are rigorously studied. The functions of modal operators over these operations are observed and studied.

Mathematics Subject Classification: 54 A 40, 03 F 55

Keywords: Fuzzy set · Intuitionistic fuzzy set · Modal operators.

1 Introduction

The notion of Fuzzy set plays an important role in Mathematics since 1965. Atanassov [1] generalized this concept into intuitionistic fuzzy set in 1983. Since then so many authors [2] [3] [4] [5] [6] [7] [8] and [9] are concentrating as well as developing the concepts like algebraic laws of IFSs, basic operations on IFSs, and modal operators of IFSs etc.In section three of this paper, we have established various interesting results using the modal logic operators over some newly defined operations namely $A * B$, $A \odot B$, $A \bowtie B$, $A \infty B$, $A \lhd B$ and $A \rhd B$ where A and B are two intuitionistic fuzzy sets.

2 Preliminaries

Definition 2.1 [10] Let X be a nonempty set. A fuzzy set A drawn from X is defined as A=$\{\prec x, \mu_A(x) \succ: x \in X\}$,where $\mu_A : x \to [0,1]$ is the membership function of the fuzzy set A. Fuzzy set is a collection of objects with graded membership i.e. having degrees of membership.

Definition 2.2 [2] Let X be a nonempty set. An intuitionistic fuzzy set A in X is an object having the form A=$\{\prec x, \mu_A(x), \nu_A(x) \succ: x \in X\}$,where the functions $\mu_A, \nu_A : x \to [0,1]$define respectively, the degree of membership and degree of non-membership of the element $x \in X$ to the set A, which is a subset of X, and for every element $x \in X$,$0 \leq \mu_A(x) + \nu_A(x) \leq 1$.
Furthermore, we have $\pi_A(x)$= 1-$\mu_A(x)$-$\nu_A(x)$ called the intuitionistic fuzzy set index

or hesitation margin of x in A.$\pi_A(x)$ is the degree of indeterminacy of $x \in X$ to the IFS A and $\pi_A(x) \in [0,1]$ that is $\pi_A : x \to [0,1]$ and $0 \leq \pi_A(x) \leq 1$ for every $x \in X$. $\pi_A(x)$ expresses the lack of knowledge of whether x belongs to IFS A or not.

Definition 2.3 [2] Let A,B be two IFSs in X. The basic operations are defined as follows:

1. $A \subseteq B \iff \mu_A(x) \leq \mu_B(x) and \nu_A(x) \geq \nu_B(x), \forall x \in X.$
2. $A = B \iff \mu_A(x) = \mu_B(x) and \nu_A(x) = \nu_B(x), \forall x \in X.$
3. $A^c = \{\prec x, \nu_A(x), \mu_A(x) \succ : x \in X\}.$
4. $A \cup B = \{\prec x, max(\mu_A(x), \mu_B(x)), min(\nu_A(x), \nu_B(x)) \succ : x \in X\}.$
5. $A \cap B = \{\prec x, min(\mu_A(x), \mu_B(x)), max(\nu_A(x), \nu_B(x)) \succ : x \in X\}.$
6. $A \oplus B = \{\prec x, (\mu_A(x) + \mu_B(x) - \mu_A(x)\mu_B(x)), \nu_A(x)\nu_B(x) \succ : x \in X\}.$
7. $A \otimes B = \{\prec x, \mu_A(x)\mu_B(x), (\nu_A(x) + \nu_B(x) - \nu_A(x)\nu_B(x)), \succ : x \in X\}.$
8. $A - B = \{\prec x, min(\mu_A(x), \nu_B(x)), max(\nu_A(x), \mu_B(x)) \succ : x \in X\}.$
9. $A \triangle B = \{\prec x, max[min(\mu_A(x), \nu_B(x)), min(\mu_B(x), \nu_A(x))],$
$min[max(\nu_A(x), \mu_B(x)), max(\nu_B(x), \mu_A(x))] \succ : x \in X\}.$
10. $A \times B = \{\prec x, \mu_A(x)\mu_B(x), \nu_A(x)\nu_B(x) \succ : x \in X\}$

Definition 2.4 [2] Let X be a nonempty set. If A is an IFS drawn from X, then,
(i) $\Box A$= $\{\prec x, \mu_A(x), 1 - \mu_A(x) \succ : x \in X\}$
(ii) $\Diamond A$= $\{\prec x, 1 - \nu_A(x), \nu_A(x) \succ : x \in X\}$

For a proper IFS, $\Box A \subset A \subset \Diamond A$ and $\Box A \neq A \neq \Diamond A$.

3 Some proposed operations in IFS

Definition 3.1 Let X be a nonempty set. If A and B be two IFSs drawn from X, then,

(i) $A * B = \{\prec x, \frac{\mu_A(x)+\mu_B(x)}{2(\mu_A(x)+\mu_B(x)+1)}, \frac{\nu_A(x)+\nu_B(x)}{2(\nu_A(x)+\nu_B(x)+1)} \succ : x \in X\}$
(ii) $A \odot B = \{\prec x, \frac{\mu_A(x)\mu_B(x)}{2(\mu_A(x)\mu_B(x)+1)}, \frac{\nu_A(x)\nu_B(x)}{2(\nu_A(x)\nu_B(x)+1)} \succ : x \in X\}$
(iii) $A \bowtie B = \{\prec x, \frac{\mu_A(x)+\mu_B(x)}{2(\mu_A(x)+\mu_B(x))+1}, \frac{\nu_A(x)+\nu_B(x)}{2(\nu_A(x)+\nu_B(x))+1} \succ : x \in X\}$
(iv) $A \infty B = \{\prec x, \frac{\mu_A(x)\mu_B(x)}{2(\mu_A(x)\mu_B(x))+1}, \frac{\nu_A(x)\nu_B(x)}{2(\nu_A(x)\nu_B(x))+1} \succ : x \in X\}$
(v) $A \rhd B = \{\prec x, \frac{\mu_A(x)+\mu_B(x)}{\mu_A(x)+\mu_B(x)+1}, \frac{\nu_A(x)+\nu_B(x)}{\nu_A(x)+\nu_B(x)+1} \succ : x \in X\}$
(vi) $A \lhd B = \{\prec x, \frac{\mu_A(x)\mu_B(x)}{\mu_A(x)\mu_B(x)+1}, \frac{\nu_A(x)\nu_B(x)}{\nu_A(x)\nu_B(x)+1} \succ : x \in X\}$

Here, $A * B$, $A \odot B$, $A \bowtie B$, $A \infty B$, $A \rhd B$, and $A \lhd B$ are all intuitionistic fuzzy sets.

Theorem 3.2 Let X be a nonempty set. If A and B be two IFSs drawn from X, then,

(a) $\Box(A * B) \subset (\Box A) * (\Box B)$
(b) $\Diamond(A * B) \supset (\Diamond A) * (\Diamond B)$

(c) $\Box(A \odot B) \subset (\Box A) \odot (\Box B)$
(d) $\Diamond(A \odot B) \supset (\Diamond A) \odot (\Diamond B)$
(e) $\Box(A \bowtie B) \subset (\Box A) \bowtie (\Box B)$
(f) $\Diamond(A \bowtie B) \supset (\Diamond A) \bowtie (\Diamond B)$
(g) $\Box(A \infty B) \subset (\Box A) \infty (\Box B)$
(h) $\Diamond(A \infty B) \supset (\Diamond A) \infty (\Diamond B)$
(i) $\Box(A \rhd B) \subset (\Box A) \rhd (\Box B)$
(j) $\Diamond(A \rhd B) \supset (\Diamond A) \rhd (\Diamond B)$
(k) $\Box(A \lhd B) \subset (\Box A) \lhd (\Box B)$
(l) $\Diamond(A \lhd B) \supset (\Diamond A) \lhd (\Diamond B)$

Proof: (a) L.H.S = $\Box(A * B)$
$= \prec \frac{\mu_A(x)+\mu_B(x)}{2(\mu_A(x)+\mu_B(x)+1)}, 1 - \frac{\nu_A(x)+\nu_B(x)}{2(\nu_A(x)+\nu_B(x)+1)} \succ$
$= \prec \frac{\mu_A(x)+\mu_B(x)}{2(\mu_A(x)+\mu_B(x)+1)}, \frac{\nu_A(x)+\nu_B(x)+2}{2(\nu_A(x)+\nu_B(x)+1)} \succ$
Again R.H.S = $\Box A * \Box B$
$\prec x, \mu_A(x), 1-\mu_A(x) \succ * \prec x, \mu_B(x), 1-\mu_B(x) \succ$
$= \prec \frac{\mu_A(x)+\mu_B(x)}{2(\mu_A(x)+\mu_B(x)+1)}, \frac{2-\nu_A(x)-\nu_B(x)}{2(3-\nu_A(x)-\nu_B(x))} \succ$
Thus the result follows.
Similarly (b) to (l) can be proved.

Remark 3.3 Let A and B be two IFSs in a nonempty set X. Then

(a) $\Box(A * B) \neq (\Box A) * (\Box B)$
(b) $\Diamond(A * B) \neq (\Diamond A) * (\Diamond B)$
(c) $\Box(A \odot B) \neq (\Box A) \odot (\Box B)$
(d) $\Diamond(A \odot B) \neq (\Diamond A) \odot (\Diamond B)$
(e) $\Box(A \bowtie B) \neq (\Box A) \bowtie (\Box B)$
(f) $\Diamond(A \bowtie B) \neq (\Diamond A) \bowtie (\Diamond B)$
(g) $\Box(A \infty B) \neq (\Box A) \infty (\Box B)$
(h) $\Diamond(A \infty B) \neq (\Diamond A) \infty (\Diamond B)$
(i) $\Box(A \rhd B) \neq (\Box A) \rhd (\Box B)$
(j) $\Diamond(A \rhd B) \neq (\Diamond A) \rhd (\Diamond B)$
(k) $\Box(A \lhd B) \neq (\Box A) \lhd (\Box B)$
(l) $\Diamond(A \lhd B) \neq (\Diamond A) \lhd (\Diamond B)$

Example 3.4 We consider $A = \prec .7, .2, .1 \succ$ and $B = \prec .6, .2, .2 \succ$.
Here
(a) $\Box(A * B) = \prec .2826, .7174 \succ$, $\Box A * \Box B = \prec .2826, .2058 \succ$
(b) $\Diamond(A * B) = \prec .8572, .1428 \succ$, $\Diamond A * \Diamond B = \prec .3076, .1428 \succ$
(c) $\Box(A \odot B) = \prec .1478, .8522 \succ$, $\Box A \odot \Box B = \prec .1478, .8522 \succ$
(d) $\Diamond(A \odot B) = \prec .9808, .0192 \succ$, $\Diamond A \odot \Diamond B = \prec .1951, .0192 \succ$
(e) $\Box(A \bowtie B) = \prec .3611, .6389 \succ$, $\Box A \bowtie \Box B = \prec .3611, .2916 \succ$
(f) $\Diamond(A \bowtie B) = \prec .7778, .2222 \succ$, $\Diamond A \bowtie \Diamond B = \prec .3809, .2222 \succ$
(g) $\Box(A \infty B) = \prec .2282, .7718 \succ$, $\Box A \infty \Box B = \prec .2282, .0967 \succ$

(h) $\Diamond(A \infty B) =\prec .9630, .0370 \succ$, $\Diamond A \infty \Diamond B =\prec .2807, .0370 \succ$
(i) $\Box(A \rhd B) =\prec .5652, .4348 \succ$, $\Box A \rhd \Box B =\prec .5652, .4117 \succ$
(j) $\Diamond(A \rhd B) =\prec .7143, .2857 \succ$, $\Diamond A \rhd \Diamond B =\prec .6153, .2857 \succ$
(k) $\Box(A \lhd B) =\prec .2957, .7043 \succ$, $\Box A \lhd \Box B =\prec .2957, .1071 \succ$
(l) $\Diamond(A \lhd B) =\prec .9616, .0384 \succ$, $\Diamond A \lhd \Diamond B =\prec .3902, .0384 \succ$

Corollary 3.5 Let X be a nonempty set. If A and B be two IFSs drawn from X, then,

(a) $\Box(A * B) \subset (A * B) \subset \Diamond(A * B)$
(b) $\Box(A * B) \neq (A * B) \neq \Diamond(A * B)$
(c) $\Box(A \odot B) \subset (A \odot B) \subset \Diamond(A \odot B)$
(d) $\Box(A \odot B) \neq (A \odot B) \neq \Diamond(A \odot B)$
(e) $\Box(A \bowtie B) \subset (A \bowtie B) \subset \Diamond(A \bowtie B)$
(f) $\Box(A \bowtie B) \neq (A \bowtie B) \neq \Diamond(A \bowtie B)$
(g) $\Box(A \infty B) \subset (A \infty B) \subset \Diamond(A \infty B)$
(h) $\Box(A \infty B) \neq (A \infty B) \neq \Diamond(A \infty B)$
(i) $\Box(A \rhd B) \subset (A \rhd B) \subset \Diamond(A \rhd B)$
(j) $\Box(A \rhd B) \neq (A \rhd B) \neq \Diamond(A \rhd B)$
(k) $\Box(A \lhd B) \subset (A \lhd B) \subset \Diamond(A \lhd B)$
(l) $\Box(A \lhd B) \neq (A \lhd B) \neq \Diamond(A \lhd B)$

Proof: (a), (c), (e), (g), (i) and (k) can be proved by using the definitions 2.4 and 3.1.
For (b), (d), (f), (h), (j) and (l), we consider the following example.
Let $A =\prec .7, .2, .1 \succ$ and $B =\prec .6, .2, .2 \succ$.
Then,
$\Box(A * B) =\prec .2826, .7174 \succ$, $(A * B) =\prec .2826, .1428 \succ$
and $\Diamond(A * B) =\prec .8572, .1428 \succ$.
$\Box(A \odot B) =\prec .1478, .8522 \succ$, $(A \odot B) =\prec .1478, .0192 \succ$
and $\Diamond(A \odot B) =\prec .9808, .0192 \succ$.
$\Box(A \bowtie B) =\prec .3611, .6389 \succ$, $(A \bowtie B) =\prec .3611, .2222 \succ$
and $\Diamond(A \bowtie B) =\prec .7778, .2222 \succ$.
$\Box(A \infty B) =\prec .2282, .7718 \succ$, $(A \infty B) =\prec .2282, .0370 \succ$
and $\Diamond(A \infty B) =\prec .9630, .0370 \succ$.
$\Box(A \rhd B) =\prec .5652, .4348 \succ$, $(A \rhd B) =\prec .5652, .2857 \succ$
and $\Diamond(A \rhd B) =\prec .7143, .2857 \succ$.
$\Box(A \lhd B) =\prec .2957, .7043 \succ$, $(A \lhd B) =\prec .2957, .0384 \succ$
and $\Diamond(A \lhd B) =\prec .9616, .0384 \succ$.

Theorem 3.6 Let X be a nonempty set. If A and B be two IFSs drawn from X, then,

(a) $\Box[(A * B)^C] = [\Diamond(A * B)]^C$
(b) $\Box[(A \odot B)^C] = [\Diamond(A \odot B)]^C$
(c) $\Box[(A \bowtie B)^C] = [\Diamond(A \bowtie B)]^C$
(d) $\Box[(A \infty B)^C] = [\Diamond(A \infty B)]^C$
(e) $\Box[(A \rhd B)^C] = [\Diamond(A \rhd B)]^C$

(f) $\Box[(A \lhd B)^C] = [\Diamond(A \lhd B)]^C$

Proof: L.H.S = $[(A * B)^C]$
$\prec \frac{\nu_A(x)+\nu_B(x)}{2(\nu_A(x)+\nu_B(x)+1)}, \frac{\mu_A(x)+\mu_B(x)}{2(\mu_A(x)+\mu_B(x)+1)} \succ$
Now, $\Box[(A * B)^C] = \prec \frac{\nu_A(x)+\nu_B(x)}{2(\nu_A(x)+\nu_B(x)+1)}, 1 - \frac{\nu_A(x)+\nu_B(x)}{2(\nu_A(x)+\nu_B(x)+1)} \succ$
Again, R.H.S = $[\Diamond(A * B)]$
$= \prec 1 - \frac{\nu_A(x)+\nu_B(x)}{2(\nu_A(x)+\nu_B(x)+1)}, \frac{\nu_A(x)+\nu_B(x)}{2(\nu_A(x)+\nu_B(x)+1)} \succ$
Therefore, $[\Diamond(A * B)]^C = \prec \frac{\nu_A(x)+\nu_B(x)}{2(\nu_A(x)+\nu_B(x)+1)}, 1 - \frac{\nu_A(x)+\nu_B(x)}{2(\nu_A(x)+\nu_B(x)+1)} \succ$
Hence the proof.

Theorem 3.7 Let X be a nonempty set. If A and B be two IFSs drawn from X, then,

(a) $\Diamond[(A * B)^C] = [\Box(A * B)]^C$
(b) $\Diamond[(A \odot B)^C] = [\Box(A \odot B)]^C$
(c) $\Diamond[(A \bowtie B)^C] = [\Box(A \bowtie B)]^C$
(d) $\Diamond[(A \infty B)^C] = [\Box(A \infty B)]^C$
(e) $\Diamond[(A \rhd B)^C] = [\Box(A \rhd B)]^C$
(f) $\Diamond[(A \lhd B)^C] = [\Box(A \lhd B)]^C$

Proof: Obvious.

4 Conclusion

We have established some interesting properties on intuitionistic fuzzy sets using modal operators.The results which are achieved in this paper will undoubtedly develop the literature. These will be very helpful for studying other new topics of IFSs in future.

References

1. Atanassov,K.T.: Intuitionistic fuzzy sets, *VII ITKR's Session,Sofia* ,(1983).
2. Atanassov,K.T.: Intuitionistic fuzzy sets, *Fuzzy Sets and Systems* **20**, 87-96, (1986).
3. Atanassov,K.T.: New operations defind over Intuitionistic fuzzy sets, *Fuzzy Sets and Systems*, **61**,2 137-142, (1994).
4. Atanassov,K.T.: Some operators on Intuitionistic fuzzy sets, *NIFS*, **3**,4 28-33, (1997).
5. Atanassov,K.T.: Intuitionistic fuzzy sets past, present and future, *CLBME-Bulgarian Academy of Science, Sofia* , (2003).
6. Bhattacharya,J.: A few more on Intuitionistic fuzzy set, *Journal of Fuzzy set valued Analysis*, **3**, 214-222, (2016).
7. Ejegwa,P.A., Akubo,A.J. and Joshua,O.M.: Intuitionistic fuzzy set and its application in career determination via normalized Euclidean distance method , *European sci. Journal*, **10**, 529-536, (2014).
8. Ejegwa,P.A., Akowe,S.O.,Otene,P.M. and Lkyule,J.M.: An overview on Intuitionistic fuzzy sets , *Int. Journal of Scientific Technology Research*, **3**, 142-145, (2014).

9. Ejegwa,P.A., Alabaa,J.T. and Yakubu,S.: Two new algebraic properties defined over Intuitionistic fuzzy sets , *Int. J. Fuzzy Mathematical Archive*, **5**, 75-78, (2014).
10. Zadeh,L.A.: Fuzzy sets, *Information and Control*, **8**, 338-353, (1965).

SMENN: A Hybrid Noise Reduction Approach for Imbalance Class Distribution

Nitin Malave
Department of Computer Enineering,
Sardar Patel Institute of Technologgy, Mumbai India
Email: nitin.malave@spit.ac.in

Anant V Nimkar
Department of Computer Enineering,
Sardar Patel Institute of Technologgy, Mumbai India
Email: anant_nimkar@spit.ac.in

Abstract. Classifiers learning with imbalanced dataset is often a challenging problem in machine learning and data mining. This issue occurs when one class consist of highly outnumbered samples whereas other contains only few. This causes traditional machine learning algorithm to be bias towards majority class. Synthetic Minority Over-sampling Technique has been the efficient method which aims to rebalance the class distribution. But this method has some bottleneck that after creating synthetic samples of minority class, it causes more overlapping regions in the areas near to class boundaries with other class samples. This tend to cause large number of samples near class boundaries to become noisy samples. Our objective is to tackle class imbalance by manipulating this noisy samples by retaining each minority samples within this overlapping regions. We propose SMENN approach which is extension of SMOTE algorithm aims to deal with these noisy samples by considering the relative distance with every other samples and remove them. We carried out our experiment of SMENN approach on two extremely imbalance real world datasets and compared with existing SMOTE algorithm and other state of the art techniques which has been deployed popularly across imbalance domain. Experimental results demonstrate that SMENN is surpassing over existing SMOTE and its other generalization with other resampling techniques.

Keywords: Class Imbalance · Machine Learning · Data Preprocessing.

1 Introduction

Classification is an important task in many machine learning problems. Traditional machine learning algorithm performs better for binary or multi-class classification by assuming the balanced class distribution within dataset. Performance of these classifiers are starting to hinder when exposed to imbalance datasets where one class is particularly outnumbered than others. This uneven or skewed distribution leads to the phenomenon of class imbalance. Various machine learning algorithms perform bias towards majority class by ignoring the minority class or simply considering them as noisy observations

[2][10]. This issue receives lot more attention as many real world problems started to suffer from class imbalance. Some popular real world case studies are fraud detection, medical diagnosis, software defects, natural disaster etc [10][13]. These case studies are highly imbalance as consist of occurring rare events very infrequently. Therefore it becomes difficult to predict future observation based on very less available information about rare events. Also these are some case studies have higher risk of misclassification and failing to predict rare events. Predicting the future occurrence of rare event based on very less available information is a concept of interest in class imbalance problems [13].

In recent decade, most of the solutions to class imbalance problem is by developing a way through re-sampling the original distribution or deploying ensemble based classifiers [1][2][3][15]. There are data level as well as algorithm level solutions for the class imblance problen as given in various studies [1][2][3]. Data level approaches involves random undersampling of majority class, random oversampling of minority class, syntheric generation of samples through SMOTE etc [20]. These are most popular techniques used for addressing the class imbalance problem as they are very simple, easy to use and does not require complex domain knowledge. RUS(Random Under-Sampling) and ROS(Random Over-Sampling) approaches have drawbacks as they cause model to become underfitted or overfit to training dataset as well as loss of important information because of randomness [1]. On the other hand, some studies involves introduction of ensemble techniques or combination of this ensemble techniques with resampling methods [17]. Bagging & boosting are some very popular ensemble approaches and are used independently or with combination of resampling techniques and proposes new frameworks such as SMOTEBoost [10], RUSBoost [1], SMOTEBagging etc [3][6].

Literature review shows that class imbalance itself is not a reason behind performance degradation of the algorithms [2], but there are certain factors regarding data distribution. When these factors are subjected to class imbalance, it becomes more complex issue to solve. Nature of class imbalance problem consist of several factors such as class separability, small sample size, within class imbalance or small disjuncts etc [5]. Existing SMOTE technique has been an efficient sampling technique for minority samples. This method avoids model from being overfitted as it creates synthetic samples instead of replicating the existing samples. It also provide a lot of variability for additionally generated synthetic samples of minority class. The SMOTE algorithm has a bottleneck, it produces overlapping regions of minority class samples within the region of majority classes. This results in categorizing most of the minority class observations as noise samples which diminish classifiers abilities to perform accurate classification. Each minority samples is very important for classification and predicting the rare events within originally imbalance data.

This paper proposes an approach called SMENN (SMOTE + Edit Noisy Neighbor of majority class) to overcome the limitation of existing SMOTE algorithm. SMENN is a extension of SMOTE algorithm and takes advantage of existing SMOTE alggorithm for creating synthetic samples of minority class by convex combination of nearest minority neighbor. This will be useful for resampling and balancing distribution of classes.

After this step, we perform selective undersampling on those majority class samples which belongs to overlapping regions. It was found that reducing this overlapping regions is possible by removing noisy majority samples and retaining each minority samples in this region. We have large number of majority samples in original distribution of data, therefore removal of these noisy samples would not causes significant performance degradation for majority class. This is because most of majority class information can be obtain from safe samples of these class. Information or patterns within minority samples is our concept of interest. Further we make use of fully connected feed forward neural network for classification. The proposed over-under sampling strategy enhances the performance of neural network classification on imbalanced datasets.

The rest of the paper is organized as follows. Section II provides literature survey of various data level as well as ensemble approaches. In section III, brief overview and architecture of proposed system is given. Section IV presents the implementation and experimental work. Section V describes various evaluation metrics used for evaluating proposed model performance. Section VI describes results and outcome of the proposed system. Finally this paper is concluded with observation we have drawn from research and experimental work.

2 Preliminaries

We have reviewed various contemporary research papers which includes state of the art techniques to deal with imbalance distribution of classes. Most of the approaches proposed to handle class imbalance can be categories into following four categories or combination of these categories.

1. Handling class imbalance by manipulating class distribution using re-sampling approaches.
2. By Selecting & extracting efficient features from original data set to obtain optimal classification results.
3. Manipulating single classifier or combination of classifiers using bagging, boosting techniques to obtain best estimator classifier results.
4. Using cost sensitive learning approaches to reduce misclassification costs for minority class.

2.1 Resampling Techniques

Re-sampling techniques are the most popular solutions used by many researchers for overcoming class imbalance problem in their experimental work. There are two reasons for the popularity of these techniques. First, these techniques are easy and simple to implement. Second, it does not require deep knowledge of machine learning domain as we can simply apply classifiers on resampled data. Random UnderSampling (RUS) [1], Random Over Sampling (ROS)[2] and SMOTE [12] are the most common resampling techniques used under this category. RUS is non-heuristic method that randomly eliminates samples of majority class to equalize the class distribution [3]. It is one of the

simplest method to execute on skewed distribution. It is an efficient method for some dataset. however, it would not work consistently with every dataset as this is a random method and may lead to loss of crucial samples of majority class. It may cause loss of important patterns from data and thus model tend to become underfit to train dataset [8][25][26]. There are some heuristic approaches already proposed that falls under undersampling domain such as Codensed Nearest Neighbor (CNN) [10], Neighborhood Cleaning Rule (NCL), Nearmiss-1, Nearmiss-2, Nearmiss-3 etc which emphasize on selective sample removal strategy. These approaches have been used with combination of other resampling methodologies [3][10][22].

Random Over Sampling (ROS) [2] is also a non-heuristic methodology that randomly replicates minority class samples for creating equal class distribution. As this approach tend to replicate only the available minority samples, it results in overfitting the model. If the available dataset is large and even extremely imbalanced, then this approach may take longer training time based on a desired ratio of distribution wanted after resampling [5]. SMOTE [12] is another oversampling technique popularly used for imbalance datasets [12][20]. This method create synthetic samples of minority class objects using its convex combination among the neighboring samples. Instead of replication, it interpolates the rare samples and thus avoids model from being overfit to train data. There are variants of SMOTE such as ADASYN [10], Borderline-Smote 1 and Borderline-Smote 2 [20] that have been developed further to improve synthetic generation of samples under certain overlapping conditions or when majority class dominates over minority class in the presence of small disjuncts. MSMOTE [10] is a modified form of SMOTE algorithms which categorize minority objects into safe, borderline and noisy samples by analyzing distances from every other (minority as well as majority) samples. It creates synthetic instances only for safe samples which represent minority objects explicitly. These approaches tries to improve classifier performance by improving true positive samples as well as F1 rate. BSMOTE-1 and BSMOTE-2 are extensions of SMOTE algorithm, developed to improve the performance of the classifiers in presence of high class overlapping [20][12]. These extentions of SMOTE algorithm focus on those minority samples which belong to overlapping regions with majority samples and create its synthetic samples in order to obtain strong boundaries for separating classes [21].

Another way of oversampling is cluster based oversampling for minority class samples(CBMOS) [10]. These methods cluster the minority samples by finding its nearest neighbor using k-NN algorithm and create its synthetic samples among that cluster region. After proper parameter tuning, this method has proven efficient when a dataset contains extreme imbalance with discrete variance among minority class. Thus it results in creating multiple small disjuncts within majority class area in feature space. CBMOS becomes prominent approach when dataset has less overlapping with other classes [10].

Wu and Liu [11] develop a distinct approach to resolve class imbalance by proving the relationship between class imbalance and their overlapping regions. To counter the learning difficulties of C4.5 and SVM algorithm, authors used Support Vector Data

Description (SVDD) method to obtain overlapping regions within feature space. Authors proposed model by using discarding, merging and separating schemes to preprocess a data and train model using C4.5, k-NN, RIPER and SVM classifiers. In the first phase, overlapping regions of samples are ignored and model learns only from non-overlapping region samples. In the next step, the data ignored by model in previous step has been considered as a separate class and merge with previously learnt model. The authors approach shows better performance improvements when overlapping is integrated with class imbalance problem by treating overlapping regions samples separately [11].

2.2 Feature Selection and Extraction

Feature selection and Extraction is one of the major step performed for solving machine learning problems. It has been employed in various domains like text classification, image processing etc. Classifier tend to ignore minority class properties by considering them as a noise, but effective feature selection from that particular class can significantly improve classifiers learning abilities and performance. Goal of feature selection is to obtain an optimal p parameters which can provide maximum variances and most efficient representation of patterns among minority class [4]. The parameter p can be manually defined or can be model adaptive. Filter, Wrapper and Embedding's are the most common feature selection methods used mostly in imbalance distribution. Filter methods are based on computation of variance and co-variance matrix among features and then rank the features according to corresponding correlations between features. Some filter methods uses probability density estimation function for feature ranking. In the wrapper method,feature ranking evaluation is based upon heuristic and stochastic search on all features. However embedding method uses sparse logistic regression with stability selection approach for ranking and selecting the optimal features. Feature selection aims to select subset of features from all available features, whereas feature extraction is use to create new features from available base features. Feature extraction is a technique of dimensionality reduction used to convert higher dimensional data into low dimensions for reducing memory storage and improving computation speed. Some of the popular extraction techniques are Principal Component Analysis (PCA) [4], Singular Value Decomposition (SVD) and Non-negative Matrix Factorization (NMF). Further variants of this methods are obtained by inclusion of costs such as cost-sensitive PCA, cost-sensitive NMF etc [2][4].

2.3 Ensemble Techniques

Most of the work done in imbalance domain is solely based on a data level approaches. Whereas there are some methodologies developed to manipulate classification algorithm manually and obtain optimal results. These approaches are called ensemble methods. Bagging and boosting are most common ensemble techniques deployed to resolve difficulties encounter by classifiers. In bagging, more than one classifiers are trained on each generated bootstrap samples, and the classified results are combined to obtain maximum voting among classifiers [10][13]. This overcomes the problem of single classifier learning limitations across certain circumstances or for hard samples and takes advantage of multiple classifiers vote (SVM, Decision tree, C4.5, k-NN, logistic regression)

to reach at the final decision. Boosting is accuracy oriented ensemble approach that tries to reduce bias on training dataset and proven to work efficiently for binary classification problems [10]. During each iteration, boosting algorithm focus more on those minority class samples by increasingg the weights of misclassified minority samples in the previous iteration. This way, it leads to obtain optimal accuracy for weak classifier. AdaBoost [19] is the most common boosting algorithm used as ensemble approach for handling class imbalance problem [10][13][14]. This algorithm is further extended by upgrading the weighting strategies for misclassified samples and is known as AdaBoost.M2 [10].

Some studies are based on data level as well as classification level approach combined together. These hybrid approaches has been developed to resample data in initial stage and manipulate single or multiple classifiers during classification phase. SMOTEBoost [10], MSMOTEBoost [10], RUSBoost [1], ROSBoost [3], DataBoost [16], MEBoost [6] are some of the popular hybrid approaches used to tackle class imbalance problem [6]. In SMOTEBoost approach, synthetic samples are generated during initial stage and later weights are updated based upon misclassified samples [2][5][6]. RUSBoost also works similarly, except it removes samples from majority class during initial stage [3]. On the other hand, SMOTEBagging [10], UnderOverBagging [8] are some of the hybrid approaches developed by integrating resampling techniques with bagging based ensemble methods.

Class imbalance has been solved by various cost sensitive approaches [14][13]. These approaches is based on assuming some costs for each category samples. This cost matrix gets updated by assuming higher misclassification costs for incorrectly classified minority objects. Cost sensitive approaches are proposed by integrating AdaBoost weights updating parameters with cost items [14]. There are three variants of cost sensitive algorithm available, based upon strategy for insertion cost items with weight updation scheme i.e AdaC1, AdaC2 and AdaC3 respectively [14][24].

3 SMENN Neural Network Classification

Proposed architecture is divided into two parts. First, we performed over-under sampling using SMENN approach and then neural network is trained on resampled dataset. Fig. 1 depicts the entire architecture of proposed methodology.

3.1 SMENN Resampling

Minority class is resampled using existing SMOTE (Synthetic Minority based Over-Sampling Technique)[12]. This method envision to rebalance the original class distribution by adding more samples of minority class. Instead of replicating the existing minority objects, it interpolates among minor class and creates synthetic samples using convex combination of nearest neighboring minority samples. Thus it avoid the model from being overfitted (after applying classifiers) and obtain synthetic but similar patterns with distributed variance among minority class objects. Synthetic samples for minority class are generated by,

For each minority sample p in S (Entire data distribution):

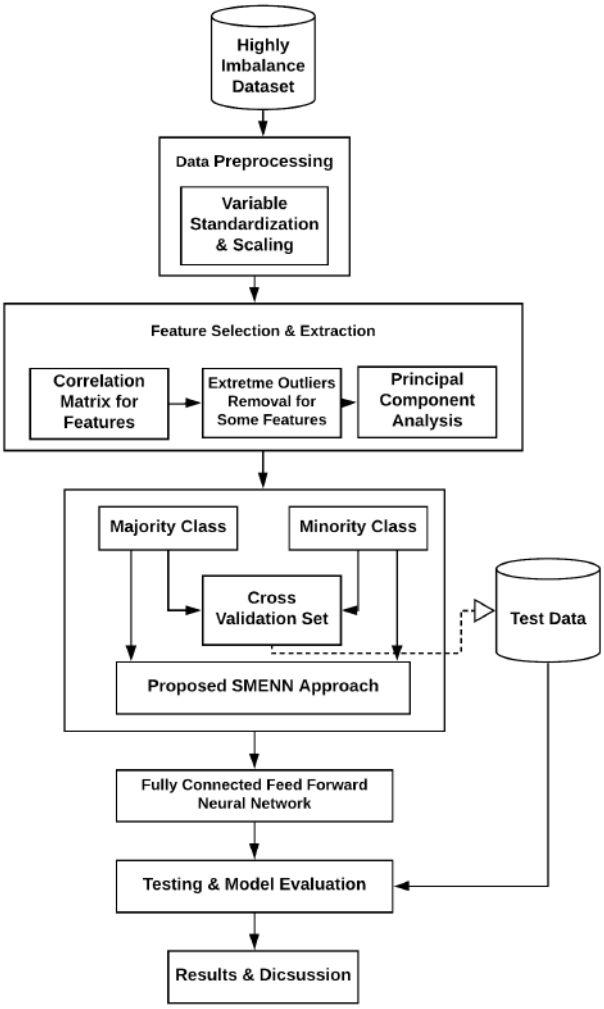

Fig. 1: Architecture of Proposed SMENN Methodology

1. Compute its k nearest neighbor of same class within S.
2. Randomly choose $r \leq k$ neighbors with replacement policy.
3. Choose a point $m^{'}$ obtained by convex combination with the r selected neighbors along the lines joining p and each of r.
4. Add synthetic points $m^{'}$ into the original distribution S, $m^{'} \subseteq S$

At this stage, dataset is resampled with minority class by adding newly created samples in it. Most of the samples added after SMOTE tries to create overlapping regions

with majority class. This overlapping regions causes hurdles for linear classifiers because most of the samples are turned out to be noisy samples after initial resampling. This noisy samples limits classifiers performance because of inabilities of linear classifiers to construct boundries to separate classes in the presence of complex overlap. Therefore we performed under sampling for only selective samples of entire dataset. We removed those noise samples of majority class which causes overlapping regions with SMOTE generated minority samples. For this, advantage of modified k-nearest neighbor algorithm notion was taken. It works similar to k-NN i.e. find closest samples of same class and manipulate other class samples present within boundary regions. The selective under sampling can be done as follows.

The set $(X_i, \theta_j)\ j = \{0, 1\}$ for binary class classification problem, constitutes the set of overlap region samples.

It's working is as follows,

1. For each sample i in overlapping region,
   (a) find its k nearest neighbors to X_i, among $(X_1, X_2, ..., X_i-1, , X_i+1, ..., X_N)$;
   (b) Compute the class θ associated with maximum number of sample among k selected neighbors.
2. Edit the distribution $(X_i, \theta_i,)$ by deleting $(X_i, \theta i,)$ if θ, belongs to majority class sample.

For our model setup, parameter $k = 3$ was tuned as vote of 3 minority class samples for decision making is considered. Majority class sample closer to 3 minority samples will be removed.

3.2 Neural Network Classification

After performing over-under sampling on imbalanced dataset, neural network classification were performed on imbalanced dataset. Neural network has a potential to work with large datasets with complex features. In boosting methods, performance depends on the selection of weak learner and their weight updation strategy. Whereas neural network has its own learning abilities based upon initial weights and its updations using bias factor. As we have few minority samples, neural network can efficiently extract scattered patterns among minority class. Fully connected feed forward neural network is trained using deep learning framework called keras (with tensorflow as a backend). The confiuration of (1-1-1:Input-Hidden-Output) layer is set for training the model. Parameters used to train this model are number of neurons in input layers are equal to number of features within dataset or (+1), with 32 nodes in single hidden layer and 2 output nodes (for binary classification problem).

Output of each hidden neuron is activated using linear activation functions and introducing some bias factor for decision support as given below,

$$b\ + \sum_{i=1}^{n} x_i w_i \tag{1}$$

Bias at hidden layer is denoted by b, x_i are net output from input layer and w_i is a weight matrix. ReLU(Rectified Linear Unit) is an activation function applied on above

weighted sum of inputs for binary classification at output nodes. ReLU ensures that the function returns 0 if it receives any negative input, but for any positive value x, it returns that value back. The expression can be written as,

$$f(x) = max(0, x) \tag{2}$$

4 Implementation

SMENN approach for resolving class imbalance problem within original dataset consist of following steps :

1. Data acquisition and exploratory data analysis on original imbalance distribution.
2. Perform data preprocessing for cleaning and standardization of variables.
3. Perform feature selection and extraction for dimensionality reduction.
4. Perform SMENN+Neural network classification and evaluate results using parameters described in section V.

4.1 Data Acquisition and Analysis

Experiment was carried out on two real world dataset which are highly imbalanced in nature. The credit card fraud dataset is real world financial customer dataset taken from internet sources whereas yeast dataset is obtained from very popular keel repository for imbalance dataset. Both datasets have continuous values for all features with 2 classes of imbalance class ratio of 1 : 9 (Minority : Majority) which is extreme class imbalance. The credit card dataset has 492 fraud samples and 2,84,315 non-fraud or healthy transaction samples. This shows that dataset contains (0.17% : 99.83%) imbalance among both classes. This dataset consist of 30 features including time and amount of transactions. On the other hand, Yeast dataset is small dataset compared to credit fraud dataset. It has 1484 samples with 8 features having continuous values. This dataset contains 1:8 imbalance ratio among negative : positive classes.

4.2 Data Preprocessing

Both datasets consist of continuous values for all features. In credit fraud dataset, out of 30 features, 28 features consist of encrypted and scaled values. The dataset is a real world customer records for financial credit loans and therefore most of the features and their values are kept private by distributers. Only feature time and amount have original values. We cannot feed these values directly to our classifier, as skewed values of these features will dominate over other features and final results will many errors with accuracy and precision. Therefore these two features were scaled to make them a standardize distribution making it compatible with existing 28 features. We scaled this features for range of [0,1].

4.3 Feature Selection and Extraction

After scaling values of these two features, refined values are inserted in original dataset. The correlation matrix were calculated for observing overall relationship among features and influence of specific feature on binary classification. Extreme outliers for some features whose correlation values are extreme positive or extreme negative were removed. These are important steps in machine learning to obtain maximum insights or patterns from each class for classification (especially for minority class as this class having only 492 samples). This helps to obtain accurate results for our SMENN model. Finally filter dataframe was passed through PCA for dimensionality reduction. The filter dataset was used for classification and result evaluation.

5 Model Evaluation Metrics

The metrics used to evaluate and compare performance of our model are accuracy, precision, recall, F1 Measure and AU-ROC curves. These are the most widely used parameter in imbalance classification problems. We have constructed confusion matrix for our model and then performed computation on values to obtain results of evaluation metrics. TP, FP, FN and TN are terminologies of confusion matrix which are described below.

1. True Positive rate (TP) : Percentage of actual positive samples correctly classified as positive
2. False Positive rate (FP) : Percentage of actual positive samples incorrectly classified as negative.
3. False Negative rate (FN) : Percentage of actual negative samples incorrectly classified as positive.
4. True Negative rate (TN) : Percentage of actual negative samples correctly classified as negative.

Accuracy is a ratio of all correctly classified samples with all classified samples by classifier.

$$\text{Accuracy} = TP + TN/TP + FP + FN + TN \tag{3}$$

Precision is a measure of ratio of correctly classified positive samples over all instances classified as positive.

$$\text{Precision} = \frac{TP}{TP + FP} \tag{4}$$

Recall is the fraction of number of data points that are in the class as per classified by the classifier.

$$\text{Recall} = \frac{TP}{TP + FN} \tag{5}$$

F1 score is a harmonic function of precision and recall.

6 Statistical Results and Evaluation

The proposed SMENN approach for class imbalance has been implemented on credit fraud dataset and Yeast dataset respectively. After performing data preprocessing and effective feature selection,dataset is resampled using SMENN approach and then subjected to neural network for classification. Fully connected feed forward neural network is used for binary classification problem in our experiment.Table I,II and III depicts results of credit fraud dataset. For credit fraud dataset, we have obtained 99.98% accuracy whereas on Yeast dataset we have obtained 98.68% accuracy. Proposed model does performed better than Adaboost ensemble technique which has accuracy of 95.29%.

Table 1: Classifiers Accuracy on Credit Fraud Dataset

Methodology	**Accuracy Score**
Logistic Regression	94.00%
K-Nearest Neighbor	93.00%
Support Vector Machine	93.00%
Decision Tree Classifier	92.00%
RUSBoost	93.15%
SMOTEBoost	97.70%
SMENN + Neural Network Classifier	99.98%

Table 2: Classifiers Performance on Credit Fraud Dataset

Methodology	**Accuracy**	**Precision**	**Recall**	**F1-Score**
Random Under Sampling	92.10%	95%	94%	94%
SMOTEBoost	97.65%	99%	98%	99%
SMENN + Neural Network Classifer	99.97%	99.89%	99.96%	99.92%

Only accuracy is not enough to evaluate model performance in imbalance domain, therefore we have compared our model with precision, recall, F1-Score and AU-ROC etc.Table III depicts results of SMENN approach and existing methodologies on Yeast dataset. Values for parameters precision, recall and F1-Score were calculated from confusion matrix with metrics rules mentioned in above section. SMENN model has increased the accuracy for Yeast dataset by reducing the misclassified minority samples. It also has obtained 95% precision, 96.44% recall and 95.71% F1-Score. It has also been proven efficient in terms of AU-ROC score. Fig. 4 depicts AU-ROC score for SMENN approach is 0.882 which is higher than 0.879 of ROS and 0.876 of SMOTE.

Table 3: Classifiers Performance on Yeast Dataset

Methodology	Accuracy	Precision	Recall	F1-Score
Nearmiss-1	90.58%	91%	89%	90%
Nearmiss-2	90.58%	91%	89%	90%
Nearmiss-3	91.92%	93%	93%	93%
Condensed Nearest Neighbor	94.39%	94%	93%	93%
Random Under Sampling	92.37%	93%	93%	93%
Random Over Sampling	95.06%	94%	93%	94%
AdaBoost Classifier	92.15%	94%	93%	93%
SMOTE	95.29%	95%	93%	94%
SMENN + Neural Network Classifier	98.68%	95%	96.44%	95.71%

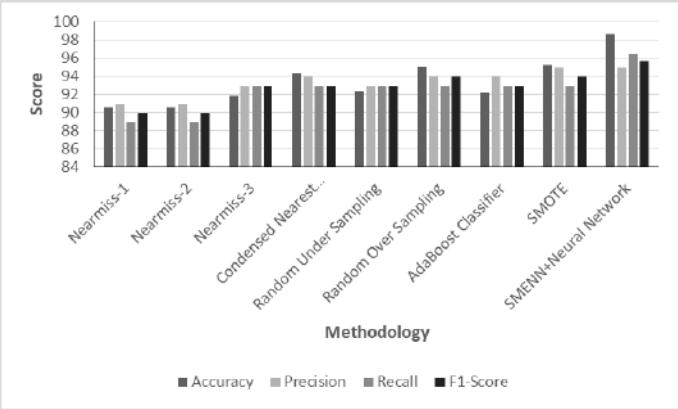

Fig. 2: Results on Yeast Dataset

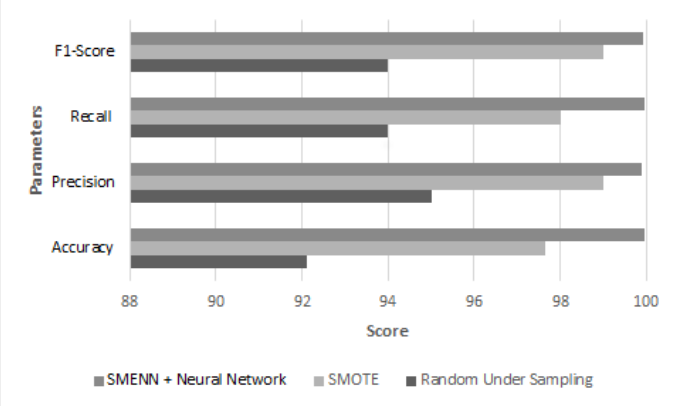

Fig. 3: Results on Credit Fraud Dataset

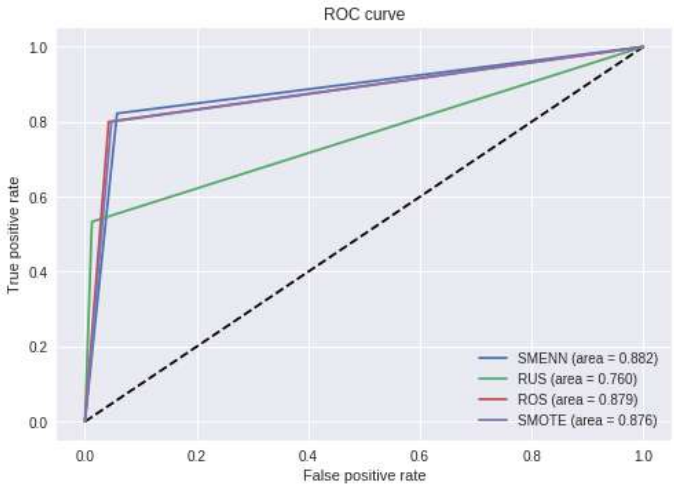

Fig. 4: AU-ROC Score on Yeast Dataset

7 Conclusion

In our studies, we have reviewed various data level as well as ensemble level approaches incorporated to handle imbalance class distribution. There are several factors regarding data distribution such as small sample size, complex class separability and presence of noise within distribution makes class imbalance a more complicated issue. Our proposed approach tackles class imbalance by reducing noise created by generating synthetic samples of minor class. Removing noise of majority class help us in reducing overlapping regions and improving learning abilities of neural networks for classification. Thus we have tried to extract maximum hidden patterns from minority class by effective feature engineering on original distribution as well as after creating synthetic samples. By retaining each minority sample within overlapping region, our approach helps in establishing clear boundaries for separating classes. We have implemented our proposed approach on two real world highly imbalanced dataset which have diverse ratio of imbalance. We have compared our approach with existing resampling and ensemble approaches on these two dataset. This SMENN based neural network classification achieves accuracy of 99.97% and 98.68% on both datasets. It also performs better in terms of precision, recall, F1-Score and AU-ROC curves. We conclude that because of the noise reduction, the proposed model has obtain optimal results for accuracy and AU-ROC.

References

1. T. Hasanin, T. Khoshgoftaar, "The Effects of Random Undersampling with Simulated Class Imbalance for Big Data", 2018, *IEEE International Conference on Information Reuse and Integration for Data Science*, IEEE, Salt Lake City, USA, pp. 70–79.

2. X. Guo, Y. Yin1, C. Dong, G. Yang, G. Zhou, "On the Class Imbalance Problem", 2008, *Fourth International Conference on Natural Computation*, IEEE, Shadong, China, pp. 192–201.
3. C. Seiffert, T. Khoshgoftaar, "RUSBoost: A Hybrid Approach to Alleviating Class Imbalance", 2010, *IEEE Transaction on Systems, Man, and Cybernatics*, Vol. 40, No. 1, pp. 185–197.
4. L. Lusa, R. Blagus, "The class-imbalance problem for high-dimensional class prediction", 2012, *11th International Conference on Machine Learning and Applications*, IEEE, Florida, USA, pp. 123–135.
5. E. Silva, C. Zanchettin, "On the existence of a threshold in class imbalance problems", 2015, *IEEE International Conference on Systems, Man, and Cybernetics(SMC)*, IEEE, Kowloon Tong, Hong Kong, pp. 2714-2725.
6. F. Rayhan, S. Ahmed, A. Mahbub, M. Jani, S. Shatabda, "MEBoost: Mixing Estimators with Boosting for Imbalanced Data Classification", 2017, *11th International Conference on Software, Knowledge, Information Management and Applications (SKIMA)*, IEEE, Malabe, Srilanka, pp. 1–12.
7. C. Bellinger, S. Sharma, N. Japkowicz, "One-Class versus Binary Classification: Which and When?", 2012, *11th International Conference on Machine Learning and Applications (ICMLA)*, IEEE, Florida, USA, pp. 102–112.
8. D. Sotiropoulos, C. Giannoulis, and G. Tsihrintzis, "A Comparative Study of One-Class Classifiers in Machine Learning Problems with Extreme Class Imbalance", 2014, *5th International Conference on Information, Intelligence, Systems and Applications*, IEEE, Crete, Greece, pp. 1–3.
9. G. Stegmayer, "High class-imbalance in pre-miRNA prediction: a novel approach based on deepSOM", 2016, *IEEE/ACM Transaction on Computational Biology and Bioinformatics (TCBB)*, IEEE Computer Society Press, Los Alamitos(CA), USA, pp. 1–14.
10. M. Galar, A. Fernandez, E. Barrenechea, H. Bustince, "A Review on Ensembles for the Class Imbalance Problem : Bagging, Boosting and Hybrid-Based Approaches", 2012, *IEEE Transactions on System, Man and Cybernatics-Part C, Application and Reviews*, IEEE, Vol 42, No. 4, pp. 463–484.
11. Haitao Xiong, Junjie Wu, Lu Liu, "Classification with Class Overlapping : A Systematic Study", 2010, *Atlantis Press*, pp. 491–497.
12. Jaesub Yun, Jihyun Ha, Jong-Seok Lee, "Automatic Determination of Neighborhood Size in SMOTE", 2016, *10th International Conference on Ubiquitous Information Management and Communication-IMCOM'16*, ACM, Danang, Viet Nam, pp. 1–8.
13. Guo Haixiang, Jennifer Shang, Gu Mingyun, Huang Yuanyue, Gong Bing, "Learning from class-imbalanced data : Review of methods and applications", 2016, *Article in Expert Systems with Applications*, Elsevier Science, Vol. 73, pp. 220–239.
14. Nikolaos Nikolaou, Narayanan Edakunni, Meelis Kull, Peter Flach, Gavin Brown1, "Cost-sensitive boosting algorithms: Do we really need them?", Open Access article at Springerlink.com, pp. 359-384, 2016.
15. Danaipong Chetchotsak, Sirorat Pattanapairoj, Banchar Arnonkijpanich, "Integrating new data balancing technique with committee networks for imbalanced data: GRSOM approach", 2015, *Cognitive Neurodynamics*, Springer, Vol. 9, Issue 9, pp. 627–638.
16. Mikel Galar, Alberto Fernandezb, Edurne Barrenecheaa, Francisco Herrerac, "EUSBoost: Enhancing Ensembles for Highly Imbalanced Data-sets by Evolutionary Undersampling", 2013, *Pattern Recognition*, Elsevier Science, Vol. 46, Issue 12, pp. 3460–3471.
17. Zhongbin Sun, Qinbao Song, Xiaoyan Zhu, Heli Sun, Baowen Xu, Yuming Zhou, "A Novel Ensemble Method for Classifying Imbalanced Data", 2014, *Pattern Recognition*, Elsevier Science, Vol. 48, Issue 5, pp. 1623–1637.

18. Zhongbin Sun, Qinbao Song, Xiaoyan Zhu, Heli Sun, Baowen Xu, Yuming Zhou, "A Novel Ensemble Method for Classifying Imbalanced Data", 2014, *Pattern Recognition*, Elsevier Science, Vol. 48, Issue 5, pp. 1623–1637.
19. S.Wang and X. Yao, "Diversity analysis on imbalanced data sets by using ensemble models", 2009, *IEEE Symposium on Computational Intelligence and Data Mining (CIDM)*, IEEE, Nashville, TN, USA, pp. 324–331.
20. Hui Han, Wen-Yuan Wang, and Bing-Huan Mao, "Borderline-SMOTE: A New Over-Sampling Method in Imbalanced Data Sets Learning", 2005, *International Conference on Intelligent Computing ICIC Advances in Intelligent Computing*, Springer, Berlin, Vol. 3644, pp. 878–887.
21. Zeping Yang, and Daqi Gao, "Classification for Imbalanced and Overlapping Classes Using Outlier Detection and Sampling Techniques", 2013, *An International Journal of Applied Mathematics & Information Sciences* , NSP, vol. 7, No. 1, pp. 375–381.
22. Dubey Rashmi, Zhou Jiayu, Wang Yalin, Thompson Paul M., Ye Jieping, "Analysis of sampling techniques for imbalanced data: An ADNI study", 2014, *NeuroImage*, Elsevier Science, Vol. 87, pp. 220–241.
23. Jing Wang, Min-Ling Zhang, "Towards Mitigating the Class-Imbalance Problem for Partial Label Learning", 2018, *24th International Conference on Knowledge Discovery & Data Mining (KDD)*, ACM, London, United Kingdom, pp. 2427–2436.
24. Bartosz Krawczyk, M. Wozniak, G. Schaefer, "Cost-sensitive decision tree ensembles for effective imbalance classification", 2014, *Applied Soft Computing*, Elsevier Science, Vol. 14, pp. 554–562.
25. Silvia Cateni, Valentina Colla, Marco Vannucci, "A method for resampling imbalanced datasets in binary classification tasks for real-world problems", 2014, *Neurocomputing*, Elsevier Science, Vol. 135, pp. 32–41.
26. Jihyun Ha, Jong-Seok Lee, "A New Under-Sampling Method Using Genetic Algorithm for Imbalanced Data Classification", 2016, *10th International Conference on Ubiquitous Information Management and Communication-IMCOM'16*, ACM, Danang, Viet Nam, pp. 1–6.

Stability and Bifurcation Analysis of a Ratio Dependent Discrete Prey-Predator Model with Chaos-Control

Prabir Chakraborty
Govt. General Degree College, Muragachha,Nadia, West Bengal, India
Email: prabirchakrabortry@gmail.com

Susmita Sarkar
Department of Applied Mathematics, University of Calcutta, Kolkata, India.
Email: susmita62@yahoo.co.in

*Uttam Ghosh
Department of Applied Mathematics, University of Calcutta, Kolkata, India.
Email: uttam_math@yahoo.co.in

Abstract. In this paper we have studied a discrete prey-predator model with ratio dependent functional response. We have discussed the existence of fixed points, their feasibility and stability algebraically. We studied Flip and Neimark-Sacker bifurcation algebraically. Then under some parametric conditions bifurcation (flip and Neimark-Sacker) and chaos analysis of the model have been carried out numerically with respect to the prey intrinsic growth rate. Theoretical results have been justified by numerical simulation. We have also studied the behavior of the system by analyzing parametric basin of attraction in two parametric space comparing intrinsic growth rate and time step. We measured the Lyapunov exponent and fractal dimension to confirm its chaotic dynamics. Finally an idea of chaos control have been proposed.

Mathematics Subject Classification: 39A30, 92D25, 92D50.

Keywords: Discrete predator – prey system · Fixed points · stability · Flip bifurcation · Neimark-Sacker bifurcation · Basin of attraction · Fractal dimension · Chaos control.

1 Introduction

The dynamical relationship between predators and prey has become an open challenge in mathematical ecology due to its universal existence and importance[1]. Many ecological evidences [2]-[4] shows that there are environment, in which the predators are in search for food (i.e. they share or fight for food). Then ratio-dependent model is more suitable, which can be defined as the per capita predator growth rate (a function of the ratio of prey to predator abundance). Here we will analyzed a ratio-dependent type prey-predator model with Michaelis-Menten type functional response [5]-[10], as

in the normalized form,

$$\begin{cases} \frac{dx}{dt} & = rx(1-x) - \frac{bxy}{x+my} \\ \frac{dy}{dt} & = -dy + \frac{fxy}{x+my} \end{cases} \tag{1}$$

where x, y indicate prey and predator density respectively. Here the parameters b, d, f, m and r satisfy the positivity condition and represent capturing rate, predator death rate, conversion rate, carrying capacity, prey intrinsic growth rate respectively. The above model (1) is considered when the population size is large. But if the population size is small or birth or death rate occurs at discrete time within the certain interval of time [11] or the population have the non-overlapping generation then the discrete model is more significant than the continuous model [12]-[14]. Now applying forward Eular scheme to the above system we get the discrete predator-prey system as follows:

$$\begin{cases} x_{n+1} & = x_n + hx_n(r(1-x_n) - \frac{by_n}{x_n+my_n}) \\ y_{n+1} & = y_n + hy_n(-d + \frac{fx_n}{x_n+my_n}) \end{cases} \tag{2}$$

where h is the step size of the discretization.

2 Qualitative study of the model

In this section we will investigate the existence and feasibility of the fixed points of the discrete dynamical system (2) and their stability conditions.

2.1 The existence of the fixed points and their feasibility

To find the fixed points of the discrete dynamical system (2), we have to solve the nonlinear system given by

$$\begin{cases} x & \Longrightarrow x + hx(r(1-x) - \frac{by}{x+my}) \\ y & \Longrightarrow y + hy(-d + \frac{fx}{x+my}) \end{cases} \tag{3}$$

The above system has three fixed points:

1. The trivial fixed point $E_0(0,0)$ is always feasible.
2. The axial fixed point $E_1(1,0)$ is always feasible.
3. The interior fixed point $E_2(x^*, y^*)$ where $x^* = 1 - \frac{b(f-d)}{mrf}$, $y^* = \frac{f-d}{md}x^*$ is feasible if $\frac{b(f-d)}{mrf} < 1$ and $f > d$.

2.2 Stability analysis of the fixed point

Now we shall discussed the local stability of the system (3) about every fixed point. The Jacobian matrix of (3) at (x, y) is given by

$$J(x,y) = \begin{pmatrix} j_{11} & j_{12} \\ j_{21} & j_{22} \end{pmatrix} \tag{4}$$

where

$$\begin{cases} j_{11} = 1 + h[r(1-x) - \frac{by}{x+my}] + hx[-r + \frac{by}{(x+my)^2}]; \quad j_{12} = -\frac{hbx^2}{(x+my)^2}; \\ j_{21} = \frac{hfmy^2}{(x+my)^2}; \quad j_{22} = 1 + h[-d + \frac{fx}{x+my}] - hy\frac{mfx}{(x+my)^2}. \end{cases} \tag{5}$$

Now the characteristic equation of this jacobian matrix (4) is

$$\lambda^2 - Tr(J)\lambda + Det(J) = 0 \tag{6}$$

where λ is the eigenvalue and $Tr(J)$ and $Det(J)$ are the trace and determinant of the above Jacobian matrix (4) respectively.

$$Tr(J) = j_{11} + j_{22}; \qquad Det(J) = j_{11}j_{22} - j_{12}j_{21} \tag{7}$$

Proposition 1. *The fixed point $E_0(0,0)$ is*

- *source if $d > \frac{2}{h}$.*
- *saddle if $0 < d < \frac{2}{h}$.*
- *non-hyperbolic if $d = \frac{2}{h}$.*

Proposition 2. *The fixed point $E_1(1,0)$ is*

- *sink if $0 < r < \frac{2}{h}$ and $\frac{f}{h} < d < \frac{2+f}{h}$.*
- *source if $r > \frac{2}{h}$ and $\frac{2+f}{h} < d < \frac{f}{h}$.*
- *saddle if $0 < r < \frac{2}{h}$ and $\frac{2+f}{h} < d < \frac{f}{h}$ or $r > \frac{2}{h}$ and $\frac{f}{h} < d < \frac{2+f}{h}$.*
- *non hyperbolic if either $r = \frac{2}{h}$ or $d = \frac{f}{h}$ or $d = \frac{2+f}{h}$.*

Thus for the fixed point $E_1(1,0)$ if $(h,r,b,m,d,f) \in R$ where $R = \{(h,r,b,m,d,f)/h = \frac{2}{r}, d \neq \frac{f}{h}, d \neq \frac{2+f}{h}, h,r,b,m,d,f > 0\}$ then one of the eigenvalue of $J(E_1)$ is -1 and the other is $\lambda = 1 - hd + f$ which is neither 1 nor -1. Therefore there is a flip bifurcation at the fixed point E_1 if h varies in the small neighborhood of $h = \frac{2}{r}$ and $(h,r,b,m,d,f) \in R$.

Now, at the interior equilibrium point (x^*, y^*) the characteristic equation of the Jacobian matrix J of the system (3) can be written as

$$\lambda^2 - Tr(J(E^*))\lambda + Det(J(E^*)) = 0 \tag{8}$$

where

$$Tr(J(E^*)) = 2 + hM \tag{9}$$

$$Det(J(E^*)) = 1 + hM + h^2N \tag{10}$$

Here

$$\begin{cases} M = -r + \frac{(f-d)}{mf}\left[b + \frac{d}{f}(b - mf)\right]; \\ N = \frac{d(f-d)}{f}\left[r - \frac{b(f-d)}{mf}\right] \end{cases} \tag{11}$$

Now let

$$F(\lambda) = \lambda^2 - Tr(J(E^*))\lambda + Det(J(E^*)) = \lambda^2 - (2 + hM)\lambda + (1 + hM + h^2N)$$

Therefore $F(1) = h^2N$ and $F(-1) = 4 + 2hM + h^2N$.Thus we can conclude[9],

Proposition 3. *The fixed point $E_2(x^*, y^*)$ is*

- *sink if one of the following condition holds,*
  1. $M^2 - 4N \geq 0$ *and* $0 < h < \frac{-M-\sqrt{M^2-4N}}{N}$.
  2. $M^2 - 4N < 0$ *and* $0 < h < -\frac{M}{N}$.
- *source if one of the following condition holds,*
  1. $M^2 - 4N \geq 0$ *and* $h > \frac{-M+\sqrt{M^2-4N}}{N}$.
  2. $M^2 - 4N < 0$ *and* $h > -\frac{M}{N}$.
- *non-hyperbolic if one of the following condition holds,*
  1. $M^2 - 4N \geq 0$ *and* $h = \frac{-M\pm\sqrt{M^2-4N}}{N}$.
  2. $M^2 - 4N < 0$ *and* $h = -\frac{M}{N}$.
- *saddle for all values of the parameter except for those values mention in the above three cases.*

Now if non-hyperbolic condition (1) of Proposition 3 holds then the one of the eigenvalue of $E_2(x^*, y^*)$ is -1 and other is neither 1 nor -1. Thus condition (1) of non-hyperbolic case can be written as,

$$FB_1 = \{(h, r, b, m, d, f)/h = \frac{-M - \sqrt{M^2 - 4N}}{N}, M^2 - 4N \geqslant 0, h, r, b, m, d, f > 0\}$$

$$FB_2 = \{(h, r, b, m, d, f)/h = \frac{-M + \sqrt{M^2 - 4N}}{N}, M^2 - 4N \geqslant 0, h, r, b, m, d, f > 0\}$$

Then the model (3) undergoes through Flip bifurcation in the neighborhood of (x^*, y^*) in the domain FB_1 and FB_2. Now if non-hyperbolic condition (2) of Proposition 3 holds then the eigenvalue of $E_2(x^*, y^*)$ are a pair of complex conjugate numbers with modulus 1. Thus condition (2) of non-hyperbolic case can be written as,

$$NSB = \{(h, r, b, m, d, f)/h = -\frac{M}{N}, M^2 - 4N < 0, h, r, b, m, d, f > 0\}$$

Then the model (3) undergoes through Neimark-Sacker bifurcation in the neighborhood of (x^*, y^*) in the domain NSB.

We draw a flowing diagram for the parameter set $m = 0.7; f = 1.2; d = 0.9; b = 1.1$ and $h \in [0, 12], r \in [0, 5]$ where blue and green curve indicate Flip and Neimark-Sacker bifurcation. The fixed points in cyan region are stable, in the yellow and magenta region are unstable and in the white region are saddle. In the Fig. 1 we can observe the Neimark-Sacker bifurcation at $(0.8, 0.4778)$ and flip bifurcation at $(0.8, 3.2166)$. [Detailed numerical analysis at that points given in Section 3].

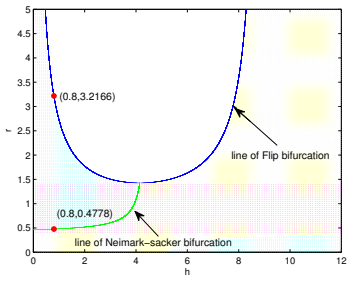

Fig. 1: Flip and Neimark-sacker bifurcation curve, stable and unstable regions.

2.3 Flip Bifurcation

For the fixed point $E_1(1,0)$ of the system (3) if $(h,r,b,m,d,f) \in R$ where $R = \{(h,r,b,m,d,f)/h = \frac{2}{r}, d \neq \frac{f}{h}, d \neq \frac{2+f}{h}, h,r,b,m,d,f > 0\}$ one of the eigenvalue of $J(E_1)$ is -1 and the other is $\lambda = 1 - hd + f$ which is neither 1 nor -1. Therefore there is a flip bifurcation at the fixed point E_1 if r varies in the small neighborhood of $r = r_0 = \frac{2}{h}$ and $(h,r,b,m,d,f) \in R$. Giving a perturbation $\overline{r}$ (where $\overline{r} \ll 1$) of the parameter r about $r = r_0$ to the system (3) we have

$$\begin{cases} x = x + h[(r_0 + \overline{r})x(1-x) - \frac{bxy}{x+my}] \\ y = y + h[-dy + \frac{fxy}{x+my}] \end{cases} \tag{12}$$

Let $u = x - x_1$, $v = y - y_1$. Then we transfer the fixed point $E_1(1,0)$ of the map (12) to the origin and we have

$$\begin{cases} u = u + h[(r_0 + \overline{r})(u+x_1)(1-u-x_1) - \frac{b(u+x_1)(v+y_1)}{u+x_1+m(v+y_1)}] \\ v = v + h[-d(v+y_1) + \frac{f(u+x_1)(v+y_1)}{u+x_1+m(v+y_1)}] \end{cases} \tag{13}$$

Expanding (13) in Taylor series at $(u,v,\overline{r}) = (0,0,0)$ keeping up-to second order terms we have,

$$\begin{cases} u &= a_{11}u + a_{12}v + a_{13}u^2 + a_{14}uv + a_{15}v^2 + b_{11}\overline{r} + b_{12}u\overline{r} + b_{14}u^2\overline{r} + o(u,v)^3 \\ v &= a_{21}u + a_{22}v + a_{23}u^2 + a_{24}uv + a_{25}v^2 + o(u,v)^3 \end{cases} \tag{14}$$

where

$$\begin{aligned} &a_{11} = 1 - r_0h; \quad a_{12} = -bh; \quad a_{13} = -r_0h; \quad a_{14} = 0; \\ &a_{15} = bhm; \quad b_{11} = 0; \quad b_{12} = -\frac{h}{2}; \quad b_{14} = -\frac{h}{3}; \quad a_{21} = 0; \\ &a_{22} = 1 - dh + fh \quad a_{23} = 0; \quad a_{24} = 0; \quad a_{25} = -fhm. \end{aligned} \tag{15}$$

We now define an invertible matrix
$T = \begin{pmatrix} a_{12} & a_{12} \\ -1 - a_{11} & \lambda_2 - a_{11} \end{pmatrix}$ and use the transformation $\begin{pmatrix} u \\ v \end{pmatrix} = T \begin{pmatrix} x \\ y \end{pmatrix}$. Then model (14) becomes,

$$\begin{pmatrix} x \\ y \end{pmatrix} = \begin{pmatrix} -1 & 0 \\ 0 & \lambda_2 \end{pmatrix} \begin{pmatrix} x \\ y \end{pmatrix} + \begin{pmatrix} f(u,v,\overline{r}) \\ g(u,v,\overline{r}) \end{pmatrix}$$

where

$$\begin{aligned} f(u,v,\overline{r}) = \frac{1}{Det(T)}\{&(\lambda_2 - a_{11})a_{13}u^2 + [(\lambda_2 - a_{11})a_{15} - a_{12}a_{25}]v^2 \\ &+ (\lambda_2 - a_{11})b_{12}u\overline{r} + (\lambda_2 - a_{11})b_{14}u^2\overline{r} + O(u,v,\overline{r})\} \\ g(u,v,\overline{r}) = \frac{1}{Det(T)}\{&(1 + a_{11})a_{13}u^2 + [(1 + a_{11})a_{15} - a_{12}a_{25}]v^2 \\ &+ (1 + a_{11})b_{12}u\overline{r} + (1 + a_{11})b_{14}u^2\overline{r} + O(u,v,\overline{r})\} \end{aligned}$$

From the center manifold theorem of Guckenheimer [15] and Robinson [16], we know that there exists center manifold $W^c(0,0)$ of model (3) at equilibrium point $(0,0)$ in the small neighborhood of $\overline{r} = 0$, whose approximate representation is given as: $W^c(0,0) = \{(x,y) : y = a_0\overline{r} + a_1x^2 + a_2x\overline{r} + a_3\overline{r}^2 + O(|x| + |\overline{r}|)^3\}$ Here

$$a_0 = 0; \quad a_2 = -\frac{a_{12}(1+a_{11})b_{12}}{Det(T)\lambda_2(\lambda_2-1)}; \quad a_3 = 0.$$
$$a_1 = \frac{1}{Det(T)(\lambda_2-2)}\{(1+a_{11})a_{13}a_{12}^2 + [(1+a_{11})a_{15} + a_{12}a_{25}]\}.$$

We can now write u, v in terms of $x, y, \overline{r}$ as

$$\begin{cases} u &= a_{12}(x + a_1x^2 + a_2x\overline{r}) \\ v &= -(1+a_{11})x + (\lambda_2 - a_{11})(a_1x^2 + a_2x\overline{r}) \end{cases}$$

Thus the map G^* , which is restricted to the center manifold $W^c(0,0)$ is

$$G^*(x) = x + f(u,v,\overline{r}) = x + h_0\overline{r} + h_1x^2 + h_2x\overline{r} + h_3\overline{r}^2 + h_4x^2\overline{r} + h_5x\overline{r}^2 + h_6x^3 + h_7\overline{r}^3 + O(|x| + |\overline{r}|)^3$$

where

$h_0 = 0; \quad h_3 = 0; \quad h_7 = 0$

$$h_1 = \frac{1}{Det(T)}\{(\lambda_2 - a_{11})a_{13}a_{12}^2 + [(\lambda_2 - a_{11})a_{15} - a_{12}a_{25}](1+a_{11})^2\};$$

$$h_2 = \frac{1}{Det(T)}\{-2[(\lambda_2 - a_{11})a_{15} - a_{12}a_{25}](1+a_{11})(\lambda_2 - a_{11}) + a_{12}(\lambda_2 - a_{11})b_{12}\};$$

$$h_4 = \frac{1}{Det(T)}\{(\lambda_2 - a_{11})a_{13}a_{12}^2(2a_2+1) - 2a_2[(\lambda_2 - a_{11})a_{15} - a_{12}a_{25}](\lambda_2 - a_{11})(1+a_{11}) + (\lambda_2 - a_{11})b_{12}a_1a_{12}(1+a_{11})^2\};$$

$$h_5 = \frac{1}{Det(T)}\{-2a_2[(\lambda_2 - a_{11})a_{15} - a_{12}a_{25}](\lambda_2 - a_{11})(1+a_{11}) + a_2a_{12}(1+a_{11})^2(\lambda_2 - a_{11})b_{12}\};$$

$$h_6 = \frac{1}{Det(T)}2a_{12}^2a_1(\lambda_2 - a_{11})a_{13}.$$

For flip bifurcation we require to show that two discriminatory quantities β_1 and β_2 be non-zero,

$$\begin{cases} \beta_1 &= \left(\frac{\partial^2 G}{\partial x \partial \overline{r}} + \frac{1}{2}\frac{\partial G}{\partial \overline{r}} \times \frac{\partial^2 G}{\partial x^2}\right)\Big|_{(0,0)} = h_2 \neq 0 \\ \beta_2 &= \left(\frac{1}{6}\frac{\partial^2 G}{\partial x^2} + \left(\frac{1}{2}\frac{\partial G}{\partial x}\right)^2\right)\Big|_{(0,0)} = h_6 + h_1^2 \neq 0 \end{cases} \tag{16}$$

Thus, from the above analysis and Theorem 3.1 of Guckenheimer[15] we have the following result.

Theorem 1. *If $\beta_1 \neq 0$ and $\beta_2 \neq 0$, then the model (3) undergoes flip bifurcation at $E_1(1,0)$ when the parameter r varies in the small neighborhood of $\overline{r}$. Moreover if $\beta_2 > 0$ (res. $\beta_2 < 0$), then the period-2 points that bifurcate from E_1 are stable (respectively, unstable).*

In the next section we will investigate the conditions of Neimark-Sacker bifurcation using the center manifold theory.

2.4 Neimark-Sacker Bifurcation

The characteristic equation (6) associated with the map (3) at $E_2^*(x^*, y^*)$ is given by

$$\lambda^2 - Tr(J(E^*))\lambda + Det(J(E^*)) = 0$$

Now roots of the characteristic equation at E^* are a pair of complex conjugate numbers λ_1, λ_2 is given by

$$\lambda_{1,2} = \frac{Tr(J(E^*)) \pm i\sqrt{4Det(J(E^*)) - (Tr(J(E^*))^2}}{2}$$

where $Tr(J(E^*)), Det(J(E^*))$ are given in (9), (10) respectively. Now the Neimark-Sacker bifurcation occur when the roots of the above equation are complex conjugate with unit modulus. Let it be occur for $r = r_1$ and we construct a set $NSB = \{(h, r, b, m, d, f)/r = r_1 = \frac{f-d}{mkf}[bk - \frac{d}{f}(b - mf)], M^2 - 4N < 0, h, r, b, m, d, f > 0\}$ (Where $k = -1 + hd\frac{(f-d)}{f}$, and M, N are defined in (11)). If we vary r in the neighborhood of $r = r_1$ keeping other parameters in NSB then the endemic equilibrium point goes through Neimark-sacker bifurcation.

Giving a perturbation r^* (where $r^* \ll 1$) of the parameter r at the neighborhood of $r = r_1$ in the map (3) we have

$$\begin{cases} x \Longrightarrow x + h[(r_1 + r^*)x(1 - x) - \frac{bxy}{x+my}] \\ y \Longrightarrow y + h[-dy + \frac{fxy}{x+my}] \end{cases} \tag{17}$$

let $u = x - x^*, v = y - y^*$. Thus from (17) we set

$$\begin{cases} u \Longrightarrow u + h[(r_1 + r^*)(u + x^*)(1 - u - x^*) - \frac{b(u+x^*)(v+y^*)}{(u+x^*)+m(v+y^*)}] \\ v \Longrightarrow v + h[-d(v + y^*) + \frac{f(u+x^*)(v+y^*)}{(u+x^*)+m(v+y^*)}] \end{cases} \tag{18}$$

Expanding above in Taylor series at $(u, v, r^*) = (0, 0, 0)$ considering up to second order we have

$$\begin{cases} u = c_{11}u + c_{12}v + c_{13}u^2 + c_{14}uv + c_{15}v^2 + d_{11}r^* + d_{12}ur^* + d_{14}u^2r^* + o(u, v)^3 \\ v = c_{21}u + c_{22}v + c_{23}u^2 + c_{24}uv + c_{25}v^2 + o(u, v)^3 \end{cases} \tag{19}$$

where

$$
\begin{aligned}
&c_{11} = 1 + r_1 h - 2r_1 h x^* - \frac{bmhy^{*2}}{(x^* + my^*)^2} \quad c_{12} = \frac{-bhx^{*2}}{(x^* + my^*)^2};\\
&c_{13} = -r_1 h + \frac{mbhy^{*2}}{(x^* + my^*)^3}; \quad c_{14} = -\frac{mbhx^* y^*}{(x^* + my^*)^3}; \quad c_{15} = \frac{mbhx^{*2}}{(x^* + my^*)^3}\\
&d_{11} = hx^* - hx^{*2}; \quad d_{12} = \frac{h}{2}[1 - 2x^*] \quad d_{14} = -\frac{h}{3};\\
&c_{21} = \frac{fhmy^{*2}}{(x^* + my^*)^2}; \quad c_{23} = -\frac{fhmy^{*2}}{(x^* + my^*)^3} \quad c_{22} = 1 + h[-d + \frac{fx^{*2}}{(x^* + my^*)^2}]\\
&c_{24} = \frac{fhmx^* y^*}{(x^* + my^*)^3}; \quad c_{25} = -\frac{fhmx^{*2}}{(x^* + my^*)^3}
\end{aligned}
\tag{20}
$$

The roots of the characteristic equation associated with the linearized map (19) at $(u, v) = (0, 0)$ is given by

$$\lambda_{1,2} = \frac{Tr(J(r^*)) \pm i\sqrt{4Det(J(r^*)) - (Tr(J(r^*))^2}}{2}$$

From $|\lambda_{1,2}(r^*)| = 1$, when $r^* = 0$ we have $|\lambda_{1,2}(r^*)| = [Det(J(r^*))]^{\frac{1}{2}}$ and

$$l = \frac{d|\lambda_{1,2}|}{dr}\bigg|_{r=r^*} = \frac{1}{2}\left[-h + h^2\frac{d(f-d)}{f}\right] \neq 0 \tag{21}$$

In addition it is required that when $r^* = 0, \lambda_{1,2}^i \neq 1, i = 1, 2, 3, 4$, which is equivalent to $Tr(J(0)) \neq -2, -1, 1, 2$.
Next we study the normal from of (18). Let $\alpha_1 = Real(\lambda_{1,2})$ and $\beta_1 = Im(\lambda_{1,2})$, and define the invertible matrix $T = \begin{pmatrix} 0 & 1 \\ \beta_1 & \alpha_1 \end{pmatrix}$ and use the transformation $\begin{pmatrix} u \\ v \end{pmatrix} = T\begin{pmatrix} X \\ Y \end{pmatrix}$,then the system (17) reduces into the following form

$$\begin{pmatrix} X \\ Y \end{pmatrix} = \begin{pmatrix} \alpha_1 & -\beta_1 \\ \beta_1 & \alpha_1 \end{pmatrix}\begin{pmatrix} X \\ Y \end{pmatrix} + \begin{pmatrix} F(u, v, r^*) \\ G(u, v, r^*) \end{pmatrix} \tag{22}$$

where

$$
\begin{cases}
F(u, v, r^*) & = \frac{1}{\beta_1}[(\alpha_1 c_{13} - c_{23})u^2 + (\alpha_1 c_{14} - c_{24})uv + (\alpha_1 c_{15} - c_{25})v^2 \\
& \qquad +\alpha_1 d_{11} r^* + \alpha_1 d_{12} u r^* + \alpha_1 d_{14} u^2 r^* + O(u, v)^3] \\
G(u, v, r^*) & = [c_{13}u^2 + c_{14}uv + c_{15}v^2 + d_{11}r^* + d_{12}ur^* + d_{14}u^2 r^* + O(u, v)^3]
\end{cases}
\tag{23}
$$

writing $u = Y, \quad v = \beta_1 X + \alpha_1 Y$ we get,

$$
\begin{cases}
F(X, Y) & = \frac{1}{\beta_1}[(\alpha_1 c_{13} - c_{23})Y^2 + (\alpha_1 c_{14} - c_{24})Y(\beta_1 X + \alpha_1 Y) + (\alpha_1 c_{15} - c_{25}) \\
& \quad (\beta_1 X + \alpha_1 Y)^2 + \alpha_1 d_{11} r^* + \alpha_1 d_{12} Y r^* + \alpha_1 d_{14} Y^2 r^* + O(X, Y)^3] \\
G(X, Y) & = [c_{13}Y^2 + c_{14}Y(\beta_1 X + \alpha_1 Y) + c_{15}(\beta_1 X + \alpha_1 Y)^2 + d_{11}r^* \\
& \qquad +d_{12}Yr^* + d_{14}Y^2 r^* + O(X, Y)^3]
\end{cases}
\tag{24}
$$

Now the considered model goes through the Neimark-Sacker Bifurcation if the following condition satisfied[15],

$$l_1 = -Re\left\{\frac{(1-2\bar{\lambda})\bar{\lambda}^2}{1-\lambda}\xi_{11}\xi_{20}\right\} - \frac{1}{2}|\xi_{11}|^2 - |\xi_{02}|^2 + Re(\bar{\lambda}\xi_{21}) \neq 0 \qquad (25)$$

where

$$\xi_{11} = \frac{1}{4}[F_{XX} + F_{YY} + i(G_{XX} + G_{YY})]$$
$$\xi_{20} = frac18[F_{XX} - F_{YY} + 2G_{XY} + i(G_{XX} - G_{YY} + 2F_{XY})]$$
$$\xi_{02} = \frac{1}{8}[F_{XX} - F_{YY} + 2G_{XY} + i(G_{XX} - G_{YY} - 2F_{XY})]$$
$$\xi_{21} = \frac{1}{16}[F_{XXX} + F_{XYY} + G_{XXY} + G_{YYY} + i(G_{XXX} + G_{XYY} - F_{XXY} - F_{YYY})]$$

here by calculation we have,

$$F_{XX} = 2(\alpha_1 c_{15} - c_{25}); \quad G_{XX} = 2c_{15}\beta_1;$$
$$F_{YY} = \frac{2}{\beta_1}[(\alpha_1 c_{13} - c_{23}) + \alpha_1(\alpha_1 c_{14} - c_{24}) + \alpha_1(\alpha_1 c_{15} - c_{25}) + \alpha_1 d_{14} r^*];$$
$$F_{XY} = \frac{1}{\beta_1}[(\alpha_1 c_{14} - c_{24})\beta_1 + 2(\alpha_1 c_{15} - c_{25})\alpha_1];$$
$$G_{YY} = 2c_{13} + 2\alpha_1 c_{14} + 2\alpha_1 c_{15} + 2d_{14} r^*; \quad G_{XY} = c_{14}\beta_1 + 2c_{15}\alpha_1;$$
$$F_{XXX} = F_{XYY} = F_{XXY} = F_{YYY} = G_{XXX} = G_{XYY} = G_{XXY} = G_{YYY} = 0.$$

Thus, eased on the above analysis we can obtained the following theorem:

Theorem 2. *If the condition (21) holds and l_1 defined in (25) is non-zero, then the model (3) undergoes Neimark-sacker bifurcation at the equilibrium point $E_2(x^*, y^*)$ provided the parameter r changes in the small neighborhood of $r = r_1$ and $(h, r, b, m, d, f) \in NSB$. Moreover, if $l_1 < 0$ (resp., $l_1 > 0$) then an attracting (resp., repelling) invariant closed curve bifurcate from the fixed point E_2 for $r > r_1$ (resp., $r < r_1$).*

3 Numerical Simulation

In this section, we represent the phase portraits and bifurcation diagrams of the model (3) to confirm the above theoretical analysis and show the complex dynamical behavior by using numerical simulations. Here we fix $h = 0.8, b = 1.1, d = 0.9, f = 1.2, m = 0.7$, and the initial value $(x_0, y_0) = (0.4, 0.2)$. By calculation we find that at $r = 0.4778$, we have the fixed point $(0.1778, 0.0846)$ and the corresponding eigenvalues $0.9939 \pm 0.1104i$ with modulus 1. Thus there should be a Neimark- Sacker bifurcation in the neighborhood of $r = 0.4778$. For $r = 3.2166$ we have the fixed point $(0.8779, 0.4180)$ and the corresponding eigenvalues are -1 and 0.7967. Thus there should be a Flip bifurcation in the neighborhood of $r = 3.2166$. Bifurcation can

be observed in Fig. 2(a) and 2(b) in (r, x) plane and in (r, y) plane respectively where r vary in the range $(0, 4.06)$. The Chaotic behavior is justified by considering maximal Lyapunov exponent diagram given in Fig. 2(c).

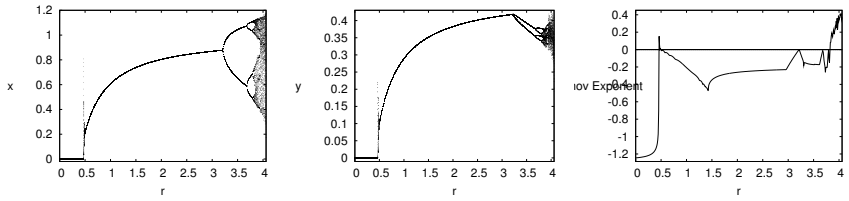

(a) (b) (c)

Fig. 2: Bifurcation diagram in the (a) (r, x) plane, (b) (r, y) plane and (c) Maximal Lynapunov exponent versus r for $h = 0.8, b = 1.1, d = 0.9, f = 1.2$ and $m = 0.7, r\epsilon(0, 4.06)$ and initial value $(x_0, y_0) = (0.4, 0.2)$.

Neimark- Sacker bifurcation at $r = 0.4778$ can be verified in the Fig. 3(a) which is a local amplification of the Fig. 2(a) in the range $r \in (0.465, 0.495)$. It shows that the fixed point (x^*, y^*) is stable when $r > 0.4778$ and loses its stability when $r = 0.4778$ and an invariant circle appear for $r < 0.4778$.

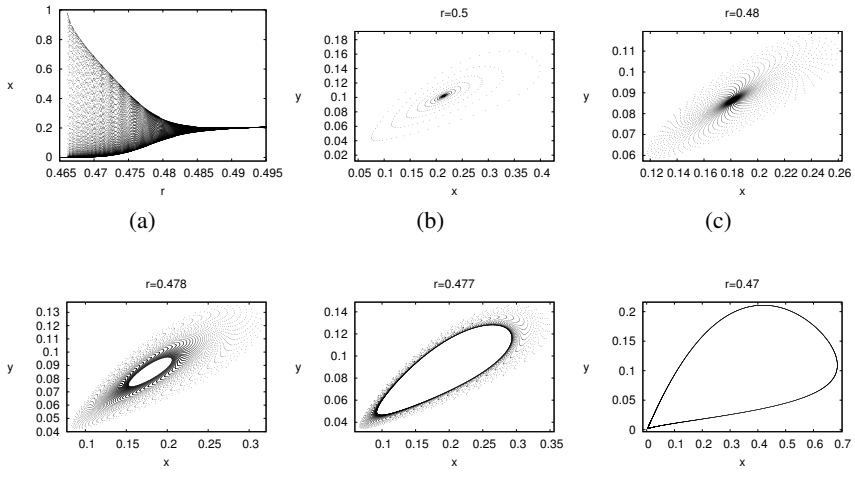

(a) (b) (c)

(d) (e) (f)

Fig. 3: (a)Neimark- Sacker Bifurcation diagram in the (r, x) plane for $h = 0.8, b = 1.1, d = 0.9, f = 1.2$ and $m = 0.7, r\epsilon(0.465, 0.495)$ and initial value $(x_0, y_0) = (0.4, 0.2)$ (b)-(f)Phase portraits for various values of r.

In Fig. 3(b)-3(f) phase portraits associated with the Fig. 3(a) are presented which clearly shows that how a stable fixed point bifurcates to a smooth invariant circle whose radius is gradually become larger with the decrease of r.

Flip bifurcation at $r = 3.2166$ can be verified in Fig. 4(a) which is a local amplification of the Fig. 2(a) in the range $r \in (3, 4.05)$. It shows that the fixed point (x^*, y^*) is stable when $r < 3.2166$ ans loses its stability when $r \geq 3.2166$. Period 2, 4, 8, 16, 32 orbits can be seen from Fig. 4(a). Fig. 4(b) is a local amplification of Fig. 4(a) in the range $r \in (3.866, 3.93)$. Period 10, 6 orbits can be seen here. Beyond this chaotic nature is observed. Phase portrait associated with Fig. 4(a) are given in Fig. 4(c)-(i). Different type of orbits can be verified there too.

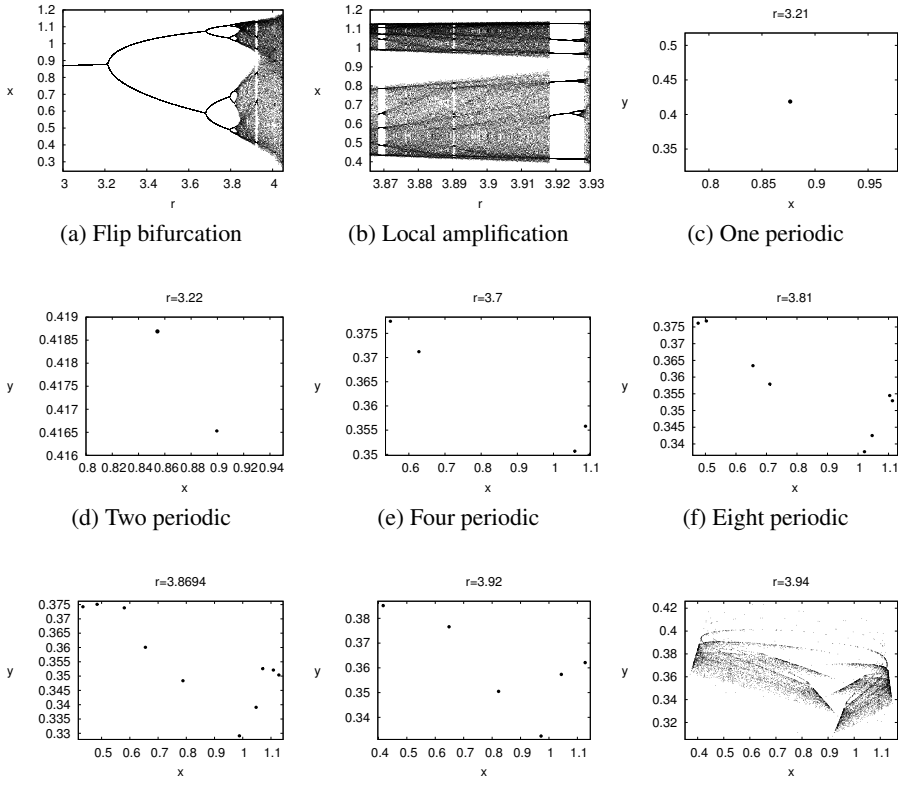

(a) Flip bifurcation (b) Local amplification (c) One periodic

(d) Two periodic (e) Four periodic (f) Eight periodic

(g) Ten periodic (h) Six periodic (i) Chaos

Fig. 4: (a)Flip Bifurcation diagram in the (r, x) plane for $h = 0.8, b = 1.1, d = 0.9, f = 1.2$ and $m = 0.7, r\epsilon(3, 4.05)$ and initial value $(x_0, y_0) = (0.4, 0.2)$ (b)Local amplification corresponding to Fig. 4(a) for $r \in [3.866, 3.93]$(c)-(i)-Phase portraits for various values of r corresponding to Fig. 4(a).

Above analysis shows that with $h = 0.8, b = 1.1, d = 0.9, f = 1.2, m = 0.7$, and the initial value $(x_0, y_0) = (0.4, 0.2)$ Neimark-Sacker bifurcation occurs at the lower end of the intrinsic growth rate $r = 0.4778$ of the prey population whereas flip bifurcation at the upper end $r = 3.2166$ which confirm the correctness of the proposition 3. Thus the model around the fixed point is stable when intrinsic growth rate r of the prey population lies in the range $0.4778 < r < 3.2166$ and loses stability out of this range. The predator-prey dynamics become chaotic when r crosses the value 3.2166. In section VI we shall see how this chaos can be controlled.

In the following Fig. 5 we demonstrate the sensitivity to the initial condition by choosing two initial point $(0.4, 0.2)$ and $(0.4001, 0.2001)$ with both x and y coordinate difference 0.0001 , and plotted against the parameter value $h = 0.8, b = 1.1, d = 0.9, r = 3.94, f = 1.2$ and $m = 0.7$. Fig. 5(a) and 5(b) shows a sensitive dependence on the initial condition for x-coordinate and y-coordinate respectively of the model (3), which is plotted against time. It shows that at the beginning the two time series are overlapped and indistinguishable; but after a number of iteration, the difference between them increase rapidly.According to the following Fig. 5 it is clear that the solution of system (3) is very sensitive to small change in the initial condition and hence chaotic dynamic is detected.

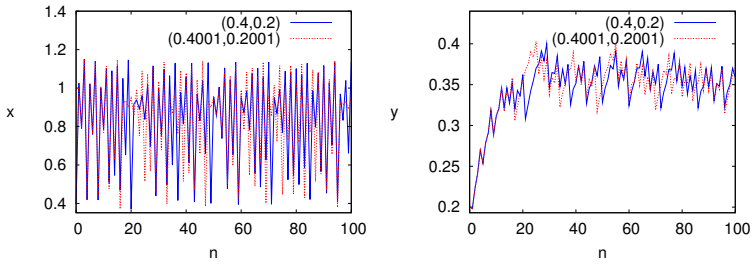

(a) (b)

Fig. 5: Sensitive dependence on the initial condition (a) in (n,x) plane and (b) in (n,y) plane, when the initial point $(0.4, 0.2)$ differ by 0.0001 in both x and y coordinate.

4 Parametric basins of attractions

In parametric basins of attractions[17] plot we matches different colors to periodic cycles of different periods in a two-dimensional parameter space. Here we plot for the set of parameter values $b = 0.06, d = 1, f = 1.4, m = 0.25$ and $r \in [0, 10]$, $h \in [0, 6.2]$ given in Fig. 6 (a). Fig. 6(b), 6(c) and 6(d) are the amplification of the Fig. 6(a) in the range $r \in [0, 10]$, $h \in [0, 0.6]$;$r \in [1.4, 2.4]$, $h \in [0.9, 1.6]$; $r \in [0.35, 0.64]$, $h \in [4.8, 6.2]$ respectively which represent how the dynamics of the system change as the prey intrinsic growth rate(r) vary with generation gap time(h). The different colors in the parametric plane (r, h) correspond to the following stable states: light bluish

violet for an attracting fixed point, dark blue represents a stable two-period cycle and yellow, pink, red, orange, light green, dark green, light blue, purple indicates three-period cycle, four-period cycle, five-period cycle, six-period cycle, seven-period cycle, eight-period cycle, nine-period cycle and ten-period cycle respectively. In the white region solutions can be quasi-periodic (invariant curves) or non-periodic (chaos; strange attractors) and in the black region solution diverges to infinity.

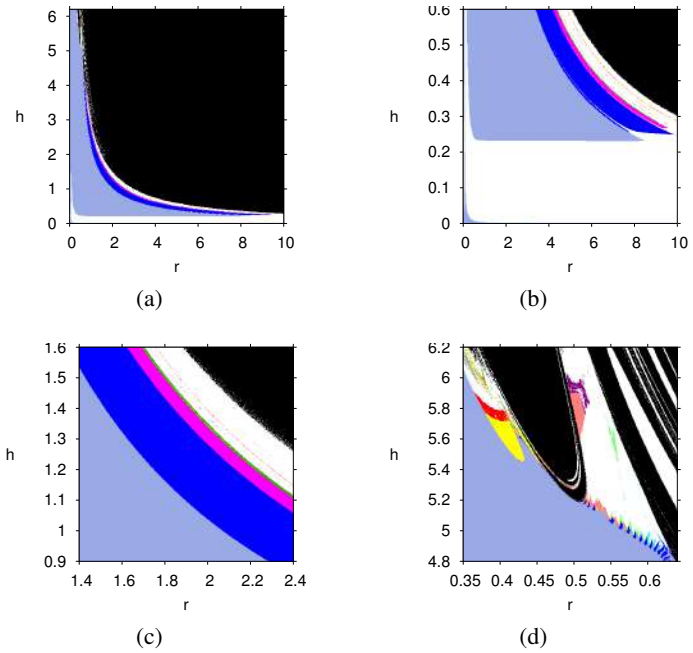

Fig. 6: The parametric basins of attraction in (r, h) plane

Observing the 2D parameter space we point out the followings:

- For the small value of h where $0 < h < 0.234$ [approximately] and different values of intrinsic growth rate(r) the system giving rise to a quasi-periodic (invariant curves) or non-periodic (chaos; strange attractors) behavior.
- For $h \in [0.234, 0.256]$ [approximately] as intrinsic growth rate(r) increases system passes through from a quasi-periodic or non-periodic orbit to stable equilibrium and then again to a aperiodic one.
- However, for even higher values of h [approximately $h = 0.256$ to $h = 4.25$], as intrinsic growth rate(r) increases, the stable fixed point goes through successive period-doubling bifurcations; two-period cycle (dark blue area), four-period cycle (pink area) and eight-period cycle (dark green area)and is giving rise to non-periodic behaviour (white area) then diverges to infinity. So, a large intrinsic growth rate(r) makes the system unstable with the increase of generation time gap(h).

– In the Fig. 6(d) we can observe different type of periodic cycle like period-2, 3, 4, 5, 6, 7, 8, 9, 10 with quasi-periodic and non-periodic regions shown in deferent color as $h \in [4.8, 6.2]$ and $r \in [0.35, 0.64]$.

5 Fractal Dimension

Strange attractors are characterized by the fractal dimension. Lyapunov exponent actually measure the chaos. The Lyapunov dimension is defined by $d_L = j + \frac{\sum_{i=1}^{i=j} \lambda_i}{|\lambda_j|}$,where $\lambda_1, \lambda_2, ...\lambda_n$ are Lyapunov exponents with j is the largest integer such that $\sum_{i=1}^{i=j} \lambda_i \geqslant 0$ and $\sum_{i=1}^{i=j+1} \lambda_i < 0$. Here the Lyapunov dimension of the two dimensional map (3) is of the form $d_L = j + \dfrac{\lambda_1}{|\lambda_2|}$, $\lambda_1 > 0 > \lambda_2$.

For the parameter set $h = 2.4, r = 1.2, b = 0.06, d = 1, f = 1.4, m = 0.25$ initial value $(0.3, 0.1)$ two Lyapunov exponent are estimated by computer simulation and are found as $\lambda_1 \approx 0.2383$and $\lambda_2 \approx -0.7946$ and the fractal dimension is 1.299 for $h = 2.4$.

For the parameter set $h = 2.44, b = 1.2, r = 0.95, d = 0.8, f = 1.2, m = 0.6$ and the initial value $(0.1, 0.2)$, two Lyapunov exponent are $\lambda_1 \approx 0.032268$and $\lambda_2 \approx -0.10379$ and the fractal dimension is 1.3109 for $h = 2.44$. The deviation of fractional dimension values from 1 to higher values is the indication of highly clumping boundary corresponding to the chaotic phase portrait zone.

6 Chaos Control

In this section , we used feedback control method[18,19] to stabilize chaotic orbits at an unstable positive fixed point of model (3). We consider the following controlled form of model (3):

$$\begin{cases} x & = x + hx(r(1-x) - \frac{by}{x+my}) + S \\ y & = y + hy(-d + \frac{fx}{x+my}) \end{cases} \tag{26}$$

with the following feedback control law as the control force:

$$S = -p_1(x - x^*) - p_2(y - y^*) \tag{27}$$

where p_1 and p_2 are the feedback gain and (x^*, y^*) is the positive fixed point of the model (3). Now the Jacobian matrix of the model (26) at the fixed point (x^*, y^*) is,

$$J(x^*, y^*) = \begin{pmatrix} j_{11-p_1} & j_{12} - p_2 \\ j_{21} & j_{22} \end{pmatrix} \tag{28}$$

where j_{11}, j_{12}, j_{21}, j_{22} are given in (5).The corresponding characteristic equation of the matrix $J(x^*, y^*)$ is,

$$\lambda^2 - (j_{11} + j_{22} - p_1)\lambda + j_{22}(j_{11} - p_1) - j_{21}(j_{12} - p_2) = 0 \tag{29}$$

Let λ_1 and λ_2 are the eigenvalues of (29), then

$$\begin{cases} \lambda_1 + \lambda_2 & = j_{11} + j_{22} - p_1 \\ \lambda_1\lambda_2 & = j_{22}(j_{11} - p_1) - j_{21}(j_{12} - p_2) \end{cases} \tag{30}$$

Then we find the lines of marginal stability by solving the equation $\lambda_1 = \pm 1$ and $\lambda_1\lambda_2 = 1$. These condition confirm that the eigenvalues λ_1 and λ_2 have modulus less than 1. Using $\lambda_1\lambda_2 = 1$ in (30) we have line l_1 as follows:

$$l_1 : \quad j_{22}p_1 - j_{21}p_2 = j_{11}j_{22} - 1 \tag{31}$$

Using $\lambda_1 = 1$ in (30) and (31) we have the line l_2 as follows,

$$l_2 : \quad (1 - j_{22})p_1 + j_{21}p_2 = j_{11} + j_{22} - 1 - j_{11}j_{22} + j_{12}j_{21} \tag{32}$$

Using $\lambda_1 = -1$ in (30) and (31) we have the line l_3 as follows,

$$l_3 : \quad (1 + j_{22})p_1 - j_{21}p_2 = j_{11} + j_{22} + 1 + j_{11}j_{22} - j_{12}j_{21} \tag{33}$$

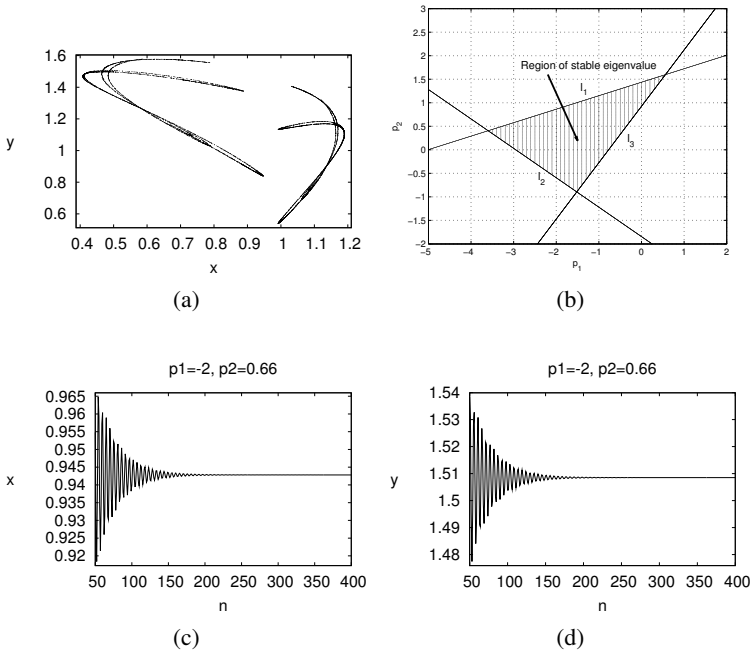

Fig. 7: (a)Phase portrait (a) Region for stable eigenvalues (b)-(c) time responses for the state x and y of the controlled model (25) for the feedback gain $p_1 = -2$ and $p_2 = 0.66$

The stable eigenvalues lie within the triangular region enclosed by the line l_1, l_2 and l_3. Therefore the numerical simulation can be done to control the unstable fixed point (x^*, y^*) by state feedback method.
For parameter set $h = 2.4, r = 1.2, b = 0.06, d = 1, f = 1.4$ and $m = 0.25$, and initial value $(x_0, y_0) = (0.3, 0.1)$ we draw the phase portrait given in Fig. 7(a) which is chaotic in nature. Now for the same set of parameter we have the region of stable eigenvalue given in Fig. 7(b). Choosing the feedback gain $p_1 = -2$ and $p_2 = 0.66$ in the triangular region, chaotic trajectory (given in Fig. 7(a)) can be stabilized at the fixed point $(0.9429, 1.5086)$(given in Fig. 7(c) and 7(d)).

7 Conclusion

In this paper we considered a discrete prey-predator model with ratio dependent functional response. From the analytical and numerical analysis it is clear that there exists different regions where the system is stable, unstable with Flip and Neimark-sacker bifurcation and chaotic. From the previous discussion it is clear that the intrinsic growth rate (r) and discretization factor (h, i.e. generation gap time) plays an important role for stabilization and dis-stabilization of the biological model. Here for the set of parameter value $h = 0.8, b = 1.1, d = 0.9, f = 1.2$ and $m = 0.7, r\epsilon(0, 4.06)$ and initial value $(x_0, y_0) = (0.4, 0.2)$ the system experiences sub-critical Neimark-sacker bifurcation, then stable then flip bifurcation and chaotic phenomenon with increase of intrinsic growth rate (r) i.e. in our model birth rate(r) plays an important role. The stable and chaotic behavior have been justified by calculating Lyapunov exponent in each case. Varying two control parameter(r and h) one can observe the chaotic phenomenon in two-dimensional parametric space which also explain how the system depend on the discretization factor. Finally by using Feedback chaos control method we are able to stabilize the chaos which has been justified for a particular parameter set given in section: VI. One can also investigate this model with Holling type I, II, III or even other different functional responses to investigate the dynamics of the system. One can also study the system by introducing allee effect and different hevesting terms.

References

1. A. A. Berryman, "The origins and evolution of predator-prey theory," Ecology, vol. 73, pp. 1530-1535, 1992.
2. R. Arditi, and A. A. Berryman, "The biological control paradox," Trends in Ecology and Evolution, vol. 6, pp. 32, 1991.
3. R. Arditi, and H. Saiah, "Empirical evidence of the role of heterogeneity in ratio-dependent consumption," Ecology, vol. 73, pp. 1544—1551, 1992.
4. L. R. Ginzburg, and H. R. Akcakaya, "Consequences of ratio-dependent predation for steady state properties of ecosystems," Ecology, vol. 73, pp. 1536—1543, 1992.
5. P. Chakraborty, U. Ghosh, and S. Sarkar, "Stability and bifurcation analysis of a ratio dependent discrete prey-predator model with linear harvesting," 4th Int'l Conf. on Recent Advances in Information Technology, IEEE Xplore, 2018.
6. D. Xiao and S. Ruan, "Global dynamics of a ratio-dependent predator-prey system," Journal of Mathematical Biology, vol. 43, no. 3, pp. 268–290, 2001.

7. S.-B. Hsu, T.-W. Hwang, and Y. Kuang, “A ratio-dependent food chain model and its applications to biological control,” Mathematical Biosciences, vol. 181, no. 1, pp. 55–83, 2003.
8. D. Xiao, W. Li, and M. Han, “Dynamics in a ratio-dependent predator-prey model with predator harvesting,” Journal of Mathematical Analysis and Applications, vol. 324, no. 1, pp. 14–29, 2006.
9. S. M. Sohel Rana, ”Chaotic dynamics and control of discrete ratio-dependent predator–prey system,” Discrete Dyn. Nat. Soc., Article ID 4537450, 2017.
10. X. Zhang, Z. Liu, ”Periodic oscillations in age-structured ratio-dependent predator–prey model with Michaelis–Menten type functional response,” Physica D: Nonlinear Phenomena, Vol. 389, pp. 51-63, 2019.
11. H. I. Freedman, ”Deterministic Mathematical Models in Population Ecology,” Marcel Dekker, New York, 1980.
12. M. Zhao, C. Li, and J. Wang, “Complex dynamic behaviors of a discrete-time predator-prey system,” The Journal of Applied Analysis and Computation, vol. 7, no. 2, pp. 478–500, 2017.
13. M. Zhao, Z. Xuan, and C. Li, “Dynamics of a discrete-time predator-prey system,” Advances in Difference Equations, vol. 191, 2016.
14. C. Wang, L. Li, Y. Zhou and R. Li, ”On a delay ratio-dependent predator–prey system with feedback controls and shelter for the prey,” International Journal of Biomathematics, Vol. 11, No. 07(2018).
15. J. Guckenheimer, and P. Holmes, ”Nonlinear Oscillations, Dynamical Systems, and Bifurcations of Vector Fields,” Springer-Verlag, New York, 1983.
16. C. Robinson, ”Dynamical Systems: Stability, Symbolic Dynamics, and Chaos,” 2nd Ed. Boca Raton, London, New York, 1999.
17. A. Gkana, and L. Zachilas, “Incorporating prey refuge in a prey-predator model with a Holling type-I functional response: random dynamics and population outbreaks,” Journal of biological physics, vol. 39(4) pp. 587-606, 2013.
18. S.N. Elaydi, ”An Introduction to Difference Equations,” Springer-Verlag, New York, 1996.
19. S. Lynch, ”Dynamical Systems with Applications Using Mathematica,” Birkhuser, Boston, 2007.

Sustainable utilization of carbon pool -A perspective

September 6, 2021

Rupak Roy[1], Srimanta Ray[2]

[1]*PhD Research Scholar, Department of Chemical Engineering, National Institute of Technology, Agartala, Tripura- 799046, India*

[2]*Assistant Professor, Department of Chemical Engineering, National Institute of Technology, Agartala, Tripura- 799046, India*

Corresponding Author: Srimanta Ray

E-mail: rays.nita@gmail.com

Tel: +91 8974867827

Abstract. Carbon is regarded as the building block of life. Approximately 50% of the total dry biomass on earth is contributed by the carbon (biotic pool). Carbon is also present in abiotic components of the earth. Carbon in biotic and abiotic compartment together forms the earth's carbon pool. The biotic carbon is known to work in a cycle without external intervention. However, few external interventions may arise owing to natural and anthropogenic process. These processes result in carbon flux or mass transfer across various pools. The carbon flux across the lithospheric and atmospheric compartment is responsible for global warming and the flux between lithospheric and hydrospheric compartment is the cause of water pollution. Thus the movement of carbon mass between compartments is the area has drawn significant research attention as these processes introduces a spectrum of environmental entanglements. Accordingly, a research scope exists towards sustainably utilizing various pools through strategic planning of carbon flux.
Keywords: Carbon flux. Carbon pool. Lignocellulosic biomass. Sustainability.

1 Introduction

Movement of carbon betwixt four major reservoirs: the atmosphere, the oceans, land, and fossil fuels are referred to as the global carbon cycle. Relocation of carbon from one stockpile to another may take place within seconds or over millennia [1].

Three major reasons account the significance of the carbon cycle. Primarily about 50% of the total dry weight of the biomass on earth is composed of carbon. Secondly, different metabolic transactions within living systems as well as in industrial systems are carried by carbon-containing compounds. The third reason for the escalating interest in the carbon cycle is the elevated usage of fossil fuels. Carbon dioxide (CO_2) and methane (CH_4) are two which are imperative carbon-containing greenhouse gases. Without the presence of these gases, the Earth's average temperature would be around -33 °C. Due to the presence of these gases in proper quantities, the mean temperature of the earth is suitable to hold different life forms. Augmentation of greenhouse gases towards the atmosphere from manufacturing bustle, notwithstanding, are broadening the concentrations of these gases, intensifying the greenhouse effect, and starting to warm the Earth [2], [3].

The global carbon cycle, therefore, is responsible for the rise in the global temperature which has resulted in the phenomena known as global warming. A steep enhance in the carbon dioxide concentration in the atmosphere has resulted from different anthropogenic activities over the past few years. The processes culpable for enumerating carbon to, and withdrawing it from, the atmosphere is not well enough understood to anticipate forthcoming levels of CO_2 with an enormous certainty. These processes are a part of the global carbon cycle [4], [5].

Major processes that introduce carbon into the atmosphere or eradicate it, such as the kindling of fossil fuels and the formulation of tree plantations, are under forthright anthropological domination. Others, such as the accretion of carbon in the hydrosphere or the lithosphere as a consequence of variations in global climate (i.e., feedbacks between the global carbon cycle and climate), are not within unequivocal human restraint except through dominating rates of greenhouse gas emissions and, hence, climatic change. Carbon dioxide plays an important role as compared to the other greenhouse gases which are under direct anthropological control and is expected to continue so in the upcoming years [6], [7].

Lignocellulosic biomass due to their carbon neutrality feature and wide abundance may be considered as one of the most dynamic key players in this critical scenario of environmental deterioration. Lignocellulosic biomass primarily comprised of lignin and cellulosic compartments and can be predominantly indicated to the biodegradable organic chunk, which originates through different biological processes and is considered as a budding determinant of renewable energy. Predominantly they can be subcategorized into certain class namely woody biomass, marine algae, agricultural residues, energy crops, etc. [6], [7]. Rational utilization of biomass derived energy needs to be bolstered at national as well as international horizon, prior to the consumption of the conventional fossil fuel inventory. European Union (EU) has adopted a goal to obtain 20% of the total energy from renewables by 2020. [8], [9].

Presently biomass subsidizes around 20% of the global energy prerequisites. Utilization of biomass-based energy ischiefly observed in rural areas as they are economical and easily accessible. Developed countries have comparatively less dependence on biomass-based energy when compared to the undeveloped nations. In the US and EU, only about 5% of the total energy requirement is accosted by biomass. Presently straightforward combustion of biomass in the furnace is the most prevailing method to obtain energy in the form of electricity and heat. [10] – [10].

The prime objective of this review includes the identification of major carbon pools present on the earth and the different fluxes within them. The global carbon cycle along with the different processes involved within the cycle has been discussed in detail. Various major environmental issues are discussed which aroused due to the anthropogenic intervention of the global carbon cycle. Lastly, few ways of mitigation have been discussed in order to circumvent the environmental problems that have been discussed earlier.

2 Global Carbon Cycle

Presence of carbon can be found in the atmosphere, lithosphere, hydrosphere, and biosphere of the earth. When considering the Earth as an entire ecosystem, these four spheres of the earth may be referred to as different carbon pools (sometimes also called stocks or reservoirs) because they act as stockpile houses for enormous chunks of carbon. Any dynamism or movement of carbon among these reservoirs or pool is called a flux. In any integrated system, fluxes hook up reservoirs together to conceive cycles and feedbacks. This dynamism of carbon results in the movement of carbon fraction from the atmosphere to green plants (containing chlorophyll) by the process of carbon fixation. These accumulated form of carbon from plants moves forward through the food chain. Upon death and decay of the plant or other members of the food chain, this stored form of carbon is being released either into the atmospheric or within the lithospheric carbon reserve. If we consider earth as an entire ecosystem, all these processes which involve the movement of carbon from one pool to another can be summed up to present the global carbon cycle. A simple schematic representation of the global carbon cycle has been portrayed in Figure 1 [11].

Figure 1: Schematic representation of the global carbon cycle.

3 Carbon Pools

Due to elevation of fossil fuel consumption in the past few years, a huge amount of CO_2 has been generated which has resulted in a spectrum of environmental entanglements like global warming, sea-water acidification, the rise in seawater level, etc. Accordingly, a significant research scope exists in order to track such dynamism of carbon from one pool to another, the driving force behind such processes and the time required during such movements of carbon from one pol to another. Banking on the aspiration, the different pools of carbon present on earth can be organized into infinite contrasting sections. On an expansive scale, carbon pool has been divided into four categories [12].

A huge portion of the carbon is stockpiled within the rocks which are located deep inside the earth's crust. They had formed overages by weathering and hardening of mud or by the deposition of the calciferous shells and skeletons of different living forms on the earth. In sync all sedimentary rocks on Earth stockpile 100,000,000 Petagrams of carbon (PgC) where one Petagram is equivalent to 1×10 [13] grams. The lithospheric carbon reserve of earth embraces approximately 4,000 PgC in the form of complex hydrocarbons. These hydrocarbons were formed overages as a result of weathering of carbonaceous materials which were deposited inside the earth's crust. Extreme

environmental conditions like elevated temperature and pressure may be considered as the major driving force behind such conversions [13].

Figure 2: Different carbon pools on earth (Source : Schlesinger Biogeochemistry 1997 and 2013 editions)

The hydrospheric reserve of the earth encompasses a huge chunk of inorganic carbon (around 38,000 PgC) which has remained in dissolved form over a huge time scale. Another petite carbon chunk of about 1,000 PgC may be found near the proximity of the ocean surface. This particular fraction of carbon may be interchanged continuously with the atmospheric carbon reserve. Various physicochemical as well as biological processes may be regarded as the driving forces behind such dynamism of carbon. However, a fraction of this carbon reserve may permanently translocate towards the ocean crust and thereby get deposited for a protracted period [16].

The atmospheric carbon pool encompasses a relatively lower carbon chunk (about 750 PgC) as compared to the other carbon pools present on earth. Carbon dioxide and methane are considered as the imperative components among various other forms of carbon present in this particular pool since they contribute towards the greenhouse effect. Although this particular carbon pool is much smaller when compared to others, it plays a crucial role in maintaining a huge number of life forms. A few years back this carbon pool measured around 560 PgC, however, due to increased human activities like deforestation, urbanization, increased fossil fuel burning, etc., has resulted in the elevation in this carbon pool. The present value of this pool is thought-provoking, and significant research attention is required in order to curtail the size of this carbon pool within safe limits [13].

The terrestrial ecosystem is regarded as another major carbon pool on earth. This pool comprises of microscopic as well as macroscopic living beings. The major chunk of this carbon pool is organic in nature since most of this carbon is of living origin. Green plants along with few species of algae (containing chlorophyll) capture CO_2 from the atmospheric carbon reserve and converts into five and six-carbon sugars by the process of photosynthesis. Apart from sugar synthesis, the absorbed carbon is also incorporated to form various tissues, resulting in their growth and development although; a fraction of this captured carbon is being released back into the atmosphere as a result of internal metabolism and respiration. The tissue thus formed has the competence to grasp a significant quantity of carbon within them. This particular pool of carbon may accounts for 560 PgC approximately. Estimation of the amount of carbon stored within the soil is a perplexing task since a major portion of soil is being constantly eroded by the rivers. However, the carbon pool stored within the soil has been estimated to be about 1500 PgC. A major fraction of this carbon pool is obtained as a result of the decay of various living forms by the action of microorganisms. This process of microbial breakdown effectively releases the captured carbon into the atmosphere in the form of CO_2 [14].

4 Carbon Flux

Carbon flux can be defined as the movement of carbon from one pool to another within a defined time frame and is expressed in kg km^2 yr^{-1}. The size of a carbon flux may vary accordingly

depending upon a particular process. More than one number of fluxes may exist within a single carbon pool. Flux may result in simultaneous addition or removal carbon from one pool [12].

Carbon sequestration is the mechanism by which chlorophyll-containing plants can convert the atmospheric form of carbon into their structural component which mainly comprises of hydrocarbons, in presence of photons. These accumulated carbon form may pass to the higher trophic levels through the food chain. After the specific lifespan of these organisms, they are either burnt in an open environment or are buried under the soil. Both these processes result in the release of the accumulated carbon within the living form into the atmospheric or the lithospheric carbon pool. It has been estimated that all the plants on the earth may cumulatively sequester a huge carbon chunk about 610 PgC within themselves and they can effectively absorb about 120 PgC/ year via photosynthesis out of which approximately 60 PgC/ year is returned back to the atmospheric carbon pool as a result of internal metabolism and respiration [7]. Apart from that, another major carbon flux may be observed when a plant during their lifecycle shed their leaves or other parts like roots, branches, etc. These fragments are ultimately decomposed by the microorganisms and the resultant carbon fraction is added to the atmospheric or the lithospheric carbon pool [14]. Microorganisms fulfill their nutritional requirement during the course of this decomposition process and as a byproduct, carbon dioxide is being released. This CO_2 flux may be estimated roughly around 60 PgC/ year [4].

The flux that takes place at the interface of the hydrospheric and the atmospheric carbon pool is due to the process of diffusion. The atmospheric carbon in the form of CO_2 partially dissolves to the uppermost layer of the seawater depending upon the partial pressure of CO_2 of both pools. Upon dissolution, an intermediate product in the form of carbonic acid is formed. The carbonate (HCO_3^-) thus formed is incorporated by various marine organisms in the form of shells. Upon the death of these marine organisms, the stored carbon within the shells gets trans-located into the sea bed [9].

4.1 Figure 3. Major annual carbon fluxes into and out of the atmosphere

The marine plants also behave in a very similar fashion when compared to the plants dwelling on the lithosphere. They sequester the dissolved CO_2 available in the seawater and produce sugars and other mandatory products required for their growth and development. This carbon flux is approximately 92 PgC / year. The energy thus stored can also be transmuted to the higher trophic levels of the food chain. Upon the death of those plants, the sequestered carbon within them gets released into the surrounding environment due to the process of decomposition by microorganisms. This decomposition process takes place at a relatively faster rate as compared to the plants dwelling in the lithosphere since most of the marine plants are herbaceous in nature. This flux of carbon is approximately found out to be 90 PgC / year [15].

The global carbon cycle is presently facing numerous external interventions due to various human activities like deforestation, uncontrolled fossil fuel consumption, etc. which has, in turn, raised a spectrum of entanglements like melting of polar ice caps, acid rain, global warming, etc. The major outcome of these activities has resulted in a net increase of the stratospheric CO_2 levels. Burning of fossil fuel is solely responsible for a net carbon flux about 5-9 PgC/ year towards the atmosphere. Deforestation may be regarded as another key player in this context as plants

can sequester a huge chunk of atmospheric carbon within them resulting in the net reduction of the stratospheric CO_2. Population outburst and industrialization are considered as the underlying motive for deforestation. Data reported that several acres of forests are cleared on a daily basis in order to obtain timber, which has different industrial as well as energetic application. These elevated human activities have resulted in a net movement of the carbon flux (about 1-2 PgC/year) towards the stratospheric carbon pool [16].

5 Environmental Issues

Burning of fossil fuels results in the emission of CO_x, NO_x, and SO_x. When these compounds react with the moisture present in the atmosphere they result in the formation of different corrosive agents like carbonic acid, nitric acid, and sulphuric acid. With the help of different agents like clouds, the air they can be transferred from one place to another and ultimately after a certain period of time, they come back to the stratosphere in the form of acid rain. They have severe deleterious impacts on monuments, farming, and human health since they are extremely corrosive in nature. Acid precipitation increases the acidity of the lithospheric and atmospheric carbon pool (where it occurs) and thereby causes intense damage to the life forms available over there. Seawater acidification has been another major threat to the environment due to acid precipitation. Apart from acid rain, many other potentially harmful substances are being generated due to human activities (chlorides, volatile organic compounds (VOCs) to name a few). Elevated human activities like use of fossil fuel-driven vehicles and burning of coal (which together accounts for 80% SO_x and 48% NO_x release) may be considered as potential bidders of acid precipitation [19].

The presence of the stratospheric ozone layer about 12-25 km above the mean sea level plays an important role by hindering the harmful ultraviolet rays from entering the atmosphere. These ultraviolet rays are potential carcinogens which may cause different types of dermatological cancers. Depletion of the ozone was observed first in 1985 by a group of a British scientist. The key reason responsible for this environmental catastrophe was identified to be N_2O and chlorofluorocarbons (CFCs) which are chlorinated and brominated organic compounds in nature. CFCs were mainly used in artificial cooling systems like refrigerators, air conditioners, and foams. Excessive use of these compounds resulted in the depletion of the stratospheric atmospheric ozone layer. In the year of 1987, an international treaty was signed among different countries in Montreal (popularly known as Montreal protocol) to minimize the production and use of CFCs and halons. These strategies were further intensified in the London Conference held in London in the year 1990. Moreover, new innovative strategies and planning were also adopted in order to find alternatives for CFCs [17].

Another pressing environmental concern in present times is global warming. Due to increased consumption of fossil fuels, and deforestation, the amount of greenhouse gases like methane, carbon dioxide, peroxyacetylnitrate (PAN) has raised above the threshold limits within the atmosphere. Among them, carbon dioxide alone contributes about 50% of the total greenhouse effect. These gases have the ability to trap the incoming solar radiation (in form of heat energy) and thus maintain the temperature suitable for livelihood. Owing to their sharp increase in their concentration, the mean atmospheric temperature is increasing at an alarming rate which further has invited a gamut of concerns. In the past few years, the mean temperature of the earth has been raised by 0.6°C. Due to this elevation in temperature polar ice cap melting has begun which has further re-

sulted in the net increase of the sea level by 20 cm. Energy-related happenings contribute both directly and indirectly to the emission of different greenhouse gases. It has been estimated that by the end of 2100, the mean temperature of the earth may rise up to 5°C. Various strategies have been undertaken by the U.S. Environmental Protection Agency (EPA) in order to combat such environmental changes. Reduction in the emission of greenhouse gas has been considered as the most effective strategy to circumvent the ongoing environmental concerns. Reforestation along with the utilization of alternative fuels which are carbon-neutral has been recommended in order to minimize the atmospheric CO_2 level. In order to circumvent all these environmental concerns, effective participation of all the developed, as well as the developing countries, is required [18], [19].

6 Ways of Mitigation

Disproportionate utilization of fossil fuels nowadays is escalating the greenhouse gas content in the atmosphere, which eventually consequences in global warming. As a remedial strategy, minimization of the lithospheric carbon reserve and at the same time employing other forms of renewable energy will consequence in the minimization of the atmospheric carbon content resulting as a remedial measure for increasing global warming [20].

Carbon sequestration is a process by which the stratospheric carbon can be captured and stored (in solid or liquid form for a relatively longer period) by a sink in order to minimize the atmospheric CO_2 level. This process can be biological as well as physicochemical. The preliminary tenacity of undertaking this is the postponement global warming and avoiding extreme climate change. It is significant to note that supplementary forms of carbon are also stockpiled for the period of this sequestration process. A more scientific explanation (and example) is the removal and storage of carbon from the atmosphere to sinks – oceans, soil, the forest through physical means and the natural process best known as photosynthesis [21].

The bio-based economy can be another excellent alternative approach in order to combat this present scenario of environmental degradation. Significant research attention, the formation of strict environmental policies, life cycle assessment of biomass-based energy systems, as well as new innovations needs to be done in order to replace the use of conventional fossil fuel with biomass-based energy systems for energy recovery [22].

Energy recovery from renewables has been escalated on a global basis in order to prevent environmental degradation. Among different available renewable energy sources, biomass-based energy recovery has been received significant research attention due to their carbon neutrality, wide availability, and ease of applicability. Process economics has been another important attribute which has widened their acceptability. However, relatively lower calorific value, bulk density (as compared to the conventional fossil fuels), seasonal supply and food to fuel ratio are few major drawbacks in context to energy recovery from biomass (EUROPE, Europe Commission) (IEA Clean Coal Center, 2005). To overcome these hurdles, conjoining biomass and coal for power cohort can be a potentially viable substitute. Co-firing readily enhances the quality of biomass in terms of calorific value. Moreover, it will also reduce the operating cost for existing industries, which solely depends upon coal as the prime source of energy (IEA Clean Coal Center, 2005). Type of biomass feedstock accessible for energy commitments comprises of agricultural residues, dedicated energy crops, biomass obtained from the forest (like leaves, twigs, etc.), biomass obtained from industry

(e.g. timber processing unit), parks and garden waste, and other. Data indicated in Table 1 gives a complete list of different potential biomass feedstock available for energy recovery along with their compositional analysis, and few common examples [22]- [23].

Supply sector	**Type**	**Example**	**Cellulose (%)**	**Hemicellulose (%)**	**Lignin (%)**	**Calorific value (MJ/kg)**
Agro residues	Dry lignocellulosic	Straw, residues etc.	20-50	15-40	20-40	13-17
Energy crops	Oil and starch energy crops	Miscanthus, sugar beet, flax etc.	30-55	20-35	25-35	15-20
Forestry	Branches, twigs	Bark, wood blocks etc.	20-45	25-40	30-55	14-19
Industry	Wood chips, saw dust	Vegetable peels, black liquor	25-50	15-35	25-45	16-19
Park & gardens	Herbs, grasses	Grass, pruning	30-45	25-45	10-30	15-18
Waste	Contaminated waste	Demolition wood, Landfill gas	10-40	5-25	15-35	16-19
Others	Roadside hay	Olive, cacao, almond	15-40	5-35	10-40	16-19

Table 1: Classification of biomass, their chemical composition, and the range of calorific value.

7 Conclusion

Population outburst, amplified urbanization has led to mounting dependency on fossil fuel usage to meet the energy demands which in turn raised a gamut of concerns like global warming, acid rain etc. Continuous upsurge in the CO_2 emission has many other damaging effects like polar ice cap melting, increase in net sea level, microbial contamination, floods, droughts etc. The emission from the burning of fossil fuels has depreciated the indoor as well as the outdoor air quality. In order to minimize such unwanted scenarios, energy retrieval from lignocellulosic biomass as a substitute to fossil fuels can be an outstanding alternative. This will also help in the fortification of public well-being. Significant research attention is still required for utilization of biomass in context to energy recovery from them in terms of process simplicity and cost to benefit economics. Pretreatment of biomass for energy densification can be another outstanding methodology for energy retrieval from biomass as because biomass has moderately less heating values as equated to the conventional fossil fuels like coal, petroleum etc. Hence more advanced research methodologies must be developed such that lignocellulosic biomass can be utilized more efficiently which will result in the minimization of the many environmental concerns as well as will be able to meet the primary energy demand of mankind.

Acknowledgement
The authors acknowledge, National Institute of Technology and Ministry of Human Resource Development, Government of India for providing financial assistantship in form of fellowship to conduct doctoral research.

References

[1] Clark D. “Are tropical forests an important carbon sink? Reanalysis of the long-term plot data”. In: *Ecological Applications* 12 (1 2002), pp. 3–7.

[2] Andres R et al. “Carbon dioxide emissions from fossil-fuel use”. In: *Tellus B* 51 (4 1999), pp. 759–765.

[3] Barber V, Juday G, and Finney B. “Reduced growth of Alaskan white spruce in the twentieth century from temperature-induced drought stress”. In: *Nature* 405 (6787 2000), pp. 668–673.

[4] Bousquet P et al. “Regional changes in carbon dioxide fluxes of land and oceans since 1980”. In: *Science* 5495 (2000), pp. 1342–1346.

[5] Broecker W. “A Ewing Symposium on the contemporary carbon cycle”. In: *Global Biogeochemical Cycles* 15 (4 2001), pp. 1031–1032.

[6] Brown S. “Management of forests for mitigation of greenhouse gas emissions”. In: *Climatic Change* (1995).

[7] Cardon Z et al. “Contrasting effects of elevated CO2 on old and new soil carbon pools”. In: *Soil Biology and Biochemistry* 33 (3 2001), pp. 365–373.

[8] Ferre Ajc and Martínez Jal. In: *Briquettes of plant remains from the greenhouses of Almería (Spain)* 3 (2009), pp. 525–534.

[9] Demirbas A. “Potential applications of renewable energy sources, biomass combustion problems in boiler power systems and combustion related environmental issues”. In: *Progress in energy and combustion science* 31 (2 2005), pp. 171–192.

[10] Khan A et al. “Biomass combustion in fluidized bed boilers: Potential problems and remedies”. In: *Fuel processing technology* 90 (1 2009), pp. 21–50.

[11] Knorr W and Heimann M. “Uncertainties in global terrestrial biosphere modeling: 1. A comprehensive sensitivity analysis with a new photosynthesis and energy balance scheme”. In: *Global Biogeochemical Cycles* 15 (1 2001), pp. 207–225.

[12] Kempe S. “Carbon in the rock cycle”. In: (1979).

[13] Houghton R and Turner W. “Carbon”. In: *The Earth as Transformed by Human Action* ().

[14] Houghton R et al. In: ().

[15] Keeling R and Garcia H. “The change in oceanic O2 inventory associated with recent global warming”. In: *Proceedings of the National Academy of Sciences* 99 (2002), pp. 7848–7853.

[16] Plattner G, Joos F, and Stocker T. “Revision of the global carbon budget due to changing air-sea oxygen fluxes”. In: *Global Biogeochemical Cycles* 16 (4 2002), pp. 43–51.

[17] White A, Cannell M, and Friend A. “Climate change impacts on ecosystems and the terrestrial carbon sink: a new assessment”. In: *Global environmental change* 9 (1999), pp. 21–30.

[18] Watson R et al. “Greenhouse gases and aerosols”. In: *Climate Change* (1990).

[19] Stephens B et al. “Testing global ocean carbon cycle models using measurements of atmospheric O2 and CO2 concentration”. In: *Global Biogeochemical Cycles* 12 (2 1998), pp. 213–230.

[20] Oechel W et al. “Recent change of Arctic tundra ecosystems from a net carbon dioxide sink to a source”. In: *Nature* 361 (6412 1993), pp. 520–523.

[21] Ko¨rner C. “Biosphere responses to CO2 -enrichment”. In: *Ecological Applications* 10 (6 2000), pp. 1590–1619.

[22] Luo Y et al. “A search for predictive understanding of plant responses to elevated”. In: 2 ().

[23] Vassilev S, Vassileva C, and Vassilev V. “Advantages and disadvantages of composition and properties of biomass in comparison with coal: An overview”. In: *Fuel* 158 (2015), pp. 330–350.

The ISI Index of Cartesian Products Related to Edge-Semitotal and Total Graphs

A. Bharali
Department of Mathematics, Dibrugarh University, 786004, India
Email: a.bharali@dibru.ac.in

J. Buragohain
Department of Mathematics, Pragjyotish College, 781009, India
Email: j.bgohain75@yahoo.com

*A. Mahanta
Department of Mathematics, Dergaon Kamal Dowerah College, 785703, India
Email: am02dib@gmail.com

Abstract. In association to a connected graph, we have many other interrelated graphs such as edge-semitotal graph $Q(G)$, total graph $T(G)$, line graph $L(G)$ and so on. The inverse sum indeg (*ISI*) index defined as

$$ISI(G) = \sum_{uv \in E(G)} \frac{1}{\frac{1}{d_G(u)} + \frac{1}{d_G(v)}} = \sum_{uv \in E(G)} \frac{d_G(u) d_G(v)}{d_G(u) + d_G(v)}$$

has drawn considerable attention in recent times because of its significant prediction ability of total surface area of octane isomers. In this paper, we investigate the ISI index of Cartesian products related to $Q(G)$ and $T(G)$ and obtain expressions for the same . Further the extremal cases of the bounds are also studied.

Mathematics Subject Classification: 05C05, 05C07

Keywords: Degree of vertex · line graph · ISI index · edge-semitotal graph · total graph.

1 Introduction

Throughout this paper we have considered only finite, simple, connected and undirected graphs. $V(G)$ and $E(G)$ represent the vertex set and edge set of a graph G respectively. We use $d_G(u)$ to denote the degree of a vertex u in G and P_n to represent a path of order n. The notations and terminologies used but not clearly stated in this article may be found in [14].

The topological index of a molecular graph is a numerical quantity modelled out of a graph's molecular structure which sets up a correlation of chemical structure of the graph with various physical, chemical and biological properties of the graph. Thousands of topological indices (also known as molecular-based structure descriptors) based on vertex-degree, distance, eccentricity, etc. have been proposed and studied since the later

part of the twentieth century. Historically the *Zagreb* indices proposed by *Gutman* and *Trinajstić* [5] were the first vertex-degree-based structure descriptors. One may refer to [6] for a deeper insight into some degree-based topological indices. Among these indices, the inverse sum indeg(*ISI*) index has garnered considerable interest because of its ability of giving a good estimate of total surface area of octane isomers. For an idea of the recent contributions related to the *ISI* index, one can refer to [1], [2], [4],[8], [9], [11], [13].

In this paper we study *ISI* index of newly defined graph operations related to edge-semitotal and total graphs based on cartesian product.

2 Preliminaries

Definition 1. First Zagreb index:*[6]* The first Zagreb index of a graph G is defined as

$$M_1(G) = \sum_{v \in V} d_v^2 = \sum_{uv \in E} (d_u + d_v).$$

Definition 2. Second Zagreb index:*[6]* The second Zagreb index of a graph G is defined as

$$M_2(G) = \sum_{uv \in E} d_u d_v.$$

Definition 3. Inverse sum indeg index:*[11]*

$$ISI(G) = \sum_{uv \in E(G)} \frac{1}{\frac{1}{d_G(u)} + \frac{1}{d_G(v)}} = \sum_{uv \in E(G)} \frac{d_G(u) d_G(v)}{d_G(u) + d_G(v)}$$

Definition 4. Line graph:*[12]* The line graph $L(G)$ of a graph G is defined to have as its vertices the edges of G, with adjacency being defined upon sharing of a common vertex between the edges in G.

To obtain the edge-semitotal graph $Q(G)$ from a graph G, we insert a new vertex into each edge of G and then join these new pairs of vertices on adjacent edges of G. We have the edges and vertices of G as the corresponding vertices in $T(G)$. Adjacency in $T(G)$ is determined by the adjacency or incidence of the corresponding elements of G. For more detail on these operations, one may refer to *Handbook of Product Graphs* by *Hammack* [7] and [3].

Now in this work we extend these operations for a graph G and propose a more generalized version of them, namely $Q_t(G)$ and $T_t(G)$ as follows.

Definition 5. *The graph $Q_t(G)$ of a graph G is obtained from G by replacing each edge uv in G by a path of length $t+1$, with u and v as the end vertices of the path and then joining each new vertex introduced for a particular edge to every new vertex corresponding to an edge adjacent to it in the original graph (see Figure 1).*

Definition 6. *The graph $T_t(G)$ of a graph G is obtained from G by adding a path of length $t+1$ parallel to each edge uv in G, with u and v as the end vertices of the*

path and then joining each new vertex introduced for a particular edge to every new vertex corresponding to an edge adjacent to it in the original graph along with the edges present in the original graph (see Figure 2).

Analogous to the Q-sum and T-sum, we define Q_t-sum and T_t-sum of two graphs as follows.

Definition 7. *The Q_t-sum $G_1 +_{Q_t} G_2$ of the two graphs G_1 and G_2 is a graph with vertex set $V(Q_t(G_1)) \times V(G_2)$ in which $(u_1, v_1)(u_2, v_2)$ is an edge if and only if $[u_1 = u_2 \in V(G_1)$ and $v_1v_2 \in E(G_2)]$ or $[v_1 = v_2 \in V(G_2)$ and $u_1u_2 \in E(Q_t(G_1))]$.*

Definition 8. *The T_t-sum $G_1 +_{T_t} G_2$ of the two graphs G_1 and G_2 is a graph with vertex set $V(T_t(G_1)) \times V(G_2)$ in which $(u_1, v_1)(u_2, v_2)$ is an edge if and only if $[u_1 = u_2 \in V(G_1)$ and $v_1v_2 \in E(G_2)]$ or $[v_1 = v_2 \in V(G_2)$ and $u_1u_2 \in E(T_t(G_1))]$.*

It is to be noted that $d_{Q_t(G)}(u) = d_G(u) \ \forall \ u \in V(G)$ and $d_{Q_t(G)}(w) = 2 + td_{L(G)}(w) \ \forall \ w \in V(Q_t(G)) \setminus V(G)$, where w is inserted into the edge uv of G as the new vertex. Also, we have $d_{T_t(G)}(u) = 2d_G(u) \ \forall \ u \in V(G)$ and $d_{T_t(G)}(w) = 2 + td_{L(G)}(w) \ \forall \ w \in V(T_t(G)) \setminus V(G)$.

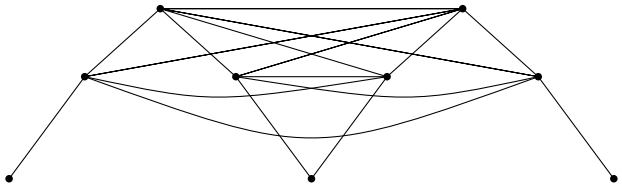

Fig. 1: An example : $Q_3(P_3)$

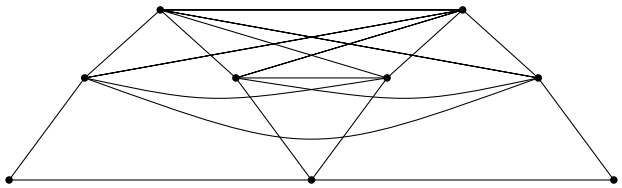

Fig. 2: An example : $T_3(P_3)$

3 Main Results

We start our discussion by stating a famous result known as Jensen's inequality.

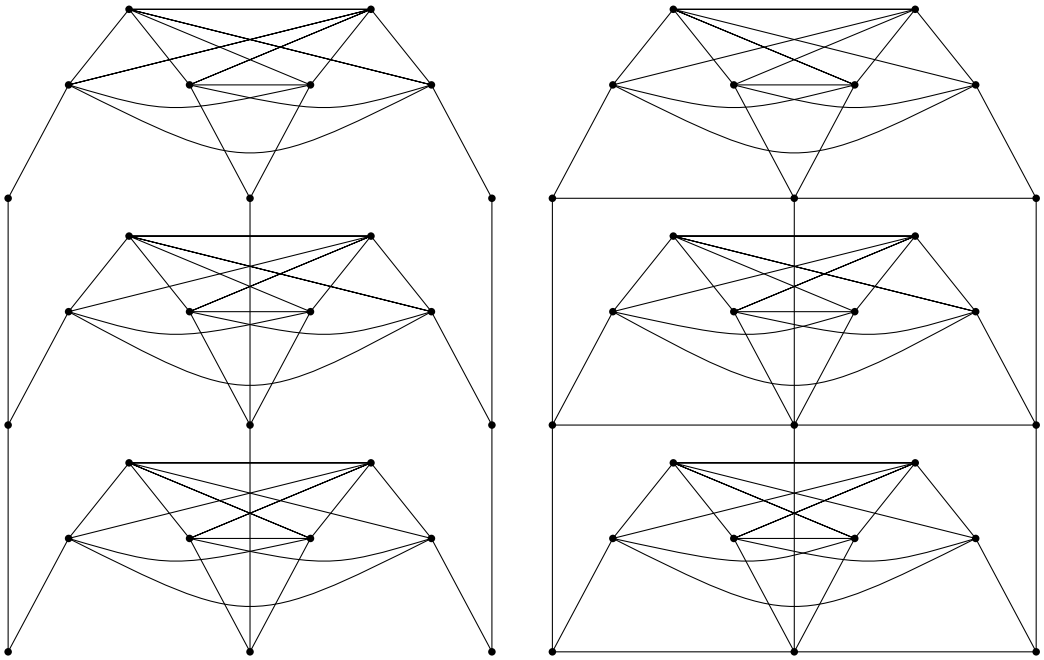

$P_3 +_{Q_3} P_3$ $P_3 +_{T_3} P_3$

Fig. 3: An example of $G_1 +_{Q_t} G_2$ and $G_1 +_{T_t} G_2$

Lemma 1. *[10] For a convex function f on the interval I with $x_1, x_2, ..., x_n \in I$,*

$$f\left(\frac{x_1 + x_2 + ... + x_n}{n}\right) \leq \frac{f(x_1) + f(x_2) + ... + f(x_n)}{n}$$

with equality holding if and only if $x_1 = x_2 = ... = x_n$.

Theorem 1. *Let G be a simple connected graph of m edges. Then,*

$$ISI(Q_t(G)) < M_1(G) + \frac{t}{2} + \frac{t}{4}M_2(L(G)) - mt.$$

Proof.

$$ISI(Q_t(G)) = \sum_{uv\in E(G)} \Big[\frac{d_{Q_t(G)}(u)d_{Q_t(G)}(x)}{d_{Q_t(G)}(u)+d_{Q_t(G)}(x)} + \frac{d_{Q_t(G)}(y)d_{Q_t(G)}(v)}{d_{Q_t(G)}(y)+d_{Q_t(G)}(v)}\Big] + \sum_{\substack{e_if_j\in E(L(G))\\ i,j=1\ to\ t}} \frac{d_{Q_t(G)}(e_i)d_{Q_t(G)}(f_j)}{d_{Q_t(G)}(e_i)+d_{Q_t(G)}(f_j)}$$

where x,y are the terminal vertices of the path inserted between u and v.

$$= \sum_{uv\in E(G)} \Big[\frac{d_G(u)\{(d_G(u)+d_G(v))t-2(t-1)\}}{d_G(u)+(d_G(u)+d_G(v))t-2(t-1)} + \frac{\{(d_G(u)+d_G(v))t-2(t-1)\}d_G(u)}{(d_G(u)+d_G(v))t-2(t-1)+d_G(u)}\Big] + \sum_{\substack{e_if_j\in E(L(G))\\ i,j=1\ to\ t}} \frac{\{2+td_{L(G)}(e_i)\}\{2+td_{L(G)}(f_j)\}}{2+td_{L(G)}(e_i)+2+td_{L(G)}(f_j)}$$

$$= \sum 1 + \sum 2$$

$$For\ \sum 1: \quad \frac{d_G(u)\{(d_G(u)+d_G(v))t-2(t-1)\}}{d_G(u)+(d_G(u)+d_G(v))t-2(t-1)}$$

$$= \frac{1}{2} f\Big[\frac{d_G(u)+(d_G(u)+d_G(v))t-2(t-1)}{2d_G(u)\{(d_G(u)+d_G(v))t-2(t-1)\}}\Big]$$

(where $f(x)=\frac{1}{x}$, which is a convex function for $x\in(0,\infty)$.)

$$\leq \frac{1}{4}\Big[f(\frac{1}{(d_G(u)+d_G(v))t-2(t-1)}) + f(\frac{1}{d_G(u)})\Big]$$

$$= \frac{1}{4}\Big[(d_G(u)+d_G(v))t-2(t-1)+d_G(u)\Big]$$

The equality case here fails for a regular graph.

$$Therefore,\ \sum 1 \leq \frac{1}{2}\sum_{uv\in E(G)}\Big[(d_G(u)+d_G(v))t-2(t-1)+d_G(u)\Big]$$

$$= \frac{t}{2}\sum_{uv\in E(G)}(d_G(u)+d_G(v)) - (t-1)\sum_{uv\in E(G)} 1 + \frac{1}{2}\sum_{uv\in E(G)} d_G(u)$$

$$= \frac{t}{2}M_2(G) - m(t-1) + \frac{1}{2}M_1(G)$$

$$
\begin{aligned}
For\ \sum 2: \quad & \frac{\{2+td_{L(G)}(e_i)\}\{2+td_{L(G)}(f_j)\}}{2+td_{L(G)}(e_i)+2+td_{L(G)}(f_j)} \\
=& \frac{1}{2}f\Big[\frac{2+td_{L(G)}(e_i)+2+td_{L(G)}(f_j)}{2\{2+td_{L(G)}(e_i)\}\{2+td_{L(G)}(f_j)\}}\Big] \\
\leq& \frac{1}{4}\Big[f(\frac{1}{2+td_{L(G)}(f_j)})+f(\frac{1}{2+td_{L(G)}(e_i)})\Big] \\
=& \frac{1}{4}\Big[2+td_{L(G)}(f_j)+2+td_{L(G)}(e_i)\Big] \\
=& 1+\frac{t}{4}\{d_{L(G)}(e_i)+d_{L(G)}(f_j)\}
\end{aligned}
$$

where equality holds if and only if G is regular.

$$
\begin{aligned}
Therefore,\ \sum 2 \leq & \sum_{e_if_j\in E(L(G))}\Big[1+\frac{t}{4}\{d_{L(G)}(e_i)+d_{L(G)}(f_j)\}\Big] \\
=& |E(L(G))|+\frac{t}{4}M_2(L(G)) \\
=& \frac{1}{2}M_1(G)-m+\frac{t}{4}M_2(L(G)). \\
Therefore,\ ISI(Q_t(G)) <& M_1(G)+\frac{t}{2}M_2(G)+\frac{t}{4}M_2(L(G))-mt.
\end{aligned}
$$

Similarly we can obtain the following result.

Theorem 2. *Let G be simple connected graph and m be the number the edges in it. Then,*

$$ISI(T_t(G)) < \frac{1}{2}M_1(G)+(2t+\frac{1}{2})M_2(G)-4mt+3m+\frac{t}{4}M_2(L(G))+2ISI(G).$$

Now we present the result for Q_t-sum and T_t-sum.

Theorem 3. *Let G_1 and G_2 be two graphs where $n_i = |V(G_i)|$ and $m_i = |E(G_i)|$; $i = 1, 2$. Then,*

$$
\begin{aligned}
ISI(G_1+_{Q_t}G_2) <& \frac{9n_2M_1(G_1)}{4}+\frac{n_1M_1(G_2)}{4}+\frac{tn_2M_2(G_1)}{4}+tn_2M_2\left(L\left(G_1\right)\right) \\
& -\left(\frac{t+7}{2}\right)m_1n_2+\frac{3}{2}m_1n_2.
\end{aligned}
$$

Proof. For simplicity, let $d\,(u,v)$ denote the degree of a vertex (u,v) in $G_1+_{Q_t}G_2$.

$$
\begin{aligned}
ISI(G_1+_{Q_t}G_2) =& \sum_{u\in V(G_1)}\sum_{v_1v_2\in E(G_2)}(\frac{d(u,v_1)d(u,v_2)}{d(u,v_1)+d(u,v_2)}) \\
& +\sum_{v\in V(G_2)}\sum_{u_1u_2\in E(Q(G_1))}(\frac{d(u_1,v)d(u_2,v)}{d(u_1,v)+d(u_2,v)}) \\
=& \sum 1+\sum 2
\end{aligned}
$$

Now,

$$\sum 1 = \sum_{u\in V(G_1)} \sum_{v_1v_2\in E(G_2)} \left(\frac{\left(d_{Q_t(G_1)}(u)+d_{G_2}(v_1)\right)\left(d_{Q_t(G_1)}(u)+d_{G_2}(v_2)\right)}{2d_{Q_t(G_1)}(u)+(d_{G_2}(v_1)+d_{G_2}(v_2))}\right)$$

For each $u \in V(G_1)$ and each $v_1v_2 \in E(G_2)$, by Jensen's inequality we have

$$\frac{\left(d_{Q_t(G_1)}(u)+d_{G_2}(v_1)\right)\left(d_{Q_t(G_1)}(u)+d_{G_2}(v_2)\right)}{d_{Q_t(G_1)}(u)+d_{G_2}(v_1)+d_{Q_t(G_1)}(u)+d_{G_2}(v_2)} \leq \frac{d_{G_1}(u)}{2}+\frac{d_{G_2}(v_1)+d_{G_2}(v_2)}{4}$$

with equality holding if and only if G_2 being regular.
Therefore,

$$\begin{aligned}\sum 1 \leq & \sum_{u\in V(G_1)} \sum_{v_1v_2\in E(G_2)} \left[\frac{d_{G_1}(u)}{2}+\frac{d_{G_2}(v_1)+d_{G_2}(v_2)}{4}\right] \\ =& \frac{m_2}{2}\sum_{u\in V(G_1)} d_{G_1}+\frac{1}{4}\sum_{u\in V(G_1)}\sum_{v_1v_2\in E(G_2)} d_{G_2}(v_1)+d_{G_2}(v_2) \\ =& \frac{2m_1m_2}{2}+\frac{n_1M_1(G_2)}{4} \\ =& m_1m_2+\frac{n_1M_1(G_2)}{4}\end{aligned}$$

Also,

$$\begin{aligned}&\sum 2 \\ =& \sum_{v\in V(G_2)} \sum_{\substack{ue\in E(Q_t(G_1)) \\ u\in V(G_1), e\in V(Q_t(G_1))\setminus V(G_1)}} \left(\frac{(d_{Q_t(G_1)}(u)+d_{G_2}(v))(d_{Q_t(G_1)}(e)+d_{G_2}(v))}{(d_{Q_t(G_1)}(u)+d_{G_2}(v))+(d_{Q_t(G_1)}(e)+d_{G_2}(v))}\right) \\ &+ \sum_{v\in V(G_2)} \sum_{\substack{e_if_j\in E(Q_t(G_1)) \\ e_i,f_j\in V(Q_t(G_1))\setminus V(G_1) \\ i,j=1\ to\ t}} \left(\frac{(d_{Q_t(G_1)}(e_i)+d_{G_2}(v))(d_{Q_t(G_1)}(f_j)+d_{G_2}(v))}{(d_{Q_t(G_1)}(e_i)+d_{G_2}(v))+(d_{Q_t(G_1)}(f_j)+d_{G_2}(v))}\right) \\ =& \sum_{v\in V(G_2)} \sum_{uw\in E(G_1)} \left(\frac{(d_{Q(G_1)}(u)+d_{G_2}(v))\left((d_{G_1}(u)+d_{G_1}(w))t-2(t-1)\right)}{(d_{Q(G_1)}(u)+d_{G_2}(v))+(d_{Q_t(G_1)}(e)+d_{G_2}(v))+(d_{G_1}(u)+d_{G_1}(w))t-2(t-1)}\right) \\ &+ \sum_{v\in V(G_2)} \sum_{\substack{e_if_j\in E(Q_t(G_1)) \\ e_i,f_j\in V(Q_t(G_1))\setminus V(G_1) \\ i,j=1\ to\ t}} \left(\frac{\left((d_{G_1}(u)+d_{G_1}(w))t-2(t-1)\right)\left((d_{G_1}(u)+d_{G_1}(w))t-2(t-1)\right)}{\left((d_{G_1}(u)+d_{G_1}(w))t-2(t-1)\right)+\left((d_{G_1}(u)+d_{G_1}(w))t-2(t-1)\right)}\right) \\ =& \sum_{v\in V(G_2)} \sum_{uw\in E(G_1)} \left(\frac{(d_{G_1}(u)+d_{G_2}(v))\left((d_{G_1}(u)+d_{G_1}(w))t-2(t-1)\right)}{(d_{G_1}(u)+d_{G_2}(v))+(d_{G_1}(u)+d_{G_1}(w))t-2(t-1)}\right)\end{aligned}$$

$$+\sum_{v\in V(G_2)}\sum_{\substack{e_if_j\in E(Q_t(G_1))\\ e_i,f_j\in V(Q_t(G_1))\setminus V(G_1)\\ i,j=1\ to\ t}}\left(\frac{((d_{G_1}(u)+d_{G_1}(w))t-2(t-1))\,((d_{G_1}(u)+d_{G_1}(w))t-2(t-1))}{((d_{G_1}(u)+d_{G_1}(w))t-2(t-1))+((d_{G_1}(u)+d_{G_1}(w))t-2(t-1))}\right)$$

For each $v\in V(G_2)$ and each $ue\in E(Q_t(G_1))$ with $u_1\in V(G_1)$ and $e\in V(Q_t(G_1))\setminus V(G_1)$, by Jensen's inequality we have

$$\frac{(d_{G_1}(u)+d_{G_2}(v))\,((d_{G_1}(u)+d_{G_1}(w))t-2(t-1))}{d_{G_1}(u)+d_{G_2}(v))+(d_{G_1}(u)+d_{G_1}(w))t-2(t-1)}\leq\frac{1}{4}\{d_{G_1}(u)+d_{G_1}(w))t-2(t-1)+d_{G_1}(u)+d_{G_2}(v)\}.$$

Here equality arises if and only if $(d_{G_1}(u)+d_{G_1}(w))\,t-2(t-1)=d_{G_1}(u)+d_{G_1}(v)$. But if we take both graphs to be regular of the same degree, then both graphs must be K_2 which is not possible here.
Again for each $v\in V(G_2)$ and each $e_if_j\in E(Q_t(G_1))$ with $e_i,f_j\in V(Q_t(G_1))\setminus V(G_1);i,j=1\ to\ t$, by Jensen's inequality we have

$$\left(\frac{((d_{G_1}(u)+d_{G_1}(w))t-2(t-1))\,((d_{G_1}(u)+d_{G_1}(w))t-2(t-1))}{((d_{G_1}(u)+d_{G_1}(w))t-2(t-1))+((d_{G_1}(u)+d_{G_1}(w))t-2(t-1))}\right)$$
$$\leq(d_{G_1}(u)+d_{G_1}(w))t-2(t-1).$$

Here the equality case fails for t=3 which gives an absurd condition.
Therefore,

$$\begin{aligned}\sum 2 \leq & \frac{1}{4} \sum_{v \in V(G_2)} \sum_{uw \in E(G_1)} \{\{d_{G_1}(u)+d_{G_1}(w))t-2(t-1)+d_{G_1}(u)+d_{G_2}(v)\}\} \\ & + \sum_{v \in V(G_2)} \sum_{\substack{e_i f_j \in E(Q_t(G_1)) \\ e_i, f_j \in V(Q_t(G_1)) \setminus V(G_1) \\ i,j=1 \text{ to } t}} \{(d_{G_1}(u)+d_{G_1}(w))t-2(t-1)\} \\ = & \frac{t}{4} \sum_{v \in V(G_2)} \sum_{uw \in E(G_1)} (d_{G_1}(u)+d_{G_1}(w)) - \frac{t-1}{2} \sum_{v \in V(G_2)} \sum_{uw \in E(G_1)} (1) \\ & + \frac{1}{4} \sum_{v \in V(G_2)} \sum_{uw \in E(G_1)} d_{G_1}(u) + \frac{1}{4} \sum_{v \in V(G_2)} \sum_{uw \in E(G_1)} d_{G_1}(v) \\ & + \sum_{v \in V(G_2)} \sum_{pq \in E(L(G_1))} \left(2+td_{L(G_1)}(q)+2+td_{L(G_1)}(q)\right) \\ = & \frac{tn_2}{4} M_2(G_1) - \frac{m_1 n_2 (t-1)}{2} + \frac{n_2}{4} M_1(G_1) + \frac{2m_1 m_2}{4} + 4n_2 |E(L(G_1))| \\ & + tn_2 M_2(L(G_1)) \\ = & \frac{tn_2}{4} M_2(G_1) - \frac{m_1 n_2 (t-1)}{2} + \frac{n_2}{4} M_1(G_1) + \frac{m_1 m_2}{2} + 4n_2 \left(\frac{1}{2} M_1(G_1) - m_1\right) \\ & + tn_2 M_2(L(G_1)) \\ = & \frac{tn_2}{4} M_2(G_1) - \frac{m_1 n_2 (t-1)}{2} + \frac{n_2}{4} M_1(G_1) + \frac{m_1 m_2}{2} + 2n_2 M_1(G_1) - 4m_1 n_2 \\ & + tn_2 M_2(L(G_1)) \end{aligned}$$

Hence,

$$\begin{aligned} ISI(G_1 +_{Q_t} G_2) < & \frac{9n_2 M_1(G_1)}{4} + \frac{n_1 M_1(G_2)}{4} + \frac{tn_2 M_2(G_1)}{4} + tn_2 M_2(L(G_1)) \\ & - \left(\frac{t+7}{2}\right) m_1 n_2 + \frac{3}{2} m_1 n_2. \end{aligned}$$

In a similar manner we can obtain the following result. The proof of the following theorem is omitted to make the presentation short.

Theorem 4. *Let G_1 and G_2 be two graphs where $n_i = |V(G_i)|$ and $m_i = |E(G_i)|$; $i = 1, 2$. Then,*

$$\begin{aligned} ISI(G_1 +_{T_t} G_2) < & \frac{1}{2}\{n_2(4-t)+m_2\} M_1(G_1) + \frac{n_1 M_1(G_2)}{4} + \frac{tn_2}{4} M_2(G_1) \\ & + \frac{tn_2}{4} M_2(L(G_1)) - \frac{(t+1)}{2} m_1 n_2 - 2m_1 n_2 + \frac{5m_1 m_2}{2}. \end{aligned}$$

4 Conclusion

The works related to the *ISI* index for various operations of graphs are found to be limited in the literature. In this work, we study the *ISI* index for extensions of $Q(G)$

and $T(G)$, namely Q_t and T_t graphs. We also establish bounds of *ISI* index of the related sums corresponding to Q_t and T_t graphs. The extremal cases of the bounds are also studied. In future study, one can consider the problem of finding better bounds of *ISI* index for these graph operations. Further, study of the extremal cases of the bounds to categorize the graphs can also be an interesting topic. In this communication, we have considered the operations based on Cartesian products only. They can be extended to other graph operations like lexicographic, join of graphs, etc.

5 Acknowledgement

Authors are grateful to all the anonymous reviewers for their valuable comments and suggestions.

References

1. An, M., Xiong, L.: Some results on the inverse sum indeg index of a graph, *Information Processing Letters* **134**, 42-46 (2018).
2. Chen, H., Deng, H.: The inverse sum indeg index of graphs with some given parameters, *Discrete Mathematics, Algorithms and Applications* **10(1)**, 1850006 (2018).
3. Eliasi, M., Taeri, B.: Four new sums of graphs and their Wiener indices, *Discrete Applied Mathematics* **157(4)**, 794-803 (2009).
4. Falahati, F-N., Azari, M., Doslić, T.: Sharp bounds on the inverse sum indeg index, *Discrete Applied Mathematics* **217(2)**, 185-195 (2017).
5. Gutman, I., Trinajstić, N.: Graph theory and molecular orbitals. Total π-electron energy of alternant hydrocarbons, *Chem. Phys. Lett.*, **17**, 535-538 (1972).
6. Gutman, I.: Degree-Based Topological Indices, *Croat. Chem. Acta*, **86(4)**, 351-361 (2013).
7. Hammack, R., Imrich, W., Klavžar, S.: Handbook of product graphs, CRC Press, (2011).
8. Hasani, M.: Study of inverse sum indeg index, *Journal of Mathematical Nanoscience*, textbf7(2), 103-109 (2017).
9. Matejić, M. M., Milovanović, I. Ž, Milovanović, E. I.: Upper bounds for the inverse sum indeg index of graphs, *Discrete Applied Mathematics* **251**, 258-267 (2018).
10. Onagh, B.N.: The harmonic index of product graphs, *Math. Sci.*, **11(3)**, 203-209 (2017).
11. Pattabiraman, K.: Inverse sum indeg index of graphs, *AKCE International Journal of Graphs and Combinatorics* **15(2)**, 155-167 (2018).
12. Raza, S., Bhatti, A. A., Ali, A.: More on comparison between first Geometric-Arithmetic index and Atom-Bond Connectivity index, *Miskolc Mathematical Notes*, **17(1)**, 561-570 (2016).
13. Sedlar, J., Stevanović, D., Vasilyev, A.: On the inverse sum indeg index, *Discrete Applied Mathematics* **184**, 202-212 (2015).
14. West, D. B.: Introduction to graph theory, Prentice Hall India, (2002).

Video-based Human Action Recognition using Multiclass Open set Classification

Swati Kulkarni
Department of Computer Engineering, Sardar Patel Institute of Technology, Maharashtra, India
Email: swati.kulkarni@spit.ac.in

Dhananjay Kalbande
Department of Computer Engineering, Sardar Patel Institute of Technology, Maharashtra, India
Email:drkalbande@spit.ac.in

Abstract. Multiclass open set classification implies the task of classi- fication in more than two known categories in open environment. The open environment is the case where all categories are not known in ad- vance. In this work, the proposed Intelligent Video Monitoring System presents human activity recognition from video-dataset using multiclass open set classification. Convolutional Neural Network is utilized for hu- man activity recognition. A new technique called CE Loss Thresholding is presented as a layer after the final layer of completely connected net- work of CNN design to accomplish openness for this classification. The Intelligent Video Monitoring System has differed applications in various fields, for example, security, sports, military applications, medical science, entertainment and many more. The implemented design for se- curity at sports complex will reduce human efforts, cost and will also be more accurate as it can identify and warn about unusual activities in real time.

Keywords: Multiclass Classification · Open Set Classification · Convo- lutional Neural Network.

1 Introduction

The advancements in computer vision and machine learning are motivating aca- demic and industrial researchers towards video event analysis where knowledge is extracted from activities being carried out in videoes. Especially the case of human activity recognition from videos can be connected to different fields like - surveillance systems from the security offices to decide anomalous or criminal action utilizing CCTV film.
In the present security monitoring systems, video substance are monitored by an administrators. As the number of screens increases, it becomes inconceivable for human operator to observe every one of the substance 24 X 7. In most of the cases, the CCTV footages are seen only after a disaster to understand the causes and causalities. In this

way, there is an extraordinary necessity of intelligent monitoring systems from the security organizations.

Human action recognition from videos has multiple applications. For exam- ple, accurate and smart observation is required for access control in sensitive zones a like military area, recognition of strange conduct at crowded places like shopping centers, railroad stations, hospitals, government structures, business premises, schools and many more where video analysis play vital role. In the medical field, even the doctors utilizes human movement recognition for various examinations and investigations. The movement recognition also very helpful to examine athletic developments and to plan reasonable and productive struc- tures for preparing. Movement recognition is also valuable in understanding and learning a passionate comprehension of creative move dance and acts like Indian Bharatnatyam and Salsa [1]. Action Interpretation from pictures can likewise be connected to web based information understanding from pictures posted on long range informal communication destinations. This data can be utilized for varied purposes.

The system presented in this work performs multiclass open set classification of human actions from video dataset. Multiclass classification is that the problem of distinguishing to that of a collection of more than two classes a brand new input belongs, on the idea of a training set of data containing inputs whose class membership is already known. However, most of the real situations demands classification of observations that doesn't belong to previously well-known class. For example, take into account CCTV footage, all actions captured don't seem to be essentially belonging from restricted trained categories. The unknown sample if tagged as known as per nearest trained category then the action predicted is inaccurate. In such cases the system ought to clearly specify unknown sample as unknown category. Such a classification wherever unknown sample isn't classified beneath well-known class rather identified as unknown or new class sample is termed as open set classification.

Consider a scenario of sports complex where activities like badminton, bowl- ing, archery, marching etc. are commonly observed. These well-known activities are the known classes and will form training dataset for the proposed system. The testing dataset consist of all known and unknown samples. However the network is trained only for the well-known classes. The test dataset may con- tain unknown samples. For each test sample, the confidence of prediction which is obtained from cross entropy loss function, is compared with threshold value and accordingly determine the class to which test data sample belongs. In other words, if the confidence of prediction is very low then the sample is classified as unknown category.

The proposed system will not only reduce human efforts but also will be cost effective, as deep convolutional neural network is used instead of any physical hardware or sensors. Three to five classes from UCF-101 video dataset are uti- lized for human action recognition issue for multiclass open set classification. UCF101 is an activity recognition video dataset of practical event recordings, gathered from YouTube. It has 101 action classes[2]. The remainder of the paper is organised as below sections namely, Background, Intelligent video monitoring system, Methodology, Implementation, Results and discussion, Conclusion and References. In the section of Intelligent video monitoring system, the new system is introduced to make current surveillance system

more intelligent and less de- pendent on human based security measures. The methodology section describes network and algorithms used. Details like tools and techniques are explained in the implementation section. Results are concluded and presented in the results and discussion. Finally the conclusion explains the overall impact of Intelligent video monitoring system on current practices of security surveillance systems.

2 Background

It was a challenging task to store information for long time and back propa- gate the error generated so that the network can be improved. This challenge was undertaken by Hochreiter in 1991 and, at that point solved it by introduc- ing a new, proficient, slope based method called "Long Short-Term Memory" (LSTM).This is oldest technique that can be effectively used for video-based human action recognition [3].However many new approaches were proposed to improve the efficiency in video analysis. In one of such efforts, author tends to the issue of human action identification as a procedure of identifying the activ- ities of the people by observing their activities and ecological conditions using SVM. It is a critical innovation which is broadly spread in light because of its promising applications in monitoring security, medicinal services and observing elderly people. The outcomes for discovery of exercises regardless of whether the individual is absent in the training set before are promising and introduced by and large identification accuracy of 89%[4]
An extensive number of datasets were created and made accessible for human activity and action recognition issue. Sixty-eight datasets were accounted for in this survey from 2001 to 2012. Weizmann, KTH, and CAVIAR are the most well- known datasets. Additionally, the creator features a standout amongst the most referred to dataset, UCF-Sports. Finally, the survey covers the requirement for a total portrayal of open datasets for video-based human action recognition and guide specialists toward that path [5]. Using UCF-101 and HMDB-51 datasets, another work shows a keen surveillance framework for elderly individuals and kids who a large portion of their time are home alone. Intelligent surveillance framework performs activity recognition utilizing three stream convolution neu- ral system. On the off chance that the framework identifies strange conduct, it raises a caution and tells relatives. The trial results demonstrate the accuracy of 93.42%. In any case, since its regulated preparing approach, the framework may fall flat for unknown information set [6]. In another work author additionally outlines the general systems for human movement recognition with correlation of different approaches connected. The dataset is a basic piece of calculation correlation and evaluation process[1].
In the current circumstance, the video event recognition is to a great ex- tent target focused. Along these lines, it faces incredible difficulties in support- able situations. To settle these difficulties the author proposed setting increased video event recognition approach. In this methodology, different sorts of settings are caught from three levels specifically image level, semantic level, and prior level [7]. Another author proposed a deep learning way to deal with identify true peculiarities in surveillance recordings. Because of the unpredictability of these practical peculiarities, utilizing just typical in-

formation alone may not be ideal for inconsistency location. They endeavour to exploit both typical and bizarre surveillance recordings [8]. However both these approaches are limited to known case prediction.

The open set recognition issue isn't very much tended to by existing calcula- tions since it requires strong speculation. To alleviate this issue, author present a new approach called "1-versus Set Machine", which shapes a choice space from the minimal separations of a 1-class or double SVM with a linear kernel [9]. This approach then became one of the early efforts for open set prediction.

In the next effort, authors define the issue as one of displaying positive train- ing information at the choice limit, where we can conjure the factual extraordi- nary esteem hypothesis. Another calculation called the PI-SVM is presented for evaluating the not standardized back likelihood of class consideration. In 2013, A Visual Recognition Challenge called as ImageNet caught the PC vision network's advantage. The best performing calculation on the 2013 ImageNet challenge, a convolutional neural system, accomplishes an error rate of 11.1%. Anyway the situation made a presumption that all classes are known during training period, which is not always the genuine case [10].

In one of the advances, author prepared a encoder network that maps an image to a latent space, and a generator network that maps latent space back to the image. The two networks are prepared together as an auto-encoder, with the target to limit the remaking blunder. Softmax Thresholding is utilized for open set characterization. Rather than methodologies for training techniques to make picture recognition models powerful to the open set of unknown classes, author proposed a strategy that requires no test-time calculation separated from a forecast for a solitary extra class [11].

By 2016, Deep networks have created huge increases for different visual recog- nition issues, prompting high effect academic and business applications. Authors present a reasoning to alter significant systems for open set acknowledgment, by exhibiting another layer, OpenMax Layer, which appraises the probability of information being from a dark class. An important part of assessing the dark probability is modifying Meta-Recognition thoughts to the establishment struc- tures in the second-last layer of the framework. OpenMax licenses rejection of "deceiving" and disengaged open set pictures showed to the system; OpenMax remarkably diminishes the amount of clear missteps made by a profound sys- tem. The proposed OpenMax, also one of the state-of-art method, beats open set acknowledgment precision of principal profound systems and furthermore profound systems with thresholding of SoftMax probabilities [12].

In 2017, creators proposed a summed up Sparse Representation based Classi- fication (SRC) figuring for open set acknowledgment where not all classes showed in the midst of testing are known in the midst of preparing. The SRC count uses class entertainment mistakes for gathering. As by far most of the discriminative information for open set acknowledgment is concealed in the tail some bit of the organized and sum of non-facilitated changing misstep flows, they demon- strate the tail of those two mistake appointments using the quantifiable Extreme Value Theory (EVT). By then they streamlined the open set acknowledgment issue into an arrangement of hypothesis testing issues. The conviction scores contrasting with the tail spreads of a novel test are then interlaced to choose its identity [13].

In 2018, in an another methodology authors present the mix of a recently planned open-

set graph-based optimum-path forest (OSOPF) classifier clubbed with genetic programming (GP) and large share casting a ballot combination strategies [14]. Few more approaches for open set classification were proposed in 2018. The vigorous research is still going on in this field. The author introduces Galaxy-X, a novel multi-class classification approach for open set recognition problems. They also introduce a novel evaluation procedure for evaluating open set classification. Experiments have been performed for handwriting digits and face recognition to find the efficiency of proposed algorithm [15]. Another ap- proach proposed was fuzzy ARTMAP based neural network to take care of the issue of single set face recognition in certifiable video surveillance situation [16]. The Deep neural networks immerged as one of the most promising technol- ogy in this field. In this work, author proposed a technique to identify camera model depending on convolutional neural networks. In contrast to conventional techniques, CNNs can naturally and at the same time remove highlights and figure out how to arrange amid the learning procedure. The CNN yields a dis- tinguishing proof score for every camera display. Exploratory correlation with a traditional two stages machine learning approach demonstrates that the pre- sented strategy can accomplish critical identification execution. The outstanding article recognition CNN models, AlexNet and GoogleNet, were likewise inspected [17].
In another effort author proposes a novel method where instead of classi- fying videos, they detect and localize all human-human activities occurring in continuous video. Using the spatio-temporal relationship match kernel, authors created complex and multiple activities detection model efficiently [18]. Another author proposes an approach called Dynamic bag of words which uses sequential nature of human activities to predict future human actions using prediction for- mulation proposed by them to measure posterior probability. The experimental results confirmed that the proposed system is able to identify the human actions at mush early stage than other existing methods [19]. Table 1 shows various algorithms proposed for Human Action Recognition and Open Set Classification:

3 Intelligent Video Monitoring System

Generally human operators are required at security offices of any premises for continuous observation of CCTV footage. In the less critical areas like shopping malls, school and colleges, sports complexes one or two officers monitor multiple screens at a time. However there is still considerable probability of missing minute details which may lead to greater mishap in future. These minute details are generally unusual activities. The proposed intelligent video monitoring system is designed to capture such details.
In this process the video clips which are being recorded on security cam- eras are sent to intelligent video monitoring system periodically. The system then classifies the frames for video clip into known and also unknown activities. Whenever an unknown activity is recorded by system, an alarm is generated at security office. Otherwise normal monitoring process continues (See Fig. 1). This way human operator now can monitor the system only if alarm generates. Hence it not only reduces the human efforts but also increases the accuracy in security measures as it can analyse very minute details from

the frames generated using video clips.

Table 1: Algorithms for Human Action Recognition and Open Set Classification

Year	Category	Algorithm
2012	Open Set Classification	1-vs-Set Machine[9]
2013	Human Action Recognition	Support Vector Machine [4]
2014	Open Set Classication	PI -SVM Algorithm[10]
2015	Human Action Recognition	Three Stream ConvNet[6]
2016	Human Action Recognition	context model based on Deep Boltzmann machine[7]
2016	Open Set Classication	OpenMax [12]
2017	Open Set Classication	Sparse Representation-based Classication (SRC) algorithm [13]
2018	Open Set Classication	Open-Set Optimum-Path Forest (OSOPF) [14]
2018	Open Set Classication	Galaxy-X [15]
2018	Open Set Classication	Softmax Threshold [11]
2018	Open Set Classication	ARTMAP [16]

4 Methodology

Convolutional Neural Network (CNN) is used for designing Intelligent video monitoring system. Fig. 2 depicts the network architecture of CNN used in the presented system.

4.1 Convolutional Neural Network

CNN is a class of deep neural network which uses multilayer perceptron in its architecture. It consists of convolution operation for feature extraction. Feature extraction process depends on structure of kernel. In case of deep learning li- braries like Pytorch, not only weights associated with neurons but also kernel learns as process progresses. We have used Kernel of size 5 X 5 with stride of 1 and zero padding. In the first layer of CNN, since we have used colour image we have three input channels. Sixteen kernels are used hence producing sixteen output channels. In the second layer of CNN we get 16 input channels from layer1 and we produce 16 output channels for further processing (see Fig. 2).

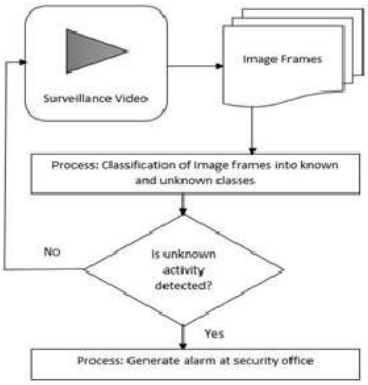

Fig. 1: Intelligent Video Monitoring System

4.2 ReLU Activation

ReLU stands for Rectified Linear Unit, which acts as activation function in this network. The function is specified as:

$$f(a) = max(0, a)$$

4.3 Max Pooling

Pooling is one of the very important concept of CNN. In case of max pooling, the input image is partitioned based on the size of kernel and maximum of those values is provided as output. It reduces the spatial size of input image.

4.4 Fully Connected Network

This layer is nothing but multilayer perceptron network, where neurons from each layer have connections to activations of previous layer. This later makes use of cross entropy loss function to calculate difference between predicted output and actual output. Stochastic gradient descent optimizer is used to back propagate the loss and adjust the weights for next epoch.

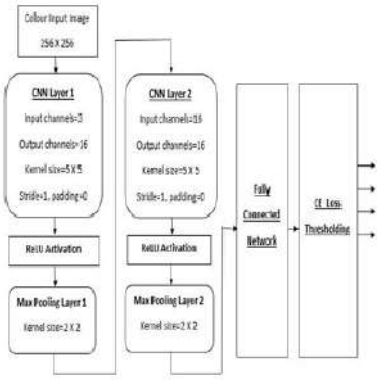

Fig. 2: Intelligent Video Monitoring System

4.5 CE Loss Thresholding

Fully connected network provides closed set classification. To make it open set, the new method called CE Loss thresholding is used at the end of fully connected layer. The cross entropy loss function is used for calculation of threshold value. Threshold is calculated at the time of training. Hence if loss at testing is greater than threshold then the input sample is considered as unknown class. Below steps are used to calculate CE Loss threshold value:

1. Training Phase: Calculate cross entropy loss for each frame in training phase.
2. Training Phase: Compare the loss value with maximum loss incurred at any point. If current loss is greater than previous maximum loss, then assign current loss to maximum loss.
3. Testing Phase: Set CE Loss Threshold value as maximum loss value calcu- lated during training phase.

Since unknown class samples will naturally have more loss than known class sample, the selected threshold value effectively differentiates unknown class samples from known class samples.

Implementation

The implementation is carried out in three stages namely, pre-processing phase I, pre-processing phase II and final phase.

1. Pre-processing Phase I: This phase consists of frame extraction for training CNN. In this phase various sports classes from UCF-101 video dataset are selected and all the videos in those classes are converted to set of image frames corresponding to each video using FFMPEG library. The images generated are of size 256 X 256 in jpeg format.
2. Pre-processing Phase II: This phase consists of dataset preparation. To cap- ture only useful information from generated images, center cropping is per- formed converting input image size to 224 X 224. These images are then converted to Pytorch Tensors. The tensors are then loaded to Train and test Data Loaders so as to make data set iterable.

3. Final Phase: Below steps are carried out in Final Phase:
– Define the Model class and forward function using Pytorch and Torch Vision libraries for utilizing deep learning framework of Convolutional Neural Network.
– Set number of epochs using below formula

$$Numberofepochs = \frac{Noofiterations}{\frac{length(Traindata)}{Batchsize}}$$

-Instantiate the model class
-Calculate the loss using cross entropy loss function
-Update the parameters using Stochastic Gradient Descent optimizer
-Train the Model.
-Perform CE Loss Threshold calculation during Training phase
-Test and Evaluate the model using Accuracy, Precision, Recall and F-measure.

5 Results and Discusssion

The classification is performed for three, four and five known classes and one unknown class. The results are evaluated on below parameters:
– Openness($O^{'}$): The openness is determined by using below formula:

$$O^{'} = 1 - \sqrt{\frac{2*nooftrainingdata}{nooftargetdata+nooftestingdata}}$$

The openness value equals to zero indicates closed set. Since we are training with three classes and testing with four including unknown class we get openness equals to 0.134.
– Precision($P^{'}$): Precision is calculated using below formula:

$$P^{'} = \frac{TPS}{TPS+FNS}$$

The results are depicted in fig 3.
-Recall($R^{'}$): Recall can be calculated as:

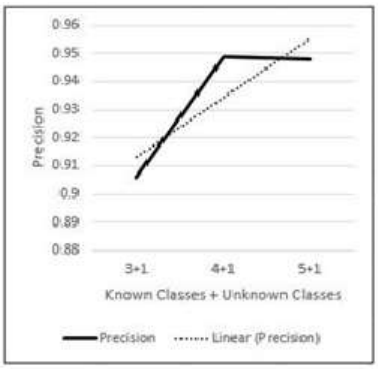

Fig. 3: Intelligent Video Monitoring System

$$R^{'} = \frac{TPS}{TPS+FPS}$$

The results are depicted in fig 4.
–F-measure($F^{'}$): F-measure is calculated as harmonic mean of precision and recall:

$$F^{'} = 2 * \frac{P^{'} * R^{'}}{P^{'}+R^{'}}$$

The results are depicted in fig 5.
–Accuracy($A^{'}$): The accuarcy is calculated as:

$$A^{'} = 100 * \frac{TPS+TNS+TUS}{total}$$
$$total = TPS + FPS + TNS + FNS + TUS + FUS$$

where, TPS and FPS stands for True positive samples and True negative samples respectively. TNS and FNS stands for True negative samples and False negative samples respectively. TUS and FUS stands for True reject
samples and False reject samples respectively for unknown class. The results are de-

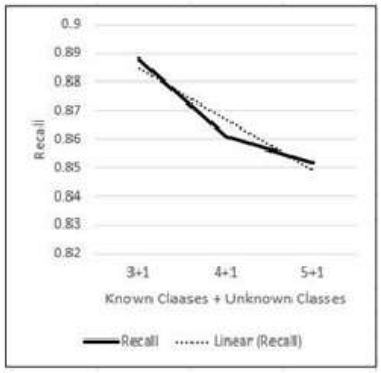

Fig. 4: Intelligent Video Monitoring System

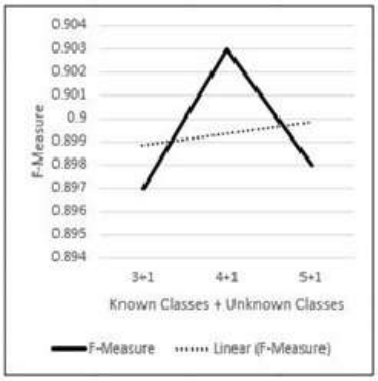

Fig. 5: Intelligent Video Monitoring System

picted in fig 6 and comparison of our model with existing state-of-the- art models is shown in fig 7.
The implementation results shows that the accuracy of 'Intelligent Video Monitoring System' is even comparable to closed set human action recogni- tion models

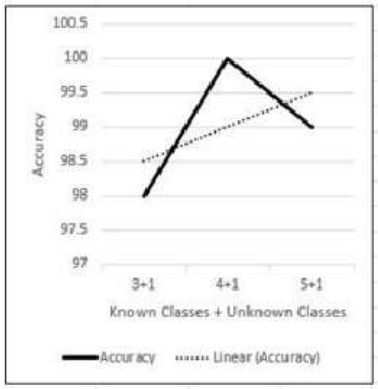

Fig. 6: Intelligent Video Monitoring System

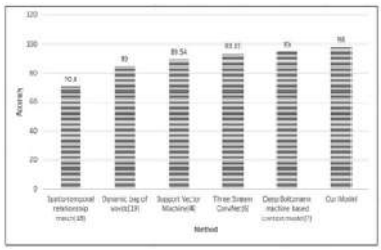

Fig. 7: Intelligent Video Monitoring System

6 Conclusion

Convolutional neural networks coupled with CE Loss Thresholding layer pro- vided 98% to 99.9% accuracy for human action recognition in open set environ- ment for three, four and five known classes of UCF-101 video dataset. Video- based human action recognition in open-set environment has varied applications in multiple domains. Especially in security domain, Intelligent video monitoring system can be effectively used to identify suspicious or criminal activity in real time. The proposed systems will not only reduce human efforts and cost but also accurately identify and warn about unusual activities captured in CCTV footage at that instant itself.

References

1. Geetanjali Vinayak Kale, Varsha Hemant Patil, "A Study of Vision based Human Motion Recognition and Analysis", International Journal of Ambient Computing and Intelligence, Volume 7, Issue 2, 2016.
2. Khurram Soomro, Amir Roshan Zamir and Mubarak Shah, "UCF101: A Dataset of 101 Human Actions Classes From Videos in The Wild", Center for Research in Computer Vision, University of Central Florida, 2012.
3. Sepp Hochreiter, Jurgen Schmidhuber, "Long Short-term Memory", Neural Com- putation, 1997.
4. Megha D Bengalur, "Human Activity Recognition Using Body Pose Features and Support Vector Machine", IEEE, 2013.
5. Jose M. Chaquet, Enrique J. Carmona a, Antonio Fernndez-Caballero, "A survey of video datasets for human action and activity recognition", Computer Vision and Image Understanding, 2013.
6. Chang-Di Huang, Chien-Yao Wang, and Jia-Ching Wang, "Human Action Recog- nition System for Elderly and Children Care Using Three Stream ConvNet", ICOT 2015, IEEE, 2015.
7. Xiaoyang Wang, "Hierarchical Context Modeling for Video Event Recognition", IEEE Transaction on Pattern Analysis and Machine Intelligence, Vol. 39, No. 9, 2017.
8. Waqas Sultani, Chen Chen, Mubarak Shah, "Real-world Anomaly Detection in Surveillance Videos", Center for Research in Computer Vision (CRCV), Uni- versity of Central Florida (UCF), 2018.
9. Walter J. Scheirer, Member, IEEE, Anderson Rocha, Member, IEEE, Archana Sap- kota, Student Member, IEEE, and Terrance E. Boult, Member, IEEE, "Towards Open Set Recognition", IEEE Transaction on Pattern Analysis and Machine Intel- ligence, 2012.
10. Lalit P. Jain, Walter J. Scheirer, and Terrance E. Boult, "Multi-Class Open Set Recognition Using Probability of Inclusion", 2016 IEEE Conference on Computer Vision and Pattern Recognition, http://link.springer.com/chapter/10.1007/978-3- 319-10578-9 26, 2014.
11. Lawrence Neal, Matthew Olson,Weng-Keen Wong, Xiaoli Fern, & Fuxin Li, "Open Set Recognition With Generated Data", Workshop track - ICLR 2018, Oregon State University, USA, 2018.
12. Abhijit Bendale, Terrance E. Boult, "Towards Open Set Deep Networks", 2016 IEEE Conference on Computer Vision and Pattern Recognition, University of Colorado at Colorado Springs, 2016.
13. He Zhang, "Sparse Representation-based Open Set Recognition", IEEE Transac- tion on Pattern Analysis and Machine Intelligence, 2016.

14. Manuel Alberto, Crdova Neira, Pedro Ribeiro, Mendes Jnior, Anderson Rocha, and Ricardo Da Silva Torres, “Data-Fusion Techniques for Open-Set Recognition Problems”, IEEE Access, Volume 6, 2018.
15. Wajdi Dhifli and Abdoulaye Banire Diallo, “Toward an Efficient Multi-class Clas- sification in an Open Universe”, International Conference on Machine Learning and Data Mining MLDM 2016, New York, USA, University of Quebec At Montreal, 2018.
16. Wasseem N. Ibrahem Al-Obaydy, Shahrel Azmin Suandi, “Open-set single-sample face recognition in video surveillance using fuzzy ARTMAP”, Neural Computing and Applications, https://doi.org/10.1007/s00521-018-3649-0, Springer, 2018.
17. Amel Tuama, Frdric Comby, Marc Chaumont, “Camera Model Identification With The Use of Deep Convolutional Neural Networks”, WIFS: Workshop on Informa- tion Forensics and Security, Dec 2016, Abu Dhabi, United Arab Emirates., IEEE International Workshop on Information Forensics and Security, 2017
18. M. S. Ryoo and J. K. Aggarwal, “Spatio-Temporal Relationship Match: Video Structure Comparison for Recognition of Complex Human Activities”, Proceedings of the IEEE International Conference on Computer Vision (ICCV), Kyoto, Japan, 2009
19. M. S. Ryoo, “Human Activity Prediction: Early Recognition of Ongoing Activi- ties from Streaming Videos”, IEEE International Conference on Computer Vision (ICCV), Barcelona, Spain, 2011

JOURNAL OF TRIPURA MATHEMATICAL SOCIETY

Notes for Contributors and Subscribers

1. The Journal is devoted to publish original research papers in different branches of mathematics and soft computing. All articles will be reviewed.
2. The submission of a manuscript implies that it is not being considered for publication elsewhere.
3. Papers should be written in English and accompanied by an abstract of about 100 words. A list of key words and AMS Subject classifications should be put at the end of the abstract.
4. The manuscript must be prepared in MS-Word and PDF format on one side of the A4 size paper in single spacing with 14.5cm×18cm [5.75″ × 7″], font sizes should be 11 and blocks of the Mathlab if any for Tables/Equations/Graphs/Figures should be converted into JPG and placed inside the text in appropriate place. The Foot-notes should be avoided.
5. References should be listed alphabetically (on first author's surname) at the end of the paper. For example.,

   [1] L. Gillman and M. Jerison, *Rings of Continuous Functions*, Van Nostrand, Princeton, 1960.

   [2] L. A. Zadeh, Fuzzy Sets, *Information and Control* , 8 (1965) 338-353.

6. The Galley proofs will be sent to the corresponding author for corrections and must be returned within 3 days from the date of receipt.
7. If an article is accepted for publication, the author will be asked to transfer the copy-right of the article to the publisher.
8. Acknowledgements if any, may be placed at the end of the paper just before the references.
9. There is no page charges for publishing an article. The corresponding author will be provided a soft copy in PDF of the published article.
10. The subscription rate per volume including ordinary postage for **Institutions -** Rs. 500.00 in India and US $100.00 elsewhere;
11. The subscription/page charge may be deposited in cash / e-transfer to TRIPURA MATHEMATICAL SOCIETY at the **State Bank of India, MBB College branch (Agartala), A/C No. 10333227328 [IFS code: SBIN0009126].**

The author(s) should submit the article to the following E-mail addresses:

Prof. Binod Chandra Tripathy, Editor-in-Chief, JTMS, Tripura University
tripathybc@yahoo.com ,

JOURNAL OF TRIPURA MATHEMATICAL SOCIETY

Website :https://sites.google.com/view/tms-in/download
E-mail:tms.agartala@gmail.com

Volume – 23 Published: December, 2021

Contents (2 pages)

JOURNAL OF TRIPURA MATHEMATICAL SOCIETY

Website : https://sites.google.com/view/tms-in/download
E-mail: tms.agartala@gmail.com

Volume – 23 Published: December, 2021

Contents (2)

Subscription of Volume- 23

Institution : Rs.500.00(India), Outside India - $100; **Individual** : Rs. 250.00

Member of TMS(from Agartala): Rs.100.00

Published and Printed by General Secretary on behalf of Tripura Mathematical Society, Agartala, India.

Editor-in-Chief: Prof.B.C.Tripathy